Accurate ion beam analysis

Ghislain Boudreault

Thesis presented to the Department of Electronic and Electrical Engineering, University of Surrey, for the award of Doctor of Philosophy (Ph.D.)

School of Electronics and Physical Sciences
University of Surrey
Guildford, Surrey GU2 7XH, UK

August 2002

Perfection is very boring, because it does not leave room for improvement.

Oscar Wilde (1854-1900)

La mort est une ligne d'arrivée d'une course entre le temps et la vie; et le temps gagne lorsqu'il est perdu.

Ghilt (1967-…)

There must be somebody there, because somebody must have *said* "Nobody."

Winnie-the-Pooh (?-…)

To my family, my precious friends, and to all of those who, in their everyday life, have breakfast with ambition, have lunch with perseverance, have dinner with passion, and sleep with dreams...

ABSTRACT

This thesis primarily deals with accuracy obtainable when using IBA (Ion Beam Analysis) techniques to characterize materials. RBS (Rutherford Backscattering Spectrometry) is the main technique used, together with EBS (Elastic Backscattering Spectrometry), ERDA (Elastic Recoil Detection Analysis) and NRA (Nuclear Reaction Analysis). An exhaustive literature review on these analytical methods is made in connection with accuracy issues such as stopping powers and multiple scattering. The experimental set-ups and procedures are described, with emphasis laid on critical aspects of work where the highest accuracy is required.

The instrumentation for dosimetry on ion implanters is first established at the 1% level for high-dose heavy implants in silicon. A new parameterisation of He stopping power in Si is used, and this latter material, via the surface yield, is used as a calibration standard. A precision (standard uncertainty) in the determination of implantation doses by RBS is conclusively demonstrated at 1.5%. The IBA DataFurnace code is validated for such accurate analysis, which can now be made routinely and rapidly. The certified Sb sample IRMM-302/BAM-L001, which has a certification of 0.6% traceable to the international standard of weight in Paris, is measured, and more importantly this measurement demonstrates the reliability of the stopping power parameterisation at 1.4%.

Using conventional ERDA, the H dose of an amorphised Si wafer, implanted with 6-keV H^+ ions, is found to be 57.8(1.0) $\times 10^{15}$ at./cm^2, which is a 1.8% standard uncertainty. The estimated combined uncertainty of this measurement is ~6%, and this mainly comes from the determination of the ERDA solid angle by using standard Kapton. The Kapton composition is carefully determined using RBS. The RBS solid angle is obtained using the amorphised silicon surface yield as a calibration standard as in the dosimetry analysis mentioned above. The ERDA H absolute dose obtained is compared with the results from other participants from all over the world in a Round Robin exercise, which includes measurements by using both He-ERDA and HI-ERDA (Heavy Ion-ERDA) together using various detectors. The results from each participant are given and compared. The overall absolute dose obtained of the implant is 57.0(1.2)$\times 10^{15}$ H/cm^2, and this represents an inter-lab reproducibility of

2.2% (standard uncertainty). Unstable surface hydrogen contamination was observed, and this surface peak was resolved by some of the methods. This implant can now be used as a standard for quantitative analysis of hydrogen.

Low-fluorine content SiO_2:F films are analysed by RBS for absolute fluorine concentration determination. Prior to the RBS analysis, the uniformity of the films and stability of F under beam irradiation is investigated. Because the RBS is not very sensitive to F and the F signal has a large matrix background, an internally consistent method of data handling, which enables the relative collected charge to be determined very precisely for the spectra from different samples, is developed. This method has as a parameter the F content, which is then extracted iteratively. A F concentration of 10 at% is determined with an estimated uncertainty of 10% (one percentage point, i.e. 10 ± 1%). The O stopping powers are found to be the main factor governing the accuracy of the absolute determination of the F content. All the other uncertainties add up to only ~1%.

The elemental composition of residual deposits from an ion implanter is thoroughly investigated using several complementary analytical methods, namely, RBS, EBS and NRA. Preliminary SEM/EDAX results are used as a guide. Depth profiles of such non-homogeneous, non-flat and brittle samples are obtained, which give an indication of the concentration of each element present. From this complete IBA elemental study, some unprecedented light is brought on both the history of the implanter and the way in which these deposits are formed.

Such an investigation is essential for a better understanding and the development/miniaturisation of semiconductors as it impressively pushes the boundaries of accuracy obtainable in IBA material characterisation.

Keywords: Ion Beam Analysis, Accuracy, RBS, ERDA, EBS, NRA, Stopping powers, Thin film, Silicon, Implant, Semiconductor, Standard

MEMORANDUM

This dissertation is submitted in fulfilment of the requirements for admission to the degree of Doctor of Philosophy at the University of Surrey. It describes the research carried out full time from August, 1999 to August, 2002 under the supervision of Dr Chris Jeynes.

All the work presented, except that acknowledged along with that from the contribution of a few collaborators which is included for completeness, is my own independent research. The contributory content is as following: sections 3.1.1 and 5.4.1, from Dr R.G. Elliman, Dr H. Timmers and Dr T.D.M. Weijers (Department of Nuclear Physics, Research School of Physical Sciences and Engineering, and also Department of Electronic Materials Engineering, Australian National University, Canberra, Australia); sections 3.3.2 and 5.4.2, from Dr Willie Lennard (University of Western Ontario, London, Canada); sections 3.3.3 and 5.4.3, from Dr E. Rauhala and Dr T. Sajavaara (Accelerator Laboratory, University of Helsinki, Finland); sections 3.4.4 and 5.4.4, from Dr R. Grötzschel (Forschungszentrum Rossendorf, Germany); sections 3.3.5 and 5.4.5, from Dr S.C. Gujrathi (Department of Physics, University of Montreal, Canada); section 6.2.1 and XRF results in section 6.5, from Dr K.S. Wong (School of Electronic & Electrical Eng., Nanyang Technological University, Singapore); and section 7.3, from Mr S. Redpath (School of Engineering, University of Surrey, Guildford, UK). Each of these sections is a paraphrase of the reports as given by the corresponding contributors; the responsibility of the exactness of the details and results given in these specific sections must fall to them.

G. Boudreault
15 August, 2002
University of Surrey

ACKNOWLEDGEMENTS

First and foremost, I would like to deeply thank my supervisor and friend, Dr Chris Jeynes, for his thorough guidance, his support, his patience, his generosity, and for keeping me extremely… busy! I have been very happy to work with someone who always demonstrates cheerfulness, is never run out of ideas, is highly respected in his field and continuously develops collaborations, and I am indebted to him for the success of my Ph.D. On a more entertaining level, I took great pleasure in letting him take care of my *English education*: I have really been amused of being introduced by him to English culture, from Oscar Wilde to King James version of the Bible passing by Winnie-the-Pooh! In short, this has been such an outstandingly good relationship that, sometimes, it was difficult to say who was the obedient servant of whom!

I cannot afford not to acknowledge my second supervisor, Professor Roger Webb, especially for being always available when I needed him to get computing problems sorted.

I am extremely grateful to SCRIBA for its financial support. I was really happy when I was offered a sponsored M.Phil. project leading to Ph.D. here at Surrey University, in the SCRIBA group, so that I could have the opportunity to do postgraduate studies and discover at the same time this nice country. Specially, I would like to thank the head of this research group, Professor Brian Sealy, who is very understanding and always took time to listen to my queries. It is also imperative to show my gratitude to Mrs Karen Arthur, the attentive secretary of IBC; I had to put my destiny in her hands a couple of times, and as you can see I am still alive!

I would like also to express my gratitude to Dr Elke Wendler, who was here for my first year, and is now at the Institut für Festkörperphysik, Friedrich-Schiller-Universität, at Jena in Germany. Her help and her complicity were invaluable. I really enjoyed to work, collaborate and share some moments outside work with her.

I must mention Dr Russell Gwilliam and specially Dr. Ahmed Nejim for their amiable collaboration inside SCRIBA. I take here occasion also to express that I extremely esteemed the kindness and professionalism of Dr Karen Kirkby; it was a real enjoyment to be involved in a few projects with her.

I cannot forget to bring up the precious help and friendly relationship of Mr Chris Burt, the technician at the D.R. Chick Laboratory. This kind of person is necessary to make a newcomer from abroad feel more comfortable in a laboratory. After Mr Chris Burt's departure, I relied on Mr Adrian Cansell and Mr John Mynard to give me a hand sometimes in the lab, and I can only be utterly grateful to them for their invaluable help and advice. Thanks also to Mr Vernon Power from the FAB lab for his constant serviceability.

Professor A.S. Clough, from the Physics department, was a major IBC user, and it was a renewed pleasure to work and interact with him in the D.R. Chick Laboratory. I sincerely appreciated his sereneness, relaxing humour and humble kindness. It is very comforting, in a world sometimes unhealthily competitive, to receive that much respect from such a well-established senior researcher when one starts his career. Thanks to him also for accepting to be my internal examiner.

Dr David Lane, from the Department of Materials and Medical Sciences, Cranfield University, played the role of the external examiner. He really went through the thesis with a tooth comb; his revision, from general aspects to minutiae, has led undoubtedly to an improved final version of the thesis. I can only be thankful to him.

I would like to express thanks to Dr Willie Lennard from University of Western Ontario, London in Canada, who devotedly and kindly received me in his laboratories, had me view them and allowed me to give a seminar there. And that was an honour for me to collaborate with him in a couple of projects subsequently. I visited the laboratories of and gave a seminar at the Institut de Physique Nucléaire de Lyon, Lyon in France, and I am grateful to Dr Alain Chevarier. I have been invited to visit the facilities of and give a seminar at the Groupe de Physique des Solides, Paris in France, and my thanks go to Dr Ian Vickridge. I am thankful to Dr Guy Ross for receiving me unexpectedly and giving me a tour of his research centre at the Institut National de Recherche Scientifique-Energie et Matériaux, at Montreal in Canada. I have been more than delighted to be given access for a visit to the access-restricted characterisation laboratories of the Musée du Louvre, Paris in France, and all my acknowledgements fall to Dr Jean-Claude Dran (Centre de recherche et de restauration des musées de France).

Such a comprehensive and in-depth work can hardly be accomplished without the contribution of some collaborators. I would be angry with myself if I did not render some credit to those who somehow made a contributory effort in some of the joint projects included in this thesis, and these are: Mr S. Redpath (School of Engineering, University of Surrey, Guildford, UK), Dr R. Grötzschel (Forschungszentrum Rossendorf, Germany), Dr S.C. Gujrathi (Department of Physics, University of Montreal, Canada), Dr E. Rauhala (Accelerator Laboratory, University of Helsinki, Finland), Dr T. Sajavaara (Accelerator Laboratory, University of Helsinki, Finland), Dr R.G. Elliman (Department of Electronic Materials Engineering, Australian National University, Canberra, Australia), Dr H. Timmers (Department of Nuclear Physics, Research School of Physical Sciences and Engineering, and also Department of Electronic Materials Engineering, Australian National University, Canberra, Australia), Dr T.D.M. Weijers (Department of Nuclear Physics, Research School of Physical Sciences and Engineering, and also Department of Electronic Materials Engineering, Australian National University, Canberra, Australia), Dr N.P. Barradas (Instituto Tecnologico Nuclear, Sacavem, Portugal), Dr U. Wätjen (EC-JRC, Institute for Reference Materials and Measurements [IRMM], B-2440 Geel, Belgium), and Dr K.S. Wong (School of Electronic & Electrical Eng., Nanyang Technological University, Singapore). The last three of them must receive my special thanks for their particular interest, involvement, and thorough revision of some of the paper work.

On a more personal level, I cannot miss the chance to thank all the people around whom I had some great time with, and my family together with some precious friends of mine in Canada, especially Mr Eric Irissou, for their support in general. I would like to address a particular thank to my officemate Miss Claudia Cerrina, who spiced up my life a little, was the one I could lean on during the hardest times, and mostly she has been an incredible source of motivation in the last moments of my Ph.D. — sorry Claudia for finishing before you!

Finally, this expression of appreciation would not be complete if I did not confess that I deeply enjoyed my stay in England, and I do not regret my choice. I even wish sometimes that our Powers that be would have put a couple of roundabouts in Quebec!

Ghislain Boudreault

LIST OF PUBLICATIONS

- Boudreault G., Jeynes C., Wendler E., Nejim A., Webb R.P., Wätjen U., *Accurate RBS measurement of ion implant doses in silicon*, Surf. and Interf. Anal., **33** (2002) 478-486

- Jeynes C., Barradas N.P., Marriott P.K., Boudreault G., Jenking M., Wendler E., Webb R.P., *Elemental thin film depth profiles by ion beam analysis using simulated annealing – a new tool*, submitted to J. of Phys. D topical review (2002)

- Boudreault G., Elliman R.G., Grötzschel R., Gujrathi S.C., Jeynes C., Lennard W.N., Rauhala E., Sajavaara T., Timmers H., Weijers T.D.M., *Round Robin: Accurate measurement of H implants in silicon using ERDA*, to be submitted to Nucl. Instr. and Meth (2002)

- Boudreault G., Jeynes C., Wong K.S., *Accurate determination of fluorine content of SiO_2:F films using RBS*, to be submitted to Surf. and Interf. Anal. (2002)

- Mefo J., Kirkby K.J., Sealy B.J., Boudreault G., Jeynes C., Collart E.J.H., *Elemental analysis of residual deposits in an ion implanter using IBA techniques*, submitted to IEEE Proceedings of the 14th International Conference on Ion Implantation Technology (IIT) (2002)

- Winston S.H., Gwilliam R.M., Sealy B.J., Boudreault G., Jeynes C., Webb R.P., Kirkby K.J., *Evaluation of the Boron activation and depth distribution using BBr_2^+ implants*, submitted to IEEE Proceedings of the 14th International Conference on Ion Implantation Technology (IIT) (2002)

- Claudio G., Boudreault G., Jeynes C., Sealy B.J., Low R., *Absolute dose performance of the SWIFT single wafer ion implanter*, submitted to IEEE Proceedings of the 14th International Conference on Ion Implantation Technology (IIT) (2002)

- Zarrug H., Mefo J., Sealy B.J., Boudreault G., Jeynes C., Webb R.P., Kirkby K.J., Collart E.J.H., *Characterization and environmental impact of plasma products within an ion implanter*, submitted to IEEE Proceedings of the 14th International Conference on Ion Implantation Technology (IIT) (2002)

- Finnis R., Boudreault G., Webb R.P., Jeynes C., Fellows D.F., van den Broek R., *A six movement goniometer for accurate automatic ion beam analysis*, Proceedings of the 15th IBA (Ion Beam Analysis) Conference (2001)

☞ Webb R.P., Winston S.H., Gwilliam R.M., Sealy B.J., Boudreault G., Jeynes C., Kirkby K.J., *Comparison of boron halide, decaborane and B implants in Si from molecular dynamics simulations*, to be submitted to Nucl. Instr. and Meth. for March 2003

GLOSSARY OF TERMS

ADC	Analogue-toDigital Converter
amu	atomic mass unit
BI	Bayesian Inference
BIPM	Bureau International des Poids et Mesures
BLR	Base Level Restoration
CAB	Cores And Bonds
CODATA	Committee on DATA for science and technology
CVD	Chemical Vapour Deposition
DMAc	DiMethyl-Acetemide
EBS	Elastic Backscattering Spectrometry
EDAX	Energy Dispersive Analysis of X-rays
ERDA	Elastic Recoil Detection Analysis
FTIR	Fourier Transform InfraRed
FWHM	Full Width Half Maximum
GUM	Guide to the expression of Uncertainty in Measurement
GVM	Generating VoltMeter
HE	High Energy
HIBS	Heavy Ion Backscattering Spectrometry
HI-ERDA	Heavy Ion-Elastic Recoil Detection Analysis
HPD-CVD	High Density Plasma-Chemical Vapour Deposition
HV	High Vacuum
IBA	Ion Beam Analysis
IBC	Ion Beam Centre

IBIC	Ion Beam Induced Current
IBM	Ion Beam Modification
ICP-IDMS	Inductive Coupled Plasma-Isotope Dilution Mass Spectrometry
IL	IonoLuminescence
INAA	Instrumental Neutron Activation Analysis
ISI	Institute for Scientific Information
ISO	International Organisation for Standardization
LE	Low Energy
LEIS	Low Energy Ion Scattering
LN	Liquid Nitrogen
MCB	MultiChannel Buffer
MCMC	Markov Chain Monte Carlo
MEIS	Medium Energy Ion Scattering
NDF	Nuno's DataFurnace
NIM	Nuclear Instrumentation Module
NRA	Nuclear Reaction Analysis
PI	PolyImide
PIGE	Proton Induced Gamma Emission
PIXE	Proton Induced X-ray Emission
RBS	Rutherford Backscattering Spectrometry
ROI	Region Of Interest
SA	Simulated Annealing
SEM	Scanning Electron Microscopy
SI	Système International
SIMS	Secondary Ion Mass Spectromety
SOI	Silicon On Insulator

STIM	Scanning Transmission Ion Microscopy
TFU	Thin Film Unit
UHV	Ultra High Vacuum
ULSI	Ultra Large Scale Integration
VLSI	Very Large Scale Integration
WiNDF	Windows Nuno's DataFurnace
XPS	X-ray Photoelectron Spectrometry
XRD	X-Ray Diffraction
XRF	X-Ray Fluorescence

CONTENTS

ABSTRACT v

MEMORANDUM vii

ACKMOWLEDGEMENTS ix

LIST OF PUBLICATIONS xiii

GLOSSARY OF TERMS xv

CONTENTS xix

LIST OF FIGURES xxv

LIST OF TABLES xxxi

CHAPTER 1
INTRODUCTION 1-1
1.1 Materials characterization 1-1
1.2 Ion Beam Analysis (IBA) 1-2
1.2.1 Rutherford Backscattering Spectrometry (RBS): Milestones 1-2
1.2.2 Different IBA techniques 1-5
1.2.2.1 Low-Energy IBA 1-5
1.2.2.2 Medium-Energy IBA 1-6
1.2.2.3 High-Energy IBA 1-6
1.3 Overview of the thesis 1-8
1.3.1 Topic: IBA and accuracy 1-8
1.3.2 Outlines 1-10

CHAPTER 2
THEORETICAL BACKGROUND 2-1
2.1 Rutherford Backscattering Spectrometry (RBS) 2-1
2.1.1 Principle 2-1
2.1.2 Scattering process 2-4
2.1.3 Collision kinematics (*what?*) 2-5
2.1.4 Cross-section (*how much?*) 2-8
2.1.4.1 Rutherford scattering 2-8
2.1.4.2 Elastic non-Rutherford scattering — Elastic Backscattering Spectrometry (EBS) 2-11
2.1.4.3 Inelastic scattering — Nuclear Reaction Analysis (NRA) 2-12
2.1.4.4 Screening correction 2-13
2.1.4.5 Multiple and plural scattering 2-14
2.1.5 Energy loss (*where?*) 2-16
2.1.5.1 Stopping cross-section 2-16
2.1.5.2 Stopping cross-section factor and surface energy approximation 2-18
2.1.5.3 Depth resolution 2-20
2.1.5.4 Energy straggling 2-20
2.1.5.5 Stopping power accuracy 2-21
2.1.6 RBS standards 2-24
2.1.7 Channelling 2-25

2.1.8 Pile-up 2-26
2.1.9 Important parameters 2-27
2.1.10 New IBA tool: DataFurnace 2-28
2.2 Elastic Recoil Detection Analysis (ERDA) 2-29
2.2.1 General description 2-29
2.2.2 Milestone 2-30
2.2.3 Collision kinematics 2-32
2.2.4 ERDA variants 2-34
2.2.4.1 Conventional ERDA 2-34
2.2.4.2 TOF-ERDA 2-36
2.2.4.3 ERDA E×B 2-38
E-E telescope ERDA 2-39
2.2.4.5 Coincidence ERDA 2-40
2.2.5 Multiple and plural scattering 2-42
2.2.6 Calibration standards 2-43
2.3 Beam damage 2-44
2.3.1 Types of processes and defects 2-44
2.3.2 Charge accumulation effects 2-45
2.3.3 Elemental losses 2-45

CHAPTER 3
EXPERIMENTAL DETAILS 3-1
3.1 Surrey (RBS, ERDA, NRA) 3-1
3.1.1 IBA facility 3-2
3.1.1.1 General description 3-2
3.1.1.2 Van de Graaff energy control and beam stabilization 3-3
3.1.2 RBS set-up 3-6
3.1.2.1 General description 3-6
3.1.2.2 Calibration of RBS scattering angle of the detectors 3-10
3.1.2.3 Electronics linearity 3-13
3.1.2.4 Electronics calibration (gain and offset) 3-15
3.1.3 ERDA experimental procedure 3-15
3.1.3.1 Goniometer and detectors 3-16
3.1.3.2 Vacuum 3-17
3.1.3.3 Electronics calibration 3-17
3.1.3.4 RBS solid angles 3-17
3.1.3.5 Glancing angle: charge correction factor 3-18
3.1.3.6 Kapton composition 3-18
3.1.3.7 ERDA detector solid angle 3-19
3.1.4 NRA set-up 3-19
3.1.4.1 Beam line (L5) 3-19
3.1.4.2 Target chamber 3-20
3.2 Jena (RBS) 3-20
3.3 Participants of the ERDA Round Robin exercise 3-21
3.3.1 Canberra (Australia) 3-22
3.3.1.1 Experimental set-up 3-22
3.3.1.2 Detection of C, O and Si 3-23
3.3.1.3 Detection of H 3-24
3.3.2 London (Canada) 3-26
3.3.3 Helsinki (Finland) 3-27
3.3.4 Rossendorf (Germany) 3-27
3.3.4.1 HI-ERDA experiment 3-27
3.3.4.2 NRA experiment 3-28
3.3.5 Montreal (Canada) 3-28

CHAPTER 4
ACCURATE RBS MEASUREMENTS OF ION IMPLANT DOSES IN SILICON 4-1
4.1 Introduction 4-1

4.2 Details on samples analysed and experiments 4-2
4.2.1 Samples analysed 4-2
4.2.2 Experiments 4-4
4.3 *Manual* data reduction (transparent) method 4-7
4.3.1 Pile-up calculation 4-7
4.3.2 Charge·solid angle product ($Q\Omega$) 4-7
4.3.3 Sensitivity and dose determination 4-10
4.4 *Machine* method: DataFurnace analysis 4-12
4.5 Results from the manual method 4-14
4.5.1 Pile-up calculation 4-14
4.5.2 Values of energies, stopping powers and Rutherford cross-sections 4-19
4.5.2.1 Common values of energies and stopping powers 4-19
4.5.2.2 Values of the averaged Rutherford cross-section for the implants 4-21
4.5.3 Solid angle and charge collection (experiments *iii*, *iv* and *v*) 4-24
4.5.4 Doses (experiments *iii*, *iv* and *v*) 4-26
4.5.5 Experiments *i* and *ii*: solid angles and doses 4-27
4.5.5.1 Solid angles 4-27
4.5.5.2 Doses 4-28
4.6 Results from the machine method: comparison with manual results 4-29
4.7 General results: time and space reproducibility 4-31
4.8 Uncertainties 4-33
4.9 Prospective 4-34
4.10 Summary 4-35

CHAPTER 5
ROUND ROBIN: MEASUREMENT OF H IMPLANTS IN SI USING ERDA 5-1
5.1 Importance of hydrogenated silicon 5-1
5.2 Sample preparation 5-3
5.3 Results from Surrey (UK): conventional ERDA 5-3
5.3.1 ERDA solid angle: H loss correction 5-3
5.3.2 Representative RBS and ERDA spectra from the Si:H sample 5-4
5.3.3 H implant fitted structure and depth profile 5-4
5.3.4 Final result: H content 5-6
5.4 Results from the other participants 5-7
5.4.1 Camberra (Australia): ΔE-E telescope ERDA 5-7
5.4.1.1 Electronics calibration 5-7
5.4.1.2 Si areal density n_{Si} 5-7
5.4.1.3 H concentration n_H 5-8
5.4.1.4 H depletion under beam irradiation 5-8
5.4.1.5 Non-uniformity of the H implant 5-9
5.4.1.6 Concentration of surface contamination (C and O) 5-10
5.4.1.7 Depth information from H data 5-10
5.4.1.8 H concentration: final result 5-11
5.4.2 London (Canada): conventional ERDA 5-11
5.4.3 Helsinki (Finland): ToF ERDA 5-12
5.4.4 Rossendorf (Germany): HI-ERDA + NRA 5-13
5.4.4.1 HI-ERDA experiment 5-13
5.4.4.2 NRA experiment 5-13
5.4.5 Montreal (Canada): ToF ERDA 5-15
5.5 Review of the results together with inter-lab reproducibility assessment 5-15
5.6 Summary 5-17

CHAPTER 6
AACCURATE DETERMINATION OF FLUORINE CONTENT OF SiO_2:F FILMS USING RBS 6-1
6.1 Introduction 6-1
6.1.1 Importance of SiO_2:F films 6-1
6.1.2 Analytical issues 6-2

6.1.2.1 Stopping powers ... 6-2
6.1.2.2 Different models (chemistries) ... 6-3
6.1.2.3 Sensitivity to F ... 6-3
6.1.2.4 Beam damage ... 6-6
6.2 Experimental details ... 6-6
6.2.1 Sample preparation ... 6-6
6.2.2 NRA experiment ... 6-7
6.2.2.1 F stability under beam irradiation ... 6-8
6.2.2.2 F uniformity ... 6-8
6.2.3 RBS experiment ... 6-8
6.3 NRA results on F stability and uniformity ... 6-9
6.4 RBS iterative method ... 6-12
6.4.1 Preliminary considerations ... 6-12
6.4.2 Information from simulated spectra ... 6-14
6.4.2.1 Relation at low energy (LE) ... 6-14
6.4.2.2 Relation at high energy (HE) ... 6-16
6.4.3 Start of the iterative process: getting the thickness of the films ... 6-17
6.4.4 Iterative process ... 6-18
6.4.4.1 Part I: Internal charge normalisation (using equation (6-2)) ... 6-18
6.4.4.2 Part II: Fluorine content determination (using equation (6-3)) ... 6-19
6.5 RBS results and discussion ... 6-19
6.6 Summary ... 6-25

CHAPTER 7
ANALYSIS OF RESIDUAL DEPOSITION IN AN ION IMPLANTER BY USING IBA TECHNIQUES ... 7-1
7.1 Introduction ... 7-1
7.2 Experimental details ... 7-3
7.3 SEM/EDAX analysis: guide for the RBS treatment ... 7-5
7.4 RBS analysis ... 7-6
7.5 EBS analysis for C detection (samples #3 and #4) ... 7-14
7.5.1 C detection using EBS ... 7-14
7.5.2 EBS analysis of samples #3 and #4 ... 7-15
7.6 Detection of F using NRA (sample #2) ... 7-18
7.6.1 Resonance curve ... 7-19
7.6.2 Reference F sample: determination of the detection of the sensitivity at the surface 7-21
7.6.3 F content of sample #2 ... 7-24
7.7 Analytical summary ... 7-26
7.8 Formation of the flakes: discussion ... 7-27

CHAPTER 8
CONCLUSION ... 8-1
8.1 Summing-up of this thesis ... 8-1
8.2 Short-term future work proposed ... 8-5

APPENDIX A
GEOMETRIC CONSIDERTIONS ... A-1
A.1 General considerations ... A-1
A.2 Backscattering spectrometry ... A-2
A.3 Recoil spectrometry ... A-3

APPENDIX B
ENERGY CALIBRATION OF THE ACCELERATOR AT SURREY IBC ... B-1
B.1 November 3rd, 2000 ... B-1
B.2 February 15th, 2001 ... B-5

B.3 April 4th, 2001 ..... B-8
B.4 June 13th, 2001 ..... B-11
B.5 September 14th, 2001 ..... B-14
B.6 Summary B-17

APPENDIX C
TERMINOLOGY OF THE GUIDE TO THE EXPRESSION OF UNCERTAINTY IN MEASUREMENT (GUM) C-1
C.1 Measurand C-1
C.2 Conventional true value C-2
C.3 Accuracy and precision C-2
C.4 Basic statistical terms and concepts C-3
C.4.1. Expectation — mean value of random variable C-3
C.4.2. Variance of random variable C-4
C.4.3. Variance of arithmetic mean C-4
C.4.4. Standard deviation of random variable C-5
C.4.5. Standard deviation of arithmetic mean C-5
C.5 Uncertainty C-5
C.5.1. Uncertainty of measurement C-5
C.5.2. Standard uncertainty C-6
C.5.3. Categories of uncertainty C-6
C.5.3.1. Uncertainty: Type A C-6
C.5.3.2. Uncertainty: Type B C-7
C.5.4. Combined standard uncertainty C-7
C.5.5. Expanded uncertainty C-7
C.6 Error of measurement C-8
C.6.1. Relative error C-8
C.6.2. Random error C-8
C.6.3. Systematic error C-8
C.6.4. Correction factor C-8
C.7 Repeatability and reproducibility of results of measurements C-9
C.7.1. Repeatability C-9
C.7.2. Reproducibility C-9

APPENDIX D
IBA FITTING CODE DATAFURNACE D-1
D.1 General description D-1
D.2 DataFurnace: getting started D-2
D.2.1. DataFurnace algorithm: introduction D-2
D.2.2. The sample D-3
D.2.3. The geometry D-4
D.2.4. Association D-5
D.2.5. The structure D-5
D.2.6. The batch D-6
D.2.7. Thin film units of depth D-6
D.3 Running DataFurnace D-7
D.3.1. Simulation and the ndf.prf file D-7
D.3.2. Fitting the data D-8
D.4 The DataFurnace algotithm D-9
D.4.1. The forward model D-9
D.4.2. Simulated annealing D-9
D.4.3. The cooling schedule D-10
D.4.4. Uncertainty estimation using Markov Chain Monte Carlo D-11
D.4.5. Grid search local minimisation D-11

APPENDIX E

REFERENCES E-1
E.1 Books and papers E-1
E.2 Companies E-19
E.3 World Wide Web sites E-20

LIST OF FIGURES

Figure 1-1 View of the internal configuration of the alpha-scattering sensor head deployed on the surface of the moon for the very first analysis of the lunar soil (from [Chu78]). 1-4

Figure 2-1 a) Non-aligned (random) and aligned (channelled) schematics. b) Example of an ion-implanted sample RBS spectrum; both the non-aligned (random) and aligned (channelled) schematics are illustrated. 2-2

Figure 2-2 Trajectories for elastic collision between two masses M_1 and M_2 in the laboratory system (L) and the center-of-mass system (COM) (from [Vic97{i}]). 2-4

Figure 2-3 The kinematical factor K as a function of the laboratory scattering angle θ_1 (see equation (2-2)) (from [Vic97{i}]). 2-6

Figure 2-4 Mass resolution $M/\Delta M$ as a function of the scattering angle θ_1 for a given energy resolution $E/\Delta E = 100$ (see equation (2-3) (from [Vic97{i}]). 2-7

Figure 2-5 Schematic of the concept of differential scattering cross-section $d\sigma/d\Omega$. The ring $d\sigma$, centred on a target nucleus, is a purely geometrical construct and not anything physical; it is related to the probability of scattering at an angle θ into the solid angle $d\Omega$. 2-9

Figure 2-6 Secondary scattering schematic (at normal incidence) (from[Tes95]). 2-15

Figure 2-7 He stopping cross-sections for C, Si and Ta target materials (from [Jey98-a]). 2-17

Figure 2-8 Schematic of the stopping cross-section factor, a useful derivative quantity for RBS. .. 2-19

Figure 2-9 Model of a lattice atoms showing the atomic configuration in the diamond-type lattice viewed along (a) random, (b) planar, or (c) axial directions (from [Chu78]). 2-26

Figure 2-10 Typical arrangement for reflexion ERDA (hydrogen profiling with an helium beam) and resulting spectrum from an implanted target. (The thin peak is due to hydrogen adsorbed on the surface.) (from [Tir96]). 2-30

Figure 2-11 Experimental set-up used in TOF-ERDA. (from [Tir96]). 2-36

Figure 2-12 The TOF-ERDA coincidence spectrum for a polyimide sample ($C_{22}H_{10}N_2O_6$) measured with a 84 MeV ^{127}I beam. Each recorded event is a data point plotted at the intersection of the measured energy (abscissa) and delayed flight time (ordinate). (from [Tir96]). 2-37

Figure 2-13 Isometric projection of the event density for the polyimide sample in Figure 2-12, illustrating the relative contribution from different sample constituents. The largest profile track is carbon, with the smaller nitrogen and oxygen components visible. The track of lowest intensity is aluminium from the target holder. Detection efficiency for hydrogen is comparatively lower, resulting in a track height much less than expected from elemental stoichiometry. (from [Tir96]). 2-37

Figure 2-14 The ERDA E×B method showing the interaction geometry, E×B filter, collimator positioning, and detector. (from [Tir96]). 2-38

Figure 2-15 Schematic view of a solid-state telescope (from [Tir96]). 2-39

Figure 2-16 Outline of a ΔE-E telescope composed of a gas ionization chamber associated with a thick silicon surface barrier detector (C, A, and G denote, respectively, the cathode, the anode, and the grid of the ionization chamber; W denotes the thin plastic entrance window) (from [Tir96]). 2-40

Figure 2-17 Experimental set-up for ERDA using the transmission geometry and coincident detection of scattered and recoiled particles (from [Tir96]). 2-41

Figure 2-18 ERDA spectra from hydrogen implanted glassy carbon (GC) and tungsten carbide (WC) samples in 24° scattering angle geometry (12°,12°) (from [Wie96]). 2-42

Figure 3-1 Sketch of ion beam analysis facility at Surrey Ion Beam Centre (D.R. Chick Laboratory): L4 is used for RBS and ERDA measurements, and L5 for the accelerator energy calibration and NRA measurements (from [My85]). 3-2

Figure 3-2 Feedback loop in the energy control of the Van de Graaff accelerator dedicated to IBA at Surrey Ion Beam Centre (from [Jey98-b]). 3-4

Figure 3-3 GVM equivalent circuit (from [Jey98-b]). 3-5

Figure 3-4 Sketch of the RBS target chamber vacuum system at Surrey Ion Beam Centre. 3-7

Figure 3-5 L4 RBS charge integration system and other target chamber components at Surrey Ion Beam Centre. 3-8

Figure 3-6 Spectroscopic electronics system at Surrey Ion beam Centre (from [Jey98-a]). 3-9

Figure 3-7 Sketch of the RBS target chamber and detection system at Surrey Ion beam Centre. 3-10

Figure 3-8 Peak channel versus pulser amplitude for both detectors A and B showing the electronics linear behaviour for pulse signal processing. 3-14

Figure 3-9 Summary of Surrey experimental procedure for the conventional ERDA analysis of H implants into Si as given in section 5.3. 3-16

Figure 3-10 Two-dimensional projection of the spectrum of ΔE versus energy (E_g) (for sample #1), after correction of kinematic energy broadening across the acceptance angle. The relative ion yields are indicated by the grey-scale (z-axis). In addition to Si ions, C and O ions from the sample surface can be identified. The low intensity haze of events above Si corresponds to electronic pile-up. 3-23

Figure 3-11 Energy spectra for Si, O and C, extracted from the two-dimensional projection of the spectrum shown in Figure 3-10 (the yield is the one as given by the grey-scale z-axis of Figure 3-10). The original 1024 channel spectrum has been compressed to 256 channels to reduce statistical scatter. The selected integration region for Si, the mid-point of this interval and the likely location of the implantation peak on this scale are indicated. The inset shows the data and the linear fit used for the energy calibration. 3-24

Figure 3-12 The extreme low-energy part of the two-dimensional projection of the spectrum which relates the E_{res} signal with that from the grid electrode and allows the identification of protons. The implanted hydrogen can be identified as intense yield in the near-surface region. The response curve for hydrogen is indicated in the direction of increasing sample depth. 3-26

Figure 4-1 Manual data reduction method. Top: energy parameters along the backscattering process both from Si substrate atoms and implanted ions, which are required for the analysis leading to the ion-implanted dose determination (see text). Bottom: corresponding RBS spectrum. 4-8

Figure 4-2 a) Spectrum (data and DataFurnace fit) from the IRMM/BAM certified Sb standard and b) Sb profile from the two detectors (open circles and solid line are from Det A and Det B, respectively) obtained using DataFurnace..... 4-13

Figure 4-3 As10 RBS spectra for count rates of a) 4kHz and b) 12kHz, together with c) the As profile calculated from the two detectors (both results are shown) by DataFurnace for the 4kHz spectra. 4-15

Figure 4-4 Signals (As and Si) and pile-up background spectrum for 12 kHz count rate for sample As10 (DataFurnace analysis)..... 4-16

Figure 4-5 As signal and pile-up background for 12 kHz count rate for sample As10 (from partial spectra in Figure 4-4): pile-up is about 15% of the signal and the non-linear distortion is about 10 % of the pile-up. 4-16

Figure 5-1 Representative simultaneous RBS/ERDA spectra from the implanted sample, with fitted spectra (Surrey). 5-4

Figure 5-2 Hydrogen fitted profile (Surrey). 5-5

Figure 5-3 Plot of representative H signal on a depth scale (see text) (Surrey). 5-5

Figure 5-4 The E_{res} spectrum of the detected protons for sample #1, in comparison with the response function of this (residual energy) electrode for high-energy protons. The response function was obtained by recording a hydrogen spectrum for a uniform Kapton sample. It is apparent that the centroid of the hydrogen distribution is inside the sample implying that the concentration of any surface hydrogen present is small compared to the implant concentration. The inset shows the reduction of the hydrogen content with increasing dose. (Canberra) 5-9

Figure 5-5 Hydrogen ERDA spectrum obtained form sample #1 (London). 5-12

Figure 5-6 Total yield of hydrogen as a function of incident iodine ions showing hydrogen depletion with incident fluence (Helsinki). 5-13

Figure 5-7 Hydrogen depth profile obtained using NRA (Rossendorf). 5-14

Figure 5-8 NRA detected hydrogen yield as a function of increasing incident dose at a depth of 100 nm: study of beam related to hydrogen release (Rossendorf). 5-14

Figure 6-1 RBS spectrum for sample #3 together with the relevant features showing elemental edges and the regions of interest ROI I, J and K. Normalised to 10 μC..... 6-3

Figure 6-2 Top) RBS spectrum of sample #3 along with the DataFurnace fit (see text for details). Bottom) Corresponding depth profile. 6-5

Figure 6-3 General view of the depth profiles (energy scans) of sample #3 as a function of time of bombardment (charge collected) in 3 different orientations..... 6-10

Figure 6-4 Five depth profiles (energy scans) obtained at different time of bombardment. 6-11

Figure 6-5 Depletion of fluorine as a function of beam irradiation..... 6-12

Figure 6-6 Simulated integrated yield in ROI I vs thin film thickness with F content of 0% at. and 5% at. Normalised to 10 μC. 1 TFU = 10^{15} atoms/cm^2. O-fixed model ($(SiO2)_{1-x}$:F_x)..... 6-14

Figure 6-7 Simulated integrated yield in ROI I vs fluorine content with thin film thickness of 5100 TFU. Normalised to 10 μC. 1 TFU = 10^{15} atoms/cm^2. O-fixed model ($(SiO2)_{1-x}:F_x$). 6-15

Figure 6-8 Simulated integrated yield in ROIs J and K (170-190) vs F content with film thickness of 5100 TFU. Normalised to 10 μC. 1 TFU = 10^{15} atoms/cm^2. O-fixed model ($(SiO2)_{1-x}:F_x$). 6-16

Figure 6-9 Comparison of the XRF and corrected RBS fluorine content using the O-fixed model $(SiO_2)_{1-x}:F_x$. The error bars are expanded uncertainties with a coverage factor k = 2. Two linear fits are shown: one where the offset is a free parameter, and another one with the offset set to 0.. 6-23

Figure 7-1 Source deterioration on the M376 ion implanter from Applied Materials UK Ltd. [App] whilst running a 7-keV B beam (25 hours, 9.4 mA), then successively H (1 hour) and AsH_3 (1 hour). 7-2

Figure 7-2 Cooled tube of the M376 ion implanter from Applied Materials UK Ltd. in which the source sits. The cooled tube, source and extraction assembly all fit in the source chamber. 7-4

Figure 7-3 Surface conditions and RBS events. a) Sample with flat surface: no alteration in energy loss. b) gap and c) edge effects due to roughness of the surface: energy-loss pattern is altered. 7-4

Figure 7-4 EDAX X-ray spectra for deposit #1. Left: side 1 (sample #1). Right: side 2 (sample #2)… 7-5

Figure 7-5 EDAX X-ray spectra for deposit #2. Left: side 1 (sample #3). Right: side 2 (sample #4)… 7-6

Figure 7-6 Data (orange) and fitted (blue) spectrum for sample #1 (source chamber, side 1). Partial fitted spectra: As (pink), C (red), Sb (green), Fe (cyan), W (navy)..... 7-7

Figure 7-7 Full scale (0-100 at.%) depth profile of sample #1 (source chamber, side 1)..... 7-8

Figure 7-8 Magnification (0-25 at.%) of Figure 7-7. 7-8

Figure 7-9 Data (orange) and fitted (blue) spectrum for sample #2 (source chamber, side 2). Partial fitted spectra: As (pink), C (red), Sb (green), Fe (cyan), W (navy)..... 7-9

Figure 7-10 Full scale (0-100 at.%) depth profile of sample #2 (source chamber, side 2)..... 7-9

Figure 7-11 Magnification (0-15 at.%) of Figure 7-10. 7-10

Figure 7-12 Data (orange) and fitted (blue) spectrum for sample #3 (cooled tube — below cathode, side 1). Partial fitted spectra: As (pink), C (red), Sb (green), Fe (cyan), W (navy)..... 7-10

Figure 7-13 Full scale (0-100 at.%) depth profile of sample #3 (cooled tube — below cathode, side 1). 7-11

Figure 7-14 Magnification (0-25 at.%) of Figure 7-13. 7-11

Figure 7-15 Data (orange) and fitted (blue) spectrum for sample #4 (cooled tube — below cathode, side 2). Partial fitted spectra: As (pink), C (red), Sb (green), Fe (cyan), W (navy)..... 7-12

Figure 7-16 Full scale (0-100 at.%) depth profile of sample #4 (cooled tube — below cathode, side 2). 7-12

Figure 7-17 Magnification (0-20 at.%) of Figure 7-16. 7-13

Figure 7-18 1.65 and 1.75 MeV proton beam backscattering spectra of samples a) #3 and b) #4. The enhanced signal around channel 280 at 1.75 MeV is due to non-Rutherford cross-sections of C; therefore this confirms the assumption of C as a constituent. 7-14

Figure 7-19 Data (orange) and fitted (blue) EBS spectrum for sample #3 (cooled tube — below cathode, side 1) Partial fitted spectra: As (pink), C (red), Sb (green), Fe (cyan), W (navy). 7-15

Figure 7-20 Full scale (0-100 at.%) depth profile of sample #3 (cooled tube — below cathode, side 1). 7-16

Figure 7-21 Data (orange) and fitted (blue) EBS spectrum for sample #4 (cooled tube — below cathode, side 2) Partial fitted spectra: As (pink), C (red), Sb (green), Fe (cyan), W (navy). 7-16

Figure 7-22 Full scale (0-100 at.%) depth profile of sample #4 (cooled tube — below cathode, side 2). 7-17

Figure 7-23 Excitation curve for the reaction $^{19}F(p,\alpha\gamma)^{16}O$ at 872.1 keV. Γ = 4.5 keV. 7-18

Figure 7-24 Interaction densities of the pγ nuclear reaction on fluorine throughout the sample for an incident beam energy of a) 872 and b) 877 keV..... 7-19

Figure 7-25 RBS collected and fitted spectra of the reference F sample..... 7-21

Figure 7-26 a) Depth profile of the reference F sample for the first 300 nm. b) Details of the whole depth profile obtained..... 7-22

Figure 7-27 872.1-keV $^{19}F(p,\alpha\gamma)^{16}O$ NRA spectrum (counted gammas) from the reference F sample. 7-23

Figure 7-28 a) $^{19}F(p,\alpha\gamma)^{16}O$ NRA normalised spectra (counted gammas) from sample #2 (source chamber, side 2) at different incident energies. b) Table of normalised integrated counts T for each energy and their ratio T_{872} to T_i. 7-25

Figure B-1 Excitation curve of the $^{27}Al(p,\gamma)^{28}Si$ resonance at 991.9 keV (energy calibration, November 3rd, 2000). B-2

Figure B-2 Excitation curve of the $^{27}Al(p,\gamma)^{28}Si$ resonance at 632.0 keV (energy calibration, November 3rd, 2000). B-3

Figure B-3 Excitation curve of the $^{19}F(p,\alpha\gamma)^{16}O$ resonance at 872.1 keV (energy calibration, November 3rd, 2000). B-4

Figure B-4 Energy calibration curve of Surrey accelerator, November 3rd, 2000. ..... B-5

Figure B-5 Excitation curve of the $^{27}Al(p,\gamma)^{28}Si$ resonance at 991.9 keV (energy calibration, February 15th, 2001). B-6

Figure B-6 Excitation curve of the $^{27}Al(p,\gamma)^{28}Si$ resonance at 632.0 keV (energy calibration, February 15th, 2001). B-6

Figure B-7 Excitation curve of the $^{19}F(p,\alpha\gamma)^{16}O$ resonance at 872.1 keV (energy calibration, February 15th, 2001). B-7

Figure B-8 Energy calibration curve of Surrey accelerator, February 15th, 2001..... B-7

Figure B-9 Excitation curve of the $^{27}Al(p,\gamma)^{28}Si$ resonance at 991.9 keV (energy calibration, April 4th, 2001). B-9

Figure B-10 Excitation curve of the $^{27}Al(p,\gamma)^{28}Si$ resonance at 632.0 keV (energy calibration, April 4th, 2001). B-9

Figure B-11 Excitation curve of the $^{19}F(p,\alpha\gamma)^{16}O$ resonance at 872.1 keV (energy calibration, April 4th, 2001). B-10

Figure B-12 Excitation curve of the $^{19}F(p,\alpha\gamma)^{16}O$ resonance at 1371.0 keV (energy calibration, April 4th, 2001). B-10

Figure B-13 Energy calibration curve of Surrey accelerator, April 4th, 2001. Erratum: in the top inset box, E_n and E_r must be substituted to E_A and E_n, respectively. B-11

Figure B-14 Excitation curve of the $^{27}Al(p,\gamma)^{28}Si$ resonance at 991.9 keV (energy calibration, June 13th, 2001). B-12

Figure B-15 Excitation curve of the $^{27}Al(p,\gamma)^{28}Si$ resonance at 632.0 keV (energy calibration, June 13th, 2001). B-12

Figure B-16 Excitation curve of the $^{19}F(p,\alpha\gamma)^{16}O$ resonance at 872.1 keV (energy calibration, June 13th, 2001). B-13

Figure B-17 Energy calibration curve of Surrey accelerator, June 13th, 2001. Erratum: in the top inset box, E_n and E_r must be substituted to E_A and E_n, respectively. B-13

Figure B-18 Excitation curve of the $^{27}Al(p,\gamma)^{28}Si$ resonance at 991.9 keV (energy calibration, September 14th, 2001). B-14

Figure B-19 Excitation curve of the $^{27}Al(p,\gamma)^{28}Si$ resonance at 632.0 keV (energy calibration, September 14th, 2001). B-15

Figure B-20 Excitation curve of the $^{19}F(p,\alpha\gamma)^{16}O$ resonance at 872.1 keV (energy calibration, September 14th, 2001). B-15

Figure B-21 Excitation curve of the $^{19}F(p,\alpha\gamma)^{16}O$ resonance at 1371.0 keV (energy calibration, September 14th, 2001). B-16

Figure B-22 Energy calibration curve of Surrey accelerator, September 14th, 2001. .....B-16

Figure C-1 Distinction between accuracy and precision. C-3

LIST OF TABLES

Table 3-1 Manual measurements of the distances as shown in Figure 3-7. 3-11

Table 3-2 Scattering angle values of both detectors A and B as measured by using a laser beam. Position 1 and 2 refer to two different arrangements. 3-12

Table 3-3 Data from the electronics linearity and constant behaviour test: pulser amplitude, peak channel and integration, time and period. 3-13

Table 3-4 Experimental set-up details for each participant in the ERDA Round Robin exercise for the measurement of hydrogen in silicon (presented in chapter 5). 3-21

Table 3-5 Experimental parameters used in the Canberra data analysis. The last two columns give the measured areal densities. 3-25

Table 4-1 Implantation energy and nominal dose for the implant into silicon samples analyzed. The UWO Bi sample came from University of Western Ontario (UWO), and was certified by W.N. Lennard at 2%. The IRMM/BAM Sb sample came from Geel, and was sent by U. Wätjen;it has a certification of 0.6% traceable to the international standard of weight in Paris. The other samples were all implanted at Surrey. 4-3

Table 4-2 Spectra from samples analyzed on five different dates and in two laboratories. The amorphised samples (marked *) had 5×10^{15} Si/cm^2 at 200 keV at ~150K. 4-5

Table 4-3 Electronics calibration numbers (gain κ and offset), Si surface yield calibration standard M_{Si} (for a 1490.4 keV and 1528.0 keV He beam energy E_0 at Surrey and Jena, respectively), and kinematical factors K (for He scattering on Si, In, As, Bi and Sb ions) corresponding to both A and B detectors at Surrey and A detector at Jena. 4-6

Table 4-4 Charge-to-number of particles conversion factor C_Q, charge normalization Q_{Norm}, and quantities required for determination of implant Rutherford cross-section (see equation (4-6)): masses M_1 and M_2 (in atomic weight) and atomic numbers Z_1 and Z_2 for the projectile (He) and the target (In, As, Bi or Sb) respectively; the factor $s\cdot e^4$ (see text); and the angular part (see equation (2-8)). 4-11

Table 4-5 As dose in sample As10 with different pile-up backgrounds (different count rates) for 2 detectors simultaneously (DataFurnace analysis). 4-17

Table 4-6a Charge collected Q, weighting factor W (for pile-up correction), implant (In, As, Bi or Sb) peak integral A_{imp}, sum of the counts c_T in each channel, acquiring livetime t_{live} and normalisation factor w (for pile-up correction) corresponding to detectorA geometry for each spectrum for each experiment. DetectorA geometry is: $\theta = 166.9°$ at Surrey and 168.0° at Jena. 4-18

Table 4-7 Energies E_0, E_a and E_l (see Figure 4-1), stopping powers $\varepsilon(E_0)$, $\varepsilon(E_a)$ and $\varepsilon(E_l)$ and stopping cross-section factors $[\varepsilon(E_0)]$ corresponding to both A and B detectors at Surrey and A detector at Jena. Stopping powers and stopping cross-section factors are evaluated in a Si matrix using the program SSTOP that refers to values as reported on in TRIM-95. 4-20

Table 4-8 α_{Si} (for a scattering event occurring from a Si ion in a slab Δx_b), energies E_c and E_b (see Figure 4-1), stopping powers $\varepsilon(E_c)$ and $\varepsilon(K_{Si}E_b)$ and stopping cross-section factors $[\varepsilon(E_b)]$ corresponding to both A and B detector geometry for experiments iii, iv and v where amorphised samples were available. Note that there is no B detector geometry for the Jena experiment (v).

Stopping powers and stopping cross-section factors are evaluated in a Si matrix using the program SSTOP that refers to values as reported on in TRIM-95. 4-21

Table 4-9a α_{imp} (for a scattering event occurring from an In, As, Bi or Sb ion implant in a slab Δx_m), energies E_n and E_m (see Figure 4-1), the screening correction $F(E_m)$ (as reported on by Tesmer and Nastasi [Tes95{x}]) and the implant (In, As, Bi or Sb) Rutherford cross-section $\sigma(E_m,\theta)$ corresponding to detector A geometry for each spectrum for each experiment. 4-22

Table 4-10 Si yield Y_b (evaluated at channel specified in Table 4-8, col28), ratio Q_{Norm}/Q, normalized (integrated charge Q normalized to Q_{Norm} as specified in Table 4-4b, col11), Si yield $Y_{b(Norm)}$, surface normalized Si yield $Y_{0(Norm)}$ (calculated from equation (4-4)) and solid angle Ω corresponding to both A and B detector geometries for each spectrum from amorphised samples for experiments iii, iv and v. Note that there is no detector B geometry for the Jena experiment (v). 4-25

Table 4-11 Implant doses D_{imp} from both A and B detector geometries and their ratio determined for each spectrum for experiments iii, iv and v. Detector A geometry is: $\theta = 166.9°$ at Surrey and 168.0° at Jena. Detector B geometry is $\theta = 133.1°$ at Surrey. Note that there is no detector B geometry for the Jena experiment (v) 4-26

Table 4-12 Average implant doses D_{imp} for In03 and As06 samples obtained from doses (marked ■ for In03 and marked ● for As06 in Table 4-11) in experiments iii, and solid angle Ω, relatively determined from these averaged doses, for both A and B detector geometries for experiments i and ii (for which no amorphised samples were available). A and B detector geometries are $\theta =$ 166.9° and 133.1° respectively (Surrey). 4-28

Table 4-13 Implant doses D_{imp} from both A and B detector geometries and their ratios determined for each spectrum for experiments i and ii. A and B detector geometries are $\theta = 166.9°$ and 133.1° respectively (Surrey). 4-29

Table 4-14 Comparison between the dose obtained with the manual data reduction method and the machine method (DataFurnace). Results from exp. iii are displayed, together with general results when including all measurements from exp. i, ii, iii and iv. 4-30

Table 4-15 Implant doses D_{imp} from the only detector geometry ($\theta = 168.0°$) for experiment v (Jena). DataFurnace analysis. 4-31

Table 4-16 Mean implant dose for each sample for each experiment separately, and total mean dose for all the experiments carried out at Surrey (i, ii, iii, iv). 4-32

Table 4-17 Time and space reproducibility of the results, together with the discrepancies (errors) from the nominal doses. Faint highlighted results refer to the certified Bi and Sb samples. 4-33

Table 4-18 Uncertainty budget. 4-34

Table 4-19 Uncertainty budget: energy loss value determination using the dose measurement method together with certified standards. 4-35

Table 5-1 Measurements of total H content (bulk + surface) in the Si:H sample (Surrey). 5-6

Table 5-2 Summary of the ToF-ERDA results (Montreal) 5-15

Table 5-3 Global summary of the results from all the participants together with the uncertainty budget 5-17

Table 6-1 SiO_2:F samples together with their description (growing conditions and film thicknesses) submitted for fluorine content determination by using RBS. 6-7

Table 6-2 Variations of integrated yields I, J and K with film thickness and fluorine content obtained from simulations. Normalised to 10 μC. 1TFU = 10^{15} atoms/cm^2. 6-13

Table 6-3 Thickness t_i together with some values from the different spectra of each sample such as charge collected Q_i, raw integrated yields I_i at low energy (LE) and J_i at high energy (HE). ... 6-17

Table 6-4 Outcomes from the iteration n = 6..... 6-20

Table 6-5 Ratio between collected charge Q_i and calculated chage $Q'_{i,6}$ for both models (chemistries). 6-21

Table 6-6 Results for the F content, including measurements for XRF and RBS. The latter include final values assuming two different chemistries, that it, $(SiO_2)_{1-x}:F_x$ (O fixed) and $SiO_{2-x}:F_x$ (O free). Both with and without F loss correction values are given for the O-fixed model. The ratio between the two chemistries is also shown. 6-22

Table 7-1 Integral from different regions of interest of the 872.1-keV F resonance curve as presented in Figure 7-23. 7-20

Table 7-2 Mean probability from different regions of interest of the 872.1-keV F resonance curve as presented in Figure 7-23. 7-21

Table 7-3 Elemental concentrations for each sample as found by RBS, EBS and NRA. 7-27

Table B-1 History of accelerator energy calibration: the nominal energy corresponding to a real energy of 1500.0 keV for each calibration date..... B-17

CHAPTER 1

INTRODUCTION

1.1 Materials characterization

Nowadays, in every domain, a wide range of samples or materials are analyzed for as many varied reasons as there are research projects. For instance, materials characterization can be helpful in determining: electrical isolation of silicon carbide semiconductor devices [Wan00-b]; improved properties of hard coatings produced by dynamic ion mixing for tribological and corrosion protection applications [Riv00]; air pollution in Singapore during a long haze period caused by a heavy forest fire in Indonesia [Orl97]; any imbalances in trace elements in localized regions of biological tissue, and as such in providing unique information on many diseases like Alzheimer's and Parkinson's [Tho96]; paint layer arrangements and pigment admixtures, and as such in distinguishing painting techniques [Nee00], etc.

The point is that it is vital that our body, our environment and the materials used in our modern world are thoroughly understood. There are many different analysis techniques available. The choice of using one in particular depends upon what has to be characterized or measured: atomic or chemical structure, composition, impurities, defects, depth profile, electronic state, physical topography, etc. But for all of these problems ion beam methods, and Ion Beam Analysis (IBA) in particular, are making essential contributions. And in many cases, the characteristic contribution of ion beam analysis is the *accuracy* of the information obtained. The obtainable accuracy by using IBA methods is the subject of this thesis.

1.2 Ion Beam Analysis (IBA)

The present work concerns specifically IBA (Ion Beam Analysis), a cluster of analysis techniques that use an ion beam probe produced by a particle accelerator. IBA really started proliferating in the 60s and 70s as a result of a great number of 1-3 MV Van de Graaff accelerators available, these machines having then become obsolete for fundamental nuclear physics research. The Handbook from Tesmer and Nastasi [Tes95] is the most useful single volume overview about IBA. The different IBA techniques are distinguishable by the different types of interaction occurring when an ion beam strikes a solid target.

When incident ions suffer backscattering from atomic nuclei constituting the target, much information can be obtained from the energy and the yield of these backscattered ions, that is, information on the composition and the concentration: this is how the so-called RBS (Rutherford Backscattering Spectrometry) technique works, and this is actually the first IBA technique that was developed. And it is the principal technique used in this thesis. For a complete survey of RBS, Chu *et al*.'s book is greatly advised [Chu78]. Briefly, the ion-target atom interaction can be described using the Coulomb potential from which the Rutherford scattering cross-section is analytically derived, which allows quantification of the results. In typical RBS experiments, a ~1-2 MeV H^+ or He^+ beam is directed onto a sample enclosed in a chamber evacuated at around 10^{-6} torr. Moreover, as incident/backscattered ions travel into/out from the target, they suffer energy loss, and depth profiling can be performed.

1.2.1 Rutherford Backscattering Spectrometry (RBS): Milestones

The RBS technique can be said to be born with one of the undoubtedly most famous papers written by Rutherford in 1911: in this paper, he gives a solution to the enigma of explaining observations of both large- and small-angle scattering of alpha particles directed onto metal foils, that is, the "nucleus" (in fact, Rutherford never used the word "nucleus"; his phrase was "charge concentration") [Rut11]. Geiger and Marsden spent the next two years carrying out experiments in order to test (and prove) Rutherford's model of the atom and his calculation of the

scattering probability (cross-section) [Gei13]. The conceptual framework on which backscattering spectrometry is based was actually erected in the years following these discoveries.

However, after Rutherford's discovery, rapidly the physics community began to be interested mostly in scrutinizing the nuclear structure. To trigger nuclear reactions, nuclear physicists needed powerful machines capable of accelerating charged particles by means of a high voltage. In 1932, Cockcroft and Walton built a cascade generator for nuclear reaction studies [Coc32]; based on an idea of H. Greinacher, they were able to multiply a given voltage by a suitable arrangement of condensers and rectifiers. Another method to produce high voltages rapidly gained popularity, and was conceived in 1931 by Van de Graaff [Gra31]: it consists of a fast moving insulating belt that carries charge, which is sprayed onto the belt at ground potential and removed at the high voltage terminal. Tens of millions of volts can be reached this way. A variant of electrostatic accelerators makes use of a potential twice: ions are oppositely charged along two acceleration stages. In these so-called tandem accelerators, negatively charged ions are injected into the accelerator, accelerated up to the positive HV terminal in the centre of the machine, stripped by a gas or foil in the terminal, become positively charged and then get accelerated again. Obviously higher energies can be reached than the single-ended machines. Another advantage is that the source is at earth potential; the tandem can be then large, relatively easy to handle, with a wider choice of available projectiles. In contrast to this type of linear electrostatic accelerator, Lawrence and Livingston built a circular machine in 1931, known as a cyclotron [Liv80]. The ions follow circular orbits in a homogeneous magnetic field, but they pass through a small potential difference repeatedly and then get accelerated. At each passage through the electrodes, the polarity of the accelerating voltage is changed, so that the ions are accelerated twice, both when entering and leaving the electrodes. Cyclotrons allow very large energies, while no high-voltage is required.

Already after World War II, a great number of 1-3 MeV Van de Graaff accelerators were at nuclear physicists' disposal for the study of nuclear matter. Although scientists were fully aware from the very beginning of the power of Rutherford backscattering spectrometry as an analytical tool, it took about 20 more years before these accelerators were dedicated to analytical studies and RBS became

a widespread analysis technique. There are mainly three reasons for this late takeoff: 1) it was only around the 1960s that the numerous small 1-3 MV Van de Graaff began to be too obsolete to probe any further inner workings of the nucleus so that they could be made available to solve problems outside the field of fundamental nuclear physics; 2) in the 1960s convenient particle detectors were developed, that is, solid-state detectors, relatively inexpensive, with good resolution, good linearity, fast response and simultaneous analysis over a wide energy range; 3) great improvements were achieved in the electronic systems for data handling and processing, that is, speed, accuracy, stability and generous capacities for data storage, all at reasonable cost.

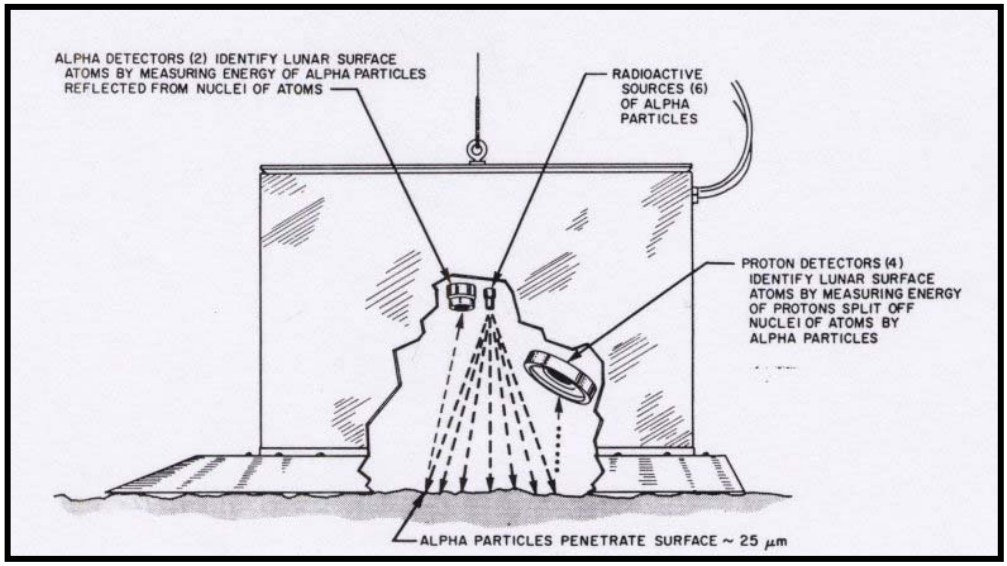

Figure 1-1 *View of the internal configuration of the alpha-scattering sensor head deployed on the surface of the moon for the very first analysis of the lunar soil (from [Chu78]).*

The first widely publicized practical application of the ideas of Rutherford, Geiger and Marsden to a problem of a non-nuclear interest appears to be the alpha-scattering experiment aiming at analyzing the composition of the lunar soil [Tur68]. As part of the scientific mission of Surveyor V, after a soft landing on September 9th, 1967, an alpha-scattering sensor head was deployed on the surface of the moon for the very first analysis of the lunar soil (Figure 1-1). Rutherford's scattering concept obtained the same kind of priority for the analysis of the Martian rocks in 1997 with Pathfinder, the first spacecraft to land on Mars since the twins Viking landers arrived almost 20 years previously (see the web site [www①]).

Most importantly for RBS was the introduction in the late 1970s of ion implantation into semiconductors processes (offering accurate control of the dopants together with uniform surface density over a whole wafer). As a matter of fact, RBS appears to be one of the most convenient analysis technique to investigate and characterize the implantation process, mainly involving ion-implanted Si-based compounds [Tow76], which has been widely used for many years and is likely to continue to be so. Section 2.1 gives an in-depth study of the RBS technique.

Over the last 30 years, a large number of IBA techniques have emerged, each of them having their own characteristics and their own range in the field of materials characterization. They are summarily described in the following section.

1.2.2 Different IBA techniques

IBA techniques can be divided into several classes depending on the energy of the probe beam particles: The Low-, Medium- and High-Energy ranges, which work at $E < 10$ keV, $10 < E < 500$ keV and E in the order of MeV/amu, respectively.

1.2.2.1 Low-Energy IBA

The two important techniques using slow ions are Low-Energy Ion Scattering (LEIS) [www④] and Secondary Ion Mass Spectroscopy (SIMS) [www⑤]. In the former, inert gas ions of a few keV are used as projectiles. Information on the atomic composition and structure of the top most atomic layer can be obtained from the scattered beam particles.

In SIMS experiments, typically 0.5-10 keV oxygen or cesium beams are directed onto samples. The mass spectrum of the atoms sputtered from the surface is measured. SIMS is very sensitive; concentrations in the order of ppm (parts per million — $1/10^6$ atom) can be detected. However, absolute quantitative analysis is problematic: it is often unclear which fraction of the sputtered particles is neutral. Depth profiles can also be made with SIMS, although dissimilar sputtering yields for different target atoms constitutes a problem. In addition, due to redistribution of the

target atoms by the sputtering the depth resolution is limited. SIMS is also a deliberately destructive technique.

Although they are not classified as IBA techniques, Auger Electron Spectroscopy (AES) and X-ray Photoelectron Spectroscopy (XPS) can use ion sputtering, by means of ion guns, for depth profiling as in SIMS to investigate surfaces.

1.2.2.2 Medium-Energy IBA

The technique that is referred to when backscattering studies involved 10 to 500 keV projectiles is known as Medium-Energy Ion Scattering (MEIS) [www⑥]. As in RBS experiments, MEIS data provides information on the mass of the scattering centres (from the energy of the backscattered projectiles) and allows depth profiling (from the projectile energy loss). Typically 100 keV H ions are used as projectiles; at this energy, the energy loss of H is maximum, therefore an optimal depth resolution is obtained. In this regime, sub-nanometer depth resolutions can be reached by using electrostatic energy analysers [Hüt96]. Just as in the RBS method, since both mass and depth must be determined from the measured energy, the problem of ambiguity arises. MEIS also uses channelling and blocking techniques to study crystallographic defects in the near surface.

1.2.2.3 High-Energy IBA

Among the IBA techniques that use fast ions (in the order of MeV/amu), we have already introduced RBS. When the Coulomb barrier is exceeded, the cross-section is no longer Rutherford, and the yield of the backscattered particles may be enhanced, which can be useful to detect low concentrations; this is a technique in itself, and it is referred to as Elastic Backscattering Spectrometry (EBS). But in this case analysts rely on an empirical cross-section database. Section 2.1.4.2 covers the EBS technique in more detail.

RBS is especially sensitive to heavy ions, and generally light ions in a heavy matrix can be analysed only with a low sensitivity. This problem can be solved by applying the scattering technique Elastic Recoil Detection Analysis (ERDA), in

which the recoil target ions are detected in the forward direction after elastic collisions with the projectiles. Again composition and depth information can be obtained. In ERDA, energy dispersive measurements are often combined with particle dispersive techniques to allow unambiguous interpretation of the data. ERDA is especially sensitive to light elements in a relatively heavy matrix. In this sense ERDA and RBS are complementary. Section 2.2 is dedicated to the ERDA technique.

When a non-elastic interaction (nuclear reaction) between the incident ion and a target ion occurred and the resultant reaction product is detected (usually gamma, proton, alpha or deuterium), the technique is called Nuclear Reaction Analysis (NRA). This technique is very useful to identify isotopes. There is often no background to the signal, but cross-sections fall by orders of magnitude. Depth information is obtained from either energy loss measurements of a nuclear product ion or from resonance depth profiling. In the latter case, a sharp resonance in the reaction cross-section is used and depth information is obtained by varying the beam energy, so the resonance occurs at varying depths. A special case of NRA is when a photon is detected, and the technique is called Particle Induced Gamma-ray Emission (PIGE). The latter can be used to perform the energy calibration of accelerators; one only has to collect gammas from different nuclear reactions occurring at several different energies for a multipoint calibration. The NRA technique is explored in section 2.1.4.3.

Particle Induced X-ray Emission (PIXE) is the technique where X-rays from inelastic collisions of the projectile with inner core electrons are detected [Joh88]. PIXE is especially sensitive to trace elements and allows the determination of concentrations at a ppm level. However, PIXE generally does not yield depth information. When lower energy photons are detected, the technique is referred to as IonoLuminescence (IL).

Combined with any IBA technique, the *channelling* or blocking method can give information on single crystal samples. Crystal orientation can be determined, amorphous layers can be measured, and damage (crystal quality) can be quantified and profiled. Channelling effect is touched on in section 2.1.7.

The ion beam can be focussed (down to one micron or less) and scanned over a given area of the sample, and then be used as a scanning ion microscope; this is referred to as *microbeam* analysis. RBS or other spectra can be collected from specific regions of the sample in this mode. However, this small beam is usually used with PIXE because of its large cross-sections. Ion Beam Induced Current (IBIC) is a microbeam technique for investigating semiconductor devices, which respond to single ion impacts: the number of charge carriers produced by individual incident ions is measured as a function of focused beam position. The development of IBIC was motivated by its use for integrated circuit analysis, where distribution of surface layers and depletion layers can be imaged [Bre98].

Finally, a very simple energy dispersive IBA technique that uses fast ions is Scanning Transmission Ion Microscopy (STIM). Energy loss of ions impinging on a relatively thick sample is measured in transmission, yielding information about the mass thickness of the sample. STIM can be used in the scanning mode, so lateral information is obtained during the measurement.

The following IBA techniques have been implemented in the new IBA code DataFurnace [Bar97-b]: RBS, EBS, ERDA, NRA and microbeam. It must be stressed that this code applies only to thin film composition depth profiling and not to the various microbeam imaging or channelling applications. In this thesis, in addition to RBS principally, the IBA techniques ERDA, EBS and NRA will be used, together with the code DataFurnace, with emphasis put on *accuracy*. For an overview on the utilization of DataFurnace, we refer the reader to appendix D.

1.3 Overview of the thesis

1.3.1 Topic: IBA and accuracy

It is essential that our bodies, our environment and the materials that we use are thoroughly *understood*. Determination of nature, concentration and distribution of elements contained in our cells, and in the materials that surround us and that we develop are a major step in the *understanding* of our world, hence the importance of materials characterization. This thesis focuses on *accurate* ion beam

analysis (involving mainly RBS and ERDA, together with EBS and NRA as complementary techniques) of advanced materials, particularly semiconductors (implanted silicon samples, insulating thin layers).

With the constantly growing need of computers and electronic devices, semiconductors are still the core of information storage and data handling; accurate characterization of advanced materials is *a priori* necessary. Electrical properties of semiconductors or insulating layers can be modified if need be, for instance, by adding dopants or impurities by ion implantation. With the driving need on more powerful computers, miniaturisation of semiconductor materials and their derivatives is not about to slow down, consequently dopant dose and distribution, and impurity content are expected to become more critical. As a matter of fact, nowadays ion implantation is carried out at both very low dose and energy. Due to extremely small dimensions, a very small change in the dose can cause significant changes in electrical properties. Improved accuracy in characterisation of advanced materials is now undoubtedly required.

As ions travel through a target between large angle nuclear scattering events, they suffer energy loss to the electronic lattice; at present, the main limitation on the accuracy obtainable by IBA has relied on the uncertainties in these energy loss values, which are rarely as good as 5% [Zie85, Tes95{i}]. This matter will be approached thoroughly throughout the thesis. Data reduction methods will be developed in order to reduce the uncertainties as much as possible. Certified and standard samples will be used for comparison and/or calibration. The experiments will be carried out at different dates and in different IBA laboratories from all over the world to ensure reproducibility of the results. The fitting code DataFurnace will be validated and used to interpret the RBS, ERDA and EBS spectra collected.

Particular attention must be paid to the terminology used throughout this thesis. It is self-evident that accurate work must be supported by the use of a consistent terminology: regarding this matter, we follow the recommendations from and the definitions as given in the *Guide to the expression of uncertainty in measurement*, or GUM [ISO93]. The reader is greatly advised to have a look at appendix C on GUM terminology before going any further with the reading of the thesis (specially chapters 4 to 7 which deal with the results obtained).

1.3.2 Outlines

At first, in **chapter 2**, concepts of RBS and ERDA techniques are treated. Details on scattering processes, collision kinematics, cross-sections, energy loss, Bragg's rule, pile-up background, channelling effects, important parameters involved, mass and depth resolution, plural and multiple scattering, beam damage, ambiguity of the spectra, different approaches to interpret the spectra, different detection systems developed, and calibration standards available are presented. EBS and NRA are also slightly introduced in the RBS section, since approached as higher-energy techniques simply outside the RBS regime. A complete literature review is made throughout.

Then, in **chapter 3**, the experimental set-ups for the different experiments carried out are described. This includes: the RBS, ERDA and NRA set-ups at Surrey; the RBS set-up at Jena (Germany); and briefly, the ERDA/NRA set-ups of the other participants in the Round Robin exercise which is the subject of chapter 5. Particulars on experimental features that are critical for accurate measurements, such as beam path and energy stability, will be given.

Chapter 4 bears upon implant into silicon dose measurements by using RBS. In the first part, a transparent manual data reduction method is developed. In the second part, the results are presented and discussed. The IBA code DataFurnace is validated and used, and the results compared to the manual analysis. The uncertainties are determined critically, and all the numbers and calculations are shown for clarity since we aim to demonstrate a level of combined uncertainty as good as 1%.

In **chapter 5**, accurate measurements of H implants in Si by using ERDA are presented. Other participants from all over the world took part on the same measurements in their own laboratories for a Round Robin exercise. Various detection systems were used. The inter-lab reproducibility is evaluated.

Chapter 6 is dedicated to accurate determination of fluorine content of SiO_2:F films by using RBS. Uniformity of the films and stability of F under ion beam irradiation is first evaluated using the nuclear reaction; the fluorine depletion under He irradiation has been estimated and accounted for. An iterative method is used to extract the F content from the RBS spectra. This method has as a parameter the F

content, which is then extracted iteratively. The IBA DataFurnace code for fitting RBS data was used to start the iterative process. All the details are given and again the uncertainties are determined critically.

In **chapter 7**, an elemental characterization of residual deposition in an ion implanter is presented. The composition of these so-called flakes along with the mechanism by which they are produced are not known, hence the importance of studying thoroughly their nature under a controlled set of beam conditions. The fact that the flakes were inhomogeneous, non-uniform and moreover non-flat added a level of difficulty in the analysis. For a thorough treatment, EBS and NRA are used as complementary techniques in conjunction with RBS.

Finally, in **chapter 8**, a summary of the work accomplished in this thesis is given. Some additional short-term future work regarding accuracy in IBA is also proposed.

CHAPTER 2

THEORETICAL BACKGROUND

2.1 Rutherford Backscattering Spectrometry (RBS)

In this summary, we mainly follow the moderately advanced treatment of Vickerman [Vic97{i}]. A few elements have also been taken from Tesmer and Nastasi [Tes95{i,ii}] (the most useful single volume overview about IBA), and from Chu *et al*. [Chu78] (the standard reference book about RBS). The accuracy question is discussed in some sections more specifically.

2.1.1 Principle

The physical principle of Rutherford backscattering spectrometry is rather simple: an ion beam (typically 1.5 MeV $^4He^+$) is directed onto a solid sample, enters the sample (losing energy through inelastic collisions with electrons), scatters on atomic nuclei (losing energy through kinematics) and travels back out (losing energy through inelastic collisions with electrons) to be detected, showing an energy distribution. Since the ion-target atom interaction can be described by two-body collisions, governed by Coulomb repulsion, the energy spectra can be converted into a target atom mass spectra. However, since the scattered particle energy is a function both of the mass and the depth of the target nucleus in the sample, the *inverse problem* posed by RBS spectrum (given the spectrum, what is the depth profile?) is non-trivial. Nevertheless, RBS enables us to answer the three fundamental quantitative characterization questions: *what* is in the sample? *how much* is there? and *where* is it (how deep is it in the sample)?

Historically, RBS experiments have been commonly carried out using $^4He^+$ with energies in the 1-2 MeV region. Here are some reasons given by Tesmer and Nastasi [Tes95{i,ii}]: there were numerous accelerators available in the 2 MV terminal voltage; energy loss data for ^4He were better known than for other ions; silicon surface barrier detectors have a good energy resolution for ^4He, at about 12 keV; the scattering cross-sections for ^4He striking elements more massive than Be are nearly Rutherford in this energy region. We can add that the depth resolution is rather good for He. Today many RBS/EBS experiments are also carried out using $^1H^+$; the energy resolution is better, and increased yields due to many non-Rutherford cross-sections for $^1H^+$ are very helpful in characterizing some elements less abundant in the sample (see section 2.1.4.2 about EBS).

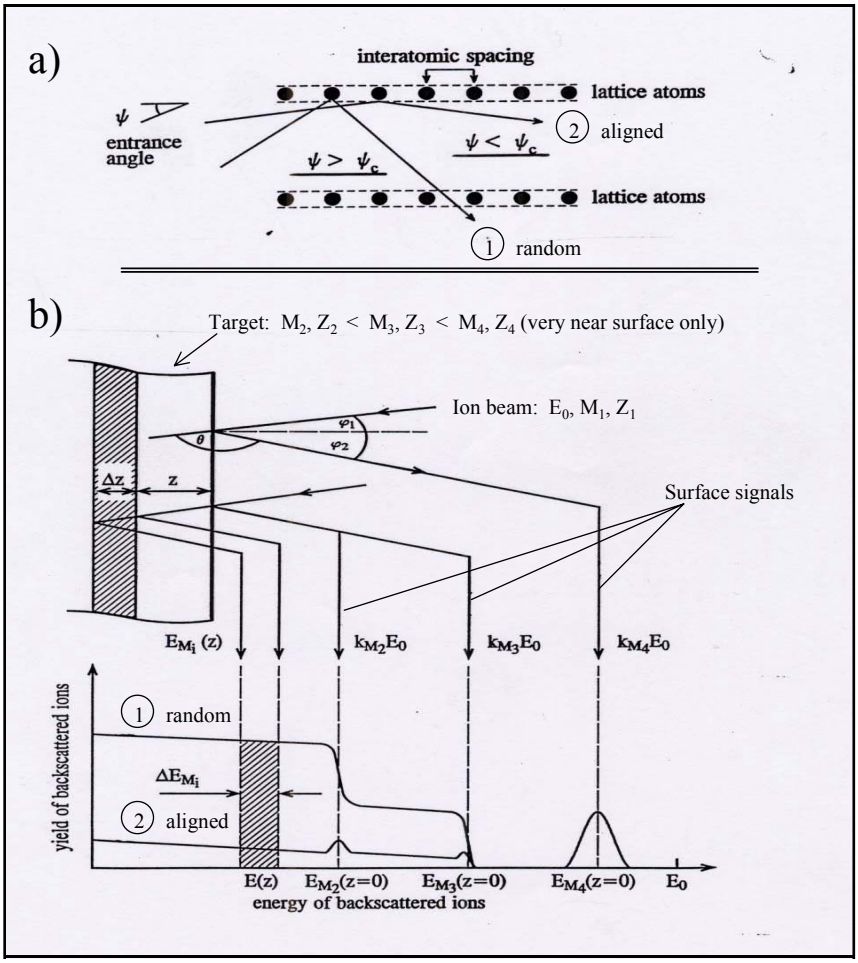

Figure 2-1 *a) Non-aligned (random) and aligned (channelled) schematics. b) Example of an ion-implanted sample RBS spectrum; both the non-aligned (random) and aligned (channelled) schematics are illustrated.*

Following again Tesmer and Nastasi [Tes95{i,ii}], what makes ^{4}He-RBS such a useful analysis technique is that: it is intrinsically an absolute method, therefore it can (very often) be performed without the use of standards; meaningful uncertainties can usually be assigned to the results; the experimental procedure is rather quick and easy, generally taking not more than 15 minutes; it is not deliberately destructive; depth profiling can be achieved (typical depth resolution within 10-30 nm). It can be added that RBS is very convenient for quantitative analysis, it has a small spectral distortion due to multiple scattering (so a simple analytical approach can be very accurate), and real time information can even be obtained (a good example of this is a study where amorphous $GeSe_2$ films with Ag overlayers were illuminated *in situ* in an RBS chamber and the evolution of the silver depth profile as a function of illumination could be investigated [Ren86]).

As will be described in the next sections, head-on collisions of ion beams with target nuclei (Coulomb interaction) gives scattering in a backward direction. Much information can be extracted from the energy spectrum of the backscattered particles. Figure 2-1 presents an RBS spectrum from an ion beam (of mass M_1, and atomic number Z_1) interacting with a target composed of a substrate (M_2, Z_2; M_3, Z_3) and some heavy impurities (M_4, Z_4) in the near surface. Both the non-aligned (random) and aligned (channelled) schematics are illustrated (note that channelling is discussed in section 2.1.7). The collision kinematics gives information about the mass of the constituents, i.e. we can answer the question "*what*?". From the electronic energy loss of the beam in the target, we can answer the question "*where*?". The analytical Rutherford cross-section is connected to the yield, in other words it answers the question "*how much*?". Briefly, it follows that RBS is a very useful technique for *quantitative* analysis. In this thesis, we will show a series of such analyses where uncertainty is determined critically at very high and sometimes unprecedented accuracy (dose measurement and He into Si stopping powers determination as presented in chapter 4). We believe that this standard of analysis ought to become more widespread.

2.1.2 Scattering process

The scattering process is illustrated in Figure 2-2. The trajectories for the elastic collision between two masses, M_1 and M_2, are depicted both in the laboratory system (L) and the centre-of-mass system (COM). Based on a simple description of the situation made through considerations including some of the parameters, the scattering process can be considered as one or a sequence of classical two-body collisions.

First, practically all scattering angles (θ_1 in Figure 2-2) used in RBS analysis are large (>125º) compared to the so-called Bohr's critical angle θ_c, which is determined by the ratio of the de Broglie wavelength λ and the distance of closest approach r_0, $\theta_c \approx \lambda / r_0$ (see again Figure 2-2). In the RBS regime, λ and r_0 are in the order of 10^{-4} and 10^{-2} Å respectively, which gives values of $\theta_c < 1º$. As a result, for such scattering angles larger than Bohr's critical angle, quantum effects can be neglected as demonstrated by Bohr in 1948 [Boh48] (see section 2.1.4.2 for details on elastic non-Rutherford scattering and section 2.1.4.3 on inelastic scattering).

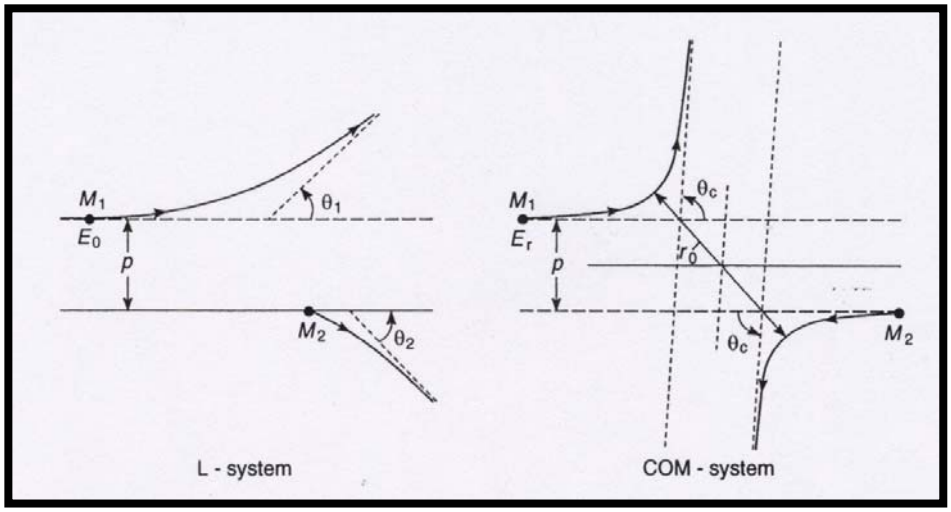

Figure 2-2 *Trajectories for elastic collision between two masses* M_1 *and* M_2 *in the laboratory system (L) and the center-of-mass system (COM) (from [Vic97{i}]).*

Typical lattice constants d are of the order of a few Angstroms, and as mentioned above typical incident ions used in RBS have a de Broglie wavelength λ around 10^{-4} Å. Since $\lambda << d$, diffraction effects from periodic crystal lattices are also negligible.

Phonon (quantum of vibrational energy, in analogy to photon, quantum of electromagnetic energy) interaction cannot be detected in the ion energy spectra since phonon energies are of the order of 0.03 eV only, that is, very small compared to the ion energies (negligible momentum transfer between incident ion and phonon). Another way to convince ourselves is to consider the collision times. These are shorter than 10^{-15} s for RBS energies, whereas thermal vibration periods are in the range of 10^{-12}-10^{-13} s: therefore, the energetic ions *see* a snapshot of a rigid lattice with atoms thermally distributed around their lattice positions.

Also in the RBS regime, the projectile penetrates deep into the atom (up to the vicinity of the nucleus) and exceeds significantly the range of interaction of the surrounding atomic electronic shell, in such a manner that the cloud of electrons has little Coulombian effect. The screening correction to be accounted for at low energies is studied in detail in section 2.1.4.4.

It follows clearly from this discussion that the interaction between an ion and a target atom in RBS experiments can be treated *a priori* as a classical two-body collision.

2.1.3 Collision kinematics (*what?*)

As a simplified treatment, we consider a mass M_1 and a mass M_2 interacting through a centrosymmetric potential $V(r)$ (see Figure 2-2). M_1 is the projectile with the non-relativistic initial energy E_0 and M_2 is the target mass initially at rest. To describe mathematically the interaction, momentum and energy conservation laws are used assuming an elastic two-body collision. These kinematical considerations give us information entirely independently from the knowledge about the details of the interaction.

By simple algebra, the resulting energy E' of mass M_1 after scattering from mass M_2 can then be calculated as a function of scattering angle θ_1 in the laboratory system. This leads to:

$$E' = KE_0 , \tag{2-1}$$

where K is the so-called kinematic factor, which depends only on the mass ratio $A \equiv M_2 / M_1$ and the scattering angle θ_1:

$$K = \left(\frac{\cos\theta_1 \pm \sqrt{A^2 - \sin^2\theta_1}}{1 + A} \right)^2 . \qquad (2\text{-}2)$$

The positive sign holds for $A > 1$ and both signs for $A < 1$. In the latter case, i.e. heavy projectile colliding with a lighter target atom, the scattering angle is limited to $\theta_1 < \arcsin A$, while for the same scattering angle there are two kinematic collisions possible in that region. In Figure 2-3 has been plotted the function $K(\theta_1)$. It is worth noting that the kinematic factor, determined from conservation laws, does not depend on the shape of the potential function.

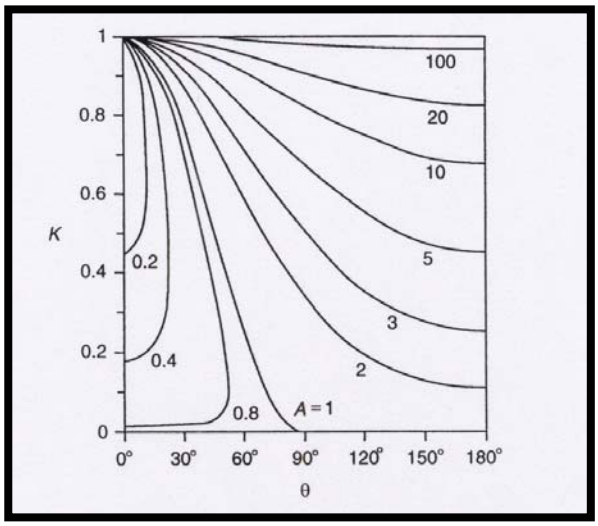

Figure 2-3 *The kinematical factor* K *as a function of the laboratory scattering angle* θ_1 *(see equation (2-2)) (from [Vic97{i}]).*

By virtue of equation (2-2), the scattered-ion energy spectra can be interpreted as mass spectra; consequently we can answer the question "*what* is inside the sample?". The mass resolution can be derived from equations (2-1) and (2-2). In quantitative terms, ΔE_1 and ΔM_2 are related to each other by: $\Delta E_1 = E_0(dK/dM_2)\,\Delta M_2$. Then the mass resolution is found to be[1]:

$$\frac{M_2}{\Delta M_2} = \frac{E}{\Delta E} \frac{A + \sin^2\theta_1 - \cos\theta_1\sqrt{A^2 - \sin^2\theta_1}}{A^2 - \sin^2\theta_1 + \cos\theta_1\sqrt{A^2 - \sin^2\theta_1}}, \qquad (2\text{-}3)$$

[1] From here to the end of section 2.1, we drop the subscript in E_0 for simplicity.

where ΔE is the energy separation, which contains contributions mainly from detector resolution, straggling, beam energy spread and various geometric effects [Oco89]. A representation of equation (2-3) is given in Figure 2-4 (assuming a constant relative energy resolution of the detector of $E/\Delta E = 100$). It can be seen that mass resolution is best for large scattering angles and about equal ion and target atom masses. But it is in fact somewhat deceptive since ΔE varies significantly with projectile masses for surface barrier detectors. For this reason, Heavy Ion Backscattering Spectrometry (HIBS) is not generally used to enhance mass resolution but rather to enhance sensitivity to low levels of surface contamination on very pure substrates [Ban98].

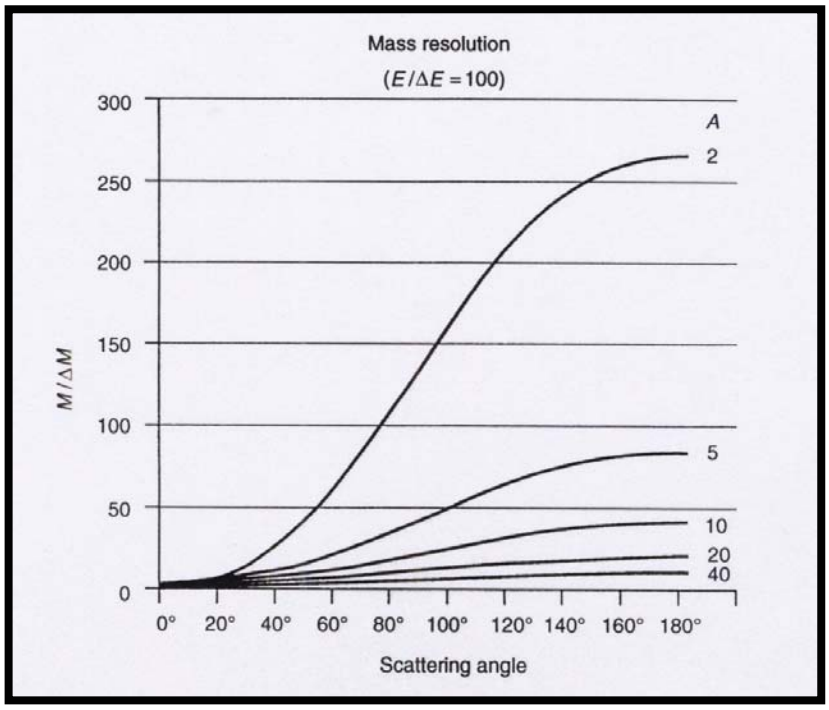

Figure 2-4 *Mass resolution* M/ΔM *as a function of the scattering angle* θ_1 *for a given energy resolution* E/ΔE = *100 (see equation (2-3) (from [Vic97{i}]).*

Some geometric considerations are made in appendix A. As explained in detail, when using light projectiles (typically He) the scattering angles in the vicinity of 180º are preferred for RBS. In this area, the energy of the scattered projectile varies slowly with θ. Furthermore, mass discrimination is largest when θ is close to 180º as discussed just above.

2.1.4 Cross-section (*how much?*)

2.1.4.1 Rutherford scattering

To work out any RBS spectrum, one also needs to know how frequently an elastic collision (scattering event) is likely to occur when incident ions of energy E traverse target particles in a thin film. In other words, given the probability of interaction, one wants to know: *how many* atoms are present in the sample? The differential scattering cross-section $d\sigma/d\Omega$ is a probability-based concept that can answer this question. In every RBS experiment, a detector is placed at a well defined angle θ_1 and counts each particle scattered into the solid angle given by the detector, (which is very small in RBS set-ups, <10 msr, and can ideally be regarded as a differential solid angle). Figure 2-5[1] gives a schematic of the concept of the differential cross-section. Let Q be the total number of particles impinging on the target and dQ the number of particles recorded by the (small) detector, then the differential cross-section is defined as:

$$\frac{d\sigma}{d\Omega} = \frac{1}{Nt}\frac{dQ}{Q}\frac{1}{d\Omega}, \qquad (2\text{-}4)$$

where N is the volume density of atoms in the target and t its thickness (Nt is therefore the areal density, in atoms per unit area).

$d\sigma$ has the dimension of area, hence the name *cross-section*. A geometrical interpretation then comes out: $d\sigma$ is related to the probability that the scattering of one incident particle by one nucleus occurs at angle θ into solid angle $d\Omega$; this can be interpreted as if each nucleus would present a surrounding (very small) circular (ring-shaped) area of a size $d\sigma$ to the (very large) cross-section area S of the beam of incident particles (see Figure 2-5). Thus the differential cross-section $d\sigma/d\Omega$ refers to the probability of scattering at angle θ per unit solid angle. It must be mentioned that equation (2-4) holds only if: the solid angle $d\Omega$ is so small that the scattering angle θ is well defined; the thickness t is small enough so that the energy loss of the particles in the target is not significant, and consequently the energy of the particles is

[1] From here, we omit the subscript *1* for the scattering angle in the equations, i.e. the scattering angle will be simply denoted θ instead of θ_1.

virtually the same through the slab *t*; the fluence *Q* is sufficiently large so that the ratio *dQ/Q* has a well-defined value; finally the circular area *presented* by each nucleus is small and the atoms within the target are randomly distributed in such a way that the differential cross-sections of the nuclei do not overlap.

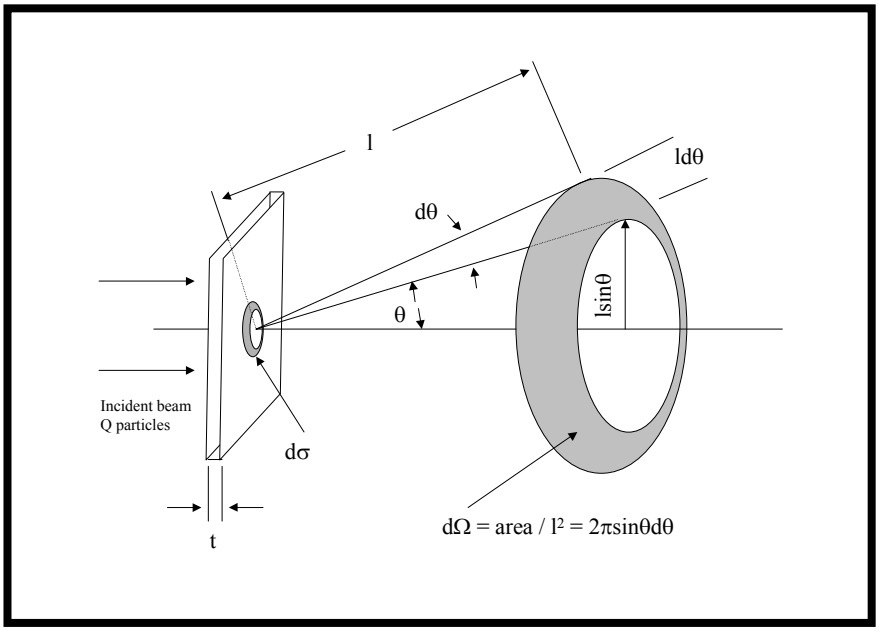

Figure 2-5 *Schematic of the concept of differential scattering cross-section* dσ/dΩ. *The ring* dσ, *centred on a target nucleus, is a purely geometrical construct and not anything physical; it is related to the probability of scattering at an angle* θ *into the solid angle* dΩ.

Energy and momentum conservation must be complemented by a specific model for the force acting during the elastic collision for the differential cross-section calculation. The interaction in the RBS regime is accurately described by the Coulomb potential between two nuclei considered as two point charges:

$$V(r) = \frac{1}{4\pi\varepsilon_0}\frac{Z_1 Z_2 q^2}{r}, \qquad (2\text{-}5)$$

where Z_1 and Z_2 are the atomic numbers of projectile with mass M_1 and target atom with mass M_2 respectively, q is the unit of electrical charge (in C), r is the distance between the two nuclei, and ε_0 is the permittivity of free space which has a value of 8.8542×10^{-12} F·m (F, farad, is the SI unit of capacitance, being the capacitance of a

capacitor that, if charged with 1 C, has a potential difference of 1 V between its plates — 1 F = 1 CV^{-1}). The term $1/4\pi\varepsilon_0$ has the value 5.610×10^{27} keV·cm·C^{-2}. Note that equation (2-5) is valid provided the distance of closest approach is large compared with the nuclear dimensions (no nuclear interaction, which is discussed in sections 2.1.4.2 and 2.1.4.3) but small compared with the atomic Bohr radius $a_o = 4\pi\varepsilon_0\hbar^2/m_e q^2 =$ 0.53 Å (no screening effect, which is treated in section 2.1.4.4), where m_e is the electron rest mass (0.511 MeV/c^2, and here c is the speed of light in vacuum) and $\hbar$ is Plank's constant ($h = \hbar/2\pi$). These assumptions having been made, the differential cross-section $d\sigma/d\Omega$ for an elastic collision is then given by Rutherford's formula [Rut11] (or more accessibly [Gol59{i}]):

$$\left(\frac{d\sigma}{d\Omega}\right)_c = \left(\frac{Z_1 Z_2 e^2}{4E_c \sin^2(\theta_c/2)}\right)^2, \tag{2-6}$$

where the subscript c indicates that the values (energy E of the projectile immediately before scattering together with the scattering angle θ) are given with respect to the COM coordinates, and e^2 is equal to $q^2/4\pi\varepsilon_0$ and has the value 1.4398×10^{-10} keV·cm. Generally the notation $\sigma(E,\theta)$ is used instead of the clumsy $d\sigma/d\Omega$ for simplicity. The transformation of Rutherford's formula from COM to L frame of reference yields, as calculated by Darwin in 1914 [Dar14] (or more accessbly [Chu78{iii}]):

$$\sigma(E,\theta) \equiv \frac{d\sigma}{d\Omega} = \left(\frac{Z_1 Z_2 e^2}{2E}\right)^2 \beta, \tag{2-7}$$

where β is the angular part which is given by:

$$\beta = \frac{\left(\sqrt{M_2^2 - M_1^2 \sin^2\theta} + M_2 \cos\theta\right)^2}{M_2 \sin^4\theta \sqrt{M_2^2 - M_1^2 \sin^2\theta}}. \tag{2-8}$$

At both low and high energies, for any projectile-target pair, departures from Rutherford's cross-section have been confirmed by experiments. As might be expected where accurate measurements are concerned, such deviations must be corrected for, and this is the subject of the following sections.

2.1.4.2 Elastic non-Rutherford scattering — Elastic Backscattering Spectrometry (EBS)

The high-energy departures of the cross-sections from Rutherford behaviour are caused by the presence of short-range nuclear forces. If the energy of the projectile is high enough so that the Coulomb barrier is exceeded, the nuclear wavefunctions then overlap. The incident nucleus can, as it were, "forget" its incident direction, and the probability of scattering into backward may be enhanced, sometimes more than a hundred times Rutherford. The cross-sections are no longer Rutherford although the interaction may remain elastic (no changes in mass in the reaction, or reaction Q value = 0); we therefore refer to this as Elastic (non-Rutherford) Backscattering Spectrometry (EBS).

These high-energy deviations of the cross-sections from Rutherford behaviour have been studied over the years. Mainly two approaches have been investigated: 1) solving the quantum-mechanical scattering problem by using an optical-model potential to describe the nuclear interaction; 2) using classical analytical calculations based on perturbing Yukawa-like nuclear interactions added to the Coulomb potential. From these approaches can be predicted the projectile energies, for various target elements, at which scattering cross-sections begin to deviate from their Rutherford values. A summary of the recent measurements and calculations from [Boz90, Boz91-a-b, Hub91] are well reported on by Tesmer and Nastasi [Tes95{iii}]. It appears that proton backscattering is non-Rutherford for elements $Z_2 \leq 15$ below 2 MeV, while cross-sections for ^{4}He up to 2 MeV are Rutherford for $Z_2 \geq 6$. High-energy non-Rutherford cross-sections cannot be accurately calculated at present, they must be measured. A series of non-Rutherford cross-section graphs for ^{1}H and ^{4}He scattered by target elements with $Z_2 \leq 20$ have been gathered together by Tesmer and Nastasi [Tes95{xi}]. But apparently, some of the former results are somewhat mistaken according to Cheng *et al.*'s measurements [Che94]. Using a ^{4}He beam presenting a beam spread of 1.28 keV, Cheng *et al.* found that: beyond 2.60, 3.20, 3.60, 3.80 and 4.50 MeV, cross-sections are non-Rutherford for F, Mg, Al, Si and Cl, respectively; cross-sections for F, Al and Cl show continuous resonance distributions over energy values just mentioned; Si shows one strong narrow isolated resonance at 4.370 MeV ±10 keV (resonance width

of 20 keV, $\sigma/\sigma_R = 2.90$), and a much stronger one at 5.375 MeV ±10 keV (resonance width of 10 keV, $\sigma/\sigma_R = 9.50$).

Elastic resonances can sometimes greatly enhanced cross-sections over Rutherford values. Analysts exploit elastic-scattering resonances, that is, the EBS technique, to increase sensitivity to low-*Z* elements and to improve accuracy in determination of stoichiometric ratios.

2.1.4.3 Inelastic scattering — Nuclear Reaction Analysis (NRA)

When the target nuclear structure is really reached by high-energy ions, the interaction may become inelastic (changes in mass in the reaction, or reaction Q value ≠ 0), and nuclear reactions can occur; when this is the case, the analysis is then the field of Nuclear Reaction Analysis (NRA). The technique of NRA has been studied in detail using scientometric methods (quantitative investigations of aspects of science) [Buj82]. The fundamental physics involved in NRA can be found in a book by Feldman and Mayer [Fel86{i}]. Tesmer and Nastasi give an overview of this method of analysis [Tes95{iv,v}].

This technique involves well-known nuclear reactions that have been studied and inventoried by nuclear physicists (some useful nuclear reactions can be found in the IBA Handbook [Tes95{iv,xii,xiii,xiv,xv}]). These reactions are isotope specific; NRA is very useful for isotope identification for analysis of particular light elements in a heavy matrix. The energy of the reaction products is not directly related to the mass of the reactant target, and it is usually higher than the energy of the incident beam (this is related to the Q value of the nuclear reaction, which is defined as the difference between the rest energies of the products and the reactants). The scattered particles are well separated from the reaction products in the spectra.

NRA spectra do not suffer from natural background from the high-*Z* components of the target in the same way as in RBS. For instance, when an oxide layer is grown on top of tantalum: due to the atomic number square dependence of the Rutherford cross-section the ratio of the tantalum-to-oxygen is 170, therefore in the RBS spectrum the oxygen can hardly be seen against such a huge background; however, if the $^{16}O(d,p)^{17}O$ reaction is used, the oxygen can be measured without background from the energetic protons emitted. On the other hand, the spectra are

sometimes difficult to interpret because peaks of different particles (or the same particles with slightly different energies) can overlap.

Depth information can be performed by using either energy-loss measurements of a nuclear product ion or from resonance depth profiling. In the latter case, a sharp resonance in the reaction cross-section is used: the beam energy is varied, so the resonance occurs at varying depths. In some cases relatively narrow resonances exist, e.g. $^{18}O(p,\alpha)^{15}N$, and these allow high-resolution depth resolution, assuming an accelerator with high energy stability and small energy spread.

As compared to RBS, NRA cross-sections fall unfortunately by orders of magnitude. Consequently, much higher beam current must be used to collect the same data (statistics). Usually there is no analytical form of the nuclear cross-sections, they must be measured.

PIGE (Particle Induced Gamma-ray Emission) is a special case of NRA when photons are detected. The energy calibration of accelerators can be easily accomplished using these reactions: collecting gammas from different nuclear reactions occurring at several different energies using a scintillation detector placed near the reaction chamber allows one to perform a multipoint calibration. This has been done for this thesis, and it is presented in appendix B.

Nuclear reactions can generate a fair amount of neutrons. Deuteron-induced nuclear reactions are more hazardous than those by an usual H or He beam; the number of generated neutrons increases exponentially with the deuteron energy. Therefore strict safety rules are essential when using particular nuclear reactions. For additional details concerning radiation safety, see [Tes95{viii,xvi}, Leo94{ii}].

2.1.4.4 Screening correction

In the low-energy regime, due to partial screening of the nuclear charges by the electron shells surrounding both nuclei, the simple Coulomb potential given by equation (2-5) is no longer valid; a screened Coulomb potential must be used in order to make appropriate corrections. Several investigations have been made over the years concerning low-energy departures from the Rutherford scattering law which are caused by screening effect of the outer and inner electrons. Some results [Wen52, Lec79, And80-a, Hau80, Mcd83] confirmed the accuracy of the low-energy

corrections suggested by L'Ecuyer *et al*. [Lec79], who present an empirical screening correction as a function of Z_1, Z_2 and E, which can stand as a universal expression. Tesmer and Nastasi give a table of such screening corrections in the range of interest for RBS [Tes95{x}].

But difficulty in the calculation of this correction, so-called F-factor, means that the uncertainty in the absolute value of the cross-section for Bi nuclei, for instance, may be as much as ½% [Wät92]. The F-factor gives a 2.4% correction for Bi but only a 1.2% correction for Sb. For a much smaller atom, the screening effect is negligible, and no correction is needed, which means a zero-uncertainty in the absolute value of the cross-section since it is analytical. Assuming a linear relationship between the screening effect correction and the uncertainty on the absolute value of the cross-section, we therefore estimate that the uncertainty of the cross-section value for Sb, relevant to the IRMM/BAM certified standard (see section 2.1.6), is about ¼%.

2.1.4.5 Multiple and plural scattering

The assumption that incoming and outgoing trajectories are linear, i.e. without significant angular deflections, is not totally true. For unscreened scattering events, the mean free path is around 1000 Å at MeV energies. So even at shallow depths, we can expect the beam to undergo secondary deflections along its path as illustrated in Figure 2-6. Therefore the RBS spectrum is somewhat modified, as such the depth-to-energy conversion scale. Secondary scattering events can be divided into two types: 1) plural scattering, which refers to a few large deviation events; 2) multiple scattering, which refers to many low angle events.

Brice formulated a general treatment [Bri73] where the scattered particles arriving at the detector are interpreted over all the possible paths including large or small secondary scattering events on either the inward or outward paths (which do not have to be well defined in this treatment). This is helpful to clarify the physics, but not treatable numerically, and it turns out that considering only single scattering, with the electronic energy loss giving no deflections, is a good approximation.

The more the particles lose energy as they penetrate the target, the more pronounced is the multiple scattering effect, due to the inverse energy square

dependence of the Rutherford scattering cross-section (see equations (2-6) and (2-7)). Moore investigated the RBS spectrum behaviour versus multiple scattering and found effectively that, for He beam at 4.0 MeV and Au target for instance, the corrections are only major in the low-energy part of the spectrum [Moo80]. Since at present no simple mechanism exists to take into account secondary scattering events (this would require some sort of Monte Carlo treatment for each particle trajectory), analysts facing any RBS spectrum would not include the low-energy part of the spectrum (from a certain depth in the target sample) in the region of interest for the analysis.

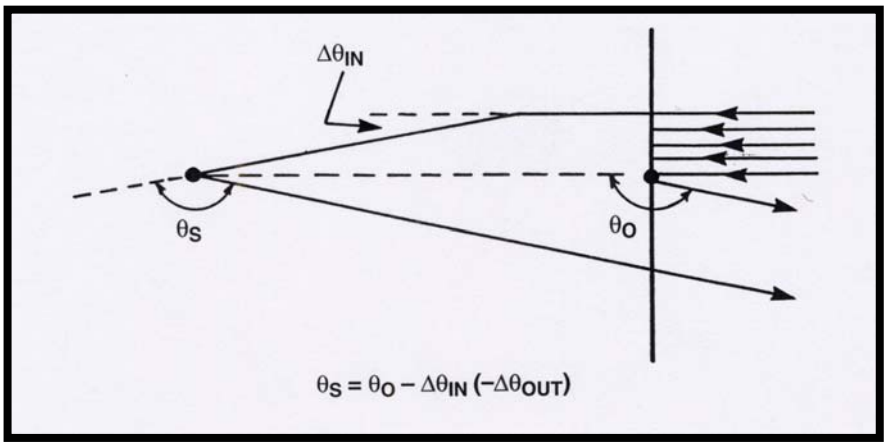

Figure 2-6 *Secondary scattering schematic (at normal incidence) (from[Tes95]).*

Some attempts have been made recently to determine plural scattering contributions on RBS energy distributions for 0.5 to 1.0 MeV ^{4}He on a 100 nm Au on Si target [Eck99]. The code SIMNRA [May97] was used to simulate comparative spectra with double scattering and compared with a full Monte Carlo code. Among others, they found that trajectories with more than nine scattering events ($\theta > 2°$ for each event) contribute to the spectrum, however, most of the scattering events result only in small deflections < 10° each. Trajectories with more than two scattering events with large deflection angles ($\theta > 20°$ for each event) are very seldom and can be neglected. Compared to the single-scattering approximation double scattering yields a much better agreement with the measured spectra. The computing time is in the range of ten minutes, which is tolerable for practical purposes. A higher accuracy

is reached if all collisions are taken into account with TRIM.SP, however, the computing times are much too long to be applicable for routine spectrum analysis.

2.1.5 Energy loss (*where?*)

2.1.5.1 Stopping cross-section

As energetic ions penetrate matter, they lose energy by a variety of collisional processes. Collisions with electrons surrounding the atoms are mainly responsible for the energy loss of the travelling ions. In the RBS regime, the nuclear energy loss is not very important, since the ions are travelling very fast (short wavelength). Only a small fraction of the primary ions come close enough to a target nucleus (impact parameters of the order of 10^{-12} cm) to undergo an elastic nuclear collision, whose kinematics is described in the previous sections. When such an ion is backscattered, its final energy is then determined by the elastic nuclear collision at a certain depth of the sample and the additional inelastic energy loss mainly due to electrons on its way in and out of the target. The deeper the probe particles are backscattered inside the sample, the more important is their total energy loss; from this we can answer the question "*where* is it?".

Here we are interested in the energy loss per unit length *dE/dx* (in eV/Å), the so-called *stopping power*. From the theoretical point of view, the Bethe-Bloch formula is the basic expression used for energy loss calculations, and it has the general form (see [Leo94{i}] or [Tes95{i}]):

$$\frac{dE}{dx} = NZ_2\left(Z_1 e^2\right)^2 f\left(E/M_1\right), \qquad (2\text{-}9)$$

where N is the atomic density of the target (NZ_2 is therefore the density of electrons of the absorbing material) and $f(E/M_1)$ is a function which depends only on the target (E/M_1 refers to the velocity of the projectile). In practice, some corrections have to be added, such as density effect and shell corrections for instance. In 1985, Ziegler *et al*. described a semi-empirical model [Zie85], on which was based the nuclear and electronic energy-loss calculations for hydrogen and helium ions in elemental targets for selected energies tabulated later on by Tesmer and Nastasi [Tes95{vix}].

Since absolute measurements of thin film thicknesses can only be made accurately in terms of weight and area, i.e. since densities of thin films are systematically uncertain, in RBS we rather use the so-called *stopping cross-section* ε instead of dE/dx. The former is simply related to the latter by the atomic density N:

$$\varepsilon(E) = \frac{dE}{dx}\frac{1}{N}. \tag{2-10}$$

The stopping cross-section ε is generally expressed in thin film thickness units (TFU), in eV/(×10^{15}at/cm^2). Some stopping cross-section curves are plotted in Figure 2-7.

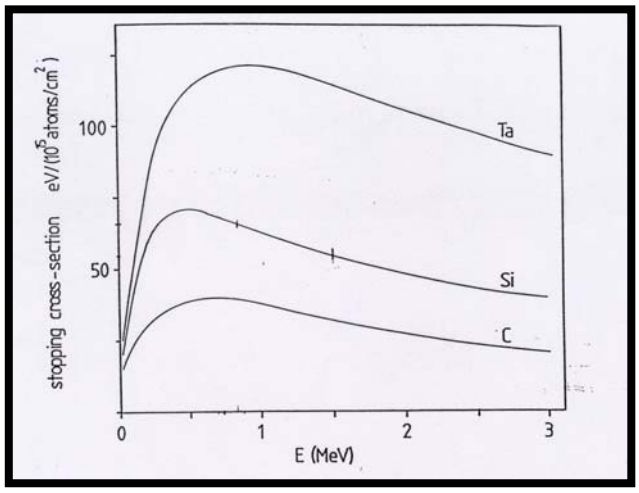

Figure 2-7 *He stopping cross-sections for C, Si and Ta target materials (from [Jey98-a]).*

In compound material the stopping is commonly calculated as the sum of the weighted elemental stopping cross-sections, this is called Bragg's rule [Bra05]. For instance, for a compound made of two constituents A and B with the relative abundance m and n respectively ($m + n = 1$), then Bragg's rule yields:

$$\varepsilon\{AmBn\} = m\varepsilon\{A\} + n\varepsilon\{B\}, \tag{2-11}$$

and consequently the specific energy loss is given by:

$$\frac{dE}{dx}\{AmBn\} = N\{AmBn\}\varepsilon\{AmBn\}, \tag{2-12}$$

where $N\{AmBn\}$ is the atomic density of the compound material.

But this approximation simply assumes that each target atom acts independently in the energy-loss process and ignores, for instance, any effects of chemical bonding in the material. It has been reported [Fen74, Zie88] that this simple rule sometimes implies uncertainties higher than 10%; they can reach 20% around the stopping maximum for light organic gases and for solid compunds containing heavier constituents, such as oxides, nitrides, etc.

Based on previous works [Cha78, Sab85, Kre80, Odd89], a model called *cores and bonds* (CAB) has been developed in order to take into account these chemical state effects [Zie88]. This model allows clearly for two contributions to the energy loss of ions in a compound: the effect of the cores, i.e. the closed electron shells of atoms, and the effect of chemical bonds (such as H — C or C == C bonds). However, the model becomes less accurate when physical state effects (stopping dependence on the physical state of the medium) appear to have more than a little effect. As an indication, it has been observed [Thw85] that for light ions stopping powers are up to 20 % larger in vapour than in the solid phase, whereas for heavier ions the opposite has been reported [Her91], that is, the stopping powers are then up to 20 % lower in gases than in solids. For a review of experiments on both chemical and physical state effects, we refer the reader to [Thw85, Twh87, Bau90].

More recently, the two empirical models (Bragg's rule and CAB) have been tested in polymers such as Makrofold, Mylar and Kapton (which are of considerable interest due to their wide use in various applications, e.g. as absorbers as discussed in section 2.2.5) [Che99]. The stopping powers of 1.0-3.0 MeV ^{4}He were measured using transmission techniques and compared to both models. These values agreed with each other within the uncertainties (< 5%), which are governed mainly by the transmission techniques. However, it was found that the CAB model yields in general higher stopping power values by a few percent (2-4%).

2.1.5.2 Stopping cross-section factor and surface energy approximation

A useful derivative quantity for RBS is the so-called *stopping cross-section factor [ε]*. Here we are interested in knowing the *energy thickness Δ* of the

film thickness *t*:

$$\Delta = KE_0 - E_2 , \tag{2-13}$$

where E_0 and E_2 are the initial energy of the projectile and the detected final energy, respectively, for a scattering event occurring at a depth *t*, and *K* is the kinematic factor (see equations (2-1) and (2-2)). This can be visualised in Figure 2-8.

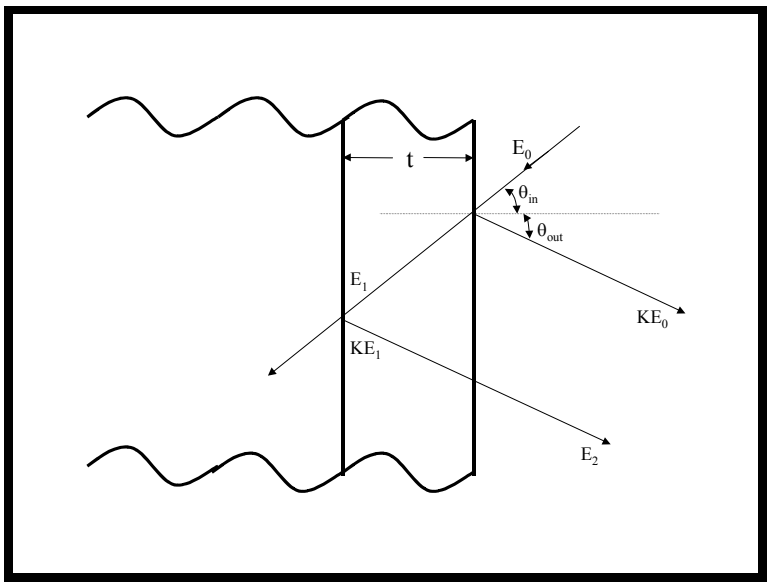

Figure 2-8 *Schematic of the stopping cross-section factor, a useful derivative quantity for RBS.*

In the surface energy approximation ($t \to 0$), assuming a constant energy loss on the way in and on the way out (as $\varepsilon(E)$ varies only slowly with *E*), we find:

$$\Delta = [\varepsilon] \cdot t , \tag{2-14}$$

where *t* is expressed in TFU ($\times 10^{15}$at/cm^2), and the stopping cross-section factor $[\varepsilon]$ is given by:

$$[\varepsilon] = \frac{K\varepsilon(E_0)}{\cos\theta_{in}} + \frac{\varepsilon(KE_0)}{\cos\theta_{out}} , \tag{2-15}$$

where θ_{in} and θ_{out} are respectively the incident and exit angles with respect to the surface normal (for normal incidence, $\theta_{in} = 0$ and $\theta_{out} = \pi - \theta$). As depicted in Figure 2-8, E_1 is the energy just before scattering; in the surface energy approximation, the

energy loss in the outward path is evaluated at the energy KE_0, not at the energy KE_1, as $E_1 \rightarrow E_0$ when $t \rightarrow 0$.

It is worth recalling that this is only an approximation, which holds for an infinitely thin layer from the surface. For a backscattering event occurring deeper in the sample, one needs to make a proper integration of the stopping powers (which are a function of energy) throughout the inward and outward path.

2.1.5.3 Depth resolution

The depth resolution is governed by the energy resolution. Firstly, it strongly depends on the value of the stopping power; the higher is the energy loss per unit thickness, the better different slabs can be discriminated on an RBS energy spectrum. It is then best for most elements in the energy range of 0.5-1.0 MeV for He where the stopping power has its maximum. Also better depth resolution can be expected for heavier materials, as high-Z elements present larger stopping powers.

But practically, the energy resolution of the system is dominated by the detector resolution, which is typically ~12 keV, and this leads to depth resolution around 10-30 nm. This can be improved, of course by using expensive high-resolution detectors, but also by using grazing angles (as more energy is lost in the way in and out of each slab thickness, again discrimination of slab thicknesses in the final RBS spectrum is enhanced). However, in the latter case, the total analysed depth is obviously reduced.

2.1.5.4 Energy straggling

As ions penetrate deeper in the sample, energy straggling occurs due to the statistical nature of the energy-loss process: when a number of particles, all having the same initial energy, have penetrated to a certain depth in the sample, their energies present a distribution of a certain width. Assuming a gaussian distribution of the energy fluctuations, Bohr in 1915 first roughly calculated this broadening, and its variance turned out to be given by [Boh15]:

$$\Omega_B^2 = 4\pi\left(Z_1 e^2\right)^2 Z_2 N t \,. \qquad (2\text{-}16)$$

So the mean-square value of the straggling in Bohr's model increases linearly with the nuclear charge Z_2 of the target material and with depth t, and surprisingly it is independent of the ion energy.

However, Bohr's calculation is only an approximation (which really fails, for example, for thick targets for which the energy loss exceeds about 25% of the incident beam energy); many works have been undertaken to improve Bohr's treatment and to develop other models over the years, so that straggling effects can be more satisfactorily accounted for. Without entering into the details, here are some of the milestones. First, an important extension to Bohr's treatment came in 1953 from Lindhard and Scharff, who proposed a simple correction for ion velocities below E_0 [keV/amu] = $75 \cdot Z_2$ [Lin53]. Then more extensive calculations were derived by some workers [Bon71, Chu76, Bes80]. Straggling in the non-Gaussian region (very low energies) and for heavier-ions energy was studied by many scientists [Liv37, Lan44, Sym48, Vav57, Tsc68, Bis75]. Charge exchange together with target non-uniformity effects become significantly important for heavier ions; the charge exchange effects are discussed in [Sof90]. Using the effective charge and scaling approach for energy straggling, together with existing H, He and heavy ion straggling data, and accounting for correlation effects and charge exchange effects, a fitting function for the model presented by Chu in 1976 [Chu76] was developed in 1991 [Yan91].

2.1.5.5 Stopping power accuracy

The measurements leading to the determination of energy loss values $\varepsilon(E)$ usually called stopping powers (or of the stopping cross-section factors $[\varepsilon(E)]$, the useful derivative quantity for RBS) are very difficult to make. Firstly, due to the stochastic nature of the energy loss process, a monoenergetic incident beam in a target suffers energy broadening during its passage, so this energy straggling effect must be accounted for. But this is not the biggest difficulty. The real problem is non-uniformity of the films, both in thickness and in composition, and the presence of surface layers which can be relatively thick and hard to characterize. As a result, as attempts to improve the reliability of the stopping power values, such measurements have been repeated many times over the last 30 years, leading to many revisions of

the stopping power tables [Zie74, Zie77, Zie80, Zie82, Zie85, Tes95{vix}, Kon98, Kla98] (and also database from TRIM-95, which is an updated version of the simulation code TRIM developed by [Zie85], and similarly database from SRIM2000 [www⑦]).

It turns out that uncertainties in stopping power values are rarely as low as 5% [Zie85, Tes95{i}]; consequently this has been the main limitation on the accuracy obtainable by RBS. The stopping parameterisation that came out with the updated simulation code TRIM-95 has been commonly *accepted*, although the actual data are unsupported in any critical way. As an example, using $^4He \rightarrow Si$ stopping cross-section values reported by Konac *et al*. [Kon98], and stopping power values for $^4He \rightarrow N,O$ from TRIM-95, Lennard *et al*. have recently simulated spectra from Si, SiO_2 and Si_3N_4 targets [Len99-a]: amongst the results, they found a ~7-8% discrepancy with the SiO_2 and Si_3N_4 experiments for ^4He energies ~1 MeV. Since quantitative RBS is generally performed at ~1-2 MeV ^4He ion energy, it is clear that we need a step jump in the accuracy and precision of the $\varepsilon(E)$ database to reach the 1% accuracy level for RBS analysis.

Recently, new data has become available permitting a different approach to normalisation in RBS. The backscattered-ion yield of a thick target in a particular energy window is determined by the number of target atoms required to give that energy loss. Thus, if the energy loss of the beam in a particular material is known precisely, then that material can be used as a calibration standard. Konac *et al*. have determined the energy loss of He in amorphous Si [Kon98]: these data are consistent with the measurements of Lennard *et al*. [Len99-a], and these together with the measurements of Bianconi *et al*. [Bia00] and Lulli *et al*. [Lul00] show that the new values are correct at about 2%. Some of Bianconi *et al*.'s data is absolutely calibrated with a claimed uncertainty of 1%. Amorphised Si is easy to prepare in an implantation laboratory and very reproducible; therefore this material can be used as a *standard*.

Some of the most accurate data of Bianconi *et al*. for Si energy loss have been re-analysed by Barradas *et al*. with a sophisticated Bayesian method [Bar02]. Where Bianconi *et al*. used only the surface Si yield of the spectrum for different incident He energies, Barradas *et al*. use the spectrum from a significant depth of the amorphised Si sample. The method therefore uses more information from the

collected data, and moreover, the data analysis handles it all in a self-consistent way and finds the best parameters of the energy-loss function consistent with the data. The Bayesian treatment yields uncertainties naturally. In this way the reliability of the new parameters can be demonstrated. As a result, this new parameterisation has been found to have a uncertainty of 2%.

For a pure Si material we can define a calibration factor $M_{Si}(E_0,\theta)$, which we call the *magic number*, and which links the surface yield Y_0 of the Si material and the energy loss:

$$M_{Si} = \frac{Y_0}{Q\Omega\kappa} = \frac{\sigma(E_0,\theta)}{[\varepsilon(E_0,\theta)]}, \tag{2-17}$$

where Y_0 is the Si surface yield in the RBS spectrum (in counts per channel), Q the total fluence incident on the target (in μC), Ω the solid angle of the detector (in msr), κ the energy calibration of the spectroscopy system (in keV per channel), $\sigma(E_0,\theta)$ the Rutherford scattering cross-section evaluated at the beam initial energy E_0 and the scattering angle θ, and $[\varepsilon(E_0,\theta)]$ the stopping cross-section factor (in eV/($\times 10^{15}$at/cm^2)) evaluated in the surface energy approximation (at beam initial energy E_0 and scattering angle θ). This equation can easily be derived from equation (2-19) introduced further below in section 2.1.9. With meticulous and repeated measurements of the solid angle and the charge collected (fluence), for a detector placed at a backscattering angle of 170° and using a 1.5 MeV He incident beam, Bianconi *et al*. found that M_{si} has a value of 28.8(3) cts/(keV·msr·μC) [Bia00]. Cross-section ratios and stopping cross-section factor ratios (evaluated in the surface energy approximation) can be used, as can be seen from equation (2-17), to extrapolate new M_{si} values for new experimental conditions. For instance, for 166.9° and 133.1° scattering angles and for a beam of 1490.4 keV, we find $M_{si}(166.9°)$ = 29.2 and $M_{si}(133.1°)$ = 31.3 cts/(keV·msr·μC), which will be useful in this work (see chapter 4). It must be noted that, for the latter calculations, stopping cross-section factor ratios were used, which change much less rapidly than stopping cross-section factors themselves because the form of the energy-loss curves is much better known than their absolute values; for this reason no significant accuracy is lost (error within ~0.1% [Jey97]).

In fact, Bianconi *et al*. determined $M_{Si}(E_0,170^0)$ (and therefore determined $[\varepsilon_0(E)]$) for several values of initial energy, that is, for E_0 = 1.0, 1.5, 2.0 and 2.5 MeV $^4He^+$ in amorphised Si [Bia00], and showed excellent correlation with Konac *et al*.'s values [Kon98] of ε at the specified points. Lennard *et al*. demonstrated that simulations of RBS spectra using Konac *et al*.'s data were in excellent agreement with real spectra [Len99-a], which indicates that the *form* of Konac *et al*.'s parameterisation of $\varepsilon(E)$ was correct. Bianconi *et al*.'s values are reproduced when Konac *et al*.'s parameterisation is increased slightly by 2%. This value of 2% was also observed by Lulli *et al*. [Lul00]. Konac *et al*. do not explicitly estimate the total uncertainty of their measurements, but they do summarise a number of contributions at the 1% level. In particular, their measurement uncertainty (given mostly by counting statistics — Type A) is "well below 1-2%", and they estimate the target areal density calibration uncertainty at "0.8-2%" and a detector energy calibration uncertainty up to 0.5%; therefore their combined uncertainty cannot be quoted as significantly better than about 2%. Consequently, a 2% discrepancy is consistent with the uncertainty of these measurements.

2.1.6 RBS standards

RBS is sometimes cited as a technique with 1% accuracy: however this depends on the accuracy of the knowledge of the product of the detector solid angle and the collected charge, that is, the number of ions incident on the sample. We are aware of no *critical* reports of RBS systems with charge collection better than 1%, and measurements of solid angle at this precision are notoriously difficult. Therefore, accurate work must be validated by standards for the charge·solid angle product.

The Bi implant into Si standard from the *Harwell series* was determined absolutely and was quoted at 2% uncertainty [Tes95{vii}], but the remaining samples from this standard should soon be re-released with individual certificates based on high-precision RBS measurements *relative* to weighed evaporated films [Wät94]. A similar 40 keV Bi implant from the University of Western Ontario, Canada, was certified (4.72×10^{15}Bi/cm^2, 4 Dec 96) by W.N. Lennard at 2% [Len99-b], and will be used in chapter 4 on accurate dose implant RBS measurements.

In conjunction with the method described in [Wät94], two completely independent methods, namely Instrumental Neutron Activation Analysis (INAA) and Inductively-Coupled Plasma Isotope-Dilution Mass Spectrometry (ICP-IDMS), were used to certify new Sb implants into Si substrates at about 0.6% [Eck01, Pri02, Eck02]. These reference samples are now designated IRMM-302/BAM-L001. We will use (again in chapter 4) one of these new certified standard samples from IRMM and BAM. More specifically, this is an Sb implant at 400keV with a certified dose of $4.81(3)\times10^{16}$Sb/cm^2 into a Si wafer with 100nm surface oxide (sample ref.#16.5), where (3) is the combined standard uncertainty u_c according to GUM [ISO93] (see also appendix C).

2.1.7 Channelling

Materials are not all amorphous or composed of randomly oriented polycrystallites. Some present structural and crystalline order, such as silicon, the most common semiconductor, or diamond (see Figure 2-9). When properly oriented (Figure 2-9b-c), rows or planes of target atoms can *steer* energetic incident ions by means of a correlated series of gentle, small-angle collisions; this is called channelling. Strings of atoms in the bulk are then *shadowed*, as a result the probability of scattering from these shadowed atoms is reduced, which leads to totally different (reduced) yields below the very near-surface in the RBS energy spectrum. In fact, when analyzing crystalline samples, it is somewhat difficult to find a *purely* non-aligned orientation (Figure 2-9a), that is, to have the target present a totally random alignment of the atoms to the incident beam. When channelling-free spectra are required for the analysis, one generally needs to amorphise the crystalline sample before carrying out the RBS experiment, by means of ion implantation for instance.

We will not go any further in the details of channelling effects, this would be beyond the scope of this work; channelling is a very large field in its own right. Let us just mention that the major applications derived from channelling effect measurements are mainly: the amount and depth distribution of lattice disorder, the location of impurity atoms in the lattice sites, and the composition and thickness of amorphous/amorphised surface layers. The general phenomenon of channelling together with its measurement and its applications have been well described by a

number of authors, such as [Mor73, Gem74, May77, Fel82, Swa82, How83]. An interesting survey can also be found in Tesmer and Nastasi [Tes95{vi}]. Low-energy channelling (below 50 keV) has been studied [Buc83, Aon89], as well as high-energy channelling (above few MeV per nucleon) [Ugg80, And80-b].

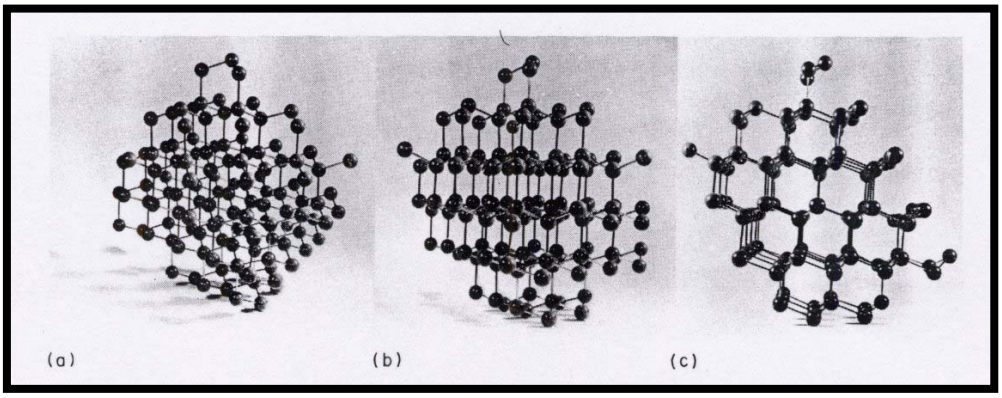

Figure 2-9 *Model of a lattice atoms showing the atomic configuration in the diamond-type lattice viewed along (a) random, (b) planar, or (c) axial directions (from [Chu78]).*

In this thesis, silicon substrate samples will be analysed (chapters 4 and 5). The channelling technique will be useful to verify the amorphisation conditions of the samples, especially in chapter 4 where non-aligned yields are required.

2.1.8 Pile-up

In RBS experiments, depending on the counting rate, pile-up may be significant. A proper treatment of pileup is essential to accurate RBS analysis, since not only can the backgrounds be relatively large, but also they are non-linear.

At relatively low counting rates, there is no need to go any further than pairwise pile-up correction. In this thesis, we will follow Jeynes *et al.*'s treatment [Jey97]. Summarily, a pairwise pile-up spectrum (whose integral must be negative since for every piled-up pulse detected and displayed at the multichannel analyser there are two real events at the detector) is calculated then subtracted from the RBS spectrum. The value of the weighting factor W (see equation (2-18)), which represents the probability of pile-up occurring due to the average count rate, is fitted to the spectrum (to the regions of the spectrum where only background signals can exist). This factor depends on various parameters, mostly on the experimental set-up

including the electronics settings (e.g. the low-level discrimination); it should be a function of the time resolution of the electronics and the count rate for the analysed spectrum. The weighting factor W is given by:

$$W = w\frac{c_T}{t_{live}}, \tag{2-18}$$

where c_T is the sum of the counts in each channel, t_{live} the acquiring livetime and w the normalization factor. The latter value was found to be $\approx 1.2\times10^{-6}$ s at the Surrey Ion Beam Centre facilities; it was measured as explained in [Bar97-a]. This pile-up treatment is implemented in the IBA code DataFurnace.

It has been shown in [Har73] how to improve the electronic pile-up rejection by an order of magnitude by increasing the time resolution of the rejector. A multiple pile-up analysis is made in [Gün88], and it is described how to reduce pile-up by another order of magnitude by reducing the effective count rate using a multisegment detector system. In [Ams92], is presented an interesting discussion about how the pile-up is affected by the electronics, and in particular the pulse shape distortion of the sum peaks. The effect of the intrinsic low-level cut-off implied by the noise-limited threshold of the low-level discriminator of the amplifier is explained in detail in [Boi97].

2.1.9 Important parameters

The most important equation we will have to deal with relates the yield Y_A (in counts per channel) for a component A of fraction f_A in matrix AB to some of the parameters described previously:

$$Y_A = \frac{Q\Omega f_A \sigma_A(E,\theta)\kappa}{[\varepsilon]_A^{AB}}. \tag{2-19}$$

For accurate quantitative RBS analysis, the measurement of the charge·solid angle product ($Q\Omega$) is rather critical; as can be seen from equation (2-19), this relies on the energy-loss values and the electronics calibration. Alternatively, one can integrate equation (2-19) over a region of interest (ROI) of the spectrum (such as the peak from some ions implanted in the sample for instance), which yields:

$$Y_{ROI} = Q\Omega f_A \sigma_A(E,\theta)(Nt)_A, \qquad (2\text{-}20)$$

where $(Nt)_A$ is the areal density (in at/cm^2) of the component A, and which gives the total integrated yield for the region of interest ROI (net peak area of the implant for instance). In that case, accurate calibration of an RBS set-up (determination of $Q\Omega$) can be made by using a certified standard sample (with an implant areal density accurately determined) as reference, as the IRMM/BAM Sb implant into silicon sample as described in section 2.1.6.

2.1.10 New IBA tool: DataFurnace

RBS analysts have to face the *inverse problem* (given the spectrum, what is the depth profile?) posed by RBS spectra. The fact that the scattered particle energy is a function both of the mass of the target nucleus, and of the depth of the target nucleus in the sample really complicates the interpretation of the spectra.

Many helpful computer simulation codes have been developed to treat quantitatively RBS spectra, notably RUMP [Doo85], SENRAS [Viz90], GISA [Saa92], RBX [Kót94] and SIMNRA [May97]. The treatment is performed in a 3-step iteration: a) assume a certain structure for the target; b) calculate the spectrum corresponding to the assigned structure; c) compare with the collected spectrum. This procedure is repeated until a reasonable fit is obtained. This trial-and-error approach is tedious and has a number of major drawbacks.

But recently, analysts have benefited from another powerful tool, that is, DataFurnace [Bar97-b, Bar98-a-b-c-d, Bar99-a-b-c, Mar98, www②, www③], an automatic *fitting* code (and not a simulation code, although simulation functions are also available as a complementary tool), based on the Simulated Annealing algorithm, so-called SA (for details about SA see the book [Aar89], or more accessibly [Kir83]). This code is capable of solving the inverse problem, even for very complex samples, and it has been developed here at the Surrey Ion Beam Centre. An interesting review on the features, applicability and validation of this very versatile and general new tool together with other approaches to handling IBA data has been proposed very recently [Jey02]. We present an overview on the utilization of DataFurnace in appendix D.

2.2 Elastic Recoil Detection Analysis (ERDA)

This overview on ERDA is mostly based on the exhaustive book by Tirira *et al*. [Tir96]; this can be regarded as the most useful practical guide to ERDA for any ion beam user. ERDA refers to the same scattering process and the kinematics as RBS, thus the details given here are only complementary. Although elastic recoil spectrometry is quite similar to backscattering spectrometry, subtle and fundamental differences exist; therefore it is worthwhile to highlight some important points. We will put an emphasis on ERDA in relation to *accuracy*.

2.2.1 General description

Briefly, when a beam of positive ions strikes a solid target, enough energy can be transferred from an incident ion to a target nucleus during their elastic collision to make the latter recoil from the target. This elastic recoil process can be described by simple kinematic equations given by the physics of elastic collisions [Tir96{i}]. Composition and depth profile of the target can then be determined by the energy of the detected recoiling nuclei: this is the so-called ERDA technique.

As before, the mass of recoil target atoms can be calculated from kinematics, and depth information is obtained from energy loss of ions and recoil atoms in the target material. If the target consists of a thin foil, recoil particles can emerge at the back surface and can be detected at ~0º angle: this experiment is called *transmission* ERDA. But in the semiconductor field, where samples are thick, as it is the case for the samples analysed in this thesis, the *reflexion* mode is most used: it consists of an ion beam impinging at grazing incidence onto the target and detecting recoils at the front surface, generally also at grazing angle (see Figure 2-10).

ERDA is primarily suitable for depth-profiling light elements in a heavy matrix, such as hydrogen in silicon. As a matter of fact, the determination of hydrogen in solids has been a driving force in the development of ERDA. Hydrogen has been long the most difficult atomic species to profile: Because of its light mass, ion backscattering cannot be used; nuclear reactions, which give good depth resolution and sensitivity, require higher energies than can be readily obtained from the numerous 2-3 MV Van de Graaff accelerators available. Other profiling

techniques are generally insensitive to hydrogen or suffer other problems. The widely used SIMS (Secondary Ion Mass Spectroscopy) for example, although very surface sensitive, requires UHV (Ultra High Vacuum) systems and very careful handling for a valid analysis of hydrogen.

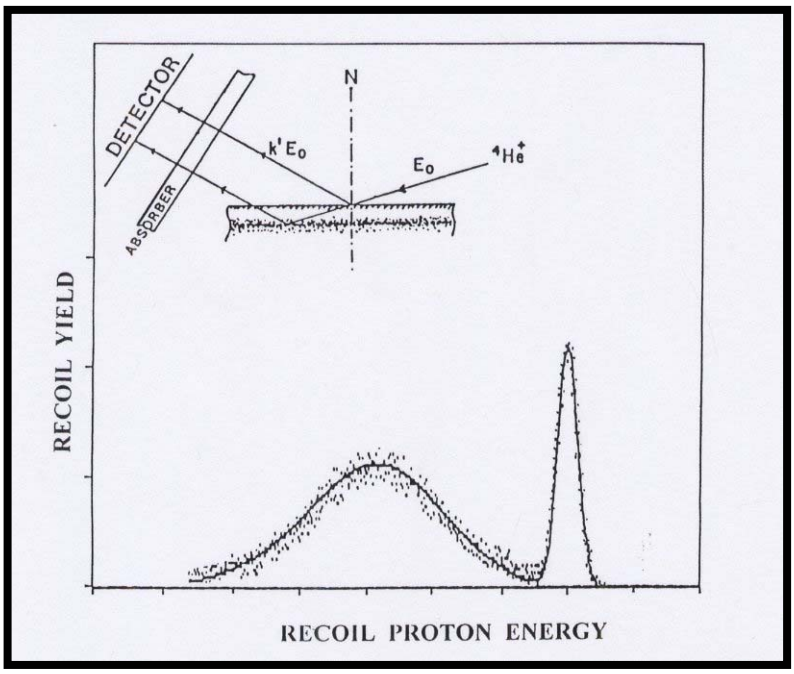

Figure 2-10 *Typical arrangement for reflexion ERDA (hydrogen profiling with an helium beam) and resulting spectrum from an implanted target. (The thin peak is due to hydrogen adsorbed on the surface.) (from [Tir96]).*

2.2.2 Milestone

ERDA is actually an old technique first introduced and described as early as 1914 [Mar14]. But it is only in recent years that this technique received considerable development. We had to wait untill 1976 for the analytical capabilities of ERDA for the analysis of light elements to be convincingly demonstrated by L'Ecuyer *et al*. [Lec76], although a few attempts of ERDA-like experiments in transmission mode had been done before [Coh72, Smi74, Moo75]. Two years later, ERDA was officially first applied as an established analysis technique using a ^{35}Cl beam at 30 MeV [Lec78]. Soon afterwards the recoil analysis technique was adapted for measurements of ^{1}H depth distributions using a ^{4}He beam from a 2.5 MV Van de Graaff accelerator [Doy79].

Theoretical and conceptual analysis of spectrum shape and height, along with considerations of such secondary effects as straggling, multiple scattering, etc, have benefited from works on Rutherford backscattering spectrometry undertaken throughout the years since the fifties. Many approaches have been studied to interpret recoil spectra. In 1986, the possibility of simulating recoil spectra successfully as a step in extracting hydrogen depth profiles from the data was highlighted [Ben86].

The work presented in [Doy88] can be considered as the first review of the physical concepts involved in ERDA, and it aimed at giving a concise step-by-step description which details the analysis of ERDA data. In this short review, the spectral scaling approach was introduced. Briefly, this consists of using interpolation of the tabulated recoil cross-sections and effective stopping powers to determine scaling factors for each channel in the recoil spectrum, and the yield-per-channel data are thereby modified to appear as though the incident projectile energy and effective stopping power are constant through the sample; then the energy scale is transformed to depth, and the yield converted to concentration. Also discussed was that analysis can be done by performing spectral simulation and this would be more generally applicable; this emphasised the importance of the development and distribution of simulation codes so that the full power of ERDA can be exploited at all IBA laboratories.

The major advances from simulation codes for ERDA came out a few years later when some theoretical approximations, that lead to relatively fast calculations for many contributions to the depth resolution, were proposed [Szi95]. These were implemented by the computer code DEPTH [Szi94] (which is not limited to ERDA analysis), and have been demonstrated to be “relatively precise, fast and valid in the most general case, showing a precision of 10% for reproducing the experimentally obtained depth or energy resolutions”. This is particularly important for ERDA because grazing angle geometries accentuate energy broadening problems.

The drawbacks of simulating ERDA spectra, particularly for more complex samples, are that it is somewhat such tedious an approach, it may require a long time and also a rather good knowledge of the detected element distribution prior to analysis. This may lead to gross errors. But recently the new very powerful fitting code DataFurnace has been released and made available to the IBA community (see

section 2.1.10 and appendix D); this is a very versatile tool, and quantitative accurate depth profiles from complex samples can be rapidly extracted.

Some other interesting studies have been carried out to handle ERDA data. An absolute, quantitative procedure was developed at the turn of the nineties, using ERDA in the energy range ≤ 1.8 MeV, to determine the hydrogen content and to describe its concentration profile in the near-surface region of solids [Tir89-a, Tir90-a, Tir90-b, Tir91-a]. The number of recoiling protons was normalized with respect to the yield of backscattered helium. The interpretation of the spectra was worked out by means of simulation-optimization procedure named the GABY code. A newly calculated expression for the elastic recoil cross-section as reported on in [Tir89-b] was used.

In the context of profiling hydrogen into crystalline-silicon (c-Si), another method has been recently proposed, which involves conversion of the channel difference between surface and bulk signals directly to depth [Ver01]. This *channel-depth conversion* method relies on RBS to unambiguously determine the depth of a buried marker (zirconium) coincident with the bulk hydrogen distribution in a series of several silicon calibration standards. The relationship between the depth to the marker and the channel difference between surface and bulk hydrogen centroids from ERDA spectra provides the analyst with the information necessary for converting ERDA channels to depth. This method has been demonstrated to offer distinct advantages over depth profiling by using computer simulation.

2.2.3 Collision kinematics

The mechanics of the collision for ERDA is exactly the same as for RBS, with the difference that we are now interested in the recoil particle rather than the (incident) scattered ion. The same considerations regarding the scattering process as the ones made in the RBS treatment hold. The problems of energy loss, energy straggling, energy resolution, mass resolution, etc, all arise in the same way. A notable difference with RBS is that whereas with RBS the L and COM coordinate systems are similar (the L system RBS cross-section can be treated as a perturbed COM system, for example), with ERDA the L system equations are rather different from the COM ones.

For a schematic of the recoil process, we refer the reader back to Figure 2-2 in section 2.1.2[1]. Using the same momentum and energy conservation laws, the relation between the energy E_r of the recoil particle and the incident energy E_0 is:

$$E_r = K_r E_0 , \tag{2-21}$$

where K_r is the kinematic factor associated with the recoil particle, and which is given by:

$$K_r = \frac{4M_1M_2\cos^2\varphi}{(M_1+M_2)^2} , \tag{2-22}$$

where M_1 and M_2 are the mass of the projectile and recoil particles, respectively, and φ the recoil angle. It is easy to see that:

$$K_r \equiv 1 - K , \tag{2-23}$$

where K is the kinematic factor associated with the scattered particle, as defined in section 2.1.3.

From the geometric considerations made in appendix A, some points can be highlighted. First, the recoil energy varies slowly with small fluctuations of φ around 0°. It is also when $\varphi = 0°$ that largest energy separation between two signals arising from two different recoil particles occurs. Therefore recoil angles in the vicinity of 0º are desirable for ERDA. But in order to avoid straggling effects and to improve depth resolution, ERDA is more generally performed in reflexion mode (glancing angles) rather than in transmission mode.

But the power of ERDA as a multi-elemental general purpose technique depends on the use of heavy-ion incident beams: this is the so-called HI-ERDA (Heavy-Ion-ERDA) technique, and it is introduced in section 2.2.4.1. The selectivity (mass resolution) is strongly increased when using heavy projectiles. Furthermore, as also discussed in appendix A, when using a projectile heavier than the target material (as for ^{4}He beam and ^{1}H target), there is a maximum value of scattering angle θ beyond which the projectile cannot be deflected from the incident beam direction; this has the advantage that by using a proper geometry, the scattered projectiles

[1] The recoil angle is denoted θ_2 in the figure; we will use φ instead when we refer to recoil geometry.

cannot reach the detector and interfere with the recoil-particle energy spectrum. It must be pointed out also that He-ERDA for H determination involves non-Rutherford cross-sections.

2.2.4 ERDA variants

Two intrinsic difficulties arise in ERDA treatment: The recoil mass and the depth of a scattering event cannot be unambiguously determined, which is referred to as *the mass-depth ambiguity* (as for RBS it is possible for recoils with different masses emerging from different depths to reach the detector with equal energies); a recoiled target atom and a scattered projectile from different events cannot be always unmistakably distinguished, which is referred to as *the recoil-projectile ambiguity* (it is sometimes impossible to determine from the detected energy alone whether a recoil target or a scattered ion was detected — this problem does not exist for RBS). Many different experimental set-ups, referring essentially to different detection systems, have been developed over the last few years in order to resolve these ambiguities. These are summarised in the following sections.

2.2.4.1 Conventional ERDA

This is the easiest experimental set-up, and is shown in Figure 2-10; this variant will be used in this work to characterize H in Si (chapter 5). A simple silicon barrier detector is used together with an absorbing foil (typically Mylar) to range out scattered projectiles, which permits one to resolve the recoil-projectile ambiguity. Multiple-element analysis can be performed, especially for profiling different isotopes of hydrogen [Pre88]. Optimization of the geometrical arrangement of the conventional ERDA technique (using alpha particles) concerning the probing depth in the energy range of 1-10 MeV is discussed in [Tur84, Pás86].

Cross-sections can deviate significantly from the Rutherford recoil cross-sections concerning both the energy and the angular dependence, as pointed out for deuterium [Bes86]. Cross-sections of hydrogen isotopes are reviewed by Tirira *et al*. [Tir96{ii}]. Some cross-section values given in Figures 5-13 to 5-16 of the IBA Handbook [Tes95] have been parameterised [NDF02{i}] and are used in the present work (chapter 5) via the code DataFurnace.

A rather good depth resolution of the order of 10 nm can be achieved under extreme experimental (geometrical) conditions [Pás91]. Better depth resolution can also be obtained by reducing the detector acceptance angle; in turn this limits the sensitivity, thus higher fluence and acquisition time are required, and sample damage is then at issue. However, it is possible to use a large detector with properly shaped slits to maintain both resolution and sensitivity [Bri90].

Although much precious information can be obtained by using all the other arrangements as introduced in the next sections below, conventional ERDA remains extensively used for profiling light elements, particularly hydrogen isotopes. The reason is that all the other techniques require more sophisticated experimental devices, and even special interpretation procedures for some of them. For more details about the conventional ERDA technique, see Tirira *et al*. [Tir96{iii}].

A way to extend both the range of analyzable elements and the total analysed depth is to increase the mass of the incident ion beam. As it uses heavy ions, this method is called HI-ERDA (Heavy-Ion-ERDA). When using a Au beam for instance, essentially the elements from the whole periodic table can be analysed. This method has been proved to reach analyzable depth greater than 1 μm, and one can expect a depth resolution as low as 1 nm in the best case. A much better mass resolution can also be obtained, and this is the driving force for using this method. HI-ERDA has been demonstrated to be an efficient method of measuring depth distributions of light elements quantitatively in the near-surface region of solids. However, this method has fallen into disuse both because of detector damage (the silicon diodes so useful for He-RBS can be significantly damaged by heavy particles and become unusable) and also because the spectra are somewhat hard to interpret due to many overlaps. There is a further difficulty: the use of heavy ions at ~1 MeV/amu implies tandem accelerators often >10 MV terminal voltage. More information about HI-ERDA can be found in Tirira *et al*.'s book [Tir96{ix}]. It is also worth noting that, although ERDA (like any IBA technique) is not deliberately destructive, heavy ion used as projectiles are likely to cause some damage to the sample being analysed; this matter about beam damage is discussed in section 2.3.

2.2.4.2 TOF-ERDA

The mass-depth ambiguity (which is so severe for HI-ERDA) is easily resolved by using the Time-of-Flight (TOF) ERDA arrangement as depicted in Figure 2-11. The duration of a given particle flight path is determined by recording start and stop signals together with the energy of the particle; the differences in the time of flight permits one to discriminate between different masses. The recoil-projectile ambiguity can be avoided by suitably choosing an experimental geometry that kinematically does not allow the heavy-ion beam to be scattered into the recoil detector (large angles). Nevertheless, as a TOF system is capable of uniquely identifying the recoil mass, it can also easily identify scattered beam contribution at the detector. This technique was introduced in the mid-1980s by various research groups [Gro83, Tho83, Whi87].

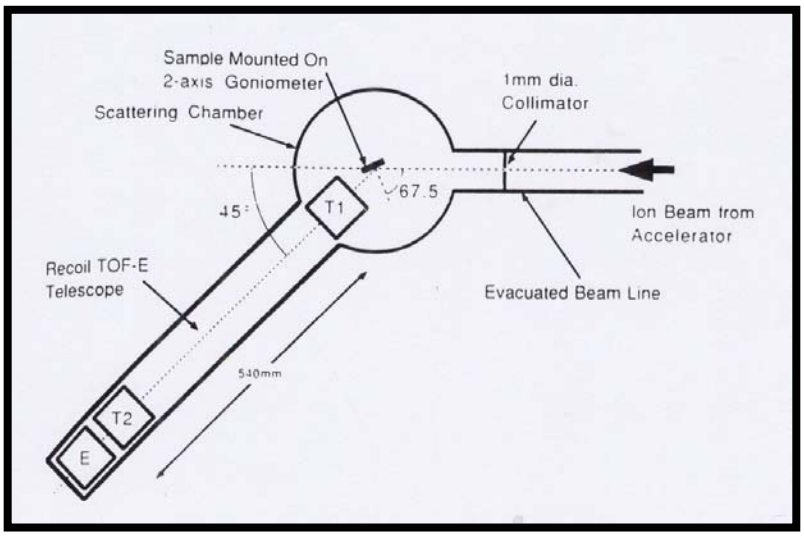

Figure 2-11 Experimental set-up used in TOF-ERDA. (from [Tir96]).

Analysis using TOF-ERDA allows good mass separation for the light-element range; with sufficient differences in their recoil masses, medium- and heavy-mass elements can also be analysed.

More details about the TOF-ERDA system are available in Tirira *et al*. [Tir96{iv}]. In Figure 2-12 and Figure 2-13 are shown typical TOF-ERDA spectra taken from [Tir96{iv}]. In the ERDA Round Robin exercise presented in chapter 5, Helsinki data are from a TOF-ERDA detection system.

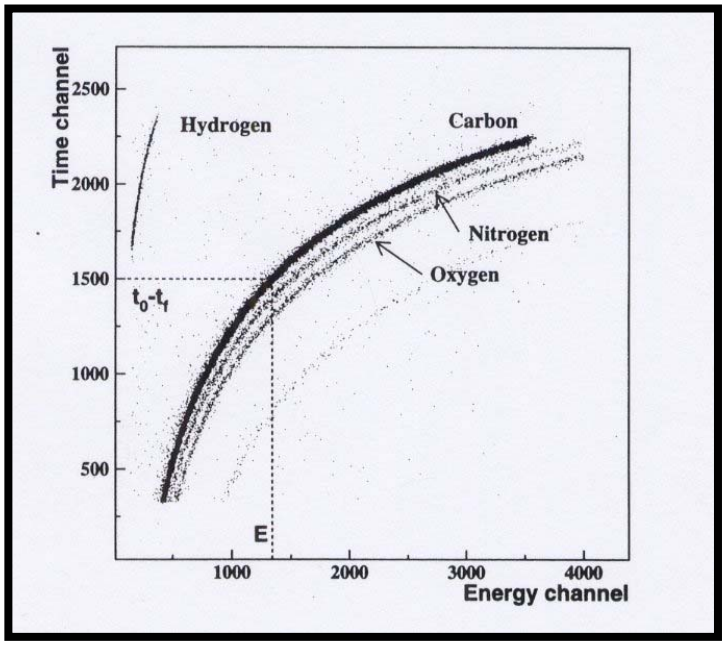

Figure 2-12 *The TOF-ERDA coincidence spectrum for a polyimide sample ($C_{22}H_{10}N_2O_6$) measured with a 84 MeV ^{127}I beam. Each recorded event is a data point plotted at the intersection of the measured energy (abscissa) and delayed flight time (ordinate). (from [Tir96]).*

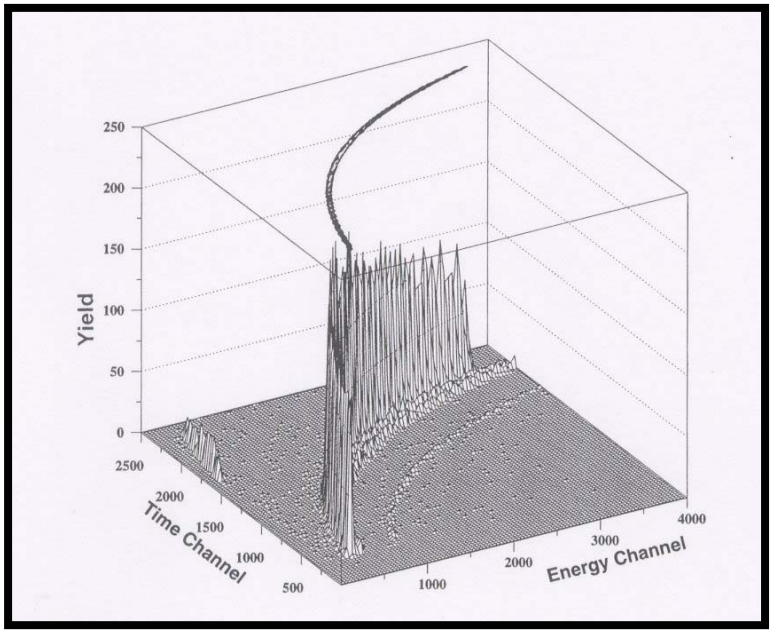

Figure 2-13 *Isometric projection of the event density for the polyimide sample in Figure 2-12, illustrating the relative contribution from different sample constituents. The largest profile track is carbon, with the smaller nitrogen and oxygen components visible. The track of lowest intensity is aluminium from the target holder. Detection efficiency for hydrogen is comparatively lower, resulting in a track height much less than expected from elemental stoichiometry. (from [Tir96]).*

2.2.4.3 ERDA E×B

An E×B filter (here E stands for electric field, and B for magnetic field) is based on the use of crossed (perpendicular and superimposed) magnetic and electric fields as an achromatic mass and charge selector in order to filter undesired particles in ERDA experiments. This arrangement was first introduced in 1984 by Ross *et al*. [Ros84], and it has been used as such afterwards [Ros92-a-b, Rou95]. A typical experimental set-up is illustrated in Figure 2-14.

The ratio *E/B* can be varied so that isolating a given ion while keeping ion deflection *nearly* energy-independent is possible; as a result, a narrow collimator can be used and recoil particles of the same element but of different energies can be detected simultaneously. The ERDA E×B and its properties allow us to measure depth profiles of all hydrogen and helium isotopes in low-*Z* materials.

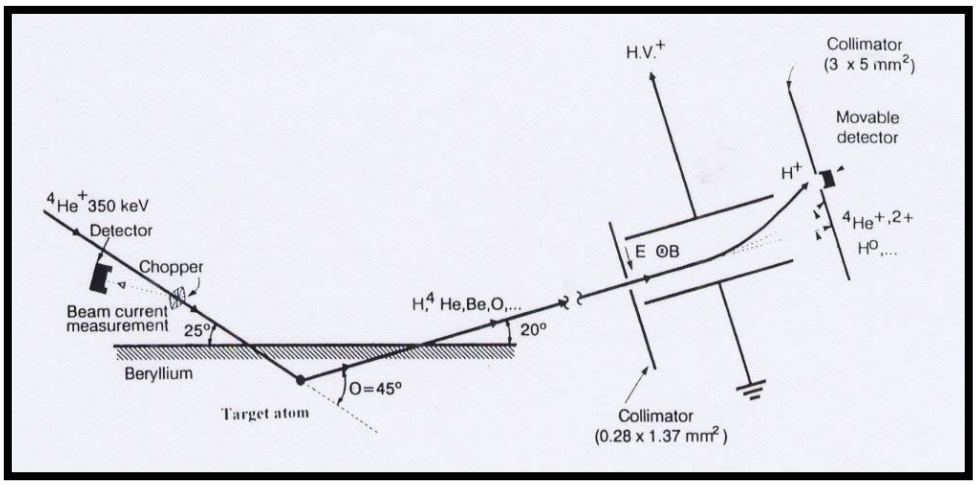

Figure 2-14 *The ERDA E×B method showing the interaction geometry, E×B filter, collimator positioning, and detector. (from [Tir96]).*

An elaborated discussion about this technique is given by Tirira *et al*. [Tir96{v}]. This method is very attractive for eliminating scattered particles. It combines also simplicity, sensitivity, and excellent depth resolution, and can be used routinely. It is undoubtedly very competitive. However, there are some limitations such as: scattering of detected particles on the collimator edges and electrodes of the electric field, which induces a large background; only one species can be analysed at a time, and the small solid angles used impose large current densities and longer

analysis time (consequently sample damage is at issue); correction for undetected charge fractions (especially neutrals). The use of position-sensitive detectors would permit different recoil species to be analysed simultaneously; the lack of such systems together with the beam damage problem has limited the acceptance of this technique.

2.2.4.4 ΔE-E telescope ERDA

The *Z*-dependence of energy loss ΔE can be measured with the so-called ΔE-E telescopes. In this configuration, mass separation can be achieved and improved by replacing the absorber foil in conventional ERDA by a thin transmission detector, either a gas-filled ionization chamber in the case of high-energy heavy-ion beams (HI-ERDA) [Pet84, Beh87, Ass94] or a solid-state transmission detector with which it is possible to discriminate H, D and T isotopes recoiled by rather low-energy 4-MeV ^{4}He projectiles [Arn92, Arn93, Pro94]. What is now measured in this ΔE detector is the stopping power of the incoming particles, in addition to the residual energy *E* from the back (thick) detector. Particle identification telescopes have been used over a quarter of a century in the field of heavy-ion nuclear physics. Figure 2-15 and Figure 2-16 show the two telescope detector configurations.

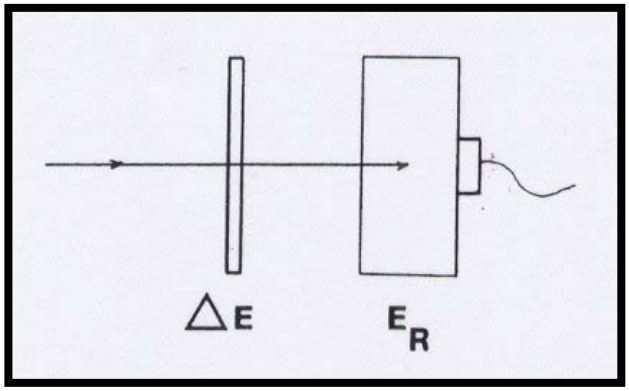

Figure 2-15 *Schematic view of a solid-state telescope (from [Tir96]).*

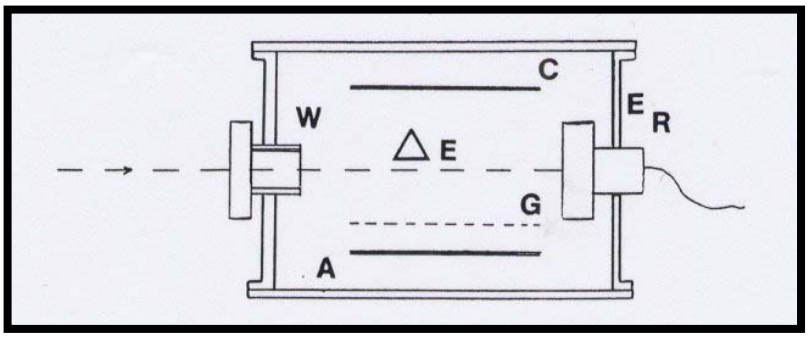

Figure 2-16 *Outline of a ΔE-E telescope composed of a gas ionization chamber associated with a thick silicon surface barrier detector (C, A, and G denote, respectively, the cathode, the anode, and the grid of the ionization chamber; W denotes the thin plastic entrance window) (from [Tir96]).*

A better depth resolution can be obtained with TOF-ERDA because carbon foils (start and stop signals) induce less straggling and angular scatter; nevertheless, TOF-ERDA presents a very low detection efficiency for hydrogen (around 30%), which is not the case for any low-*Z* ion with the ΔE-E telescope ERDA system.

For further details on ΔE-E telescope detection system, the reader is referred again to Tirira *et al.*'s work [Tir96{vi}]. This system will be treated further in depth in chapter 3 and 5 where the Round Robin ERDA experimental procedures and data from Canberra are fully presented.

2.2.4.5 Coincidence ERDA

Coincidence techniques have appeared to be an attractive alternative to overcome the problem of mass-depth and recoil-projectile ambiguities. As a matter of fact, by detecting both recoiled and scattered particles in time coincidence, one can unambiguously perform mass identification, and moreover obtain complete information about a scattering event (angles and energies of both recoiled and scattered particles). An arrangement of coincidence measurements is given in Figure 2-17.

The coincidence ERDA variant can be divided into two groups. In the first group, denoted as CERDA (Coincident Elastic Recoil Detection Analysis), mass selectivity together with background signal reduction are performed by properly *adjusting* scattering and recoil angles; one wants essentially to discriminate a specific

recoiled particle. The first ERDA experiment described in the literature was actually a CERDA-like one [Coh72].

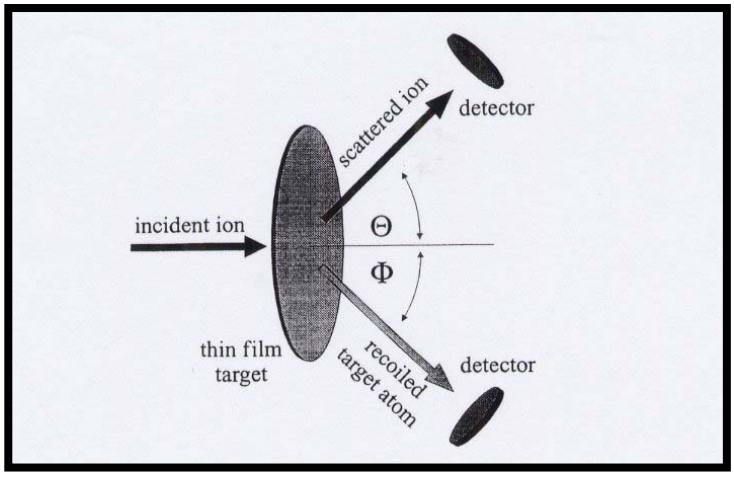

Figure 2-17 *Experimental set-up for ERDA using the transmission geometry and coincident detection of scattered and recoiled particles (from [Tir96]).*

The second group, denoted as SRCS (Scattering Recoil Coincidence Spectrometry) or ERCS (Elastic Recoil Coincidence Spectrometry), was proposed in the late eighties [Chu89, Chu98]. The key idea is to replace the measurement of scattering and recoil angles by measuring the energies of scattered and recoiled particles in time coincidence instead. The major advantage lies in the use of detectors subtending large solid angles, thus increasing the sensitivity of the measurements significantly without sacrificing depth resolution [Hof90]. ERCS is preferably applied to profile light elements in heavier matrix and in cases where a low beam current (< 1nA) or a low total ion dose is required to reduce damage, e.g. to study polymer samples, or for microbeam analysis. The work given in [Hof91] presents a sort of universal data analysis procedure for ERCS.

A general feature of coincidence techniques is their great sensitivity; a detection limit of a few ppm can be obtained. Improvements in the sensitivity, depth resolution, and in mass selectivity can be accomplished with large-area position-sensitive detectors [Tir96{viii}]. One drawback of this technique is that it requires at least one particle to be transmitted through the sample without significant energy loss; it can thereby be applied only to free-standing, sufficiently thin films a few

micrometers thick together with transmission geometry. For a complete review of coincidences ERDA techniques, see Tirira *et al*. [Tir96{vii}].

2.2.5 Multiple and plural scattering

The effects of multiple and plural scattering on depth resolution and low energy background in ERDA spectra have been explored in the last few years. ERDA spectra from two different (*Z*) materials implanted with hydrogen are shown in Figure 2-18 in order to highlight the three general features of such typical hydrogen ERDA spectra, that is, the presence of: (i) a surface hydrogen peak (of different intensity but the same energy width); (ii) a nearly Gaussian bulk implanted hydrogen peak; (iii) a continuous almost constant low-energy background. Some striking conclusions have been drawn in [Wie96].

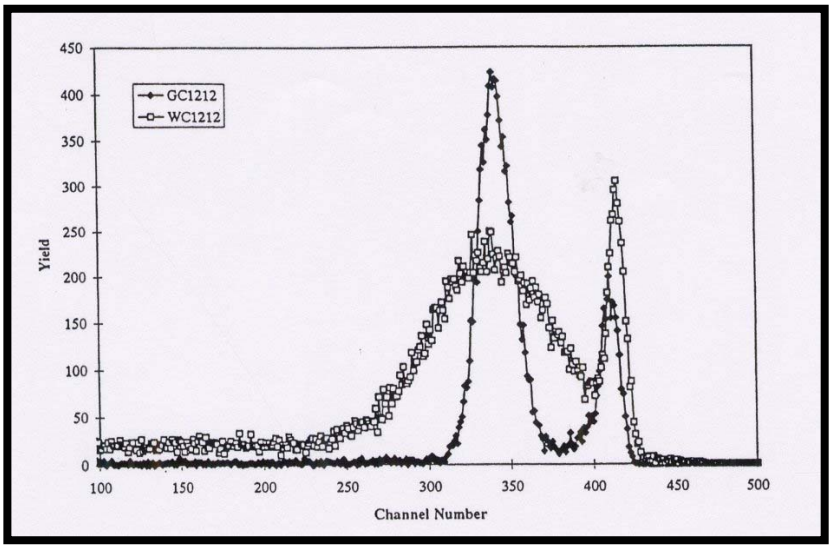

Figure 2-18 *ERDA spectra from hydrogen implanted glassy carbon (GC) and tungsten carbide (WC) samples in 24° scattering angle geometry (12°,12°) (from [Wie96]).*

Firstly, it has been established that the major factor limiting the depth resolution of hydrogen characterization using ERDA is multiple scattering of both projectile and recoil particles in the sample; multiple scattering angular distributions as calculated using the method given in [Sig74, Bir89] agreed with the experimental results. This effect presents a very strong *Z*-dependence (this can be seen clearly in Figure 2-18); the depth resolution is expected to be very low in heavy materials.

Reducing the scattering angle improves the depth resolution (due to an increase in the ion path length for a given depth), however the analysis depth is also reduced this way.

The study has also conclusively shown that the sensitivity of hydrogen detection is limited mostly due to double scattering effects, which generate a long low-energy tail in the spectrum. Increasing the ERDA scattering angle helps lower the level of this background, but in exchange as just mentioned above the depth resolution will be worst. It has also been found that this level of background is most likely proportional to both the amount of hydrogen in the sample, and the *Z* of the sample material as a consequence of larger scattering angles and cross sections.

In the study presented in [Wie98] the considerations about multiple scattering made previously have been explored further using single scattering simulation codes. It has been shown that multiple scattering strongly affects ERDA experiments in contrast to its relatively small effects in RBS measurements due to the different kinematics and geometry involved. It has also been clearly demonstrated, by comparing simulations from the code RBX [Kót94], which does not include multiple scattering effects, and the code DEPTH [Szi94, Szi95], which does (but does not handle low-energy tails generated by double scattering effects), to ERDA data, that interpretation of ERDA spectra can be markedly erroneous when multiple scattering effects are ignored; DEPTH successfully reproduced the ERDA hydrogen spectra for different materials and scattering angles whereas RBX failed.

2.2.6 Calibration standards

Characterization is often performed by using calibration standards. ERDA experiments are often performed in order to measure hydrogen isotopes content. But hydrogen usually has a rather high mobility in condensed matter, analysts thus face a problem in the case of hydrogen determination.

Utilisation of high-content hydrogen materials as standards, such as Mylar and polyimide (Kapton), is very common [Tir90-b]. Such materials present two advantages: They can be found as thin films (from 3-20 μm) or as thick samples (from 50 μm up to several hundred micrometers); they are also believed to have an homogenous hydrogen composition both in depth and laterally. Nonetheless, the

question of sensitivity of polymer structure under ion beam bombardment arises: as irradiation goes on, elemental losses occur, and the analysts thus rely on the reproducibility of losses for any accurate analysis. We will use kapton as a standard for the conventional ERDA characterization of H into Si in chapter 5.

Some other examples of hydrogen calibration standards are: hydrogen-implanted monocrystals [Tir91-a], hydrated materials of known composition such as mica-muscovite [Tou89] or hydrogenated tantalum [Hjö89], metal hydrides with a known stoichiometry as TiH_2 [Tir90-b], and more recently specially prepared depth calibration standards [Ver01].

2.3 Beam damage

Although ion beam analysis is not deliberately destructive, sample degradation under ion beam bombardment is difficult to avoid. Sometimes beam damage cannot be neglected and must be taken into account; it all depends on the type of sample to be analysed, and also the type of analysis (nature and energy of the beam, sensitivity or incident beam fluence).

2.3.1 Types of processes and defects

With regard to damage induced by ion beam irradiation of common materials, two main classes of interactions are involved: electronic processes, which refer to interactions between incident ions and electrons in the target medium; and ballistic processes, which refer to collisions of the incident ions with target atoms nuclei. The defects created can be divided into two types: point defects, which involve the crystalline structure (vacancies and interstitials), the electronic structure (colour centres), or the chemical structure (bond breaking); and extended defects, which in fact result from an accumulation of point defects (vacancy clusters, dislocation loops, etc). Transmutation of target atoms by nuclear reactions can be classified as a third class of interaction; but it has much less important consequences as well as the advantage of being completely predictable.

2.3.2 Charge accumulation effects

Charge accumulation in the near-surface region of insulating materials may cause target alteration and perturbations in the analytical process. This charge accumulation is due to both ion implantation and secondary electron and ion emission, resulting in huge electric fields near the surfaces of insulating targets. In some cases, the consequences are important, ranging from target modification (elemental migration under electric field) to severe target damaging (dielectric breakdown).

2.3.3 Elemental losses

In thin film analysis by ion beam irradiation, elemental losses may occur due to sputtering effects. It has been established [Sig69] that the elemental sputtering yield Y_i is a function of the nuclear stopping power $\varepsilon_n(E)$, the surface binding energy of the target U_{si}, the angle between the incident beam direction and the surface normal, and the ratio M_i/M_l of the target atom i and incident ion l masses. As far as MeV light-ion bombardment of solid targets is concerned, sputtering can generally be neglected as the typical order of magnitude for Y_i is about 10^{-4} atoms/incident ion for protons [Tro94]. But more significant elemental losses during ion beam analysis are expected to occur with elements having a very low vaporization heat such as hydrogen, nitrogen and oxygen, and with volatile elements or mobile species like weakly bonded cations and anions (alkali and halogen).

As an example, let us consider the case of the irradiation of a 25-μm thin polyester sample ($C_{10}H_8O_4$) coated with a 100-nm gold layer by a 3-MeV $^4He^+$ microbeam (100 μm^2, 1 nA, 1000 s). In transmission geometry, approximately 2.4×10^4 recoil protons will be detected [Tir91-a]. But for such an investigation, respective elemental losses in various polymers range from 10 to 30% for carbon and nitrogen, and 20 to 60% for hydrogen and oxygen, depending on the experimental configuration adopted [Tro91, Tir91-b, Mer93]. This indicates that more than 10% of the total number of chemical bonds can be destroyed within the irradiated area.

In chapter 5, in the Round Robin ERDA analysis of H into Si, elemental losses of hydrogen due to beam irradiation will be accounted for. Also in chapter 6,

prior to the RBS analysis of the fluorinated silicon-oxide samples, we will evaluate the stability of F under beam irradiation (together with uniformity of the films) by using the nuclear reaction $^{19}F(p,\alpha\gamma)^{16}O$ at 872.1 keV.

CHAPTER 3

EXPERIMENTAL DETAILS

In this chapter, we describe the different experimental set-ups used throughout this thesis. Most of the experiments were carried out at the Surrey Ion Beam Centre. In section 3.1, we describe in detail the Surrey IBA facilities, which include the accelerator, the beam line, the principal reaction chamber used in this work, that is, the RBS target chamber, and all the main equipment; we put a strong emphasis on what is particularly important for work on ion beam analysis where the highest accuracy is required. We briefly describe also the experimental procedure followed for the ERDA analysis (chapter 5) and the experimental set-up used for NRA measurements (chapters 6 and 7, and appendix B). Some of the dose measurements presented in chapter 4 were made at Jena (Germany); we give some details on the Jena accelerator and RBS set-up in section 3.2. Finally, in section 3.3, we present briefly the IBA facilities of the other participants (Canberra, London, Helsinki, Rossendorf and Montreal) in the Round Robin exercise being the subject of chapter 5; particular attention is given to the experimental procedure followed by Canberra, as they came out with the most interesting ERDA data (ΔE-E telescope HI-ERDA multielemental analysis using a 200-MeV Au beam).

3.1 Surrey (RBS, ERDA, NRA)

In this section, we will summarise what was previously thoroughly documented by Hemment *et al*. [Hem83], Mynard *et al*. [Myn85], Jeynes [Jey98-a] and Jeynes *et al*. [Jey98-b]. All RBS and ERDA experiments at Surrey

presented in this work were carried out using L4 (line 4) in the D.R. Chick Laboratory; a general view of the facilities is sketched in Figure 3-1. L5 (line 5), which was used for the accelerator energy calibration (appendix B) and for NRA measurements (chapters 5 and 6), is also shown.

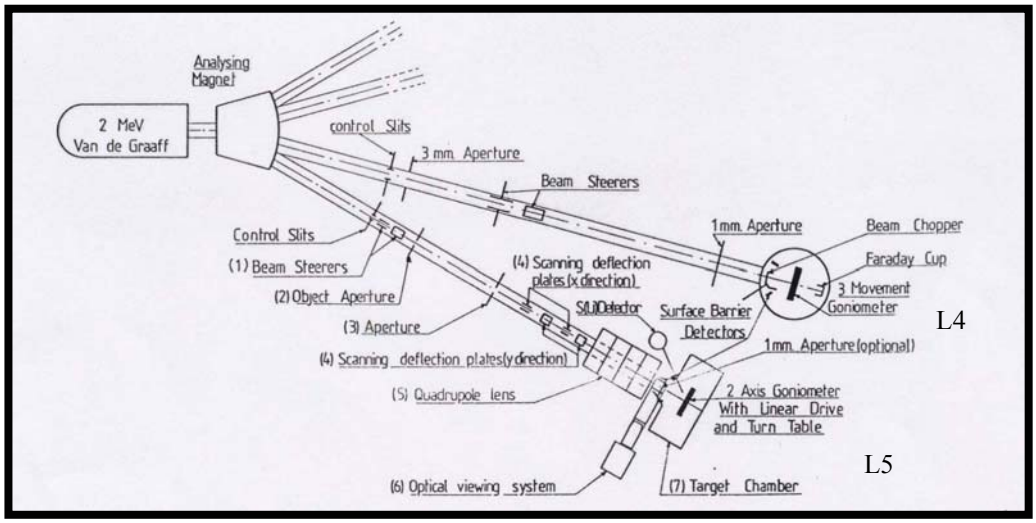

Figure 3-1 *Sketch of ion beam analysis facility at Surrey Ion Beam Centre (D.R. Chick Laboratory): L4 is used for RBS and ERDA measurements, and L5 for the accelerator energy calibration and NRA measurements (from [My85]).*

3.1.1 IBA facility

Section 3.1.1.1 is simply aimed at enumerating and describing without many details the main components of this conventional IBA facility, which are illustrated in Figure 3-1. In section 3.1.1.2, we give particulars on the experimental features that are critical for any accurate measurements.

3.1.1.1 General description

The **accelerator** dedicated to IBA is an old 1953 High Voltage Engineering 2 MV Van de Graaff. This instrument had a maximum terminal voltage degraded to 1.5 MV at this time. The energy calibration was done at different dates using three or four points and is given in appendix B. The beam energy must be known at better than 1 keV for such work based on accurate measurements as

targeted in this thesis; see section 3.1.1.2 for more details about the critical question of energy control from the **generating voltmeter** (GVM).

The switching (analyzing) **magnet** is positively controlled on the value of a NMR gaussmeter probing the magnetic field. This meter is sensitive to mG where typical magnetic field used is around 5000 G, that is, a sensitivity of the order of 10^{-6}. The feedback circuit together with the magnet power supply is easily capable of controlling at the 0.01 G level (not so easy with this very high inductance circuit however).

The energy can be controlled at another stage further in the set-up, by using magnet **analyzing slits,** electrodes from which a logarithmic difference signal is derived. This error signal is fed to the grid of a high voltage valve controlling the potential of the corona points (see section 3.1.1.2 for more details).

The **ion source** extraction optics depends critically on the shape of the plasma boundary, and therefore ion source plasma instabilities can cause small changes in the direction of the beam. With such a large optical lever this can give rise to significant differences in the path of the beam through the magnet, which will result in beam energy shifts from the slit control. Energy shifts of over 16 keV at 1.5 MeV, or over 1%, have been reported. As explained in more detail in section 3.1.1.2, **beam path stabilization** is based on a direct measurement of the terminal voltage with a generating voltmeter (a *charge mill*); an error signal is derived from another precision potentiometer and used to set an electrostatic field across **beam deflection plates** before the magnet.

Two **viewers** (V1, V2) together with a series of **moveable apertures** (A1, A2) along L4 allow the verification of the existence of the beam and its focus condition. The usual **beam steerer** plates are put before the collimating aperture (A2), which is just before the target chamber, for beam condition control (beam defining) at the entrance of and inside the chamber.

3.1.1.2 Van de Graaff energy control and beam stabilization

For accurate energy spectroscopy, accelerator energy control and beam stabilization are crucial. Ideally accelerator energy control is required at the 10^{-4} level. At the Surrey Ion Beam Centre, as reported in [Jey98-b], the position of

the beam in the beam line together with the beam energy stabilization are made with a precision of about 100 eV and an error within about 500 eV. This is electronically achieved with a feedback loop to electrostatic beam steerers before the analyzing magnet using the generating voltmeter (GVM) to fix the entry point of the beam into the analyzing magnet. The control scheme of the instrument is shown in Figure 3-2. In principle the ultimate accuracy relies on the mechanical stability of the whole structure. Here it is worthwhile to present some elements of the detailed description made by Jeynes *et al*. [Jey98-b].

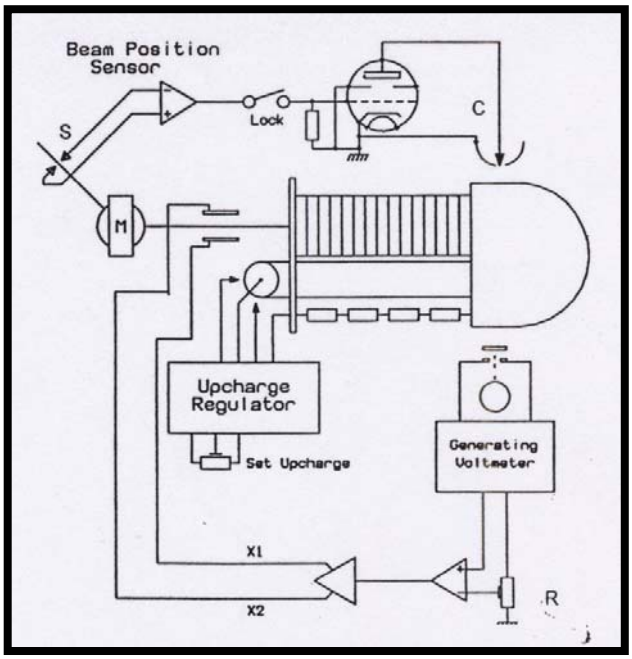

Figure 3-2 *Feedback loop in the energy control of the Van de Graaff accelerator dedicated to IBA at Surrey Ion Beam Centre (from [Jey98-b]).*

The GVM has a motor-driven rotor and a fixed, insulated stator. The rotor, which has sectors cut out of it, revolves so that it alternately exposes and shields the high-voltage terminal to the stator plates. Essentially the amplitude V_{out} of the triangular wave AC (alternating current) voltages electrostatically induced on the stator is directly proportional to that on the high-voltage terminal. An (simplified) equivalent circuit can be seen in Figure 3-3. C_1, C_2 and C_3 are respectively the capacitance of: the stator to the high voltage terminal; the stator to the rotor; and the stator to the ground. C_2 varies as the rotor turns and reaches a maximum when the induced voltage is a minimum, i.e. when the stator gets completely shielded from the

terminal voltage by the rotor; it goes down to approximately zero for the opposite orientation. Thus C_1 varies indirectly with C_2 as the rotor turns. As a result, the variation in V_{out} increases as the variation in C_2 increases, which is influenced by any variation in C_1.

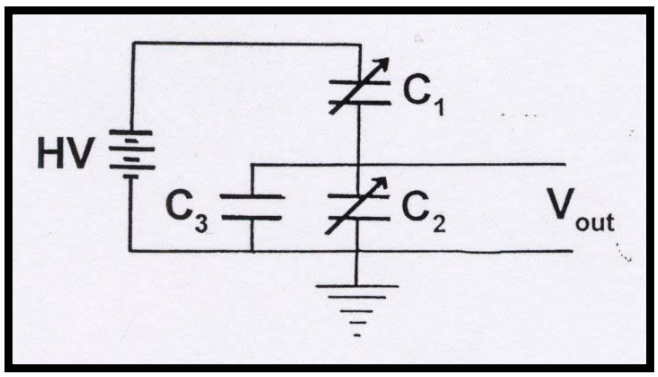

Figure 3-3 *GVM equivalent circuit (from [Jey98-b]).*

The fluctuations in the terminal voltage can arise from many sources, e.g. variations in the belt-charging process and discharges along the insulating surfaces of drain resistors and voltage stand-off insulators. As illustrated in Figure 3-2, any fluctuation between the output from the GVM and a stable reference voltage at R generates control voltages X_1 and X_2 that deflect the ion beam before it enters the magnet M. The beam is also sensed after it passes through the analysis magnet at the position S by slits. The error signal from these slits (generated by any movement of the beam) is used to determine the bias of the corona stabilizer circuit, therefore controlling the corona current at C.

The accuracy of the GVM is sensitive to its geometric relationship with respect to the high voltage terminal. The variations in the stator-rotor gap d must be kept as small as possible while keeping d as large as practicable. It has been shown that the GVM output voltage varies up to 5% mm^{-1} with d. This means that the rotor average position must be kept within ± 200 nm to obtain stability at the 10^{-4} level. This is achieved simply by means of sprung motor bearings.

It has also been established that there is approximately a $1/D$ dependence of the output voltage V_{out} due to C_1 given by the high-voltage terminal to stator spacing D. For a typical spacing D = 250 mm, the 10^{-4} level of stability requires that D is

stable to 25 μm. This means that, for a thermal expansion coefficient of about 3×10^{-5} K^{-1} considering a typical tank diameter of 1 m, the temperature must be controlled to within three degrees. There may also be a small dependence of C_1 on the permittivity of the insulating gas, which could be influenced by any pressure and mixture variations or ionisation of the gas. As a result, it is necessary to calibrate the GVM after each removal of the tank (as the GVM is coupled directly to the tank).

3.1.2 RBS set-up

This section deals with the components of the Surrey RBS set-up. First, a general description of the set-up is presented. Then some particular points related to accurate work are explored, such as: measurements of the scattering angle of the detectors, electronics behaviour, and electronics calibration.

3.1.2.1 General description

The cylindrical **target chamber** has dimensions of approximately 43 cm height and 32 cm diameter. **Vacuum** is ensured by using conventional **rotary pump** (for primary vacuum and backing) and **diffusion pump** (for high vacuum, up to 10^{-6} torr), topped with a LN (liquid nitrogen) cold trap. A sketch of this typical target chamber vacuum system is given in Figure 3-4.

Around eight samples can be mounted on the **holder**, which fits on the **goniometer**. The latter has three motions: one translation (Y) and two rotations (θ and φ). There are 160 steps/mm and 100 steps/degree for the Y and θ - φ motions, respectively. Positioning the samples in the beam direction and rotating them (for instance for grazing angle measurements or for rocking) are therefore very accurately feasible when required.

Charge collection is done by using a standard design **current integrator,** from which logic output signals are sent to the **dual scaler** (which is simply a dual counter for logic pulses) for charge counting. A simplified sketch of the charge integration system, which is in fact not really a proper Faraday cup, is given in Figure 3-5. The sample plate is raised to a positive potential of about 200 V in order to perform **secondary electron suppression**. It also has an **earthed electron**

suppression plate fitted over to aid charge collection. A final **fixed aperture** has been installed at the entrance of the target chamber, with a **suppression electrode** facing the final beam defining aperture A2; this is to reduce electrons in the chamber which would be sucked up by the biassed target plate and cause a charge collection error. With such a set-up the charge collection is not expected to be better than 1%; notwithstanding, from the results obtained in section 4.5.3 of this work the charge integration was found to be as good as 1.1%.

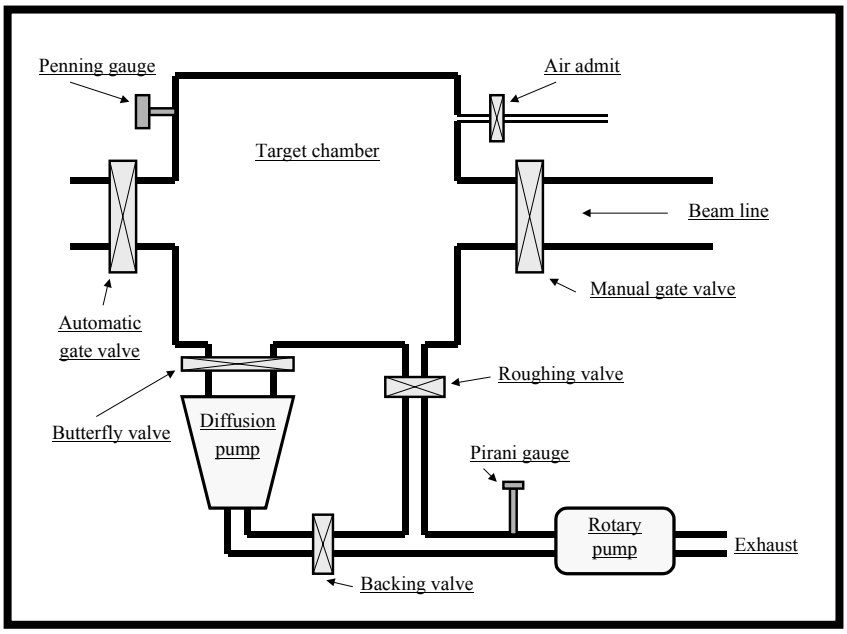

Figure 3-4 *Sketch of the RBS target chamber vacuum system at Surrey Ion Beam Centre.*

Two **detectors** have been installed, one at ~165° (called detector A) and the other at ~135° (called detector B); see section 3.1.2.2 for the accurate calibration of the scattering angles. Since low scattering angles increase both kinematical broadening and cross-section ($sin^{-4}(\theta/2)$ dependence), a 50 mm^2 and a 25 mm^2 are used at the 165° and the 135° positions, respectively. The detectors are ion-implanted silicon diodes, with quoted resolutions of 11 keV. The surface dead layer is mainly due to the electrode, which is nominally 40 $\mu g/cm^2$ of Au and Al. The sensitive thickness (depletion layer thickness) is 0.1 mm at full bias, which is enough to stop 3-MeV H or 10-MeV-He particles. See section 3.1.2.4 to learn more about the non-linear effects coming from these detectors and which distort RBS spectra.

Preamplification of the signals are ensured by using very sensitive low-noise charge-sensitive **Ortec 142A preampliers**, powered from the rear socket of the amplifier unit.

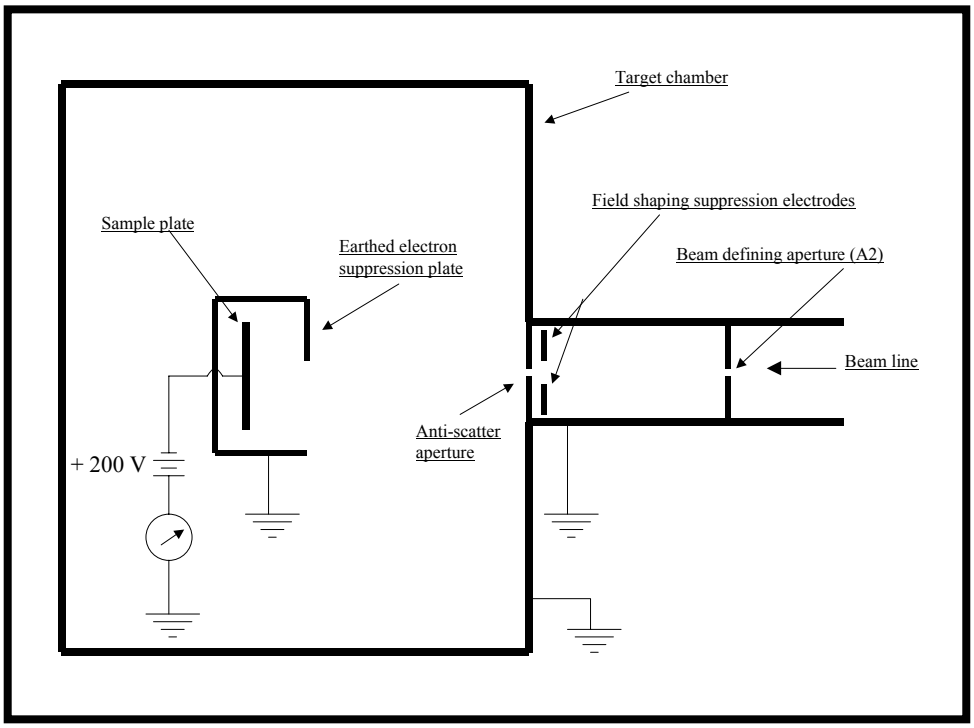

Figure 3-5 *L4 RBS charge integration system and other target chamber components at Surrey Ion Beam Centre.*

Electronics modules are fitted into the **NIM** (Nuclear Instrumentation Module) racking system, which is in widespread use for spectroscopy. The amplifier, pulser and bias supply should all be in the same rack for best noise performance. The NIM bin is kept *on* to avoid drift during the warming up period. The spectroscopic electronics system is depicted in Figure 3-6.

Amplification of the signals is made by using pulse-shaping spectroscopic **Ortec 572 amplifiers**. They accept a short rise-time/long fall-time pulse positive input from the charge-sensitive preamplifier, and generate a near Gaussian pulse suitable for input to ADC (Analogue-to-Digital Converter). The quoted (integral) non-linearity is typically 0.025 % with 0.5 μs shaping. They have a pulse pile-up detection circuit, which generates inhibit logic signals used to gate the ADC. They have a base level restoration (BLR) circuit, so that pulses separated only by a few shaping times can be measured accurately without the effect of the long trailing edge

of the pulse from the preamplifier dominating. The time resolution of the pulse pile-up circuitry is about 0.5 μs.

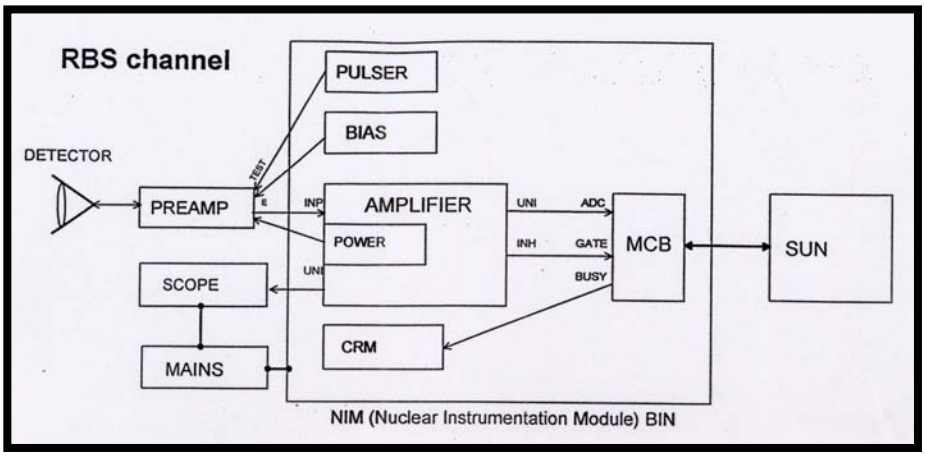

Figure 3-6 *Spectroscopic electronics system at Surrey Ion beam Centre (from [Jey98-a]).*

The output analogue signal from the amplifier is sent to an **Ortec 917 MCB** (multichannel buffer). This is a successive approximation ADC with a fixed 15 μs conversion time and quoted integral non-linearity of 0.5%.

An **Ortec 419 precision pulse generator** is useful for testing the electronics before the beam is available, and is used as beam energy stability monitor, and electronic noise monitor. It can be used as a livetime monitor, but we did not do this, relying instead on the ADC livetime output; this is however less accurate. Linear behaviour (both with time and amplitude of signals) of the electronics is essential for accurate work; the pulse generator has been used in section 3.1.2.3 to test the linearity of the electronics.

Calibration of the electronic gain (and offset) can be completed routinely with an Au/Ni/SiO_2/Si calibration sample and a calibration routine. It turns out to be accurate, although it is not yet known how much the calibration parameters drift with time on undisturbed electronics. Accurate electronics calibration is discussed in more detail in section 3.1.2.4.

3.1.2.2 Calibration of RBS scattering angle of the detectors

A sketch of the RBS target chamber can be seen in Figure 3-7, showing all the parameters required for the measurement of the detectors geometry. The incident beam has to go through a hole (anti-scatter aperture) of less than 1 cm diameter at the entry point of the chamber. Any sample submitted to RBS is clipped onto a plate, which fits on the holder of the goniometer. The latter is stiffly attached to the upper lid of the chamber. There are two surface barrier detectors simultaneously used as two independent analysis channels.

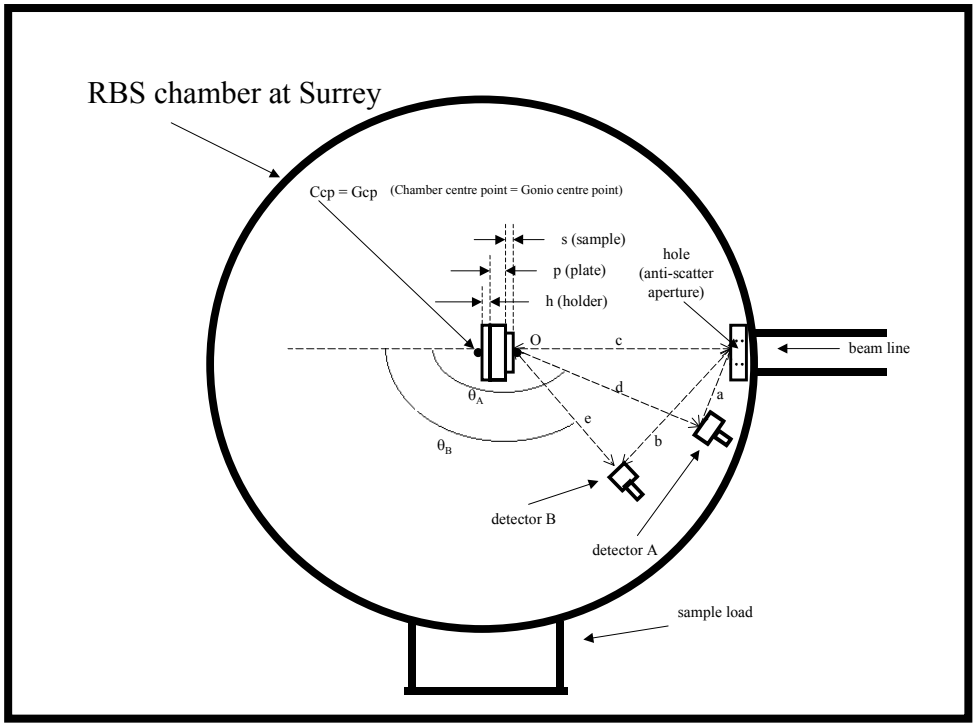

Figure 3-7 *Sketch of the RBS target chamber and detection system at Surrey Ion beam Centre.*

At first, it was verified that the Gcp (Goniometer centre point) matches with the Ccp (Chamber centre point). We put a piece of plastic-coated paper (a particle beam can leave a brown spot when crossing this kind of paper after few seconds) on the holder, and placed the goniometer at the normal position. We bombarded the paper with the beam (He at 1.5 MeV) until a brown spot appeared. Afterwards we moved the lid (to which the goniometer is attached) 90° clockwise, and rotated the goniometer back to the normal position (90° counterclockwise rotation). We

bombarded again the paper long enough for the formation of another brown spot on it. The two spots overlapped each other within a negligible distance of less than ~0.2 mm. Since the two spot coincided, we can affirm that the Gcp and Ccp are a unique point. We repeated this calibration, but using this time a ruler and measuring the distance between the holder and the sample load; as expected we obtained without any distinguishable difference the same result before and after the rotation of both the lid and the goniometer.

Then we measured the distance between the Ccp and the edge of the holder (distance *h* in Figure 3-7). We used again a piece of plastic-coated paper stuck on the holder. The goniometer placed at the normal position, we bombarded the paper until a brown spot appeared. Then we rotated the goniometer 25° clockwise, and exposed again the paper to the beam. We obtained a brown spot approximately 0.8 mm away on the right from the central spot (when at normal position). With a simple geometric calculation, we found that the holder surface is around 1.72 mm away from the Ccp. If we add the 3.00 mm thickness *p* of the plate and the three quarters of cm thickness *s* of a typical sample, it turns out that the RBS surface interaction between the beam and the target material occurs at about 5.47 mm in front of the centre of the chamber.

Table 3-1 *Manual measurements of the distances as shown in Figure 3-7.*

	h (mm)	**p** (mm)	**s** (mm)	**a** (mm)	**b** (mm)	**c** (mm)	**d** (mm)	**e** (mm)
Volunteer-1	1.72	3.00	0.75	49.95	97.60	131.73	92.27	77.15
Volunteer-2				49.40	98.60	133.13	94.12	76.20
				A dominating error of ~2 mm can be estimated for these values (see text)				

The next step was to measure the scattering angle of the detectors. As a first attempt, this was done *manually*, i.e. by simply using a ruler (with an estimate of the uncertainties). To obtain the angle of the detectors, first we had to determine the distances *a*, *b*, *c*, *d* and *e*, as illustrated in Figure 3-7. These measurements were made by two different volunteers, and are given in Table 3-1. Each distance was evaluated using a spring caliper, and then a vernier caliper to measure the length of the spread caliper legs. Since the interior of the small chamber was not totally accessible (the goniometer is attached to the upper lid), the measurements with the

spring caliper were not very easy to make and have been set to be uncertain within approximately 2 mm; this value will be in fact the dominating uncertainty in the determination of the scattering angles.

Using the cosine law we can calculate the scattering angles. For example, for detector A we can use the following equation:

$$c^2 + d^2 + 2cd\cos\theta_A = a^2 . \qquad (3\text{-}1)$$

For detector B, the parameters b, e and θ_B are simply substituted to a, d and θ_A in the same equation. The uncertainties can be determined by calculating the angles with extreme values for the measurements, i.e. taking into account the dominating estimated 2 mm uncertainty. For instance, using a + 2 mm, c – 2 mm and d – 2 mm (or a – 2 mm, c + 2 mm and d + mm) in equation (3-1), we obtained a maximal uncertainty of ≈2.0° for the determination of detector A scattering angle. It comes out that 164.2° ± 2.0° and 132.8° ± 2.7° are the scattering angles for detector A and B, respectively, as measured *manually*. Although the measurements were done thoroughly, they were done manually, and this leads to large uncertainties, up to 2% for detector B.

Table 3-2 *Scattering angle values of both detectors A and B as measured by using a laser beam. Position 1 and 2 refer to two different arrangements.*

	Scattering angle [°]		Error [%]
	Position 1	Position 2	
Detector A	166.9	163.0	0.3
Detector B	133.1	130.4	0.4

Such manual measurements, using simple rulers, lead unacceptably to too large uncertainties for any work aiming at high accuracy analysis (at the 1% level). Therefore it is greatly worthwhile to repeat this scattering angle calibration more accurately; using a laser beam, for example, would lead definitively to more precise values of scattering angle. As a second attempt, we directed a laser beam in the beam line towards a reflective silicon sample put on the goniometer, and by moving the latter in order to get the beam reflected back on the laser module, then reflected on

each detector, we determined the scattering angles. Precision of the position of each reflection (on the laser module and on the detectors) was estimated to be better than ¼°, which leads to an uncertainty of less than ½° for each scattering angle value. This means an uncertainty of less than 0.4%. The values are displayed in Table 3-2, in the "position 1" column. In the middle of this thesis, some work was required inside the chamber, and the detectors had to be moved around; their scattering angle were measured again using the laser beam, and the new scattering angle values are also displayed in Table 3-1, in the "position 2" column.

3.1.2.3 Electronics linearity

It is important that pulse signals are electronically processed without fluctuation (drift) with time, and also linearly with amplitude (energy). As a matter of fact, calibration of the electronics gain and offset (as discussed in detail in section 3.1.2.4) assumes *a priori* such a constant and linear behaviour. We have tested the linear and constant behaviour (mainly governed by the ADCs) of the electronics altogether for both channels (detectors A and B) using the pulse generator.

Table 3-3 *Data from the electronics linearity and constant behaviour test: pulser amplitude, peak channel and integration, time and period.*

Detector	*Pulser Amplitude [arbitrary units]*	*Channel*	*Counts*	*Time [s]*	*Period [ms]*
A	4.72	455	5482	79.20	14.45
	3.57	346	5529	79.88	14.44
	2.35	230	5513	79.69	14.45
	0.80	81	5560	80.24	14.44
B	4.72	451	5629	81.24	14.44
	3.57	343	5565	80.32	14.44
	2.35	228	5561	80.28	14.44
	0.80	81	5604	80.88	14.44

A spectrum of pulses generated at a period of ~14 ms (as roughly measured with an oscilloscope) was recorded for different amplitudes for about 80 s. The gain

of the amplifiers was kept at a fixed value. The channel corresponding to each peak together with its integration are presented in Table 3-3. The period obtained is also listed; a mean value of 14.44 ms ± 0.03% has been found, and this confirms the constant behaviour of the electronics with time.

In Figure 3-8 we have plotted the variation of the position (channel) of the peak in function of pulser amplitude. As can be seen, the electronics has a linear behaviour as a function of signal amplitude: the linear regressions obtained give a correlation coefficient of 0.999988 and 0.999995 for detectors A and B, respectively. A small offset of about 5 or 6 channels is observed due to a dc level from the ADCs; this can be restored to zero by using the zero-adjust function.

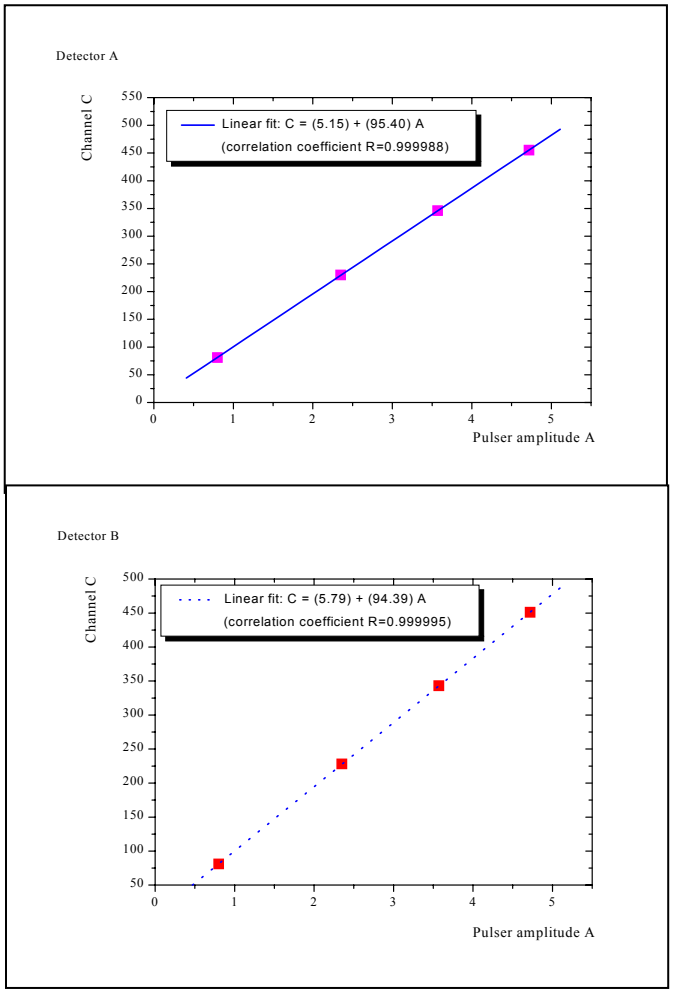

Figure 3-8 *Peak channel versus pulser amplitude for both detectors A and B showing the electronics linear behaviour for pulse signal processing.*

3.1.2.4 Electronics calibration (gain and offset)

Work where the highest accuracy is required cannot be validated without a thorough energy calibration (gain and offset) of the detection electronics. By reference to an especially prepared Au/Ni/SiO_2/Si calibration sample an automatic routine was developed to determine spectral edges, peaks and areas, and hence a very accurate electronics calibration as described by Jeynes *et al*. [Jey98-b]. Corrections for the non-linear effects due to the behaviour of the surface barrier detectors used (even if the electronics is perfectly linear) which were studied by Lennard *et al*. [Len90] are accounted for. These effects are: energy loss of the particle in the detector dead layer (entrance window); nuclear energy loss of the particle in the detector which does not generate electron-hole pairs; and the non-linearity in the pulse height due to a slight dependence of the energy required to create electron-hole pairs on the cascade density.

The positions of the peaks and edges are obtained first approximately by a peak identification routine and then precisely using a truncated half-Gaussian [Jey85]. With another routine [Jey97], the pulse pile-up is automatically and properly taken into account. The thicknesses of each layer are also accounted for, and the final precision of the determination of the position of the signals is about 0.1 channel. Relative signal energies are then obtained with a precision of 500 eV for a typical 1.5-MeV He beam energy.

3.1.3 ERDA experimental procedure

In this section, we mainly focus on the experimental procedure followed by Surrey for the ERDA analysis of hydrogenated silicon implants as given in section 5.3. The target (end) chamber on L4, downstream the RBS (middle) chamber, but which is not shown in Figure 3-1, was used for this experiment. A 1.506-MeV ^{4}He probe beam of about 30nA and nominally 1 mm diameter was used in a conventional set-up. The machine energy calibration was performed as given in section B.4. Measurements were made at 13.3° and 15.0° incident angles. The experimental procedure is schematically summarised in Figure 3-9. We go through all the steps in the following sections.

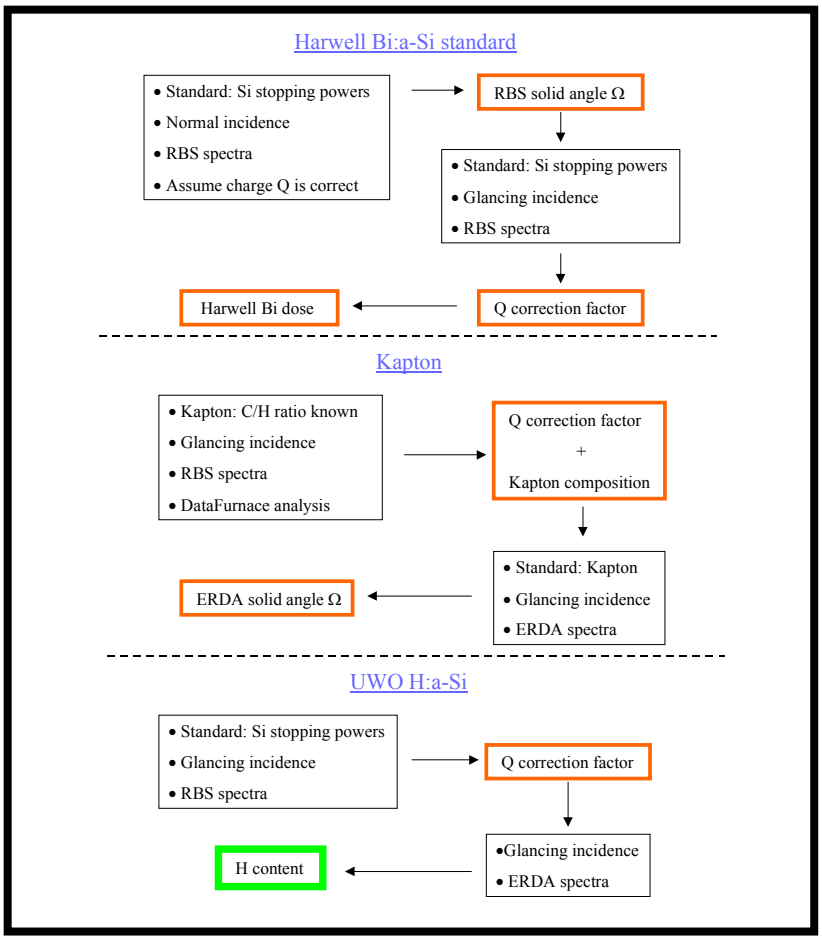

Figure 3-9 *Summary of Surrey experimental procedure for the conventional ERDA analysis of H implants into Si as given in section 5.3.*

3.1.3.1 Goniometer and detectors

A precision 6 movement goniometer was used [Hol00] with ORTEC electronics including 3 PC-ADCs, all controlled by in-house software [Fin01]. Recoil measurements were made using a 3×29mm Hamamatsu photodiode, mounted vertically, with a 6 micron (57605 TFU) Mylar film (C_{10} H_8 O_4 from Goodfellow Metals) covering it. RBS measurements were also simultaneously carried out with two Ortec ion-implanted Si detectors from; the detector sizes were nominally 50mm^2 and 25mm^2.

The detector angles were determined using the goniometer to find the deflection angles required to move a laser beam from normal to the detectors. The normal position could be determined to one step (0.005 degrees). The forward recoil

angle was 26.6º, and the backscattering angles were 148.8º and 118.8º for the 50 and 25 mm^2 detectors respectively.

Charge collection was from the target plate, which was held at a positive voltage relative to the chamber. This is remarkably effective at normal beam incidence, but becomes unreliable at glancing angles, especially for samples that charge.

3.1.3.2 Vacuum

The cryopumped vacuum system operated at about 10^{-7} mbar. The beam lines were diffusion pumped and ran at typically 10^{-6} mbar but there was a LN (liquid nitrogen) cooled beam line component about 50cm long and 1cm diameter for differential pumping and for keeping hydrocarbons from the beam line out of the target chamber.

3.1.3.3 Electronics calibration

The electronics calibration for the RBS detectors was performed with a Au/Ni/SiO_2/Si sample using the procedure of Jeynes *et al* [Jey98-b] (see also section 3.1.2.4). The ERDA detector was calibrated using two beam energies (1506 and 1405 keV) and interpreting the energy shift in the spectrum assuming energy-loss database values [Zie85] for the energy lost in the range foil.

The Kapton sample (standard) gave a distinct energy shift, which could be interpreted as charging of the sample at around +10kV. In principle this changes the gain of the electronics and introduces a bias into the results, but we think this effect is smaller than other errors and we ignore it, correcting the fitted spectra simply with the offset.

3.1.3.4 RBS solid angles

The RBS detector solid angles were determined at normal incidence assuming the charge was correct and using the new knowledge of the Si stopping powers [Kon98, Len99-a, Bia00] parameterised by [Bar02] and validated against the new Sb standard from IRMM, Geel by [Bou02] (this publication is the analysis

presented in chapter 4). The values found were 1.334 and 0.727 msr for the 50 and 25 mm^2 detectors, respectively.

3.1.3.5 Glancing angle: charge correction factor

These RBS detector solid angles found above were used to determine the *Q* (charge) correction factor from the Si signals at two glancing incidence angles. The corrections are: 1.43 at 15.0° and 1.56 at 13.3°. Note that these factors are determined independently for each spectrum.

Then the Bi content of the Harwell series standard (see section 2.1.6) was measured in order to verify the correctness of the determination of the charge correction factor when using glancing incidence. This was for two detectors and three beam incidence angles (0°, 13.3° and 15.0°), that is, six independent determinations. A value of $4.51(11)\times10^{16}$ Bi/cm^2 was found, which compares well with the certified value (4.72(10)) and also with the value determined from the IRMM Sb standard by Boudreault *et al*. (4.64(7)) [Bou02] (or see the study presented in chapter 4).

3.1.3.6 Kapton composition

A Kapton (polyimide: $C_{22}H_{10}N_2O_5$) sample, 0.025mm thick CR grade from Goodfellow Cambridge Ltd. [Goo], was used to calibrate the ERDA solid angle (see next section). This material has a dielectric strength of 290kV/mm^2 (and can therefore stand off ~10kV). It includes a filler for its enhanced properties: this is proprietary but since the thermal conductivity of the CR grade is near to that of the MT grade (known to have an alumina filler) it is reasonable to suppose that the filler is alumina. The film is fabricated by Dupont using a DMAc (dimethyl-acetemide) former, but this is thought to be at rather low concentrations (~1%?).

Therefore we expect the Kapton film composition to be a mixture of PI (polyimide) and alumina, at the accuracy of the analysis. We determined the PI/alumina ratio by RBS using 4 different areas of the sample and the same two different glancing incidence angles, assuming the C/H ratio is known. Note that the charge was determined by the spectral heights of the RBS spectra (assuming that the

C/H ratio is known). It turns out that the correction required to the nominal collected charge is 1.04(2). The alumina content was found to be 8.8(5) at%, using all 16 RBS spectra (4 areas, 2 angles, 2 detectors) together with the fitting code DataFurnace. Hence we used a composition for the Kapton of:

$$(C, H, N, O, Al) = (51.4, 23.4, 4.7, 17.0, 3.5).$$

3.1.3.7 ERDA detector solid angle

Then, now that the kapton composition has been determined (assuming that the H content is known) we can use the H signal to fix the ERDA detector solid angle. Note that strictly it is the solid angle *ratio* with the RBS detectors that is being determined, since we use the charge as a free parameter throughout this analysis. From the 8 sets of spectra (4 areas, 2 beam incident angles) we obtain as a solid angle for the ERDA detector 2.19(14) msr. This is a 6.4% standard uncertainty.

3.1.4 NRA set-up

The experiments using nuclear reactions, such as the accelerator energy calibration (appendix B) and NRA analysis (chapters 6 and 7), were all carried out using the target chamber on L5 (see Figure 3-1). In this section we describe very briefly the particularities of this experimental set-up dealing with the detection of gamma rays from nuclear reactions.

3.1.4.1 Beam line (L5)

As for L4, L5 is equipped with control slits, two moveable apertures, beam steering plates, and it has an identical vacuum system. However, before the entrance of the chamber, there is a series of quadrupole lens, which is able to focus the beam down to a few microns. Between these magnetic lens and the second aperture, there are X and Y scanning deflection plates.

3.1.4.2 Target chamber

The size of the target chamber is similar to the RBS chamber on L4; however it has a cuboid instead of cylindrical shape. The vacuum system is also similar to that of the RBS chamber. The back wall is simply removed to load the samples.

The chamber is equipped with a sample holder with a linear drive. An optical viewing system enables one to set the beam properly when using the microbeam. An RBS detector can be put inside. But for gamma detection from nuclear reactions, a ~12 cm^2 circular NaI scintillation detector was used and placed outside the chamber, in the forward direction behind the back wall.

3.2 Jena (RBS)

For the study on accurate dose measurements of implant into silicon by using RBS, which is presented in chapter 4, some of the experiments were carried out at Jena, Germany (a member of our research group took part to the experiments there). For fear of being redundant, as an in-depth description (with additional comments about accurate analytical work) of the IBA facilities at Surrey have been made in the previous section, we only mention here a few experimental details.

The accelerator in Jena is a 1997 HVEE 3 MV Tandetron. The energy calibration was via the 3.05-MeV He elastic scattering resonance on O which confirmed the previous machine calibration carried out in February 1998 using the Al p-gamma resonance at 991.9 and 632.0 keV. Unlike Surrey, the accelerator directly controls the energy from a generating voltmeter.

The Jena accelerator was one of those used in the recent international collaboration for the new and very accurate determination of the Si surface yield as a calibration standard for RBS [Bia00]. The measurements in Jena were on a system with demonstrably good charge collection, since the absolute results reported from this laboratory in [Bia00] were very accurate.

3.3 Participants of the ERDA Round Robin exercise

In chapter 5, we present the results from a Round Robin exercise for the measurement of hydrogen implanted into silicon by using ERDA techniques. The results from Surrey (our results) are minutely given and discussed, whereas only the general results from the other participants (Canberra, London, Helsinky, Rossendorf and Montreal) are given, and this is relevantly for comparison and inter-lab reproducibility assessment. Then we thought it would be interesting to give also a few details about the experimental procedure of each IBA laboratory participant (Surrey's experimental procedure is presented further above in section 3.1.3); this is the aim of this section. Because Canberra performed a very interesting ΔE-E telescope ERDA multielemental analysis, we have decided to present their experiment more exhaustively, and they will be introduced first.

But firstly, we have summarised the details of the experiments carried out by the different IBA participants with their various ERDA detection systems in Table 3-4. The incident angles are given from the surface of the sample (reflexion mode: grazing angles). Each participant carried out an ERDA-type experiment; the Rossendorf team performed additionally an NRA analysis.

Table 3-4 *Experimental set-up details for each participant in the ERDA Round Robin exercise for the measurement of hydrogen in silicon (presented in chapter 5).*

Participant	*Method*	*Beam*	*Angles*		*Solid angle [msr]*	*Detector*	*Standard*
			Recoil [°]	*Incident [°]*			
Canberra	ΔE-E telescope ERDA	200 MeV ^{197}Au	45.9	22.5	3.50	Position-sensitive gas ionization detector + Mylar window	Si stopping powers
London	Conventional ERDA	1.6 MeV ^{4}He	~24			Si detector + 6 μm Mylar range foil	Kapton, Mylar
Surrey	Conventional ERDA	1.5 MeV ^{4}He	26.6	13.3 15.0	2.16	Si detector + 6 μm Mylar range foil	Kapton Si stopping powers
Helsinky	ToF ERDA	53 MeV $^{127}I^{10+}$	40	20		ToF-E detector	Si stopping powers
Rossendorf	HI-ERDA	35 MeV $^{35}Cl^{7+}$	38		2.1	Si detector + 18 μm Al range foil	D-implanted reference target
	NRA	6.4-6.7 MeV ^{15}N	Forward direction			4" NaI(Tl)	Kapton
Montréal	ToF ERDA	40 MeV $^{63}Cu^{8+}$ 30 MeV $^{35}Cl^{5+}$				For Si, O, C : ToF-E detector For H : Si detector + 13 μm Mylar/17 μm Al range foils	Si stopping powers

3.3.1 Canberra (Australia)

Canberra used a position-sensitive gas ionization detector with HI-ERDA (ΔE-E telescope ERDA) [Tim98, Tim00-a-b]. At the Australian National University facilities, the pressure inside the gas ionization detector can be optimised for heavy-ion detection [Ell00]. In the latter mode protons recoiling with high energies are transmitted through the detector, with only energy-loss information being obtained. This mode has the advantage that hydrogen can be quantified simultaneously with heavy elements and was therefore the method of choice for this study (see section 5.4.1). The achievable depth-resolution for hydrogen in this mode is, however, much reduced. The position-sensitive gas ionization detector has been developed for the specific demands of ERDA analysis with heavy-ion beams [Tim00-a-b]; it is located inside a large scattering chamber (radius 1 m) at the end of a beam line at the 14UD Pelletron accelerator.

3.3.1.1 Experimental set-up

From the available section of the wafer, two samples were cut and mounted. The energy of the ^{197}Au beam was (200.05 ± 0.10) MeV. It was collimated in front of the sample using four slits, which were 200 mm apart. The first and third slit had the nominal dimensions of 0.5 mm × 3 mm and the second and fourth had the dimensions of 1 mm × 4 mm, respectively. The angle between sample normal and beam was 67.5°. The detector was located within the plane defined by beam and sample normal, at a scattering angle of 45.9°, 278 mm from the sample. The detection solid angle was (3.50 ± 0.05) msr. Recoil ions entered the detector through a (0.50 ± 0.03) μm thick Mylar window supported by a rectilinear grid of gold-coated tungsten wires. Propane gas was passed through the detector at a constant pressure of 80 mbar. The pressure in the scattering chamber was ~5×10^{-6} mbar.

The detector has a subdivided anode with two ΔE- and a residual energy E_{res}-electrode. The pulse amplitudes from these electrodes can be combined to obtain the total ion energy. The detector also features a grid electrode between Frisch grid and anode, which provides an independent energy signal [Tim00-a-b]. This signal (E_g),

amplified with high gain, also provides the trigger for the electronic acquisition of events, including proton events.

3.3.1.2 Detection of C, O and Si

The event-by-event data were sorted into spectra following the measurements. With the exception of hydrogen which is identified differently [Ell00], detected elements are evident in the two-dimensional projection of the ΔE-E_g spectrum, which is shown in Figure 3-10 for one of the samples. Apart from the Si recoil ions, O and C events associated with the sample surface are apparent. As part of the sorting process, position information for each event was used to correct the kinematic energy spread over the acceptance angle of 3.9°, thus retaining the energy resolution of the detector [Tim00-a-b]. The horizontal position of the ions on entry into the detector was obtained from the relative response of the two sawtooth subdivisions of the second ΔE-electrode on the anode. The vertical position of the ions was ignored in this case, since it is insignificant in the context of these measurements.

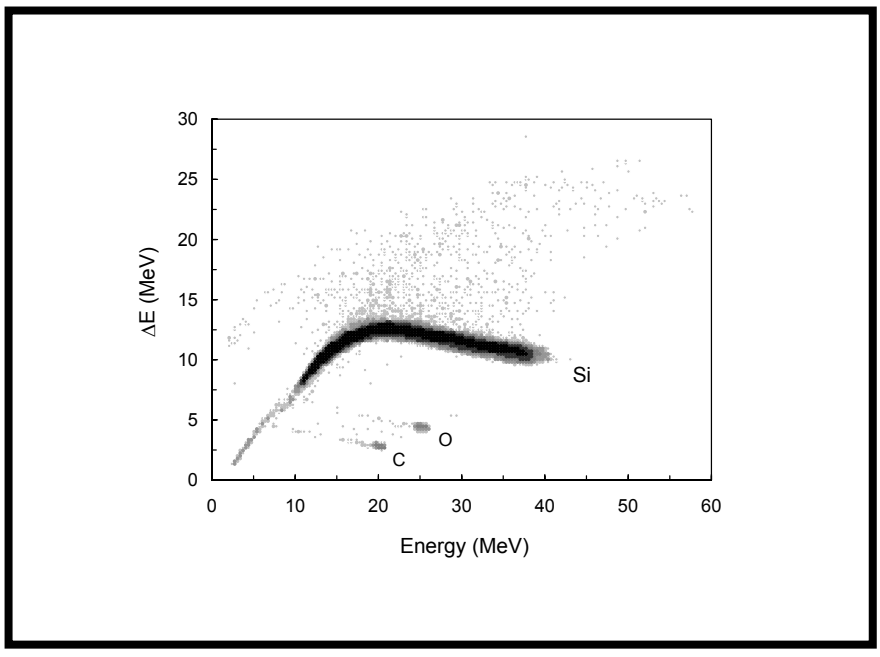

Figure 3-10 *Two-dimensional projection of the spectrum of* ΔE *versus energy (*E_g*) (for sample #1), after correction of kinematic energy broadening across the acceptance angle. The relative ion yields are indicated by the grey-scale (z-axis). In addition to Si ions, C and O ions from the sample surface can be identified. The low intensity haze of events above Si corresponds to electronic pile-up.*

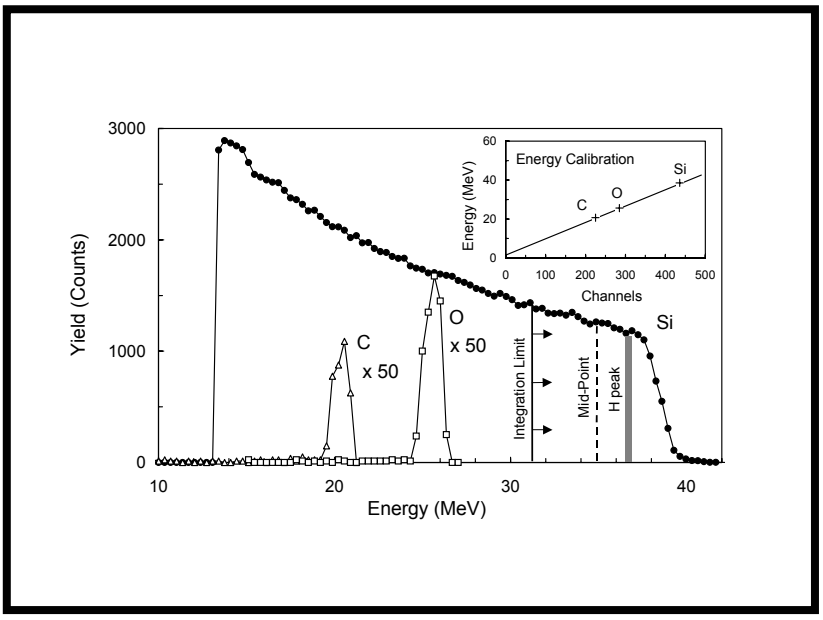

Figure 3-11 *Energy spectra for Si, O and C, extracted from the two-dimensional projection of the spectrum shown in Figure 3-10 (the yield is the one as given by the grey-scale z-axis of Figure 3-10). The original 1024 channel spectrum has been compressed to 256 channels to reduce statistical scatter. The selected integration region for Si, the mid-point of this interval and the likely location of the implantation peak on this scale are indicated. The inset shows the data and the linear fit used for the energy calibration.*

For both samples energy spectra for C, O and Si, shown in Figure 3-11, were extracted from the two-dimensional projection. In the case of Si the high energy part of the spectrum (≥ 31.3 MeV) was integrated, which represents an energy interval of 7.32 MeV, whereas for C and O the surface peaks were integrated. The integrated yields are given in Table 3-5.

3.3.1.3 Detection of H

The hydrogen events were identified in the extreme low energy part of the two-dimensional projection of the E_{res}-E_g spectrum, shown in Figure 3-12, where the protons are completely separated from other low-energy ions [Ell00]. The spectrum was calibrated by modelling the detector response using tabulated stopping powers for protons in propane. Since higher-energy protons pass through the sensitive volume of the detector, only a fraction of their energy is detected. The E_{res}-E_g spectrum is therefore complex, containing contributions from both stopped and transmitted protons with the response curve bending over at the point of maximum energy loss under both electrodes (we do not go into details for the explanation of

this complex response curve, this would lie beyond the scope of the study). The indicated region corresponds to hydrogen recoils from near the sample surface and shows a large yield of detected protons. This region was therefore taken to represent the implanted hydrogen and integrated. The results are given in Table 3-5. Apart from this intense signal a smaller number of counts along the response curve indicate the presence of a uniform trace concentration of hydrogen throughout wafer.

Table 3-5 *Experimental parameters used in the Canberra data analysis. The last two columns give the measured areal densities.*

Element	#	*Yield*[1)]	*Surface*[2)] *[ch]*	*Surface E [MeV]*	ΔE_{win}[3)] *[MeV]*	ΔE_{phd}[4)] *[MeV]*	n[5)] $[10^{15}at/cm^2]$	n_H[6)] $[10^{15}at/cm^2]$
H	1	10024	—	—	—	—	59.2 ± 4.2	60.5 ± 4.2
	2	9937					60.9 ± 4.3	62.4 ± 4.3
C	1	300	225	21.0	0.3	—	6.3 ± 0.6	—
	2	285					6.2 ± 0.6	—
O	1	488	285	26.9	0.5	0.8	9.8 ± 0.9	—
	2	457					9.5 ± 0.9	—
Si	1	112986	436	42.3	1.2	2.5	2048 ± 142	—
	2	109017						

[1)] *given are for H all counts associated with the near-surface region, for C and O the integral of the surface peaks, and for Si the sum of events with energies ≥ 31.3 MeV.*
[2)] *for C and O the centroid of the surface peak, for Si the half-maximum of the high energy edge.*
[3)] *the energy deposited in the detector window (0.5 μm Mylar).*
[4)] *the pulse height deficit of the detector signal for ions recoiling from the sample surface, determined using the empirical formula from [Wei01].*
[5)] *the areal density given for silicon corresponds to the selected energy interval of 7.32 MeV, for carbon and oxygen the surface concentration is given, for hydrogen the value includes both, the implanted concentration plus any surface hydrogen present.*
[6)] *the areal densities for hydrogen after correction for beam-induced de-sorption.*

Unfortunately this method does not permit one to separate the surface hydrogen from the bulk hydrogen. Notwithstanding, it remains an interesting study and it has some advantages: large solid angle, multielemental analysis, elements from the whole periodic table can be analysed, no detector damage problems, and both mass-depth and recoil-projectile ambiguities can be resolved.

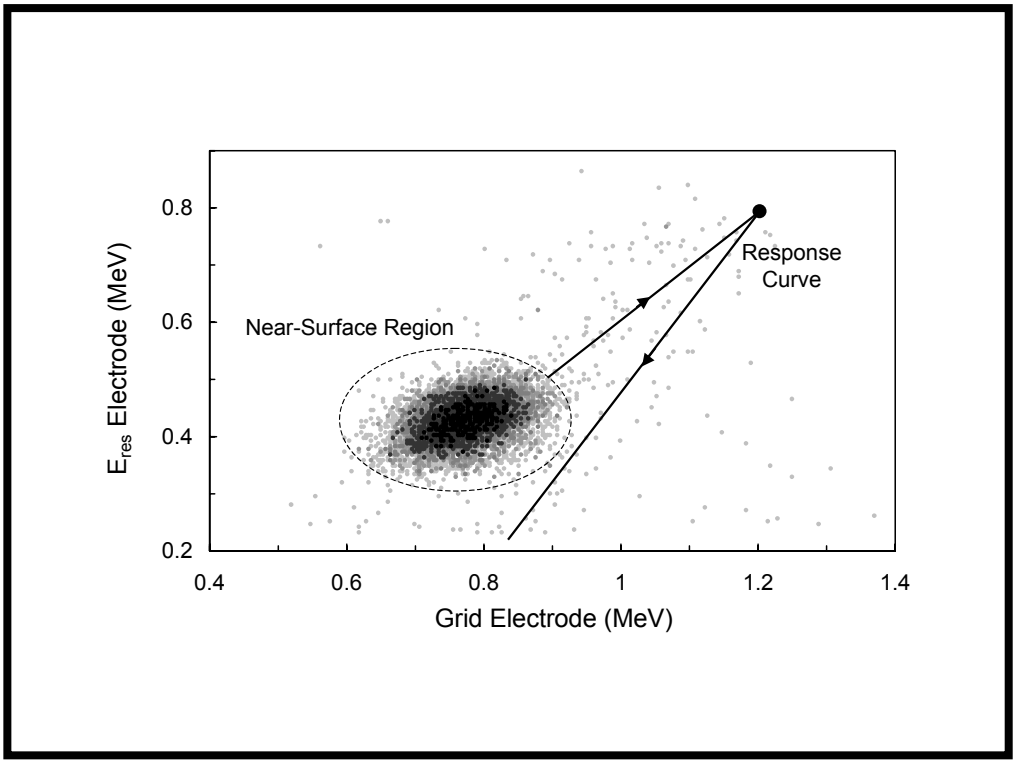

Figure 3-12 *The extreme low-energy part of the two-dimensional projection of the spectrum which relates the* E_{res} *signal with that from the grid electrode and allows the identification of protons. The implanted hydrogen can be identified as intense yield in the near-surface region. The response curve for hydrogen is indicated in the direction of increasing sample depth.*

3.3.2 London (Canada)

Two pieces of the hydrogenated-silicon wafer were measured using a 1.6-MeV ^{4}He beam at a forward angle of approximately 24° in a conventional ERDA set-up. Both Kapton and Mylar targets were used as standards to get absolute amounts of hydrogen. Charge collection was monitored by means of an intermittent Faraday cup that intercepts the beam in front of the target with a duty cycle (beam on fraction) of roughly 63%. A second Faraday cup was put downstream to calibrate the beam monitor.

3.3.3 Helsinki (Finland)

The experiment was carried out using a ToF-E set-up with two timing gates and an energy detector. The experiment features were: 53-MeV $^{127}I^{10+}$ beam, beam spot size of ~10 mm^2, beam current of ~0.2 nA, 20° incidence angle, 40° recoil angle, collection time of ~4600 s, event-by-event data collection. The beam current was measured from a Faraday cup in the target holder. The thickness of the carbon foil was 5 μg/cm^2.

As the detection efficiency of the timing gates for hydrogen is energy dependent and quite low, the hydrogen energy spectra were obtained from the energy detector. Since detection efficiency for heavier recoil atoms is very close to 100%, the data were collected using both coincident signals from ToF and E-detector, and non-coincident signals from the E-detector. The small background was subtracted from the final results. The surface peaks of C and O did not have an effect on the results. The area of hydrogen depth profile was normalized to the signal of silicon. The measurement set-up was the very same set-up used in the analysis of each element from over 500 samples each year and described in [Jok96].

3.3.4 Rossendorf (Germany)

Both NRA and conventional HI-ERDA experiments were carried out at Rossendorf for the characterisation of the hydrogen content of the H implant into Si. We give information on both experimental procedures.

3.3.4.1 HI-ERDA experiment

This experiment was performed using a 35-MeV $^{35}Cl^{7+}$ beam of ~1 mm^2 spot size, together with a silicon detector covered with an 18 μm Al stopper foil, placed at a recoil angle of 38° and presenting a solid angle of 2.1 msr. The beam dose measurement was done indirectly by backscattering from a rotating sector beam shutter (Au on Al) regularly calibrated against a Faraday cup. A total fluence of 3.1×10^{12} ions struck the sample. The data were calibrated using a D-implanted reference target.

3.3.4.2 NRA experiment

The NRA experiment was carried out using a ^{15}N beam with energy increasing from 6.385 MeV in steps of 15 keV for a total span of about 250 keV, with a beam spot size of ~20 mm^2. The narrow and isolated resonance in the reaction:

$$^{1}H + ^{15}N \rightarrow ^{4}He + ^{12}C + \gamma,$$

at 6.385 MeV and producing 4.43-MeV gamma-rays was then used [Lan76].

Stepping the beam energy through allowed one to depth-profile the hydrogen as the incident N ions slow down passing through the sample and reach the resonance energy at some depth. The energy loss was calculated from SRIM2000 database [www⑦] assuming pure silicon (including a 10% H concentration has no effect on the peak integral). A 4″ NaI(Tl) gamma detector was used in forward direction. The charge was again collected from backscattering from a rotating beam shutter. The system is described in more detail in [Rud86]. The data were normalized by using a Kapton standard sample .

3.3.5 Montreal (Canada)

A series of 8 different measurements were made from 2 samples of the hydrogenated-silicon wafer by using 2 different beams (40-MeV $^{63}Cu^{8+}$ and 30-MeV $^{35}Cl^{5+}$) and 2 different absorbers (13 μm Mylar and 17 μm Al). Hydrogen was detected in a conventional set-up by using a selective absorber technique whereas Si and surface impurity elements C and O were detected in ToF ERDA mode. For more details on the Montreal arrangement see [Guj90].

Thickness of Mylar and Al absorbers were deduced by using precision microbalance (weighing method) as well as 5.484-MeV α particles from ^{241}Am source (energy-loss method); the results from the two methods agreed with each other within 1.5%. The energy-loss parameters from TRIM95 were used. Relative concentrations of all the elements were calculated with respect to the Si substrate to avoid the uncertainties associated with the exact knowledge of the total beam dose.

CHAPTER 4

ACCURATE RBS MEASUREMENTS OF ION IMPLANT DOSES IN SILICON

4.1 Introduction

Ion implantation processes are universally used in semiconductor processing, and especially in the fabrication of integrated circuits on silicon. Rutherford backscattering spectrometry is an important technique for characterising the absolute implant dose because it is based on analytical cross-sections and because it does not have matrix-dependent sensitivity factors. Its disadvantage is that it is relatively insensitive since the cross-sections are quite low, and also it is only for heavy implants in a light substrate that the signal from the implant is relatively background-free. Among the cluster of related IBA techniques, only RBS has analytical (that is, Rutherford) cross-sections, and it is therefore RBS that we use for this standards work.

In this work we aim to establish the instrumentation for dosimetry on ion implanters at the 1% level for high dose heavy implants in silicon. This is expected to be a worst case for the implanter instrumentation since secondary electron generation is reduced for light ions and low beam currents. The only *critical* RBS analysis that we are aware of near 1% accuracy (apart from [Wät94] on the Bi-implanted silicon reference material) is the determination of the stoichiometry of InGaAs samples by Jeynes *et al*. [Jey97]: in this case normalisation uncertainties were excluded by the analytical procedure employed, but even in this favorable case

the authors concluded that the number of other uncertainties at the ¼% level would make combined uncertainties much better than 1% hard to achieve.

Amorphised Si is easy to prepare in an implantation laboratory and very reproducible: we use this material as a standard and compare it with the certified Sb reference material (see section 2.1.6 on RBS standards). This comparison is based on the precisely known values for energy loss of He in Si (as discussed in section 2.1.5.5 on stopping power accuracy). The method we use has been used before in standards work in the validation of the Ta_2O_5 electron spectroscopy standard by IBA methods [Sea88]. This did not achieve a combined uncertainty better than 2% and the accuracy of the RBS part of this work was limited by the quoted 2.2% uncertainty of the value of energy loss of He in Ta that was used.

We used two methods of data reduction. The first, the *manual method*, uses well-defined approximations and simple data manipulations to *transparently* obtain a result. All the steps will be explained, the uncertainties will be determined critically, and all the (intermediate) numbers and calculations will be shown for clarity and in order to establish the reliability of the results since we aim to demonstrate a level of accuracy as good as 1%. The second method, the *machine method*, uses the fitting code DataFurnace [Bar97-b] (also appendix D), which requires the user to believe that the internal calculations of the code are valid. Of course, we wish to use a convenient code, but for *critical* work we need to be able to justify the results simply. The agreement of the machine and manual methods is a validation of the DataFurnace code.

We would like to inform the reader that a summary of the study presented in this chapter has already been published [Bou02].

4.2 Details on samples analysed and experiments

4.2.1 Samples analysed

In total 11 implant into silicon samples were submitted for RBS dose measurements. Table 4-1 lists the samples that were measured on five

separate occasions in two laboratories (Surrey and Jena) along with their implantation energy and nominal dose.

Three of them are In implants: In01 is a piece taken from a 50 keV implant at a nominal 1×10^{15} at/cm^2 dose; In02 and In03 are pieces of a nominally 1×10^{15} at/cm^2 dose 4" wafer implanted for Surrey QA (quality assurance), the former taken from the edge and the latter from the centre. Six are As implants, with different combinations of implantation energies and nominal doses. They are low-energy 4" wafer implants (between 2 and 4 keV), except As06 and As10, which are 70 keV and 100 keV respectively; the nominal doses vary from 1×10^{15} at/cm^2 to 5×10^{15} at/cm^2. These samples were all implanted at Surrey for implantation quality control.

Table 4-1 *Implantation energy and nominal dose for the implant into silicon samples analyzed. The UWO Bi sample came from University of Western Ontario (UWO), and was certified by W.N. Lennard at 2%. The IRMM/BAM Sb sample came from Geel, and was sent by U. Wätjen;it has a certification of 0.6% traceable to the international standard of weight in Paris. The other samples were all implanted at Surrey.*

Sample	*Energy (keV)*	*Nominal dose ($x10^{15}$ at/cm^2)*	*Comment*
In01	160	1	In implant, wafer 1
In02	160	1	In implant, edge of wafer 2
In03	160	1	In implant, center of wafer 2
As05	2	1	As implant
As06	70	4	As implant
As07	4	3	As implant
As08	4	1	As implant
As09	2	3	As implant
As10	100	5	As implant
Bi11	40	4.72(10)	UWO Bi implant
Sb12	400	48.1(3)	IRMM-302/BAM-L001 Sb implant

The last two samples in Table 4-1 are of particular interest. Bi11 is a Bi “Harwell” standard sample [Tes95{vii}], and was certified at 2% by W.N. Lennard at University of Western Ontario (UWO). The sample Sb12 is the certified Sb sample designated IRMM-302/BAM-L001, it comes from U. Wätjen at Geel, and has a certification of 0.6% traceable to the international standard of weight in Paris;

therefore this sample is particularly important for this work on high-accuracy dose measurements. More details on Bi11 and Sb12 are given in section 2.1.6.

4.2.2 Experiments

All the experiments were carried out at normal incidence. Using channelling techniques together with crystalline silicon samples, the normal position of the goniometer was determined within ½º. In this range of uncertainties in tilt angle, uncertainties introduced in the dose measurement are not significant.

The electronics dead time for each spectrum was the average value taken from the ADC. This measurement depends on the beam current being reasonably constant, which it is on our instrument. It would be more accurate to use the electronics logic busy signals to gate the charge collection counter. However, for the main part of this work we do not depend on accurate charge collection since we perform an internal normalisation.

Table 4-2 gives some details (calibration, spectra collected and some comments) on the five experiments carried out at Surrey and Jena at different dates. The accelerator energy calibration corresponding to the experiments carried out at Surrey is the one given in appendix B.1. In03 and As06 implanted samples were each measured at least three times both before and after amorphisation. Amorphisation was by a cooled Si implant at 200 keV and 5×10^{15} Si/cm^2. The initial measurements at Surrey (experiments *i* and *ii*) of the In and As implant series were relative only, since reliable standards (amorphised samples) for charge·solid angle product determination were not included. The final measurements at Surrey (experiments *iii* and *iv*) and the Jena ones (experiment *v*) include those on amorphised implanted Si samples, together with the UWO standard sample and the certified IRMM/BAM standard. Note that the Bi sample had also 5×10^{15} Si/cm^2 at 200 keV at ~150K for amorphisation; this is not expected to affect (modify) the dose of the implant [Len99-b]. The measurements done in Jena were on a system with demonstrably good charge collection, since the recent absolute results reported from this laboratory were very accurate [Bia00]: however, in this work we make no absolute measurement of detector solid angle at either Jena or Surrey. Thus, multiple independent

measurements (double detectors, different dates, different labs) on several samples are included and the reproducibility of the method can be assessed.

Table 4-2 *Spectra from samples analyzed on five different dates and in two laboratories. The amorphised samples (marked *) had 5×10^{15} Si/cm^2 at 200 keV at ~150K.*

Experiment (lab/date)	*Sample*	*Spectrum*
Surrey October 1999 (i)	In01	In01o01
		In01o02
	In02	In02o01
		In02o02
	In03	In03o01←
		In03o02←
Surrey November 1999 (ii)	As05	As05o01
	As06	As06o01←
	As07	As07o01
	As08	As08o01
	As09	As09o01
Surrey June 2000 (iii)	In03	In03y01*
	In03	In03y02*
	As06	As06y01
	As07	As07y01
	As10	As10y01*
		As10y02*
		As10y03*
		As10y04*
		As10y05*~
	Bi11	Bi11y01*
		Bi11y02*
		Bi11y03*
		Bi11y04*
	Sb12	Sb12y01~
Surrey August 2000 (iv)	As10	As10L01*
		As10L02*
		As10L03*
		As10L04*
		As10L05*
	Bi11	Bi11L01*
		Bi11L02*
		Bi11L03*
	Sb12	Sb12L01
Jena October 2000 (v)	In03	In03J01*
		In03J02*
		In03J03*
	As10	As10J01*
		As10J02*
		As10J03*
	Bi11	Bi11J01*
		Bi11J02*
	Sb12	Sb12J01
		Sb12J02

"o" in spectra names stands for "old"; data from first experiments carried out at Surrey in 1999 (two different experiments, one for In samples the 7th October 1999 and another one for As samples the 12th November 1999), and in which we failed in determining the solid angle absolutely (no amorphised samples).

"←" data from Surrey 1999 experiments used to determine the solid angle relatively to results from Surrey June 2000 experiments in which we could achieve the solid angle calculation absolutely.

"y" in spectra names stands for "young"; data from subsequent experiments carried out at Surrey in June 2000 (performed in two days, the 12th and the 13th June 2000), and in which we succeeded in determining the solid angle absolutely using amorphised samples.

"L" in spectra names stands for "latest"; data from the latest experiment carried out at Surrey.

"J" in spectra names stands for "Jena"; data from the experiment carried out at Jena (Germany).

"*" Spectra collected from samples as amorphised (and used to determine the solid angle absolutely).

Electronics calibration numbers (gain κ and *offset*) for each experiment carried out, together with the Si surface yield calibration standard M_{Si}, as defined in

section 2.1.5.5, and kinematic factors *K* corresponding to the different geometries are given in Table 4-3.

Table 4-3 *Electronics calibration numbers (gain* κ *and* offset*), Si surface yield calibration standard* M_{Si} *(for a 1490.4 keV and 1528.0 keV He beam energy* E_0 *at Surrey and Jena, respectively), and kinematical factors* K *(for He scattering on Si, In, As, Bi and Sb ions) corresponding to both A and B detectors at Surrey and A detector at Jena.*

Table 4-3a

	1i κ (keV/ch)	1ii κ (keV/ch)	1iii κ (keV/ch)	1iv κ (keV/ch)	1v κ (keV/ch)	2i Offset (keV)	2ii Offset (keV)	2iii Offset (keV)	2iv Offset (keV)	2v Offset (keV)
Su-A det (θ=166.9° E_0=1490.4 keV)	3.024	3.021	3.741	2.909	—	55.16	58.99	40.03	54.51	—
Su-B det (θ=133.1° E_0=1490.4 keV)	3.107	3.080	4.386	2.854	—	36.56	57.13	30.35	39.75	—
Je-A det (θ=168.0° E_0=1528.0 keV)	—	—	—	—	4.091	—	—	—	—	44.84

Table 4-3b

	3 M_{Si} (E_0, θ) (cts/msr·keV·μC)	4 K_{Si}	5a K_{In}	5b K_{As}	5c K_{Bi}	5d K_{Sb}
Su-A det (θ=166.9° E_0=1490.4 keV)	29.323	0.5675	0.8714	0.8097	0.9272	0.8782
Su-B det (θ=133.1° E_0=1490.4 keV)	31.302	0.6167	0.8892	0.8352	0.9375	0.8952
Je-A det (θ=168° E_0=1528.0 keV)	27.766	0.5668	0.8711	0.8093	0.9270	0.8780

Suffixes i, ii, iii, iv *and* v *refer to the different experiments as specified in Table 4-2. Suffixes a, b, c and d refers to In, As, Bi and Sb data, respectively. Su-A, Su-B and Je-A stand for Surrey A and B and Jena A detectors, respectively.*

4.3 *Manual* data reduction (transparent) method

4.3.1 Pile-up calculation

The pile-up is calculated by a simple binary convolution of the spectrum with itself, assuming that all pileup-built pulses have an energy which is the sum of the two pile-up pulses, as discussed in section 2.1.8. We recall here that any signal where the pile-up background is significant will also itself be *reduced* by pile-up. Therefore, any such signal must have a non-linear pile-up background. Consequently, a proper treatment of pile-up is essential to accurate dose determination by RBS, since not only can the backgrounds be relatively large, but also they are non-linear as just mentioned.

Achieving this pairwise pile-up correction is the very first step in the analysis. We recall also that this pile-up calculation is implemented in the code DataFurnace, and the code will be used in fact to subtract the pile-up background from the spectra. Then the whole manual analysis will be done using the pileup-corrected spectra only.

4.3.2 Charge·solid angle product ($Q\Omega$)

The purpose here is to accurately determine the surface yield Y_0 from the sub-surface yield so as to use the *magic number* of equation (2-17) to obtain the charge·solid angle product ($Q\Omega$). For a given charge, the solid angle subtended by the detector is evaluated. The solid angle is extracted from each (non-aligned) spectrum; a mean value and an uncertainty are derived from the whole set of solid angles determined. In fact, this is the uncertainty of the charge·solid angle product which is derived. If we could perform charge collection *perfectly* (let us imagine an *ideal* Faraday cup), we would obtain an identical solid angle value for each spectrum (with *perfect* charge collection, the Y_0/Q ratio would be a constant within statistical fluctuations); so the apparent variation in the solid angle is really a variation in the collected charge. This procedure is equivalent to normalizing the $Q\Omega$ product to the amorphised Si yield using the absolutely determined Si energy-loss values as a standard. Should all the spectra be normalized to the same charge before any

calculation, and the $Q\Omega$ random uncertainty will then be governed by the Y_0 yield fluctuations only.

Prior to the calculation of the solid angle, we need to evaluate the Si surface yield Y_0 from each of the (non-aligned and charge-normalized) spectra collected from the amorphised samples. Assuming that these spectra are channelling-artefact free, Y_0 can be evaluated by using a yield Y_b from a thin layer below the surface, and which can be correlated to Y_0 (see below) and read (nearly) anywhere else near the Si surface signal. One has to bear in mind that the implantation profile is near, but not at, the surface; consequently at these depths the beam has lost a small amount of energy, therefore both $\sigma(E)$ and $\varepsilon(E)$ are modified. This situation is pictured in Figure 4-1. The presence of the implant will cause a slight dip in the Si signal for that depth: the energy of this Si signal is labelled "too close" in the figure. For this analysis Y_b has to be measured at an energy E_c suitably far from $E_{too\ close}$.

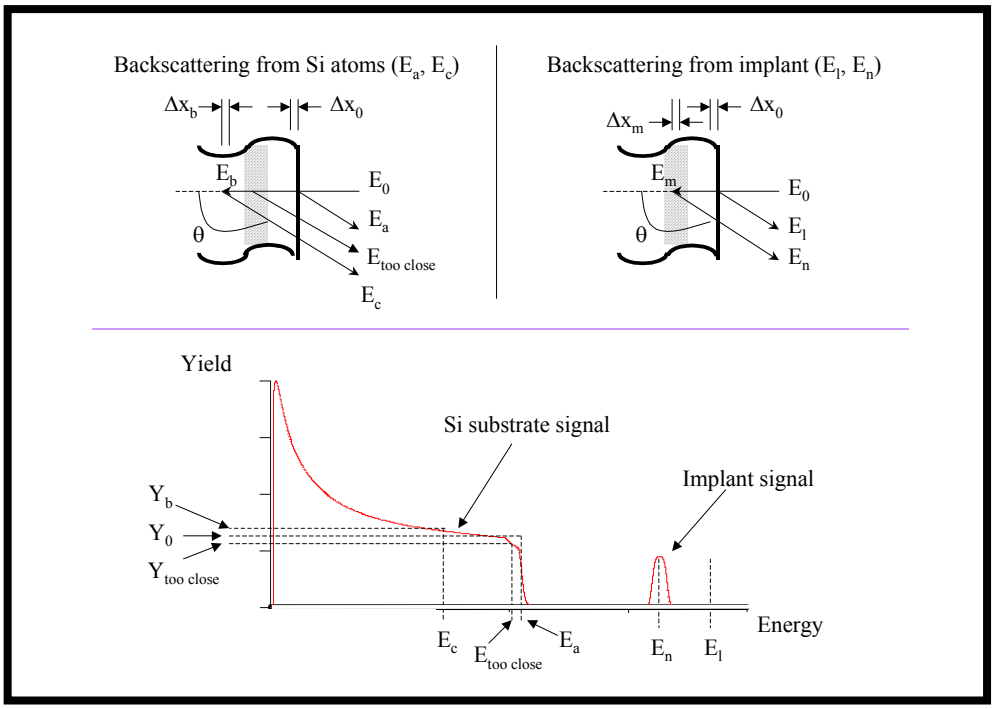

Figure 4-1 *Manual data reduction method. Top: energy parameters along the backscattering process both from Si substrate atoms and implanted ions, which are required for the analysis leading to the ion-implanted dose determination (see text). Bottom: corresponding RBS spectrum.*

Let us define here some energy quantities: E_0, E_a, E_b and E_c, respectively the incident beam energy, the particle energy after scattering from a Si atom at the

surface (slab Δx_0), the inward beam energy at a slab Δx_b, and the exit particle energy for a scattering event occurring from a Si atom in a slab Δx_b, which can be all visualized in Figure 4-1. E_a is easily obtained by doing:

$$E_a = K_{Si}(\theta)E_0\,, \tag{4-1}$$

as defined by equation (2-1) in fact, and where $K_{Si}(\theta)$ is the Si kinematical factor for a scattering angle θ (as calculated by equation (2-2)). Then, once an E_c and Y_b set has been chosen at a channel *not too close* where the Si signal drops, the corresponding E_b value must be calculated; we can use the energy-loss ratio method [Chu78{i}], which leads to the equation:

$$E_b = \frac{E_c + \alpha_{Si}E_0}{K_{Si} + \alpha_{Si}}, \tag{4-2}$$

where:

$$\alpha_{Si} \cong \frac{\varepsilon(E_a)}{\varepsilon(E_0)\cos(\pi - \theta)}. \tag{4-3}$$

α_{Si} is in fact the ratio of the energy lost along the outward track $\Delta E_{out} = K_{Si}E_b - E_c$ to that lost along the inward track $\Delta E_{in} = E_0 - E_b$, which is to a good approximation assumed to be independent of depth ($\alpha = \Delta E_{out}/\Delta E_{in} \approx const$) and, as a result, determined from the surface energy approximation. The uncetainty in E_b when using this approximation for α is less than 0.2% provided the scattering layer is less than 2500×10^{15} Si/cm^2 from the surface.

Finally, Y_0 can be calculated with the following expression:

$$Y_0 = Y_b\left(\frac{E_b}{E_0}\right)^2 \frac{[\varepsilon(E_b)]}{[\varepsilon(E_0)]}\frac{\varepsilon(E_c)}{\varepsilon(K_{Si}(\theta)E_b)}, \tag{4-4}$$

where $[\varepsilon(E_i)]$ refers to the stopping cross-section factor and $\varepsilon(E_i)$ to the energy-loss value, both evaluated in a Si matrix at the surface energy approximation [Chu78{ii}]. We point out here that stopping cross-section factor ratios and energy-loss ratios are used, where no significant accuracy is lost as mentioned in section 2.1.5.5. The uncertainty in Y_0 when using this approximation (energy-loss ratio method) for α is

less than 0.25% provided the scattering layer is less than 2500 $\times 10^{15}$ Si/cm^2 from the surface.

4.3.3 Sensitivity and dose determination

The next step is the evaluation of the ion implanted sensitivity S_{imp}, that is, the number of implanted ions per cm^2 per count (in the implant peak). But, due to the fact that the implanted ions are not at the surface but rather slightly buried within the Si matrix, we need first to calculate the inward beam energy at which the scattering event occurred as the implanted ion scattering cross-section at this energy is required for the S_{imp} calculation.

Similarly, as we did for Si, let us define again some energy quantities: E_l, E_m and E_n, respectively the particle energy after scattering from an implant atom at the surface (slab Δx_0), the inward beam energy at a slab Δx_m, and the exit particle energy for a scattering event occurring from an implant atom in a slab Δx_m, which can all be visualized in Figure 4-1 as well. As previously done for E_a, E_l is easily obtained using equation (4-1) and substituting the implant kinematical factor K_{imp} in. Then correspondingly, substituting subscripts *l*, *m*, *n* and *imp* to subscripts *a*, *b*, *c* and *Si* respectively, the quantity needed E_m can be calculated through equations (4-2) and (4-3). Note that E_m corresponds to the energy at the mean depth of the implant distribution, and it is used as the energy before scattering for each event, which is a good approximation provided the implant distribution is not too large; no proper integration is performed with the manual method.

Lastly, the implant dose D_{imp} can be determined by multiplying the sensitivity S_{imp} by the number of counts A_{imp} in the implant peak (see equation (2-20):

$$D_{imp} = S_{imp} A_{imp} = \frac{1}{\Omega C_Q Q F_{imp}(E_m)\sigma(E_m,\theta)} A_{imp}, \qquad (4\text{-}5)$$

where C_Q is the charge-to-number of particles conversion factor (which means that $C_Q Q$ is the total number of incident particles), $\sigma(E_m,\theta)$ the implant Rutherford scattering cross-section evaluated at the energy E_m and the scattering angle θ, and $F_{imp}(E_m)$ the correction factor for the partial screening of the nuclear charges by the electron shells surrounding both nuclei. This screening-effect correction factor

$F_{imp}(E_m)$ is not negligible, of the order of few percents at the energy range we generally use. $\sigma(E_m,\theta)$ is in fact the differential cross-section $d\sigma/d\Omega$ for an elastic collision as given by Rutherford's formula (see equation (2-7)); however the notation $\sigma(E_m,\theta)$ is generally used for simplicity. A convenient constant to remember in evaluating equation (2-7) is $e^2 = 1.4398\times10^{-10}$ keV·cm. If these units are used and E_m is given in keV, equation (2-7) leads to a Rutherford cross-section given in cm^2/sr. If Ω is given in msr in equation (4-5) and we want to evaluate the dose in at/cm^2 from the same equation, it would be rather convenient to rewrite equation (2-7) as following:

$$\sigma(E_m,\theta) \equiv \frac{d\sigma}{d\Omega} = \left(\frac{Z_1 Z_2}{2E_m}\right)^2 se^4\beta\,, \qquad (4\text{-}6)$$

where s is the sr-to-msr conversion factor so that $s\cdot e^4 \approx 2.0730\times10^{-23}$ keV^2·cm^2.

Table 4-4 *Charge-to-number of particles conversion factor* C_Q*, charge normalization* Q_{Norm}*, and quantities required for determination of implant Rutherford cross-section (see equation (4-6)): masses* M_1 *and* M_2 *(in atomic weight) and atomic numbers* Z_1 *and* Z_2 *for the projectile (He) and the target (In, As, Bi or Sb) respectively; the factor* $s\cdot e^4$ *(see text); and the angular part (see equation (2-8)).*

Table 4-4a

6	7	8a	8b	8c	8d	9	10a	10b	10c	10d
C_Q (part/μC)	M_1	M_2 (In)	M_2 (As)	M_2 (Bi)	M_2 (Sb)	Z_1	Z_2 (In)	Z_2 (As)	Z_2 (Bi)	Z_2 (Sb)
6.2415×10^{12}	4.0026	114.82	74.922	208.98	121.75	2	49	33	83	51

Table 4-4b

11	12	13a	13b	13c	13d	
Q_{Norm} (μC)	$s\cdot e^4$ (keV^2·cm^2)	β (In)	β (As)	β (Bi)	β (Sb)	
50	2.0730×10^{-23}	0.2560	0.2552	0.2565	0.2561	*Su-A det* (θ=166.9°)
		0.3523	0.3515	0.3527	0.35	*Su-B det* (θ=131.1°)
		0.2549	0.2541	0.2554	0.2550	*Je-A det* (θ=168.0°)

a, b, c and d refer to In, As, Bi and Sb data. Su-A, Su-B and Je-A stand for Surrey A and B and Jena A detectors. Col13 is calculated from equation (2-8).

There will be many intermediary calculations and results eventually, and we will gather all the numbers required in tables together with their history (equations and/or columns from [previous] tables they are obtained from) in order to make everything clearer and double-checking of the final results possible, even if it is not always imperatively relevant. Having this in mind, in Table 4-4 are gathered together the numbers that will be required to determine the implant Rutherford cross-section given by equation (4-6), together with the charge-to-number of particles conversion factor C_Q and the charge value Q_{norm} to which the spectra will be normalised.

4.4 *Machine* method: DataFurnace analysis

Firstly, we can contrast the machine method with the manual method. In the latter, the implant dose is determined from the area of the corresponding signal (in counts), with a sensitivity (in atoms/cm^2/count) determined at the mean depth of the implant (E_m in Figure 4-1). The sensitivity varies significantly with depth, on account of the $1/E^2$ dependence of the Rutherford cross-section (see equation (2-7), or equation (4-6)), and therefore this is an approximation which a proper numerical integration would avoid. With the machine method this integration is carried out by the DataFurnace code (and, of course, also any other code that could be used for this purpose).

An important aim of this work is indeed to validate the use of the DataFurnace code, so that RBS dosimetry work can be carried out routinely and rapidly at the highest achievable accuracy. The simple samples we have analysed are amenable to the manual method, with uncertainties that we determine further below in section 4.8). Therefore, DataFurnace is validated if it gives the same results. Our manual method may not be valid for the crucial IRMM/BAM certified sample since the Sb profile extends over such a large energy range, the Sb peak concentration is so high, and because the spectrum is further complicated by the presence of the SiO_2 layer (see Figure 4-2). For this spectrum DataFurnace is very convenient (although other codes can be used: for example, Børgesen *et al*'s code SQUEAKIE [Bør82] would work if the O signal was separated). Note that the "profile" command in the code RUMP [Doo85] does not use self-consistent energy loss and is therefore inaccurate for significantly varying composition.

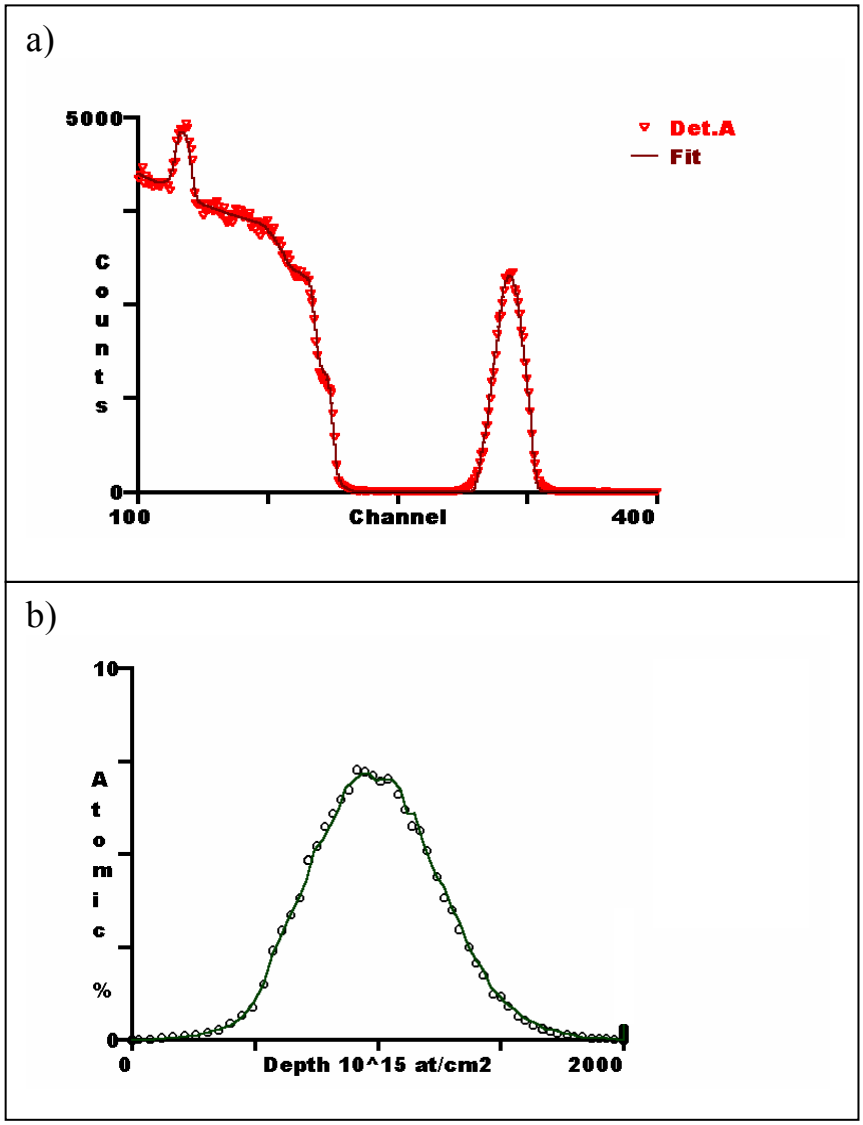

Figure 4-2 *a) Spectrum (data and DataFurnace fit) from the IRMM/BAM certified Sb standard and b) Sb profile from the two detectors (open circles and solid line are from Det A and Det B, respectively) obtained using DataFurnace.*

The DataFurnace has to be used in a special way to obtain traceable accuracy. Figure 4-2a shows a spectrum from the IRMM/BAM certified standard together with a calculated spectrum from a depth profile obtained from a DataFurnace fit. This fit does not give us the Sb dose accurately, but it does give the accurate (non-linear) depth scale, that is, the variation of the energy-loss function with depth. The Si signal of the substrate fits rather well: this is because we have used the correct Si stopping powers as described above. The Sb signal is not fitted very well in the tails of the implant distribution but this will not give much error since the energy loss due to the discrepancy in the number of implant atoms is not significant. The Si signal in the

oxide is not well fitted due to imperfection in the O energy-loss functional shape in the energy-loss database.

If the fit is *close* to the spectrum then the depth scale will be reasonably accurate. The depth scale is non-linear due both to the energy loss being a function of E and also to the varying composition with depth. The Sb profile is then calculated channel by channel directly from the (pileup-corrected) data using the (non-linear) energy loss from the (varying) composition that is determined by the DataFurnace fit. Figure 4-2b shows the Sb depth profiles for each detector. In fact, the bulk of the Sb implant is in the Si substrate; this implant amorphises the Si crystal but also causes a large dip in the Si signal.

Note that DataFurnace does *not* use signal areas as a fitting parameter, and therefore accurate dose measurements always have to use this type of data reduction where the dose is essentially derived from a (corrected) spectral area. Figure 4-2b (and also Figure 4-3c) shows profiles in this form. Of course, these profiles are not the real ones: they are broadened due to detector resolution and energy straggling.

4.5 Results from the manual method

4.5.1 Pile-up calculation

We present here some results of the proper treatment of pile-up, essential to accurate dose determination by RBS; note that, for simplicity, DataFurnace was used for this pile-up calculation. Figure 4-3 shows RBS spectra for count rates of ~4 kHz (Figure 4-3a) compared to an extreme case of ~12 kHz (Figure 4-3b) for sample As10. For the extreme case of ~12 kHz count rate, the partial spectra (As, Si and pile-up background spectra) are shown in Figure 4-4, and the As signal as a region of interest is given in Figure 4-5. The pile-up background is about 15% of the As signal and the non-linear distortion is about 10% of the pile-up; for this case this means that subtracting the background from the As signal using intuitively a simple straight line introduces directly an error of 1.5%! In both cases two spectra were taken simultaneously (detectors A and B).

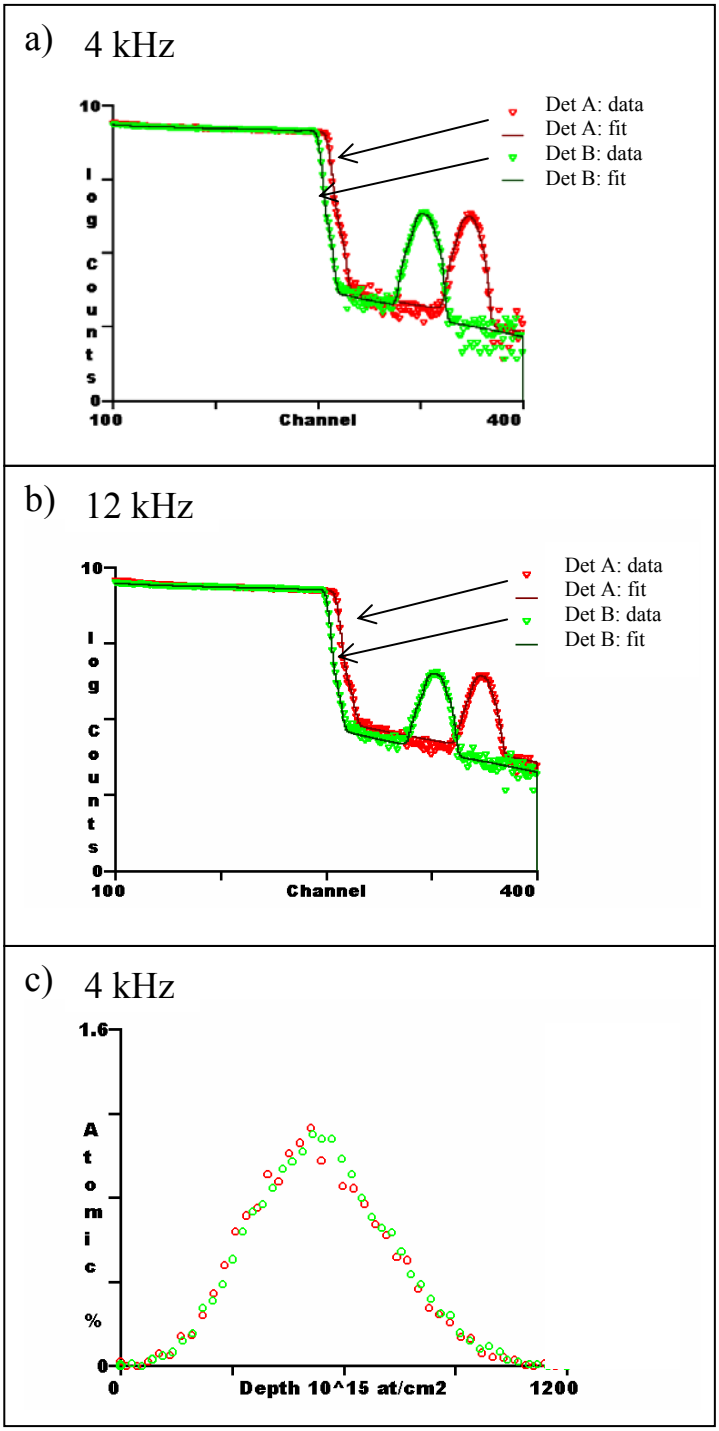

Figure 4-3 *As10 RBS spectra for count rates of a) 4kHz and b) 12kHz, together with c) the As profile calculated from the two detectors (both results are shown) by DataFurnace for the 4kHz spectra.*

To validate our simplified pileup calculation we have determined the dose in sample As10 at two different count rates, as shown in Table 4-5. Although detectors A and B have an approximate 1% systematic difference in this case, the difference

between the doses determined at these different count rates is only approximately 1%. Figure 4-3c shows the As profile calculated from the two detectors by DataFurnace for the 4 kHz spectra. Therefore we do really determine pile-up background to better than 10% with this simple model, as estimated in [Jey97].

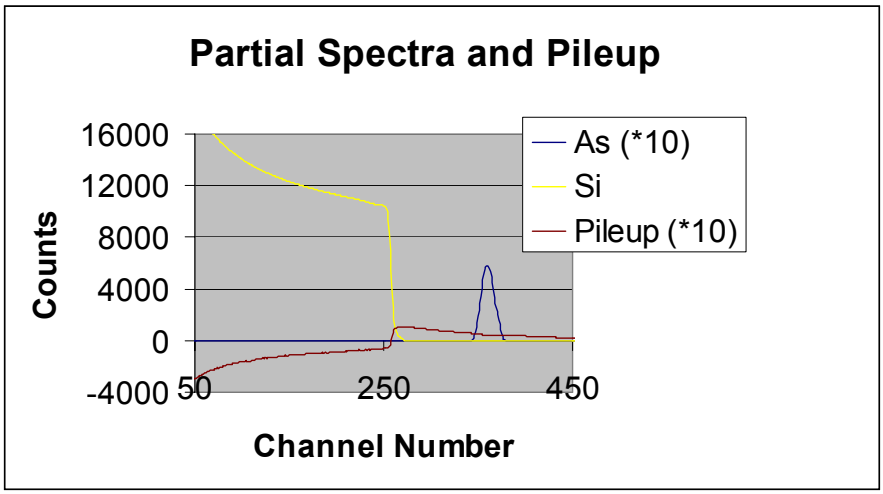

Figure 4-4 *Signals (As and Si) and pile-up background spectrum for 12 kHz count rate for sample As10 (DataFurnace analysis).*

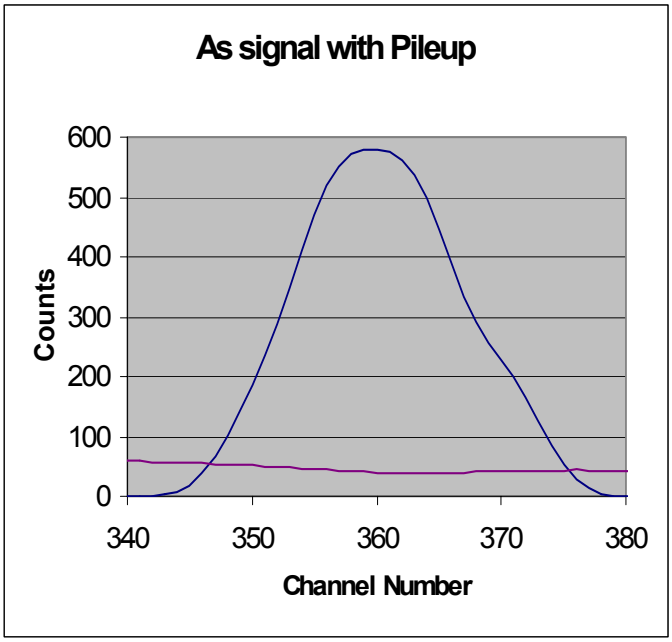

Figure 4-5 *As signal and pile-up background for 12 kHz count rate for sample As10 (from partial spectra in* Figure 4-4*): pile-up is about 15% of the signal and the non-linear distortion is about 10 % of the pile-up.*

In Table 4-6a and Table 4-6b are given the charge collected Q and the implant (In, As, Bi or Sb) peak integral A_{imp}, together with the values related to the pile-up calculation, that is, the weighting factor W, the sum of the counts in each channel c_T, the acquiring livetime t_{live} and the corresponding normalization factor w. Table 4-6a refers to detector A geometry, and Table 4-6b to detector B geometry (note that there is only one detector at Jena, i.e. for experiment v). As can be seen, as calculated using equation (2-18) (for Surrey multiplying by a factor $10/Q$ due to the way w has been calculated and normalized) we approximately found the estimated 1.2 μs/count value of the normalization factor w at Surrey (note the value of the weighting factor W is given so that the unit of the normalization factor w is μs). Jena data has not been treated manually due to files incompatibility with software used to handle data at the time of analysis; consequently, throughout the remainder of this chapter, any value specifically related to the transparent manual treatment will not be displayed for this experiment.

Table 4-5 *As dose in sample As10 with different pile-up backgrounds (different count rates) for 2 detectors simultaneously (DataFurnace analysis).*

Sample	*Count Rate (kHz)*	D_{imp} *Detector A* ($\times 10^{15}$ *at/cm*^{2})	D_{imp} *Detector B* ($\times 10^{15}$ *at/cm*^{2})
As10	~ 4	4.90	4.94
	~ 12	4.92	5.01

Table 4-6a *Charge collected* Q*, weighting factor* W *(for pile-up correction), implant (In, As, Bi or Sb) peak integral* A_{imp}*, sum of the counts* c_T *in each channel, acquiring livetime* t_{live} *and normalisation factor* w *(for pile-up correction) corresponding to detectorA geometry for each spectrum for each experiment. DetectorA geometry is:* θ = *166.9° at Surrey and 168.0° at Jena.*

		14	15	16	17	18	19
Experiment	*Spectrum*	*Q (μC)*	*W*	A_{imp} *(cts)*	c_T *(cts)*	t_{live} *(s)*	*w* $(x10^{-6}s)$
Surrey October 1999 (i)	In01o01	50.5231	50703	9925	8958842	1796.80	2.0
	In01o02	53.9865	42570	10385	9675384	2339.88	1.9
	In02o01	49.1634	49851	10205	8786432	1804.38	2.1
	In02o02	53.8102	39070	11280	9757418	2559.54	1.9
	In03o01<--	49.8161	47209	10173	8810338	1818.42	2.0
	In03o02<--	52.7776	35838	10640	9438086	2625.80	1.9
Surrey November 1999 (ii)	As05o01	84.1505	116919	6720	15971851	2148.54	1.9
	As06o01<--	48.7467	64911	15253	9176481	1254.70	1.8
	As07o01	50.7141	71106	12006	9748579	1390.58	2.0
	As08o01	96.7624	120416	7695	18442070	2664.08	1.8
	As09o01	62.8786	39206	15851	8479317	1770.36	1.3
Surrey June 2000 (iii)	In03y01*	60.4774	55392	12336	9917111	1798.20	1.7
	In03y02*	54.3214	39776	11297	8137436	1661.70	1.5
	As06y01	38.0810	35841	12024	6431424	1180.26	1.7
	As07y01	55.2155	38339	12713	7667538	1581.08	1.4
	As10y01*	29.7893	25371	13516	4539653	851.98	1.6
	As10y02*	19.6617	15234	9070	3014292	602.96	1.5
	As10y03*	19.5995	15487	9111	2969570	550.62	1.5
	As10y04*	19.6081	19573	8762	2952906	478.62	1.6
	As10y05*~	32.0425	20739	14831	4911216	1153.16	1.5
	Bi11y01*	11.1897	12608	27588	1859940	322.84	2.0
	Bi11y02*	19.3939	21333	48148	3210849	580.22	2.0
	Bi11y03*	14.1450	19016	34996	2324194	340.40	2.0
	Bi11y04*	11.9478	16052	29657	1969110	308.58	2.1
	Sb12y01~	5.8354	5497	60788	974517	230.20	2.2
Surrey August 2000 (iv)	As10L01*	11.3820	9302	5532	2052221	443.32	1.8
	As10L02*	13.7505	11619	6692	2403797	542.18	1.9
	As10L03*	8.5521	6015	4134	1503702	396.18	1.9
	As10L04*	8.7842	7161	4181	1540105	378.46	2.0
	As10L05*	11.8699	10200	5495	2141244	505.56	2.0
	Bi11L01	7.9343	4591	20368	868377	282.20	1.9
	Bi11L02	7.5947	7513	19291	1440969	329.94	2.3
	Bi11L03	8.5140	7448	21910	1624692	424.56	2.3
	Sb12L01	4.5751	4198	48441	799037	186.94	2.1
Jena October 2000 (v)	In03J01*	24.6656					
	In03J02*	24.6237					
	In03J03*	49.4701					
	As10J01*	14.1729					
	As10J02*	24.5004			N/A		
	As10J03*	24.4779					
	Bi11J01*	24.2696					
	Bi11J02*	14.6486					
	Sb12J01	24.5802					
	Sb12J02	24.5889					

In principle, col19=(col15·col18)/col17 as stated by equation (2-18); but the way the weighting factor W *has been calculated and normalized at Surrey, we must multiply by 10/*Q, Q *being col14, in order to obtain the normalization factor* w. *Moreover, the value of the weighting factor* W *is given so that the unit of the normalization factor* w *is μs.*

Table 4-6b *AsTable 4-6a, but for detector B geometry. Detector B geometry is* θ = *133.1° at Surrey. Note that there is no detector B geometry for the Jena experiment* (v).

		14	15	16	17	18	19
Experiment	*Spectrum*	*Q* (μC)	*W*	A_{imp} (cts)	c_T (cts)	t_{live} (s)	*w* ($x10^{-6}s$)
Surrey October 1999 (i)	In01o01	50.4084	55282	11585	9284834	1792.72	2.1
	In01o02	54.0659	48911	12177	9868879	2343.32	2.1
	In02o01	49.0429	52178	11830	9206624	1799.96	2.1
	In02o02	53.8728	41709	12911	10070823	2562.52	2.0
	In03o01<--	49.6666	55169	11716	9244313	1812.96	2.2
	In03o02<--	52.8327	40863	12494	9781010	2628.54	2.1
Surrey November 1999 (ii)	As05o01	84.6409	120599	7935	15895793	2161.06	1.9
	As06o01<--	49.0621	69069	17547	9113611	1262.82	2.0
	As07o01	51.0357	74363	13956	9765131	1399.40	2.1
	As08o01	97.2883	127878	8947	18419855	2678.56	1.9
	As09o01	63.4867	37644	18241	8312182	1787.48	1.3
Surrey June 2000 (iii)	In03y01*	61.0283	50009	14606	9815263	1814.58	1.5
	In03y02*	54.8883	36979	13006	8027187	1679.04	1.4
	As06y01	38.4617	30214	14134	6327010	1192.06	1.5
	As07y01	55.9287	32988	15174	7381615	1601.50	1.3
	As10y01*	30.0879	23529	15615	4477615	860.52	1.5
	As10y02*	19.8417	14589	10509	2978242	608.48	1.5
	As10y03*	19.8551	14509	10447	2908771	557.80	1.4
	As10y04*	19.7630	17132	10506	2886859	448.40	1.3
	As10y05*~	32.3737	19268	17165	4801092	1165.08	1.4
	Bi11y01*	11.2279	11148	32208	1818796	323.94	1.8
	Bi11y02*	19.6499	17597	56557	3178442	587.88	1.7
	Bi11y03*	14.2871	15270	40773	2270621	343.82	1.6
	Bi11y04*	12.0500	13016	34406	1921732	311.22	1.7
	Sb12y01~	5.8739	3966	70460	954788	231.72	1.6
Surrey August 2000 (iv)	As10L01*	11.4641	10399	6049	1932823	446.52	2.1
	As10L02*	13.9027	12219	7519	2333231	548.18	2.1
	As10L03*	8.6178	5439	4705	1456822	399.22	1.7
	As10L04*	8.8431	6972	4839	1499638	381.00	2.0
	As10L05*	11.9634	9910	6404	2051278	509.54	2.1
	Bi11L01	8.0883	5340	22856	829270	287.68	2.3
	Bi11L02	7.7108	7233	22159	1362908	334.98	2.3
	Bi11L03	8.6624	7751	25136	1542577	431.96	2.5
	Sb12L01	4.6084	4027	55522	783537	188.30	2.1

4.5.2 Values of energies, stopping powers and Rutherford cross-sections

In order to determine the dose using the manual data reduction method described further above, we need to determine first some quantities from the spectra. We will display here all these intermediary data, so that double-checking of the final results can be done.

4.5.2.1 Common values of energies and stopping powers

In this section we just display and comment about the values that are required and are common to any sample or any spectrum for a given geometry. They are the energy values E_0, E_a, E_b, E_c and E_l (as illustrated in Figure 4-1). For some of them, we also need either their corresponding stopping power or stopping cross-section values.

In Table 4-7 are presented the values for the energies E_0, E_a and E_l, the stopping powers $\varepsilon(E_0)$, $\varepsilon(E_a)$ and $\varepsilon(E_l)$ and the stopping cross-section factors $[\varepsilon(E_0)]$ corresponding to both A and B detectors at Surrey and A detector at Jena. Stopping powers and stopping cross-section factors were evaluated in a Si matrix (in a good approximation the samples can be considered as a Si matrix exclusively as far as energy loss is concerned, since the ions implanted inside account for an extremely low percentage of the total number of atoms) using the program SSTOP, which refers to values as reported on in TRIM-95. Note also that all the values displayed in Table 4-7 are, for a given geometry and beam energy, independent of the different experiments (they do not depend on the electronics calibration).

Table 4-7 *Energies* E_0, E_a *and* E_l *(see Figure 4-1), stopping powers* $\varepsilon(E_0)$, $\varepsilon(E_a)$ *and* $\varepsilon(E_l)$ *and stopping cross-section factors* $[\varepsilon(E_0)]$ *corresponding to both A and B detectors at Surrey and A detector at Jena. Stopping powers and stopping cross-section factors are evaluated in a Si matrix using the program SSTOP that refers to values as reported on in TRIM-95.*

Table 4-7a

	20 E_0 (keV)	21 $\varepsilon(E_0)$ (eV/(10^{15} at/cm^2))	22 $[\varepsilon(E_0)]$ (eV/(10^{15} at/cm^2))	23 E_a (keV)	24 $\varepsilon(E_a)$ (eV/(10^{15} at/cm^2))
Su-A det (θ=166.9°)	1490.4	55.10	98.50	845.8	65.48
Su-B det (θ=133.1°)	1490.4	55.10	127.90	919.1	64.18
Je-A det (θ=168.0°)	1528.0	N/A			

Table 4-7b

	25a E_1 (keV) (In)	25b E_1 (keV) (As)	25c E_1 (keV) (Bi)	25d E_1 (keV) (Sb)	26a $\varepsilon(E_1)$ (eV/(10^{15} at/cm^2)) (In)	26b $\varepsilon(E_1)$ (eV/(10^{15} at/cm^2)) (As)	26c $\varepsilon(E_1)$ (eV/(10^{15} at/cm^2)) (Bi)	26d $\varepsilon(E_1)$ (eV/(10^{15} at/cm^2)) (Sb)
Su-A det (θ=166.9°)	1298.7	1206.7	1381.8	1308.9	57.93	59.36	56.68	57.77
Su-B det (θ=133.1°)	1325.3	1244.8	1397.3	1334.2	57.52	58.76	56.45	57.39
Je-A det (θ=168.0°)	N/A							

a, b, c and d refers to In, As, Bi and Sb data, respectively. Su-A, Su-B and Je-A stand for Surrey A and B and Jena A detectors respectively. Col23 = col4·col20 and col25 = col5·col20 as stated by equation (4-1) (substituting subscripts l *and* In, As, Bi *or* Sb *to subscripts* a *and* Si *for col25).*

For a given geometry and beam energy, the values given in Table 4-8 depends upon the experiment (electronics calibration) and are related to the determination of the Si surface signal, and this is reliable only for amorphized

samples as explained in section 4.3.2. Thus only samples from experiments *iii*, *iv* and *v* were worked out for that purpose (experiments *i* and *ii* will be treated further below in section 4.5.5). These values are: α_{Si} (for a scattering event occurring from a Si atom in a slab Δx_b), energies E_c and E_b, stopping powers $\varepsilon(E_c)$ and $\varepsilon(K_{Si}E_b)$ and stopping cross-section factors $[\varepsilon(E_b)]$. Again we refer the reader to Figure 4-1 for the visualisation of these values. Stopping powers and stopping cross-section factors are also evaluated in a Si matrix using the program SSTOP that refers to values as reported on in TRIM-95.

Table 4-8 α_{Si} *(for a scattering event occurring from a Si ion in a slab* Δx_b*), energies* E_c *and* E_b *(see Figure 4-1), stopping powers* $\varepsilon(E_c)$ *and* $\varepsilon(K_{Si}E_b)$ *and stopping cross-section factors* $[\varepsilon(E_b)]$ *corresponding to both A and B detector geometry for experiments* iii, iv *and* v *where amorphised samples were available. Note that there is no B detector geometry for the Jena experiment (*v*). Stopping powers and stopping cross-section factors are evaluated in a Si matrix using the program SSTOP that refers to values as reported on in TRIM-95.*

		27	28	29	30	31	32	33
Experiment	*Detector geometry*	α_{Si}	E_c *(ch)*	E_c *(keV)*	$\varepsilon(E_c)$ *(eV/(10^{15} at/cm^2))*	E_b *(keV)*	$\varepsilon(K_{Si}E_b)$ *(eV/(10^{15} at/cm^2))*	$[\varepsilon(E_b)]$ *(eV/(10^{15} at/cm^2))*
Surrey June 2000 (iii)	A (θ=166.9°)	1.220	170	676.0	68.54	1395.4	66.45	100.3
	B (θ=133.1°)	1.705	170	775.9	66.74	1428.7	64.85	129.4
Surrey August 2000 (iv)	A (θ=166.9°)	1.220	215	679.8	68.47	1397.6	66.43	100.2
	B (θ=133.1°)	1.705	250	753.3	67.15	1419.0	64.96	129.7
Jena October 2000 (v)	A (θ=168.0°)	N/A						

Col27 = col24 / (col21·cos(π-θ)) as stated by equation (4-3). Col29 = (col28·col1) + col2, which comes from the electronics calibration. Col31 = (col29 + col27·col20) / (col4 + col27) as stated by equation (4-2).

4.5.2.2 Values of the averaged Rutherford cross-section for the implants

To determine the implant dose we need to determine the Rutherford scattering cross-section for the interaction of the incident He ions with the implanted atoms. As mentioned, this should not be evaluated at the incident beam energy E_0 since the implant is buried and the averaged interaction energy E_m is significantly

less than E_0. For most of our samples E_m is around 2% lower than E_0; this implies a correction of the order of 5% since the Rutherford cross-section varies as $1/E^2$.

Table 4-9a α_{imp} *(for a scattering event occurring from an In, As, Bi or Sb ion implant in a slab* Δx_m*), energies* E_n *and* E_m *(see Figure 4-1), the screening correction* $F(E_m)$ *(as reported on by Tesmer and Nastasi [Tes95{x}]) and the implant (In, As, Bi or Sb) Rutherford cross-section* $\sigma(E_m,\theta)$ *corresponding to detector A geometry for each spectrum for each experiment.*

Experiment	Spectrum	39 α_{imp}	40 E_n (ch)	41 E_n (keV)	42 E_m (keV)	43 $F(E_m)$	44 $\sigma(E_m,\theta)$ ($\times 10^{-27}$ cm^2/msr)
Surrey October 1999 (i)	In01o01	1.079	397	1255.8	1468.4	0.988	5.910
	In01o02	1.079	397	1255.8	1468.4	0.988	5.910
	In02o01	1.079	397	1255.8	1468.4	0.988	5.910
	In02o02	1.079	397	1255.8	1468.4	0.988	5.910
	In03o01<--	1.079	397	1255.8	1468.4	0.988	5.910
	In03o02<--	1.079	397	1255.8	1468.4	0.988	5.910
Surrey November 1999 (ii)	As05o01	1.106	380	1207.0	1490.5	0.993	2.593
	As06o01<--	1.106	373	1185.8	1479.5	0.993	2.632
	As07o01	1.106	380	1207.0	1490.5	0.993	2.593
	As08o01	1.106	379	1204.0	1488.9	0.993	2.599
	As09o01	1.106	380	1207.0	1490.5	0.993	2.593
Surrey June 2000 (iii)	In03y01*	1.079	326	1259.6	1470.3	0.988	5.886
	In03y02*	1.079	326	1259.6	1470.3	0.988	5.886
	As06y01	1.106	305	1181.0	1477.0	0.993	2.637
	As07y01	1.106	311	1203.5	1488.7	0.993	2.596
	As10y01*	1.106	298	1154.8	1463.3	0.993	2.687
	As10y02*	1.106	298	1154.8	1463.3	0.993	2.687
	As10y03*	1.106	298	1154.8	1463.3	0.993	2.687
	As10y04*	1.106	298	1154.8	1463.3	0.993	2.687
	As10y05*~	1.106	298	1154.8	1463.3	0.993	2.687
	Bi11y01*	1.056	356	1371.8	1485.3	0.976	16.576
	Bi11y02*	1.056	356	1371.8	1485.3	0.976	16.576
	Bi11y03*	1.056	356	1371.8	1485.3	0.976	16.576
	Bi11y04*	1.056	356	1371.8	1485.3	0.976	16.576
	Sb12y01~	1.077	315	1218.4	1444.1	0.988	6.612
Surrey August 2000 (iv)	As10L01*	1.106	380	1159.7	1465.9	0.993	2.681
	As10L02*	1.106	380	1159.7	1465.9	0.993	2.681
	As10L03*	1.106	380	1159.7	1465.9	0.993	2.681
	As10L04*	1.106	380	1159.7	1465.9	0.993	2.681
	As10L05*	1.106	380	1159.7	1465.9	0.993	2.681
	Bi11L01	1.056	453	1372.1	1485.5	0.976	16.597
	Bi11L02	1.056	453	1372.1	1485.5	0.976	16.597
	Bi11L03	1.056	453	1372.1	1485.5	0.976	16.597
	Sb12L01	1.077	401	1220.8	1445.3	0.988	6.610
Jena October 2000 (v)	N/A						

Col39 = col26 / (col21·cos(π-θ)) as stated by equation (4-3) (substituting subscripts l *and I*n, As, Bi *or* Sb *to subscripts* a *and* Si*). Col41 = col40·col1 + col2, which comes from the electronics calibration. Col42 = (col41 + col39·col20) / (col5 + col39) as stated by equation (4-2) (substituting subscripts* m*,* n *and* In, As, Bi *or* Sb *to subscripts* b*,* c *and* Si*). Col44 = (col9·col10 / 2·col42)^2·col12·col13 as stated by equation (2-7) (or equation (4-6)). Erratum: for experiment* iii*, the value* 2.07×10^{-23} *was used instead of* 2.073×10^{-23} *(col12).*

Table 4-9*b* *As Table 4-9a, but for detector B geometry. Note that there is no detector B geometry for the Jena experiment (*v*).*

Experiment	*Spectrum*	39 α_{imp}	40 E_n *(ch)*	41 E_n *(keV)*	42 E_m *(keV)*	43 $F(E_m)$	44 $\sigma(E_m,\theta)$ $(\times 10^{-27}$ $cm^2/msr)$
Surrey October 1999 (i)	In01o01	1.528	398	1273.0	1468.8	0.988	8.129
	In01o02	1.528	398	1273.0	1468.8	0.988	8.129
	In02o01	1.528	398	1273.0	1468.8	0.988	8.129
	In02o02	1.528	398	1273.0	1468.8	0.988	8.129
	In03o01<--	1.528	398	1273.0	1468.8	0.988	8.129
	In03o02<--	1.528	398	1273.0	1468.8	0.988	8.129
Surrey November 1999 (ii)	As05o01	1.561	386	1245.9	1490.9	0.993	3.570
	As06o01<--	1.561	377	1218.2	1479.3	0.993	3.626
	As07o01	1.561	386	1245.9	1490.9	0.993	3.570
	As08o01	1.561	385	1242.9	1489.6	0.993	3.576
	As09o01	1.561	386	1245.9	1490.9	0.993	3.570
Surrey June 2000 (iii)	In03y01*	1.528	283	1271.5	1468.1	0.988	8.124
	In03y02*	1.528	283	1271.5	1468.1	0.988	8.124
	As06y01	1.561	270	1214.5	1477.7	0.993	3.629
	As07y01	1.561	276	1240.8	1488.7	0.993	3.575
	As10y01*	1.561	262	1179.4	1463.1	0.993	3.702
	As10y02*	1.561	262	1179.4	1463.1	0.993	3.702
	As10y03*	1.561	262	1179.4	1463.1	0.993	3.702
	As10y04*	1.561	262	1179.4	1463.1	0.993	3.702
	As10y05*~	1.561	262	1179.4	1463.1	0.993	3.702
	Bi11y01*	1.499	309	1385.5	1485.6	0.976	22.793
	Bi11y02*	1.499	309	1385.5	1485.6	0.976	22.793
	Bi11y03*	1.499	309	1385.5	1485.6	0.976	22.793
	Bi11y04*	1.499	309	1385.5	1485.6	0.976	22.793
	Sb12y01~	1.524	271	1218.9	1442.7	0.988	9.115
Surrey August 2000 (iv)	As10L01*	1.561	403	1189.9	1467.5	0.993	3.685
	As10L02*	1.561	403	1189.9	1467.5	0.993	3.685
	As10L03*	1.561	403	1189.9	1467.5	0.993	3.685
	As10L04*	1.561	403	1189.9	1467.5	0.993	3.685
	As10L05*	1.561	403	1189.9	1467.5	0.993	3.685
	Bi11L01	1.499	467	1372.6	1480.3	0.976	22.990
	Bi11L02	1.499	467	1372.6	1480.3	0.976	22.990
	Bi11L03	1.499	467	1372.6	1480.3	0.976	22.990
	Sb12L01	1.524	417	1229.9	1447.3	0.988	9.071

The values we need to determine here are: α_{imp} (for a scattering event occurring from an In, As, Bi or Sb ion implant in a slab Δx_m) as calculated using equation (4-3) (substituting subscripts *l* and *In, As, Bi* or *Sb* to subscripts *a* and *Si*); energies E_n, and E_m as calculated using equation (4-2) (substituting subscripts *m*, *n* and *In, As, Bi* or *Sb* to subscripts *b*, *c* and *Si*); the screening correction $F(E_m)$, as given by Tesmer and Nastasi [Tes95{x}]; and finally the implant (In, As, Bi or Sb) Rutherford cross-section $\sigma(E_m,\theta)$ as calculated using equation (2-7) (or equation (4-6)). Again we refer the reader to Figure 4-1 for the schematic. These values are tabulated in Table 4-9a and Table 4-9b for the detector A and B geometries respectively (we recall that there is only one detector at Jena).

4.5.3 Solid angle and charge collection (experiments *iii*, *iv* and *v*)

In Table 4-10 are shown the solid angle values as calculated from the appropriate absolute Si surface energy-loss factor calibration M_{si}, which is defined by equation (2.17). This has been done for each spectrum from experiments *iii*, *iv* and *v* (where amorphized samples were available), assuming that the collected charge is accurate in each individual case (experiments *i* and *ii* analysis is given in section 4.5.5). Prior to the solid angle calculation, we had to determine Y_b (the Si yield evaluated at the channel specified in Table 4-8, col28), which we normalized and became $Y_{b(norm)}$ (charge Q normalized to Q_{Norm} as specified in Table 4-4b, col11), and then we derived $Y_{0(norm)}$ (normalized Si surface yield) using equation (4-4).

Note that this procedure is equivalent to normalising the charge·solid angle product to the amorphised Si yield using the absolutely determined Si energy-loss values as a standard. Since the solid angle is a constant of the apparatus and the charge·solid angle product is what is actually being determined, the apparent variation in the solid angle in Table 4-10 is really a variation in the collected charge. In a word, Table 4-10 represents a measurement of the charge collection repeatibility via the *fluctuations* of the solid angle values, which is as good as approximately 1.4% (standard deviation) for Surrey. But, since about 0.8 % of these fluctuations is due to counting statistics (on average, we have approximately nearly 15 000 counts in the yield Y_0 as can be seen in col34 in Table 4-10), the charge collection appears to be as good as 1.1%.

If one has a closer look at the results shown in Table 4-10, it can be noticed that the solid angle values obtained for detector A for experiments *iii* and *iv* are 5.180 and 5.431 msr, respectively, which is an appreciable discrepancy of ~5%. The most plausible explanation for this is the following. It was somewhat hard to insert the detector A into the socket, and it has been noticed sometimes that experiments would be carried out whilst the detector A was not plugged in completely. When this is the case, the detector and the sample are roughly 2 or 3 mm closer to each other than when the detector is fully inserted into the socket. From the details on the RBS target chamber as given in Figure 3-7 and Table 3-1 in section 3.1.2.2, it is easy to calculate

that such a mishandling can lead to a difference of approximately 5% in the solid angle value.

Table 4-10 *Si yield* Y_b *(evaluated at channel specified in Table 4-8, col28), ratio* Q_{Norm}/Q*, normalized (integrated charge* Q *normalized to* Q_{Norm} *as specified in Table 4-4b, col11), Si yield* $Y_{b(Norm)}$*, surface normalized Si yield* $Y_{0(Norm)}$ *(calculated from equation (4-4)) and solid angle* Ω *corresponding to both A and B detector geometries for each spectrum from amorphised samples for experiments* iii*,* iv *and* v*. Note that there is no detector B geometry for the Jena experiment (*v*).*

			34	35	36	37	38
Experiment	*Detector geometry*	*Spectrum*	Y_b *(cts)*	Q_{Norm}/Q	$Y_{b\,(Norm)}$ *(cts)*	$Y_{o\,(Norm)}$ *(cts)*	Ω *(msr)*
Surrey June 2000 (iii)	A (θ=166.9°)	In03y01*	37543	0.8268	31039	28571	5.228
		In03y02*	33564	0.9204	30894	28438	5.204
		As10y01*	18691	1.6785	31372	28878	5.284
		As10y02*	11975	2.5430	30453	28032	5.129
		As10y03*	11967	2.5511	30529	28102	5.142
		As10y04*	12011	2.5500	30628	28193	5.159
		As10y05*~	19898	1.5604	31049	28581	5.230
		Bi11y01*	6917	4.4684	30908	28451	5.206
		Bi11y02*	12032	2.5781	31020	28554	5.225
		Bi11y03*	8615	3.5348	30452	28032	5.129
		Bi11y04*	7154	4.1849	29939	27559	5.043
						mean	5.180
						std.dev.	0.067 (1.29%)
	B (θ=133.1°)	In03y01*	39555	0.8193	32407	31016	4.522
		In03y02*	35184	0.9109	32051	30675	4.472
		As10y01*	19088	1.6618	31720	30359	4.426
		As10y02*	12721	2.5199	32056	30680	4.473
		As10y03*	12702	2.5182	31987	30614	4.463
		As10y04*	12414	2.5300	31407	30059	4.382
		As10y05*~	20463	1.5445	31604	30248	4.410
		Bi11y01*	7176	4.4532	31956	30585	4.459
		Bi11y02*	12315	2.5445	31336	29991	4.372
		Bi11y03*	8947	3.4997	31311	29968	4.369
		Bi11y04*	7453	4.1494	30925	29598	4.315
						mean	4.424
						std.dev.	0.060 (1.37%)
Surrey August 2000 (iv)	A (θ=166.9°)	As10L01*	5600	4.3929	24600	22690	5.340
		As10L02*	6879	3.6362	25014	23072	5.430
		As10L03*	4356	5.8465	25467	23490	5.529
		As10L04*	4447	5.6920	25313	23347	5.495
		As10L05*	5865	4.2123	24705	22787	5.363
						mean	5.431
						std.dev.	0.081 (1.50%)
	B (θ=133.1°)	As10L01*	4732	4.3614	20638	19608	4.393
		As10L02*	5806	3.5964	20881	19839	4.444
		As10L03*	3668	5.8020	21282	20219	4.530
		As10L04*	3620	5.6541	20468	19446	4.356
		As10L05*	4992	4.1794	20864	19822	4.441
						mean	4.433
						std.dev.	0.065 (1.47%)
Jena October 2000 (v)	A (θ=168°)	N/A					

Col35 = col11/col14 and Col36 = col34·col35 (charge normalisation). Col37 = col36·(col31/col20)^2*·(col33/col22)·(col30/col32) as stated by equation (4-4). Col38 = col37/col1·col3·col14 as stated by equation (2-17).*

4.5.4 Doses (experiments *iii*, *iv* and *v*)

In this section, we present the final results, that is, the doses obtained, as given by the manual data reduction method from each spectrum for experiments *iii*, *iv* and *v* where amorphised samples were available. The doses were calculated using equation (4-5) along with the required intermediate values used from the previous tables. Note that only mean values of Ω as an internal normalisation are used from col38 in Table 4-10; this can give an uncertainty as small as 0.4% (as given by the standard deviation of the arithmetic mean) for the $Q\Omega$ product, that is, for the charge integration.

Table 4-11 *Implant doses* D_{imp} *from both A and B detector geometries and their ratio determined for each spectrum for experiments* iii, iv *and* v. *Detector A geometry is:* $\theta = 166.9°$ *at Surrey and* $168.0°$ *at Jena. Detector B geometry is* $\theta = 133.1°$ *at Surrey. Note that there is no detector B geometry for the Jena experiment* (v).

		45	46	47
Experiment	*Spectrum*	D_{imp}*(A detector)* $(\times 10^{15}$ *at/cm*$^2)$	D_{imp}*(B detector)* $(\times 10^{15}$ *at/cm*$^2)$	*Ratio (A)/(B)*
Surrey June 2000 (iii)	In03y01*	1.05 ■	1.04 ■	1.015
	In03y02*	1.08 ■	1.05 ■	1.031
	As06y01	3.64 ●	3.60 ●	1.014
	As07y01	2.74	2.74	1.002
	As10y01*	5.18	5.04	1.028
	As10y02*	5.27	5.13	1.027
	As10y03*	5.20	5.09	1.020
	As10y04*	5.12	5.14	0.996
	As10y05*~	5.28	5.16	1.024
	Bi11y01*	4.69	4.65	1.009
	Bi11y02*	4.72	4.67	1.012
	Bi11y03*	4.70	4.61	1.019
	Bi11y04*	4.71	4.61	1.023
	Sb12y01~	49.2	48.2	1.021
			mean	1.017
			std.dev.	0.010 (0.99%)
Surrey August 2000 (iv)	As10L01*	5.30	5.21	1.016
	As10L02*	5.34	5.35	0.999
	As10L03*	5.31	5.33	0.997
	As10L04*	5.23	5.39	0.972
	As10L05*	5.10	5.28	0.964
	Bi11L01	4.61	4.52	1.021
	Bi11L02	4.57	4.61	0.991
	Bi11L03	4.64	4.65	0.996
	Sb12L01	47.7	48.5	0.982
			mean	0.993
			std.dev.	0.018 (1.86%)
Jena October 2000 (v)	N/A			

Col45-46 = col16 / (col38·col6·col14·col43·col44) as stated by equation (4-5) (note that only mean values of Ω *from col38 are used). Col47 = col45 / col46. Further below, are averaged the doses obtained for In03 sample (marked ■) and doses for As06 sample (marked ●), and these mean values are used to relatively-determine the solid angle for both A and B detector geometries for experiments* i *and* ii *(for which no amorphised samples were available).*

Table 4-11 shows all the doses determined independently for both detectors for experiments *iii*, *iv* and *v* (note that the manual analysis was not possible for experiment *v* at Jena due to software-handling incompatibility with the files). The ratio of the doses measured from the two detectors (which should ideally, of course, be unity) is also displayed. This highlights the value of using double detector data collection: internal consistency of data does increase confidence in the results. An A/B ratio of 1.017 and 0.993 is obtained for experiment *iii* and *iv*, respectively; this is within the uncertainties, as estimated in section 4.8. Note that anti-correlated errors in the electronics calibration of the two detectors (gain) can give apparently significant non-unity values for the A/B dose ratio. The standard deviation of this ratio is <2%; the precision of this ratio measurement is a consequence of the statistics collected and the fluctuations in the pile-up correction, and it is consistent with an estimated 1% combined uncertainty (on each individual dose) given by these two effects.

In the next section we will average the doses obtained for In03 sample (marked ■) and doses for As06 sample (marked ●), and these mean values will be used to relatively-determine the solid angle for both A and B detector geometries for the experiments *i* and *ii* (for which no amorphised samples were available).

4.5.5 Experiments *i* and *ii*: solid angles and doses

4.5.5.1 Solid angles

For experiments *i* and *ii*, we could not directly determine the solid angle presented by the detectors (no amorphised samples available). Therefore we have to determine the solid angle *relatively* using the doses obtained from the same samples *absolutely* analysed in later experiments.

We have calculated the average dose from the ones obtained in experiment *iii* for sample In03 (results marked ■ in Table 4-11) and also from the ones for sample As06 (results marked ● in Table 4-11). These average values can be seen in Table 4-12. Then they were used to relatively-determine the solid angle for both A and B detector geometries for the experiments *i* and *ii* by using equation (4-5). The results are also presented in Table 4-12. Note that these relative measurements of solid angle

are dependent on the uncertainty of charge collection (1.1%), statistics and pile-up fluctuations (1%)

.

Table 4-12 *Average implant doses* D_{imp} *for In03 and As06 samples obtained from doses (marked ■ for In03 and marked ● for As06 in Table 4-11) in experiments* iii, *and solid angle* Ω, *relatively determined from these averaged doses, for both A and B detector geometries for experiments* i *and* ii *(for which no amorphised samples were available). A and B detector geometries are* θ = *166.9° and 133.1° respectively (Surrey).*

	48				49	50
Sample	*Average D_{imp} (from exp. iii ■ and ● marked values, Table 4-11) ($x10^{15}$at/cm^2)*	*Experiment*	*Detector geometry*	*Spectrum*	*Ω (msr)*	*Mean Ω (msr)*
In03	1.06	i	A	In03o01<--	5.286	5.253
				In03o02<--	5.219	
			B	In03o01<--	4.439	4.445
				In03o02<--	4.451	
As06	3.62	ii	A	As06o01<--	5.299	5.299
			B	As06o01<--	4.396	4.396

Col49 = col16 / (col48·col6·col14·col43·col44) as stated by equation (4-5).

4.5.5.2 Doses

Using the solid angle values relatively determined in the previous section (Table 4-12) and following the same procedure as previously, we have calculated the doses from each spectrum for experiments *i* and *ii*. The results are presented in Table 4-13. Again there is consistency: the independent measurements from the two detectors agree with each others (mean ratios close to unity) at about 1%, and we see <2% variation (standard deviation) in this A/B ratio.

Table 4-13 *Implant doses* D_{imp} *from both A and B detector geometries and their ratios determined for each spectrum for experiments* i *and* ii*. A and B detector geometries are* θ *= 166.9° and 133.1° respectively (Surrey).*

		51	52	53
Experiment	*Spectrum*	D_{imp} *(A detector)* $(x10^{15}at/cm^2)$	D_{imp} *(B detector)* $(x10^{15}at/cm^2)$	*Ratio (A)/(B)*
Surrey October 1999 (i)	In01o01	1.02	1.02	0.994
	In01o02	0.99	1.01	0.985
	In02o01	1.08	1.07	1.013
	In02o02	1.08	1.06	1.018
	In03o01<--	1.06	1.06	1.001
	In03o02<--	1.04	1.05	0.989
			mean	1.000
			std.dev.	0.013 (1.31%)
Surrey November 1999 (ii)	As05o01	0.90	0.93	0.959
	As06o01<--	3.54	3.57	0.991
	As07o01	2.74	2.76	0.992
	As08o01	0.89	0.92	0.967
	As09o01	2.94	2.92	1.005
			mean	0.983
			std.dev.	0.019 (1.93%)

Col51-52 = col16 / (col50·col6·col14·col43·col44) as stated by equation (4-5). Col53 = col51 / col52.

4.6 Results from the machine method: comparison with manual results

So far, we have obtained the dose of all the implants from 4 different experiments by using the transparent manual data reduction method (data from experiment *v*, Jena, could not be handled manually), which is a long and tedious process (the only advantage being its transparency). We now want to use the IBA code DataFurnace to analyse the same spectra and compare the doses obtained with those from the manual treatment. Since in both cases the same algorithm (same forward model) and same databases (for Rutherford cross-sections and for He into Si stopping powers) are used, only small discrepancies should occur. The only differences ought to be that DataFurnace replaces the surface energy approximation to the stopping powers (and the energy-loss ratio method) with a proper integral approach, and the tails of the implant signal are accurately identified. The difference between manual and DataFurnace results should then be below the ½% level.

Table 4-14 shows a comparison of the results obtained using DataFurnace with those using the manual method for subset of the data (experiment *iii*). The ratio manual/machine is very close to unity with an uncertainty (standard deviation) of less than 0.5%. For the whole data set, we get a ratio of 1.000 with an uncertainty of

0.41 %. This identity therefore validates the correctness of the DataFurnace code. But it must be pointed out that this measurement is quite sensitive to the pile-up correction, therefore the consistency greatly depends upon the correctness of the determination of the background (although for us this was not a problem as we used DataFurnace to subtract the pile-up background from the spectra in both manual and machine methods). It is worth noting that results from DataFurnace are obtainable much more rapidly compared to those from the manual method.

Table 4-14 *Comparison between the dose obtained with the manual data reduction method and the machine method (DataFurnace). Results from exp.* iii *are displayed, together with general results when including all measurements from exp.* i, ii, iii *and* iv.

Detector	*Spectrum (experiment iii)*	*Manual* ($\times 10^{15}$ *at/cm^2*)	*DataFurnace* ($\times 10^{15}$ *at/cm^2*)	*Ratio*
A (θ=166.9°)	In03y01*	1.05	1.05	1.005
	In03y02*	1.08	1.08	1.002
	As06y01	3.64	3.64	1.001
	As07y01	2.74	2.74	1.001
	As10y01*	5.18	5.18	1.001
	As10y02*	5.27	5.26	1.002
	As10y03*	5.20	5.24	0.992
	As10y04*	5.12	5.11	1.001
	As10y05*~	5.28	5.27	1.002
	Bi11y01*	4.69	4.69	1.000
	Bi11y02*	4.72	4.71	1.003
	Bi11y03*	4.70	4.70	0.999
	Bi11y04*	4.71	4.72	0.998
	Sb12y01~	49.2	49.2	1.001
			mean	1.001
			std.dev.	0.003 (0.30%)
B (θ=133.1°)	In03y01*	1.04	1.04	0.999
	In03y02*	1.05	1.05	0.999
	As06y01	3.60	3.59	1.001
	As07y01	2.74	2.74	1.000
	As10y01*	5.04	5.04	1.000
	As10y02*	5.13	5.14	0.998
	As10y03*	5.09	5.10	0.999
	As10y04*	5.14	5.14	0.999
	As10y05*~	5.16	5.15	1.002
	Bi11y01*	4.65	4.64	1.002
	Bi11y02*	4.67	4.65	1.004
	Bi11y03*	4.61	4.61	1.000
	Bi11y04*	4.61	4.62	0.997
	Sb12y01~	48.2	47.3	1.019
			mean	1.002
			std.dev.	0.005 (0.54%)
Including all measurements from exp. i, ii, iii and iv			**mean**	1.000
			std.dev.	0.004 0.41%

The data from the Jena experiment (exp. *v*) could not be treated manually, but they have been analysed using DataFurnace. The results are shown in Table 4-15.

Table 4-15 *Implant doses* D_{imp} *from the only detector geometry (*θ *= 168.0°) for experiment v (Jena). DataFurnace analysis.*

Experiment	*Spectrum*	D_{imp}*(A detector)* $(\times 10^{15}$ *at/cm*^{2}*)*
Jena October 2000 (v)	In03J01*	1.12
	In03J02*	1.09
	In03J03*	1.12
	As10J01*	5.29
	As10J02*	5.30
	As10J03*	5.25
	Bi11J01*	4.63
	Bi11J02*	4.70
	Sb12J01	49.1
	Sb12J02	48.8

4.7 General results: time and space reproducibility

The experiments were carried out at different dates and in different laboratories. In this section we aim at rearranging the results in order to verify their time and space reproducibility, thereby the reliability of the dose measurement.

Firstly, we have calculated the mean dose values obtained for each sample for each experiment separately, and these are displayed in Table 4-16: col54 refers to experiments *i* and *ii* (they regrouped different samples, that is, only In samples for *i* and only As samples for *ii*), col55 to *iii*, col56 to *iv*, and col58 to *v*. We have also calculated the mean dose values (col57) for each sample for the whole set of measurements made in Surrey exclusively (exp. *i*, *ii*, *iii* and *iv*). We will need all these values to verify the time and space reproducibility further on. Note that col57 is, for a given sample, the weighted mean of col54, col55 and col56. It should be note that, for a given sample, different spectra were taken on different spots: therefore we will assume that the implantation was carried out uniformly over the whole sample in each case.

Table 4-16 *Mean implant dose for each sample for each experiment separately, and total mean dose for all the experiments carried out at Surrey (*i, ii, iii, iv*).*

Sample	54 mean D_{imp} Su-1999 **(i and ii)** ($x10^{15}$at/cm^2)	55 mean D_{imp} Su-June 2000 **(iii)** ($x10^{15}$at/cm^2)	56 mean D_{imp} Su-Aug 2000 **(iv)** ($x10^{15}$at/cm^2)	57 mean D_{imp} Surrey **(i, ii, iii, iv)** ($x10^{15}$at/cm^2)	58 mean D_{imp} Jena **(v)** ($x10^{15}$at/cm^2)
In01	1.01	—	—	1.01	—
In02	1.07	—	—	1.07	—
In03	1.05	1.06	—	1.05	1.11
As05	0.91	—	—	0.91	—
As06	3.55	3.62	—	3.58	—
As07	2.75	2.74	—	2.75	—
As08	0.91	—	—	0.91	—
As09	2.93	—	—	2.93	—
As10	—	5.16	5.29	5.23	5.28
Bi11	—	4.67	4.60	4.64	4.67
Sb12	—	48.3	48.2	48.2	49.0

Note that col57 is, for a given sample, the weighted mean of col54, col55 and col56.

Table 4-17 summarises the overall results, showing the variation with time and with space, and showing the mean values for the whole data set. The values displayed in col59 are the (*i*,*ii*)/*iii* dose ratios (col54/col55) and *iii*/*iv* dose ratios (col55/col56), and those in col60 are the Surrey/Jena dose ratios (col57/col58). Then the first important result is that the data is consistent: the time and space ratios (col59 and col60) are respectively 0.995 ± 0.015 and 0.978 ± 0.022, with standard deviations around 2%, in agreement with the estimated uncertainties as presented in section 4.8.

In col61 in Table 4-17 are listed the overall mean implant doses, that is, combining all the results from all the experiments carried out both at Surrey and Jena (exp. *i*, *ii*, *iii*, *iv* and *v*). It should be noted that col61 is, given a sample, the weighted mean of col57 and col58. The dose discrepancies, or errors, from nominal doses for each sample have been calculated (col63). Then the second important result is that the measured doses of the standard samples are consistent with the certified values: the measured Bi and Sb implant doses are respectively only 1.70% and 0.83% (relative error) different from the certified values, which indicates that the parameterisation of the Si energy-loss function is *correct* to within the uncertainties as evaluated in the following section. The results for the samples implanted exclusively at Surrey can be considered as a guidance for quality assurance.

Table 4-17 *Time and space reproducibility of the results, together with the discrepancies (errors) from the nominal doses. Faint highlighted results refer to the certified Bi and Sb samples.*

time reproducibility ↓ space reproducibility ↓

	59	60	61	62	63
sample	*mean D_{imp} ratio:* (i,ii)/iii / iii/iv (Surrey)	*mean D_{imp} ratio: Surrey/Jena*	*overall mean D_{imp} (Surrey+ Jena) ($\times 10^{15}$at/cm^2)*	*nominal dose ($\times 10^{15}$at/cm^2)*	*discrepancy (or error) from nominal dose (%)*
In01	—	—	1.01 {1.19}	1	1.00
In02	—	—	1.07 {0.89}	1	7.00
In03	0.991	0.946	1.07 {2.73}	1	7.00
As05	—	—	0.91 {2.93}	1	-9.00
As06	0.981	—	3.58 {1.23}	4	-10.50
As07	1.004	—	2.75 {0.42}	3	-8.33
As08	—	—	0.91 {2.40}	1	-9.00
As09	—	—	2.93 {0.33}	3	-2.33
As10	0.975	0.991	5.23 {1.86}	5	4.60
Bi11	1.015	0.994	4.64 {1.15}	**4.72(10)**	**-1.70**
Sb12	1.002	0.984	48.5 {1.61}	**48.1(3)**	**0.83**
mean	0.995	0.978			
Std.dev.	0.015 (1.51%)	0.022 2.25%			

Note that col61 is, for a given sample, the weighted mean of col57 and col58. Col59 = col54-55/col55-56. Col60 = col57/col58. Col62 repeats the nominal dose values given much further above in Table 4-1. Col63 = ((col61 – col62)/col62)·100.
Numbers in {} represent the uncertainty (standard deviation) of the repeated measurements of the sample in %..
Numbers in () are the uncertainties in the last figures.

4.8 Uncertainties

For clarity we have collected the estimated uncertainties (u) in Table 4-18. The estimated combined uncertainty (u_c) is 1¼%. If, with a longer analysis and more accurate pile-up correction, the uncertainties due to the pile-up and the counting statistics can be reduced then the precision available could be improved to

~0.9 %. If the electronics calibration can be improved to ¼% (not shown in the table), the available precision is reduced to just under 0.8%. The estimate of 1¼% combined uncertainty is validated by the spatial and temporal total variation of less around 2.0% shown in Table 4-17 (ratio uncertainties have to be summed in quadrature).

Table 4-18 *Uncertainty budget.*

CURRENTLY			FEASIBLE	
Effect	**Uncertainty (u) [%]**	**Comments**	**Uncertainty (u) [%]**	**How?**
Charge-solid angle product	**0.4**	Internal normalisation	**0.35**	Improve counting statistics
Rutherford cross section Screening correction	**0.25**	For Sb implanted certified sample	**0.25**	
Beam energy	**0.12**	0.06 % error from calibration, and E^{-2} dependence of σ	**0.12**	
Scattering angle	**0.3**	½° error, and $\approx (\sin\theta/2)^{-4}$ dependence of σ	**0.3**	
Electronics calibration	**0.5**		**0.5**	
Counting statistics	**0.7**	Sum of 2 detectors at 1 % each	**0.35**	Longer acquisition time
Pileup background	**0.7**	Estimated at 10 % of pileup for As signal and 4 kHz counting rate	**0.35**	1) better time resolution 2) lower counting rate
Total (u_c)	**1.25**		**0.89**	

4.9 Prospective

From the dose measurement method developed together with the DataFurnace analysis carried out in this work, it turns out that the new He into Si energy-loss values (Bianconi *et al.*'s data re-analysed by Barradas *et al.* [Bar02]) appear to be *reliable*. The absolute accuracy is determined from the certification uncertainty of the reference material Sb in Si, which is 0.6% (combined standard uncertainty of this measurement). Then, adding uncertainties in quadrature (measurement and

certification uncertainties), the He into Si energy loss is currently determined within 1.4%, and we could expect a possible improvement to 1.1%, as shown in Table 4-19.

Table 4-19 *Uncertainty budget: energy loss value determination using the dose measurement method together with certified standards.*

	Currently (u) [%]	Feasible (u) [%]
Dose measurement method	1.25	0.89
Sb standard certification	0.6	0.6
Total (u_c)	1.39	1.07

This work done on implant dose determination can be extended to very accurate (below 1.5%) energy-loss value determination. In effect, it turns out that that new *reliable* values of stopping powers for other elements can be determined using appropriate certified samples similar to the IRMM/BAM Sb, that is, another substrate (instead of silicon) with any ion implanted with a dose certification. And this can now be done readily using DataFurnace. One only needs to adjust the substrate stopping power until the dose obtained matches the certified nominal ion implant dose.

4.10 Summary

We have demonstrated precision in the determination of implantation doses by RBS at around 1.5% by a series of measurements (that is, the average value of the standard deviations as shown in col61 in Table 4-17) over a year and in two different laboratories. This is consistent with the expected 1¼% estimated combined uncertainty from a careful consideration of the instrumental behaviour. Some samples led to a dose determination uncertainty slightly over 2% (see Table 4-17, sample In03), but this dispersion may be due to implant non-uniformity. We have

also, *inter alia*, validated the DataFurnace code, by comparison of its results with results calculated by hand with a transparent algorithm.

We have measured the certified Sb dose on an implanted standard sample relative to the Si stopping powers parameterised by Barradas *et al*. [Bar02], who have re-analysed some of the most accurate data of Bianconi *et al*. [Bia00] using a sophisticated Bayesian method. This new parameterisation is consistent with the recent measurements of energy loss in silicon: these new values compare well with Konac *et al*.'s values [Kon98] when the latter are increased by about 2%. The dose we measure on the certified standard relative to the Si yield is consistent with the certified value, which demonstrates the reliability of the stopping power parameterisation at about 1.4% (given by the total combined uncertainty, that is, including both measurement and certification uncertainties). The determination of the energy-loss values themselves has uncertainty cited at no better than 2%, so that this work has significantly improved the accuracy of these important values.

However, we have only used an incident beam of 1.5 MeV He. To obtain values for the whole stopping power function we should analyse spectra from the standard sample for a range of incident beam energies, and repeat the method of Barradas *et al*. Currently the problem with this is that the stopping powers for O are demonstrably poor, and the spectrum for the Sb standard sample cannot be fitted accurately. When the O stopping powers have been determined more accurately it will be worth repeating the measurements for the Si stopping.

A careful uncertainty budget shows that this method cannot readily yield total uncertainty significantly better than about 1% with the present instrumentation.

Finally, we have demonstrated that dose measurements can be made routinely and rapidly, relative to an amorphised Si substrate, at state-of-the-art accuracy. We have shown a transparent calculation method valid for simple samples and which can be implemented in a spreadsheet [www②], and we have shown that DataFurnace gives correct answers which are also valid for complex samples.

CHAPTER 5

ROUND ROBIN: MEASUREMENT OF H IMPLANTS IN SI USING ERDA

A 200-mm amorphised Si wafer was implanted at Axcelis Technologies Inc. [Axc] with 6-keV H^+ ions at a nominal dose exceeding 1×10^{16}at/cm^2. The uniformity of the implant was better than 2% over the wafer. Samples of the wafer were shared among the participants of the Round Robin exercise, and analysed for absolute H dose by elastic recoil detection, including both He-ERDA and HI-ERDA together using various detectors. This chapter deals with giving in detail the results from Surrey, and presenting summarily the results from the other participants with a particular emphasis, however, laid on the interesting ΔE-E telescope ERDA multielemental analysis from Canberra (even though, in the end, the ΔE-E detector was unable to resolve the surface H peak satisfactorily). The results are compared and the inter-lab reproducibility is evaluated. For the details on the experimental set-up and procedure used by Surrey and the other participants, we refer the reader back to section 3.1.3 and section 3.3. The first section of this chapter aims at highlighting the importance of such hydrogenated-silicon materials.

5.1 Importance of hydrogenated silicon

Silicon has been the most widespread semiconductor used in VLSI for many years now (ULSI for the more recent years) due to its efficient electrical

properties together with the fact that a perfect crystal of silicon can be easily obtained with extremely high purity [Cam96]. Amorphous-silicon (a-Si) can be also easily prepared by a variety of techniques, like sputter deposition [Hir91] or CVD (Chemical Vapour Deposition) [Pie99, Ses01].

Silicon is believed to present no hydrogen contamination in the bulk material, and it has, on the other hand, high efficiency in trapping ion-implanted hydrogen. It was found that hydrogen trapped in the amorphous matrix is able to greatly modify the physico-chemical properties of the material [Dea73]. It was shown that hydrogenated amorphous-silicon (a-Si:H) can be doped, and that the inclusion of H into Si in its amorphous phase allowed the electrical properties to be controlled by doping with substitutional impurities [Spe75]; the study led to the conclusion that, with the incorporation of hydrogen, the room temperature conductivity can be varied by orders of magnitude when using conventional n- and p-type dopants. This then opened up totally new areas of investigation. Hydrogen was found to be an electronically active impurity in Si with some unique properties: it can passivate other impurities and defects, both at the interface and in the bulk. Soon transport studies in doped amorphous-silicon emerged [LeC79]. It was established that the properties of an a-Si:H alloy are closely related to its hydrogen content and to the nature of silicon-hydrogen bonds [Pee81].

The interest in amorphous semiconductor alloys technology continuously increased and gave rise to a number of important applications of these materials. Hydrogenated silicon began to be an attractive material for photovoltaic devices [Car77]. In the early 80s, we saw the first successful application of boron-doped a-$Si_{1-x}C_x$:H films as window layers in amorphous-silicon solar cells [Taw81]. Thereafter, this material has been extensively used as window-side p-layer in almost all high-efficiency amorphous-silicon p-i-n solar cells. A remarkable review on a-$Si_{1-x}C_x$:H thin film is given in [Bul87]. Nowadays the literature about the use of hydrogenated silicon in photovoltaic cells is mushrooming.

a-Si:H films optoelectronic applications are now numerous. These films are a well-known type of photoluminescent Si material, and as thin-film transistors, for instance, are widely used as the active elements in large-matrix liquid crystal displays [Suz91]. Important device structures from a-Si:H which have been demonstrated to date include also MOS devices [Sop01], and Vidicon arrays as

photoactive devices [Fut00]. We cannot afford not to mention, in the field of Silicon On Insulator (SOI) material technology, the use of H ion beams into Si in the so-called Smart-Cut process [Bru96], which appears to be highly suitable for making high quality SOI wafers with the great advantages of low defect density and thickness homogeneity.

5.2 Sample preparation

The samples used in this study come from a 200-nm amorphised Si wafer implanted by Axcelis Technologies Inc. [Axc] with 6-keV H^+ ions at a nominal dose exceeding 5×10^{16} atoms/cm^2. Unfortunately, we do not know much more about the preparation of the sample, apart from the claimed 2% uniformity of the implant over the wafer. Samples of the wafer were then shared among the participants for absolute H dose measurements.

5.3 Results from Surrey (UK): conventional ERDA

The detailed experimental procedure followed by Surrey is given in section 3.1.3. It may be worth looking back at Figure 3-9 for a schematic summary of this procedure.

5.3.1 ERDA solid angle: H loss correction

From the 8 sets of Kapton spectra (4 areas and 2 beam incident angles) for the determination of the ERDA solid angle, a *dose effect* has been observed. As a matter of fact, the first and second measurements (2 beam incident angles) of the 4 pairs give 2.26(15) and 2.13(11) msr as solid angle values, respectively. As H is lost with increasing bombardment the number of counts for a given incident charge falls. This is the same effect as reducing the solid angle for a fixed H content. Thus the effect observed is as expected. Hence we have an estimate of the beam damage effect, and can estimate an ERDA solid angle value corrected for H loss in the Kapton as being 2.39(20) msr by extrapolating back to zero dose.

5.3.2 Representative RBS and ERDA spectra from the Si:H sample

The simultaneous RBS and ERD spectra from the H implant for one typical measurement are shown in Figure 5-1. Only one RBS detector is shown for clarity. The fit is also shown in this figure: this was obtained using DataFurnace with an *ultra-slow cooling* fit [Bar98-a] (or see appendix D) and with the charge and gain fixed. The offset was allowed to vary, but this is rather well determined for any given value of gain. The minimum layer thickness was 50 TFU. As can be observed, the RBS signal is *not* fitted well; this is because the charge·solid angle product is not a free parameter in the analysis.

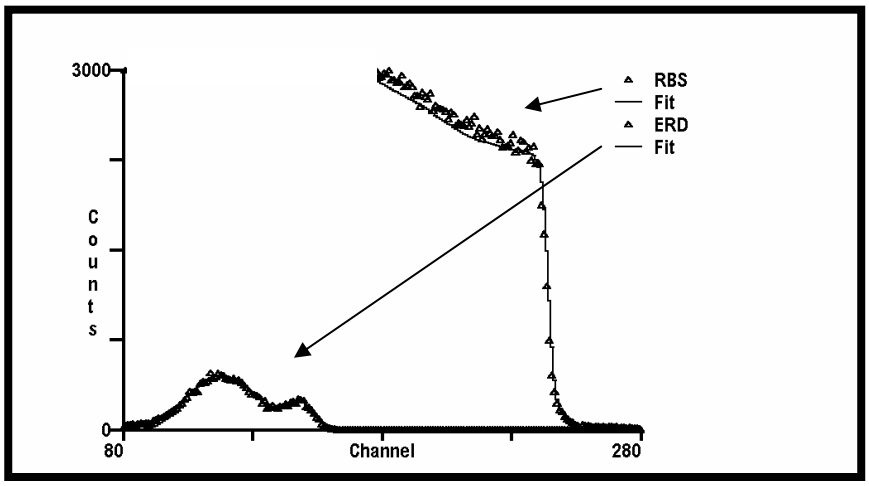

Figure 5-1 *Representative simultaneous RBS/ERDA spectra from the implanted sample, with fitted spectra (Surrey).*

5.3.3 H implant fitted structure and depth profile

The fitted structure obtained for the H implant is illustrated in Figure 5-2. All the seven samples gave a similar result. It is interesting that for the 7 independent fits the Simulated Annealing algorithm found the surface H peak, this is quite unambiguous for this data.

It should be pointed out that the effective detector resolution (after the range foil) is about 40keV: this value is obtained by fitting surface H peaks on samples

with no (intentional) H-content. This version of DataFurnace does not calculate the straggle in the foil explicitly.

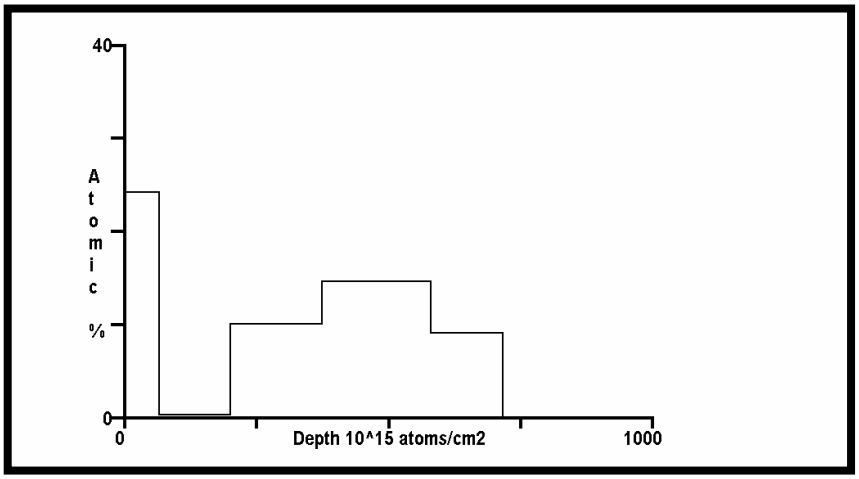

Figure 5-2 *Hydrogen fitted profile (Surrey).*

The representative depth profile of the H content from the same measurement is presented in Figure 5-3. For details about such representative depth profiles as obtained by DataFurnace, see comments on Figures 4-2b and 4-3c at the end of section 4.4 (the last two paragraphs).

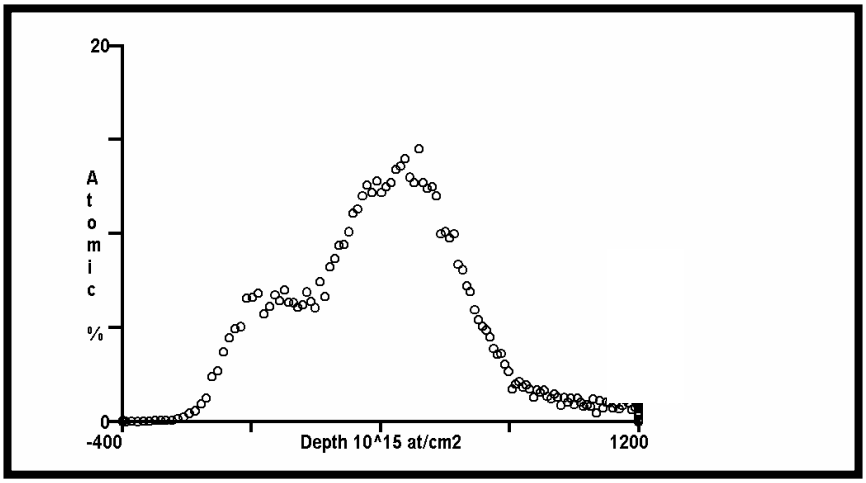

Figure 5-3 *Plot of representative H signal on a depth scale (see text) (Surrey).*

5.3.4 Final result: H content

Combining the 7 measurements and using the corrected solid angle of 2.39 msr, we obtain 57.8(1.0) and 13.9(1.3) TFU for the implant ERDA detection and the surface peaks respectively, which gives a total H amount of 71.7(2.2) TFU. Note that the multiple scattering tail was ignored in this analysis. The results are displayed in Table 5-1.

Table 5-1 *Measurements of total H content (bulk + surface) in the Si:H sample (Surrey).*

measurement	*H content* $[\times 10^{15} at/cm^2]$			*charge* $[\mu C]$	*area*	*incident angle* $[^\circ]$
	bulk	*surface*	*total*			
M1	58.5	15.3	73.8	8.48	a	15
M2	58.3	14.5	72.8	8.05	b	15
M3	59.3	15.7	75.0	8.49	c	15
M4	57.0	12.6	69.6	9.01	c	13
M5	57.0	13.9	70.9	8.86	d	13
M6	58.1	12.9	71.0	8.57	d	15
M7	56.4	12.5	68.9	8.65	c	15
mean	57.8	13.9	71.7			
std.dev. (%)	1.8	9.3	3.1			

The measurements presented in Table 5-1 are listed in chronological order. Bulk H loss by beam damage can be investigated by comparing the results from the same series of measurements from the same irradiated area on the sample. A charge between 8 and 9 μC was invariably collected for each measurement. *M3*, *M4* and *M7* were made on the same area *c*, and *M5* and *M6* on *d*. The ratio *M3/M4* gives 1.04, but *M4/M7* gives only 1.01, which is well within the standard uncertainty of 1.8% of the whole set of measurements. Moreover, the ratio *M5/M6* is 0.98! Therefore this data does not show any significant bulk H loss (from the implant) due to beam irradiation.

5.4 Results from the other participants

Five other laboratories from different parts of the world have analysed pieces from the same hydrogenated-silicon wafer for hydrogen dosimetry. Their experimental procedure has been described in section 3.3, and their results are given in the following sections. The Canberra team carried out an interesting ΔE-E telescope ERDA multielemental analysis; we put a particular emphasis on the aspects of their treatment, which is discussed first in the next section.

5.4.1 Camberra (Australia): ΔE-E telescope ERDA

5.4.1.1 Electronics calibration

The energy scale of the silicon spectrum was calibrated by associating the position of the half-maximum of the high-energy edge for Si and the centroids of the surface peaks for O and C with surface scattering. The channel numbers and energies are given in Table 3-5. Energy loss in the detector window and the pulse height deficit of the detector signal [Wei01] were taken into account. This gave an energy interval of 85.1 keV per digital channel and an offset of 1.5 MeV.

5.4.1.2 Si areal density n_{Si}

It has been assumed that the small hydrogen, carbon and oxygen concentrations do not contribute significantly to the energy loss of the ions in the sample. The silicon stopping powers have been taken from SRIM2000 [www⑦]. Initially, the areal density for silicon n_{Si}, corresponding to the integration interval of 7.32 MeV, was calculated using stopping powers for the incident energy of the Au projectiles and the energy of Si ions recoiling from the sample surface, which are 3515.8 eV/(10^{15} atoms/cm^2) and 651.1 eV/(10^{15} atoms/cm^2), respectively. By taking into account the incidence and exit angle, with respect to the sample surface, which are 22.5^o and 23.4^o, respectively, this gives an areal density of n_{Si} = 2043×10^{15} atoms/cm^2. Over this thickness the Au beam loses 18.8 MeV, whereas the Si recoil ions deposit 3.4 MeV.

In order to improve the accuracy of the analysis, the above calculation was repeated using energies and stopping powers for scattering events in the middle of the selected depth interval. The stopping powers at this point are 3462.9 eV/(10^{15} atoms/cm^2) and 659.1 eV/(10^{15} atoms/cm^2), respectively. This increases n_{Si} only marginally by 5×10^{15} atoms/cm^2, confirming that the approximation of constant energy loss rates over the selected depth interval is appropriate. It should be noted that the areal density n_{Si} is the most uncertain parameter in the analysis, because of the uncertainties associated with the two stopping power values, which in either case is of the order of at least 10%. This propagates to a systematic uncertainty of 7% for n_{Si}.

5.4.1.3 H concentration n_H

Since the detected yields can be expressed as the product of incident dose, areal density, differential recoil cross-section dσ and detector solid angle, it follows that the hydrogen concentration n_H is given by:

$$n_H = n_{Si} \times \frac{d\sigma_{Si}}{d\sigma_H} \times \frac{Y_H}{Y_{Si}}, \qquad (5\text{-}1)$$

where Y_H/Y_{Si} represents the measured yield ratio for H and Si. The cross-section ratio is $d\sigma_{Si}/d\sigma_H = 0.326$. Using this value and the detected yields given in Table 3-5, the implanted hydrogen concentrations have been derived with equation (5-1) as $n_H = (59.2 \pm 4.2)\times10^{15}$ atoms/cm^2 for sample #1 and $(60.9 \pm 4.3)\times10^{15}$ atoms/cm^2 for sample #2, respectively. Since all other uncertainties are considerably lower, only the systematic uncertainty of n_{Si} has been considered in the uncertainty estimate.

5.4.1.4 H depletion under beam irradiation

Using the differential recoil cross-section for Si at E_{beam} = 191 MeV of 33.1 barn/sr the total projectile doses have been calculated as 4.8×10^{11} and 4.6×10^{11} ions, respectively. The systematic uncertainty of the doses is 7%, dominated by the uncertainties associated with n_{Si}. The beam spot area on the tilted sample surface was approximately 5 mm^2. The total fluence of Au ions incident on the material was thus ~10^{13} ions/cm^2.

In order to establish if any hydrogen was de-sorbed during the analysis, the hydrogen yield was integrated for sequential, equal dose intervals. The results, displayed in the inset of Figure 5-4, are consistent for both samples and show that the hydrogen concentration decreases by ~5% during the measurement. Fitting and extrapolation to zero dose increases the measured concentration for both samples with n_H = (60.5 ± 4.2)×10^{15} atoms/cm^2 for sample #1 and (62.4 ± 4.3)×10^{15} atoms/cm^2 for sample #2, respectively. It should, however, be noted that the large electronic energy loss of the Au ions may have caused additional, undetected rapid de-sorption of surface hydrogen.

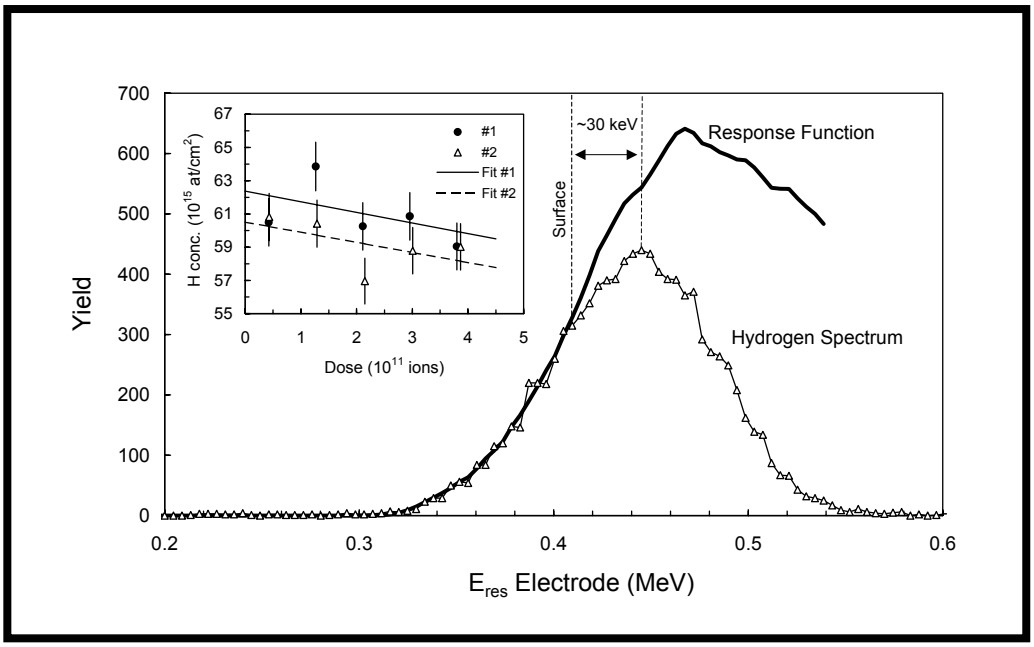

Figure 5-4 *The* E_{res} *spectrum of the detected protons for sample #1, in comparison with the response function of this (residual energy) electrode for high-energy protons. The response function was obtained by recording a hydrogen spectrum for a uniform Kapton sample. It is apparent that the centroid of the hydrogen distribution is inside the sample implying that the concentration of any surface hydrogen present is small compared to the implant concentration. The inset shows the reduction of the hydrogen content with increasing dose. (Canberra)*

5.4.1.5 Non-uniformity of the H implant

The ratio of the two measured concentrations is not affected by the systematic uncertainty of n_{Si}, but only limited by counting statistics. This implies a non-uniformity of the hydrogen implant across the waver of the order of (3.1 ± 1.5) %

and agrees within uncertainties with the expectation that the implant non-uniformity is less than 2%. The best result for the hydrogen concentration in the silicon wafer is thus the average of both measurements, which is $n_H = (62 \pm 4) \times 10^{15}$ atoms/cm^2.

5.4.1.6 Concentration of surface contamination (C and O)

Using the same procedure as in the analysis of the hydrogen content, the surface concentrations of carbon and oxygen have been derived as $(6.3 \pm 0.5) \times 10^{15}$ atoms/cm^2 and $(9.7 \pm 0.8) \times 10^{15}$ atoms/cm^2, respectively.

5.4.1.7 Depth information from H data

In an attempt to extract some depth information from the hydrogen data, the E_{res} spectrum has been compared with the response of this (residual energy) electrode to protons recoiling from the surface region of a sample [Ell00]. This is shown in Figure 5-4. The response function was obtained from a spectrum for a uniform Kapton (polyimide polymer $C_{22}H_{10}O_5N_2$) sample, which was recorded under identical experimental conditions. To achieve better definition, the Kapton spectrum was smoothed. The half-maximum of this response function may be associated with surface scattering. It is apparent that the centroid of the hydrogen spectrum is at a higher energy of $E_{res} \cong 0.44$ MeV, suggesting that most of the hydrogen is somewhat inside the sample. This is consistent with expectation and implies that the implanted hydrogen concentration is the dominant contribution to the hydrogen integral and that any hydrogen surface contamination, if at all present, accounts only for a small fraction of the integral. Better identification of such a contribution could be achieved by reducing the beam energy and stopping all protons in the detector, however, this generally reduces the efficacy of heavy-ion detection, and was thus not attempted in this study.

Comparison with the response function shows that the width of the hydrogen peak is of the same order as the achievable resolution, so that the peak shape does not contain much information about the hydrogen profile.

The energy difference of ~30 keV between the E_{res} signal of surface scattering and the centroid of the hydrogen spectrum is equivalent to a difference in

recoil energy of $\Delta E \cong 70$ keV. For the experimental geometry used, this corresponds to a thickness interval of $(670 \pm 70)\times10^{15}$ atoms/cm^2 (134 nm) and is of the order of the projected range of 6 keV protons in silicon which is 530×10^{15} atoms/cm^2 (106 nm).

5.4.1.8 H concentration: final result

Since the hydrogen is concentrated at a well-defined depth inside the sample, it is appropriate to correct the measured areal densities for the energy dependence of the recoil cross-section. The differential recoil cross-section for protons at the location of the implantation peak at a depth of 530×10^{15} atoms/cm^2 is 97.2 barn/sr. This has to be related to the mid-point of the selected depth interval (~1000 atoms/cm^2), where the differential cross-section for Si recoils is 33.1 barn/sr. The correct ratio of the differential cross sections is thus $d\sigma_{Si}/d\sigma_H = 0.341$, which gives a hydrogen concentration of $n_H = (64 \pm 4) \times10^{15}$ atoms/cm^2.

5.4.2 London (Canada): conventional ERDA

The measurements from the 2 samples gave 61×10^{15} and 57×10^{15} atoms/cm^2 as amount of implanted hydrogen, which results in 59×10^{15} atoms/cm^2 assuming uniformity over the wafer. The estimated combined uncertainty is around 5×10^{15} atoms/cm^2.

No apparent hydrogen loss with incident fluence has been observed by reference to Kapton and Mylar standards.

The surface hydrogen peak was resolved, as can be seen in Figure 5-5. Amounts of 10.0×10^{15} and 10.8×10^{15} atoms/cm^2 were found for samples #1 and #2 respectively, which gives an average of 10.4×10^{15} atoms/cm^2. This is slightly higher than the surface areal density of $3\text{-}4\times10^{15}$ H/cm^2 generally found for any *clean* sample (Au, GaAs, Si, etc) using the system at London. Note that some efforts were made to etch (using HF) the surface hydrogen off the implanted samples, but conclusively without success; it seems that the surface hydrogen is rather tightly bonded.

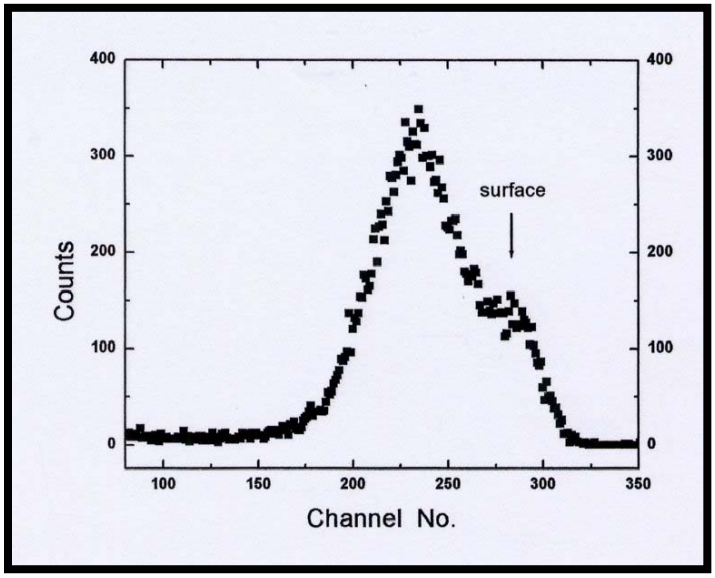

Figure 5-5 *Hydrogen ERDA spectrum obtained form sample #1 (London).*

5.4.3 Helsinki (Finland): ToF ERDA

As the measurement was made in a "list mode", the hydrogen profile could be monitored during all the way through. The total amount of hydrogen detected diminished by about 10% throughout the experiment; this can be seen in Figure 5-6, by comparing the yield with increasing iodine dose. Approximately half of the hydrogen loss was due to surface peak sputtering and half because of hydrogen loss in the implanted peak. The former occurs at the beginning of the experiment and the latter continues to the end. This loss has been taken into account in the analysis.

The surface peak could not be very well separated from the implanted peak as the latter was broadened due to multiple scattering and detector energy resolution.

In addition to hydrogen loss, the peak profile changed slightly over the measurement. At first H seems to concentrate at the depth of highest concentration, but this peak disappeared as measurement went on.

Current measurement was not accurate due to a separate Faraday cup in the target holder. However, the iodine dose was not used in the analysis of the hydrogen implanted dose.

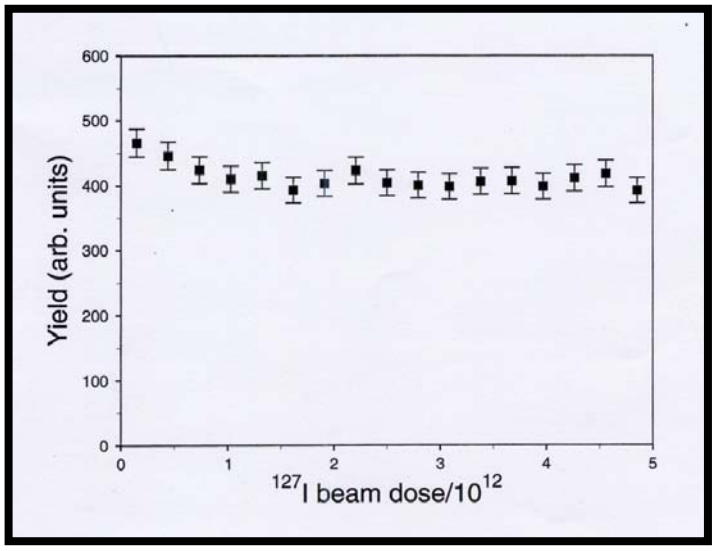

Figure 5-6 *Total yield of hydrogen as a function of incident iodine ions showing hydrogen depletion with incident fluence (Helsinki).*

With background reduction and irradiation loss taken into account, the final result is $(56 \pm 3)\times10^{15}$ atoms/cm^2 for the hydrogen implanted dose. The combined uncertainty is mainly due to hydrogen loss estimation difficulties and stopping power (SRIM1996) uncertainties; statistics played a minor role.

5.4.4 Rossendorf (Germany): HI-ERDA + NRA

5.4.4.1 HI-ERDA experiment

The HI-ERDA experiment led to a measurement of a total of 66×10^{15} H/cm^2. Unfortunately, the surface peak could not be subtracted due to bad energy resolution.

5.4.4.2 NRA experiment

The NRA analysis allowed one to resolve the hydrogen surface contamination. The values found are 57×10^{15} atoms/cm^2 and 6.3×10^{15} atoms/cm^2 for the implanted hydrogen and the surface hydrogen, respectively, which gives a total amount of 63.3×10^{15} H/cm^2. The H depth profile obtained is presented in Figure 5-7.

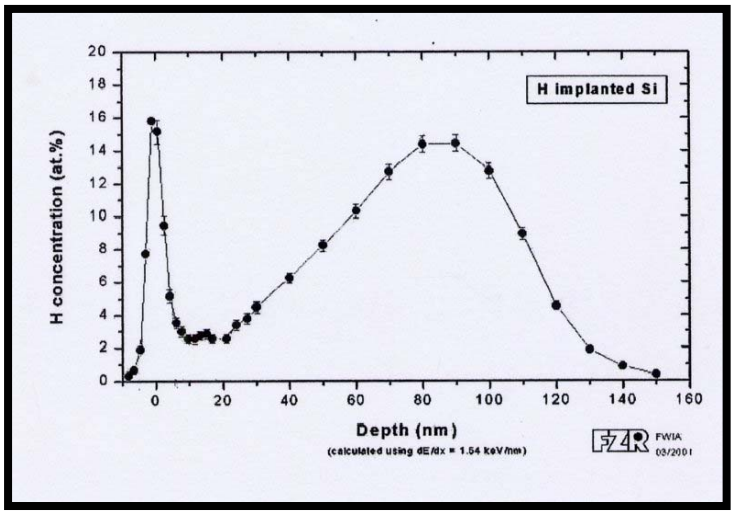

Figure 5-7 *Hydrogen depth profile obtained using NRA (Rossendorf).*

An attempt was made to get an idea of the beam related H release during the measurement. The yield of detected hydrogen was measured as a function of incident ion dose just below the peak at a depth of 100 nm at a fresh spot. The results are shown in Figure 5-8. As can be observed, the dose-dependent decrease of the yield is relatively low and it is not evident whether there is a remarkable hydrogen release during the measurement or only a peak broadening with a constant integral.

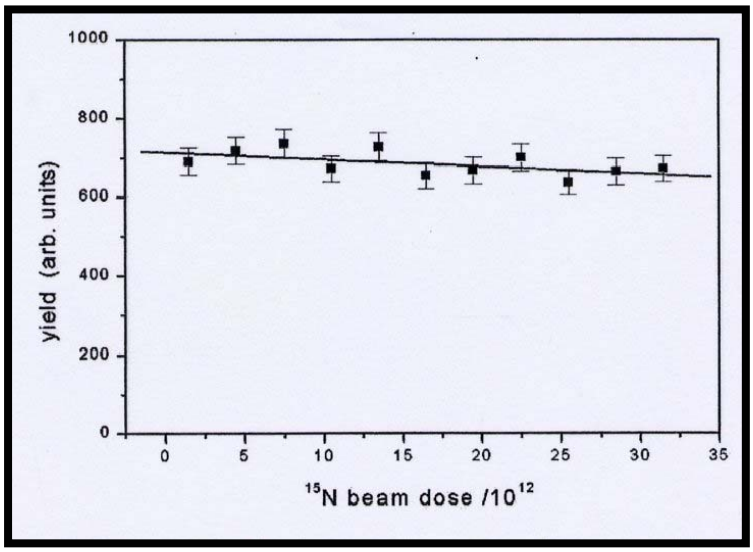

Figure 5-8 *NRA detected hydrogen yield as a function of increasing incident dose at a depth of 100 nm: study of beam related to hydrogen release (Rossendorf).*

5.4.5 Montreal (Canada): ToF ERDA

The results obtained from the series of 8 different sets of data (2 samples, 2 different beams, 2 different absorbers) are displayed in Table 5-2. The implanted hydrogen fluence is then is found to be (mean value) 55.5×10^{15} atoms/cm^2 with a standard uncertainty of 1.7%. Concentrations of surface contaminants (C and O) as well as the changes in implanted H concentration in target matrix had a negligible effect on the deduced implanted fluence. However, in the reported results the relative concentrations of all the detected elements were deduced by using an iterative depth profile technique accounting for the layer-by-layer changes in the matrix composition as described in [Oxo90].

Table 5-2 *Summary of the ToF-ERDA results (Montreal).*

beam	*absorber*	*sample*	*Implanted H fluence ($\times10^{15}$ atoms/cm^2)*
40-MeV $^{63}Cu^{8+}$	13 μm Mylar	#1	55.0
40-MeV $^{63}Cu^{8+}$	13 μm Mylar	#2	54.7
30-MeV $^{35}Cl^{5+}$	17 μm Al	#1	53.8
30-MeV $^{35}Cl^{5+}$	17 μm Al	#2	56.0
40-MeV $^{63}Cu^{8+}$	17 μm Al	#1	55.3
40-MeV $^{63}Cu^{8+}$	17 μm Al	#2	56.0
30-MeV $^{35}Cl^{5+}$	13 μm Mylar	#1	56.4
30-MeV $^{35}Cl^{5+}$	13 μm Mylar	#2	56.6
		mean	55.5
		std.dev.	1.0 (1.7%)

5.5 Review of the results together with inter-lab reproducibility assessment

Each participant of the Round Robin came out with its own analytical procedure though they were all aiming at making the same measurement, that is, the determination of the H content of the Si:H sample. It is worth giving a summing-up of some features of everyone's particular analysis:

- Canberra cannot resolve the surface with the detector settings used; this innovative detector is designed for the detection of heavy ions and is not optimised for simultaneous hydrogen determination;
- Canberra and Helsinki's combined uncertainty u_c estimates are based on stopping power uncertainty;
- London's estimate of the combined uncertainty is from geometrical uncertainty;
- Surrey's standard uncertainty is from 7 measurements of one sample, and the combined standard uncertainty u_c estimate is from the reproducibility of Kapton composition;
- Helsinki could make no precision (standard deviation) estimate — one measurement only;
- Rossendorf could not resolve the surface peak with HI-ERDA, but could do so by using resonant NRA and stepping the energy through about 250 keV;
- Montreal's standard uncertainty is from 8 measurements (2 samples, 2 beams, 2 absorbers). They made no estimate of the surface hydrogen;
- Surrey explicitly characterised their Kapton grade as 18.3 wt% Al_2O_3;
- Surrey measured the incident charge·solid angle product by performing simultaneous RBS measurements and using the silicon stopping powers together with Kapton as standards.

We present in Table 5-3 a global summary of the results from all the participants together with the uncertainty budget. Combining all the results, the dose of the hydrogen implant was found to be $57.0(1.4)\times10^{15}$ atoms/cm^2. The standard uncertainty of this measurement is only 2.5%; this compares with an 8% result in the last Round Robin exercise for hydrogen determination in 1978 [Zie78].

As can be seen, hydrogen contamination was found at the surface, and it has been measured as $8.9(4.1)\times10^{15}$ atoms/cm^2. The 46% standard uncertainty can be attributed to sample instability. In addition, the surface hydrogen is unstable under heavy-ion beams. Surface resolution is essential in this analysis in order to resolve the unstable surface signal; in this matter, HI-ERDA techniques failed due to bad energy resolution. As a general comment, light ion beams and Si detectors with range foils performed excellently in this application; it turns out that conventional ERDA is still a very suitable technique for this kind of analysis.

Estimates of the combined uncertainty of the measurements for each participant are about 6%. The apparent 2.5% reproducibility of the results is therefore suspected to be accidental.

Table 5-3 *Global summary of the results from all the participants together with the uncertainty budget.*

participant	*H content [×10^{15} atoms/cm^2]*			*combined uncertainty (u_c) for implanted H determination [%]*
	surface	*implant*	*total*	
Canberra	—	—	64	6.3
London	10.4	59	69.4	8.3
Surrey	14	57.6(1.0)	71.6	6
Helsinki	5	56	61	5.4
Rossendorf (ERDA)	—	—	66	?
Rossendorf (NRA)	6.3	57	63.3	?
Montreal	—	55.5(1.0)	—	?
mean	8.9	57.0		
std.dev.	4.1 {46%}	1.4 {2.5%}		

Numbers in {} represent the uncertainty (standard deviation) of the measurements in %..
Numbers in () are the uncertainties in the last figures.

5.6 Summary

Six participants in a Round Robin exercise were supplied with samples from a 200-nm amorphised Si wafer implanted by Axcelis Technologies Inc. with 6-keV H^+ ions for absolute H dose measurements. The experiments were carried out using He-ERDA and HI-ERDA techniques together with various detectors. The results were compared and evaluated.

The dose of the implant was found to be 57.0(1.4)×10^{15} H/cm^2; this is an inter-lab reproducibility of 2.5% (standard deviation). Unstable surface hydrogen contamination was observed; surface resolution was therefore highly required in order to identify the hydrogen contribution from the surface.

This implant can now be used as a standard for quantitative analysis of hydrogen. It can be pointed out that conventional ERDA, although the less sophisticated and less costly technique, performed exceedingly well in this application.

CHAPTER 6

ACCURATE DETERMINATION OF FLUORINE CONTENT OF SIO2:F FILMS USING RBS

Ten SiO_2:F thin film samples with various growing conditions, F concentrations and film thicknesses were submitted to RBS for absolute fluorine concentration determination. Uniformity of the films and stability of F under beam irradiation is investigated using NRA prior to the RBS analysis. An internally consistent method of data handling, which enables the relative collected charge to be determined very precisely for the spectra from the different samples, was used. The method has as a parameter the F content, which is then extracted iteratively. The IBA DataFurnace code for fitting RBS data was used to start the iterative process. This particular approach is explained in detail. The RBS results will be compared with XRF (X-Ray Fluorescence) results.

6.1 Introduction

6.1.1 Importance of SiO_2:F films

As the density of electronic devices increases with the development of ULSI circuits, parasitic capacitance effects become more critical. Among the low dielectric constant materials that have been proposed to reduce the parasitic

capacitance of interlayer dielectrics are the fluorinated silicon-oxide compounds [Hom93, Hom96, Lee96]. There are some advantages in using SiOF films [Lax95]: it reduces the dielectric constant not too drastically while retaining many of the properties of the silicon dioxide; there is strong compatibility between SiOF and SiO_2 films technologies; fluorinated silicon dioxide films also show improved gap filling and planarizability.

High fluorine content films have been found to be sensitive to water absorption [Lee98, Wan00-a]. Improvement of water resistivity has however been observed with carbon-doped SiO_2:F films [Lub99].

It has also been reported that fluorocarbon/SiO_2 composite films showed good thermal stability and good adhesion on a silicon substrate [Kim96].

6.1.2 Analytical issues

Structure information on fluorinated silicon oxide films can be obtained by using different techniques such as XRD (X-Ray Diffraction), FTIR (Fourier Transform InfraRed) and XPS (X-ray Photoelectron Spectroscopy) [Wan00-a, Din01-a-b]: crystallinity can be investigated with XRD, chemical bonding states with FTIR, and chemical composition with XPS. But in this chapter, we will present how to determine *accurately* the fluorine content of SiO_2:F thin films by using RBS exclusively.

6.1.2.1 Stopping powers

The RBS analysis of the fluorinated silicon oxide films will be done using Barradas *et al*.'s parameterisation of He in Si [Bar02], and the stopping power database of TRIM-95 [www⑦] for He in O. The former parameterisation was validated at 1.4% against the new certified IRMM-302/BAM-L001 Sb standard sample in chapter 4 (see also [Bou02]), whereas the latter database is not known at better than 5-10 %.

6.1.2.2 Different models (chemistries)

For the analysis of these fluorinated silicon-oxide samples, two different models, or chemistries of the films, were assumed and studied. The first possible chemistry is $(SiO_2)_{1-x}:F_x$, which implies that O is fixed (silicon dioxide), and which we call the *O-fixed model*. The second is $SiO_{2-x}:F_x$, which implies that the F atoms substitute for the O atoms, and which we call the *O-free model*.

6.1.2.3 Sensitivity to F

An RBS spectrum obtained for sample #3 (see section 6.2.1 on sample preparation) is shown in Figure 6-1 together with the relevant features, i.e. the elemental edges and some regions of interest (ROIs *I*, *J* and *K*). The front and back edge signals of each element present in the thin layer (Si, O, F) can be well identified. The F signal is very low as expected since it is present at low percentage.

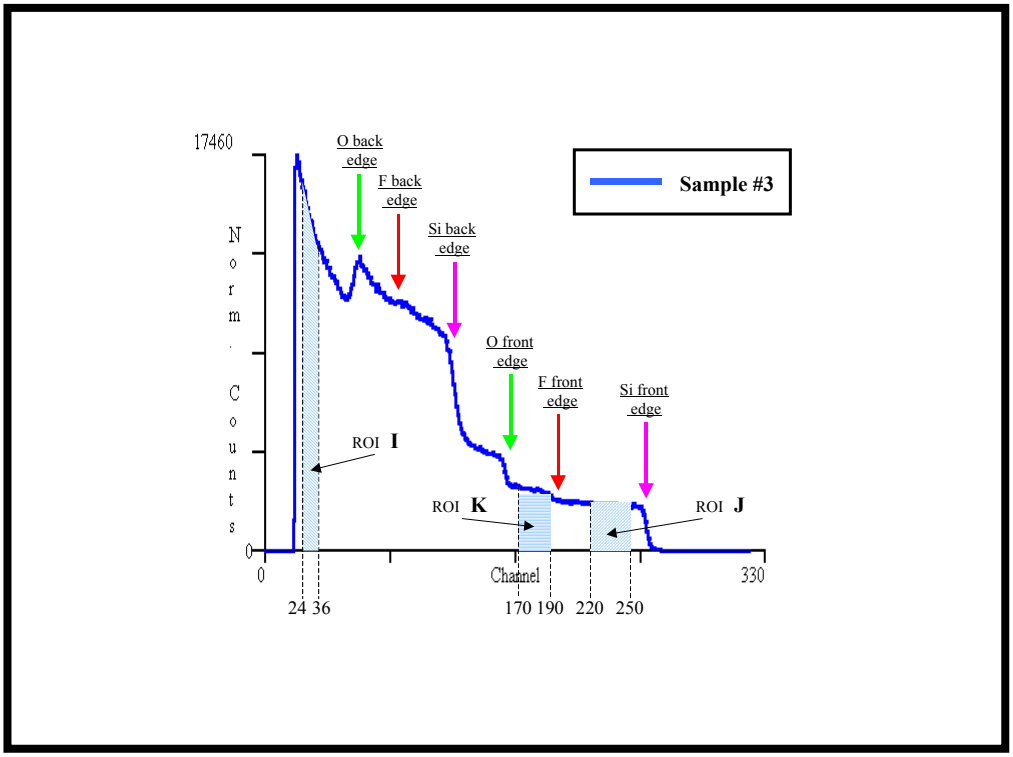

Figure 6-1 *RBS spectrum for sample #3 together with the relevant features showing elemental edges and the regions of interest ROI* I, J *and* K. *Normalised to 10 μC.*

RBS is not very sensitive to F, especially to such a low concentration, moreover the F signal is superimposed on a large matrix background. The statistics is relatively low, so is the signal/noise ratio. The latter is around 0.12 when the F signal is superimposed to the Si one only, and can be as low as 0.03 when superimposed to both Si and O signals in the low-energy part of the RBS spectrum.

A conventional way to extract some information on the fluorine content would be to measure the step height of the F edge so as to obtain a F:Si ratio. Simulation of the result can show internal consistency. However, this method only probes very near the surface.

Having said that, the fitting code DataFurnace may be used to get some information, but one has to be prudent and careful in handling the data and interpreting the outcomes. For instance, the step height cannot be explicitly fitted, but if a good fit is obtained the step height is reliably estimated. Self-consistency of the results is explicit. In order to obtain a good fit, the relative charge must be known precisely; an error here will cause a systematic channel-dependent bias in the fit which will distort the F step height. Also, to obtain a good fit, the *ad hoc* multiple-scattering correction must be applied. To do this robustly, we determine a cubic-form correction on the Si signal for a plain SiO_2 sample following the procedure in [Bar98-c], and use this correction unchanged for all the other samples. We do not allow any adjustment of gain, multiple-scattering coefficients or charge during the fit since they can only introduce uncertainty; pulser monitoring indicates no electronics shift, and the fixed Si edge shows no beam energy drift. We can correct for relative stopping power shape errors, and obtain very precise film compositions and thicknesses, with explicit assumptions and a reliable procedure.

However one cannot obtain straightforwardly the most accurate value for the F content by simply fitting the spectra with DataFurnace since the detected charge is uncertain at the >1% level. To obtain a precise relative charge we use an internally consistent iterative method of data handling; this is presented in section 6.4, and it involves the ROI *I*. The statistics in this latter region of interest can be relatively high (as shown in Table 6-3), therefore we can expect to obtain a normalised charge as precise as ~½%. Note that the DataFurnace analysis can be considered as *model-free*, as no particular chemistry is imposed; the iterative (manual) method of section 6.4 imposes sharp chemical assumptions.

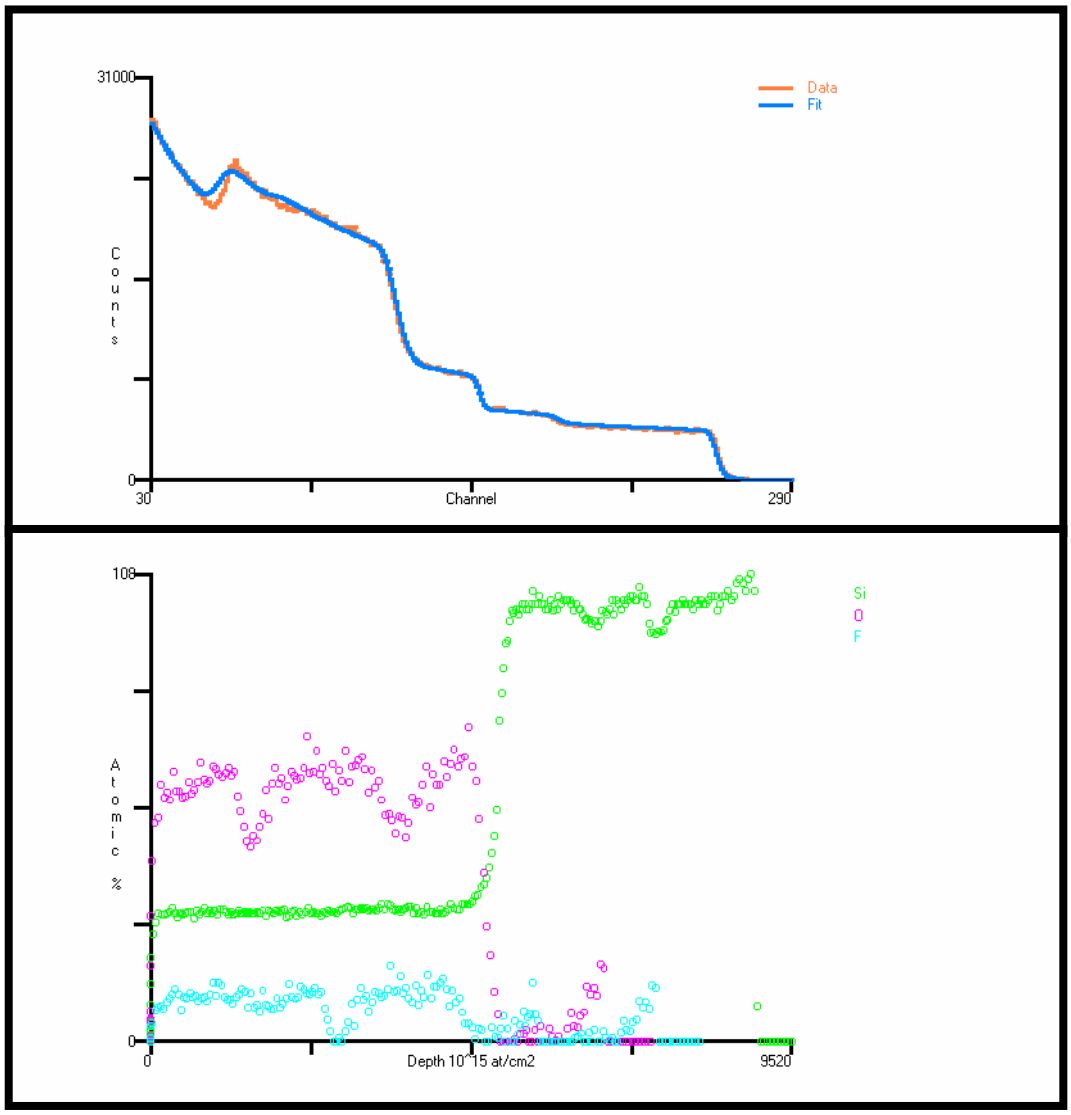

Figure 6-2 *Top) RBS spectrum of sample #3 along with the DataFurnace fit (see text for details). Bottom) Corresponding depth profile.*

In Figure 6-2 is illustrated an example of a DataFurnace fit (top) along with the depth profile obtained (bottom) for sample #3 following the assumptions above (insisting on a layer uniform with depth, with a fixed cubic correction on the Si signal, with fixed gain, with a charge fitted to the low-energy ROI iteratively). A straggling function fitted to the Si interface signal is also added. There is a mismatch of the back interfaces of both the O and F signals with the DataFurnace fit: this indicates that the shape of the database stopping cross-section function is in error for both O and F. The dips in the O and F profiles are due to mismatches in fitting back edges (only one channel mismatch for the high back silicon edge, for instance, is ample to create such important local inconsistencies).

6.1.2.4 Beam damage

The occurrence of ballistic damage during charged particle irradiation is well known. Atoms at the near-surface occasionally receive sufficient kinetic energy to be ejected, or sputtered, from the target surface. In IBA this is almost invariably insignificant. However, substantial elemental loss during IBA is expected to occur with volatile elements such as fluorine.

Therefore, prior to the RBS analysis, we will evaluate the stability of F under beam irradiation by using the nuclear reaction $^{19}F(p,\alpha\gamma)^{16}O$ at 872.1 keV; the experimental details and the results are presented in sections 6.2.2.1 and 6.3, respectively. Using the same nuclear reaction, it will be also possible to verify the uniformity of the fluorinated films; sections 6.2.2.2 and 6.3 give the experimental particulars and results, respectively. We refer the reader back to section 2.3 for more details on beam damage.

6.2 Experimental details

This section presents the experimental details for both NRA and RBS experiments carried out to obtain information on the F stability under beam irradiation, the uniformity of the films, and the F content. The accelerator energy calibration corresponding to these experiments is the one given in appendix B.2; the uncertainty on the beam energy is less than 4 keV (< 0.3 %). First we give some details on the sample preparation.

6.2.1 Sample preparation

Ten SiO_2:F samples were deposited by high density plasma chemical vapour deposition (HDP-CVD) using SiH_4, SiF_4, O_2 and Ar source gases. The flow ratio of SiF_4 to O_2 was used to vary the fluorine content. SiOF films with F concentrations from 0 to 10 %, and film thicknesses from 5×10^{18} to 8×10^{18} atoms/cm^2 were deposited for accurate fluorine content determination by using RBS.

The HDP-CVD was calibrated against XRF, and the film thicknesses against ellipsometry. The description of the different samples as given by the sender is

presented in Table 6-1. Sample #10 contains no fluorine, and will be considered as a *control sample* (reference) throughout the analysis (it will be denoted as *c10*).

Table 6-1 *SiO_2:F samples together with their description (growing conditions and film thicknesses) submitted for fluorine content determination by using RBS.*

Sample	*Remark*
1	Low fluorine content SiO_2 (819 nm)
2	Intermediate fluorine content SiO_2 (866 nm)
3	High fluorine content SiO_2 (850 nm)
4	High fluorine content SiO_2, high source power (839 nm)
6	No Ar, high source power plasma (824 nm)
7	No silane plasma (786 nm)
9	Medium amount silane plasma (822 nm)
10	SiO_2 (control sample) (821 nm)
11	Intermediate fluorine content SiO_2
12	Intermediate fluorine content SiO_2

6.2.2 NRA experiment

To evaluate the fluorine depletion together with the uniformity of the fluorinated films, the NRA technique was used. The nuclear reaction $^{19}F(p,\alpha\gamma)^{16}O$ at 872.1 keV was suitable for this purpose, and the microbeam scan line was used together with a 5″ NaI(Tl) scintillation detector [Myn85] (see also section 3.1.4). In this beam line configuration the solid angle of this detector is approximately 0.7 sr and the beam can be scanned over a relatively large area.

6.2.2.1 F stability under beam irradiation

A 850 nm high-fluorine content SiO_2 sample (#3) was first put under p beam irradiation (high fluence) in order to assess the stability of F under irradiation and estimate the depletion of F. Merely by counting the gammas detected at successive time intervals while the sample is irradiated, we can test the stability of F under proton irradiation: if the numbers of gammas detected decreases with time of bombardment (with increasing collected charge), this means that F depletion occurred. A total fluence of 756 μC struck the sample over a 28 mm^2 surface. The beam energy ranges from 870 up to 930 keV and was stepped through by intervals of ~5 keV 5 times.

6.2.2.2 F uniformity

By varying the p-beam energy, we can depth-profile the fluorine content. Bearing in mind the reaction occurs at 872.1 keV (Gaussian shape, with a 4.5 keV width), by increasing the beam energy it is possible to probe deeper inside the sample since particles lose energy while travelling into matter. Thus a depth profile can be extracted to assess the uniformity of F. Any non-uniformity of the fluorine content will result in a non-linear profile (number of gammas detected per μC versus energy plot).

6.2.3 RBS experiment

The RBS analysis was performed with an 1.480(6)-MeV $^4He^+$ (appendix B.2). An implanted silicon detector was used at a scattering angle of 163.0^0, which was measured as discussed in section 3.1.2.2; the uncertainty in this angle is estimated at about ½%. The electronics calibration was done with an uncertainty of about ½% as presented in section 3.1.2.4.

6.3 NRA results on F stability and uniformity

In Figure 6-3 is presented a 3D-graph (with multiple orientations) giving a general view of the data collected (5 energy scans). One axis is the beam energy, the second is the number of gammas detected per μC, and the last is the charge collected in μC per mm^2 (which can be regarded as a time bombardment scale). The energy (depth) scans show an approximate regular shape, which indicates an uniformly distributed fluorine content all over the sample. It can also be observed, at first sight, that no significant depletion of F occurred with time (irradiation); only a slightly decreasing number of gammas were detected over more than 27 μC/ mm^2.

In Figure 6-4, the 5 depth profiles (energy scans) obtained are shown separately (2D-graphs). The linear distribution confirms the uniformity of the F with depth. The five depth profiles have been linearly fitted in the flat region (approximately between 886 and 906 keV), assuming a zero slope. The variation of the different heights of these linear regressions with time of bombardment then gives the evolution of F depletion due to irradiation (the number of gammas detected are proportional to the fluorine content). In Figure 6-5, we have plotted these numbers of gammas detected as a function of charge collected per unit of surface. Despite the depletion decay with time of bombardment is expected to be exponential, the points can be merely well fitted assuming a linear behaviour in this case (it was verified that the exponential trend is locally nearly linear for this data — an exponential fit does not bring more information). The relation obtained is as following:

$$[\textit{gammas detected}] = 2203(33) - 6(2)\cdot[\textit{charge per area}], \qquad (6\text{-}1)$$

where the charge and area are expressed in μC and mm^2, respectively. At time $t = 0$, this leads to an extrapolation of 2203(±1.5%) gammas detected. A collected charge of 9 μC over 2 mm^2, which are typical conditions used in the RBS, leads to a number of gammas detected of 2176. This corresponds to about 1.2% of fluorine released. But this holds for a p beam at around 900 keV. However, the RBS experiment carried out for F content determination was with He at ~1.5 MeV. The energy deposited (by inelastic energy-loss process) by a 900-keVp and a 1500-keV He beam in a 2.5×10^{18}at/cm^2 silicon-dioxide matrix is ~18 keV and ~111 keV, respectively. Assuming that F loss is linear with energy deposited, we can estimate that the typical

fluorine depletion of He RBS is about 7.4%. This is a substantial correction which we discuss later in the light of the results.

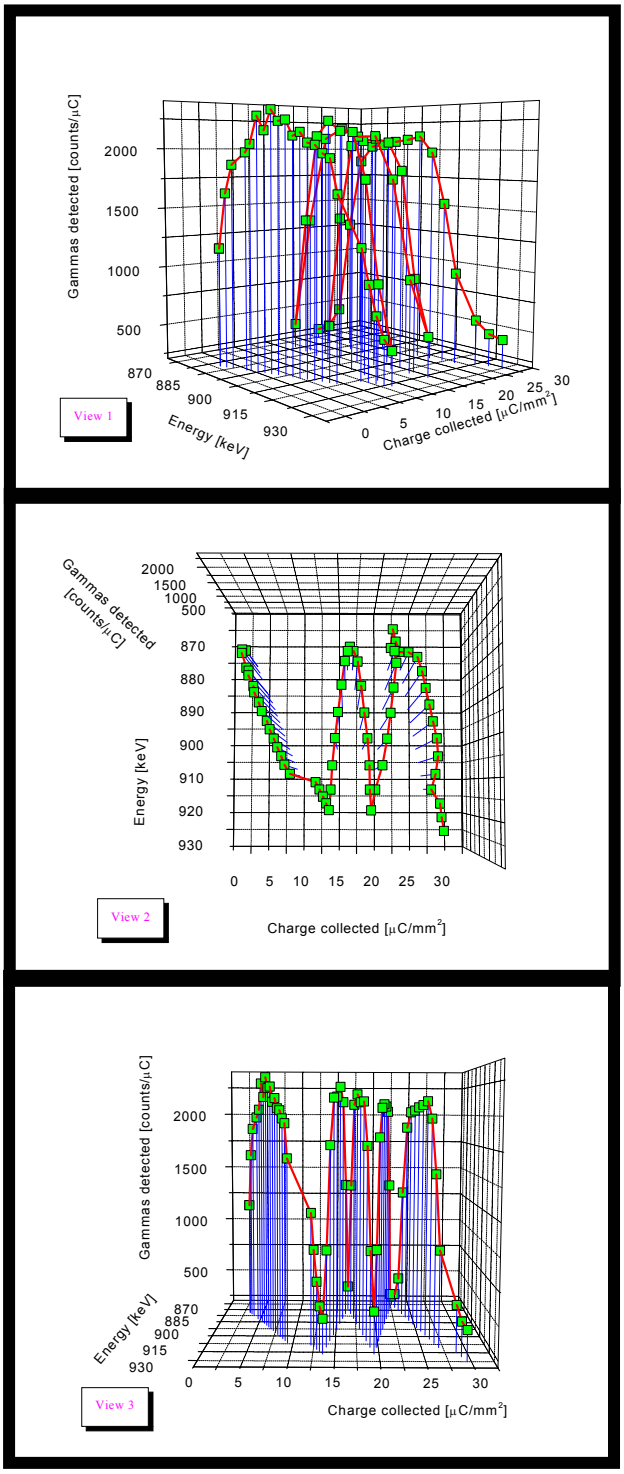

Figure 6-3 *General view of the depth profiles (energy scans) of sample #3 as a function of time of bombardment (charge collected) in 3 different orientations.*

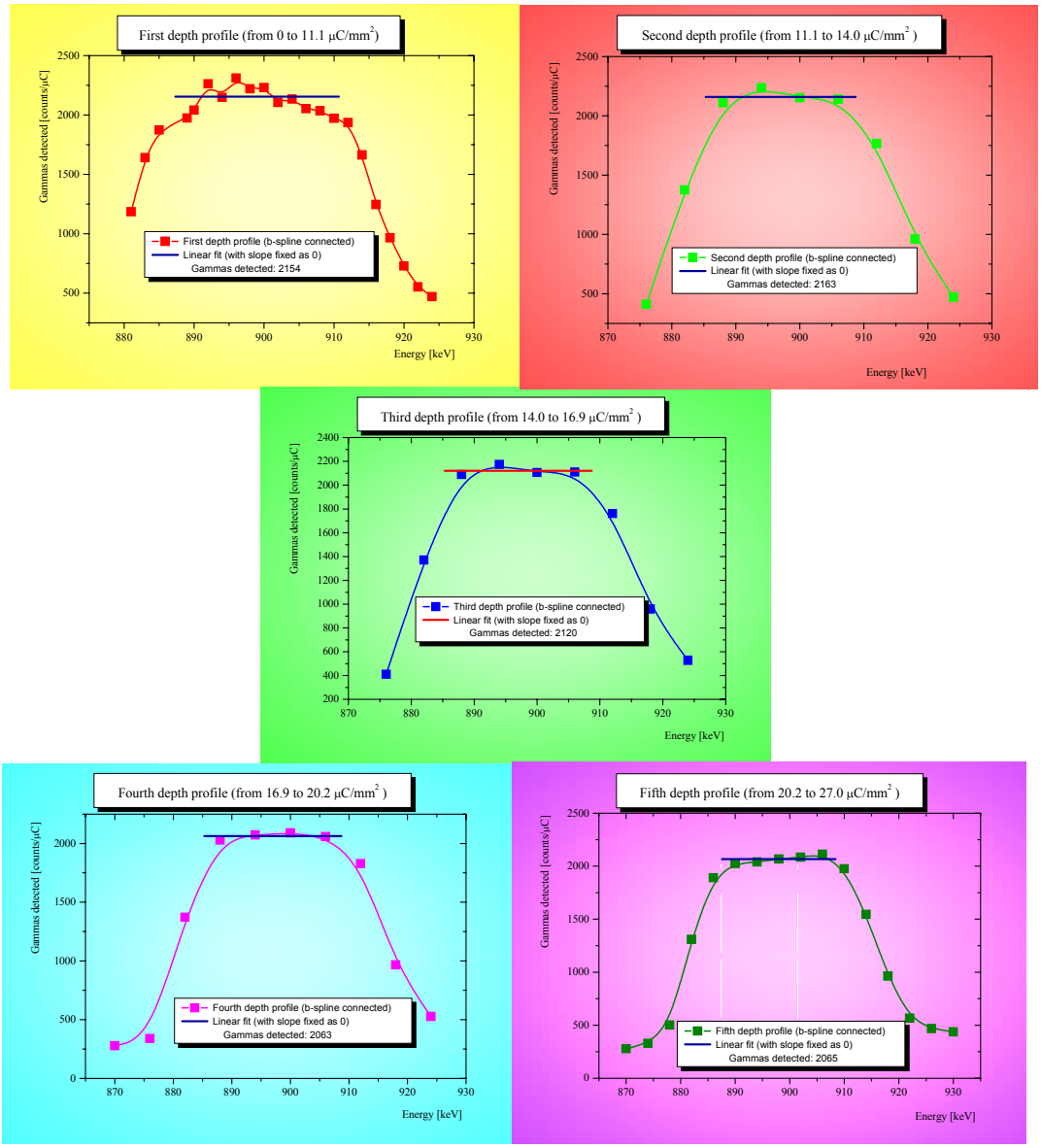

Figure 6-4 *Five depth profiles (energy scans) obtained at different time of bombardment.*

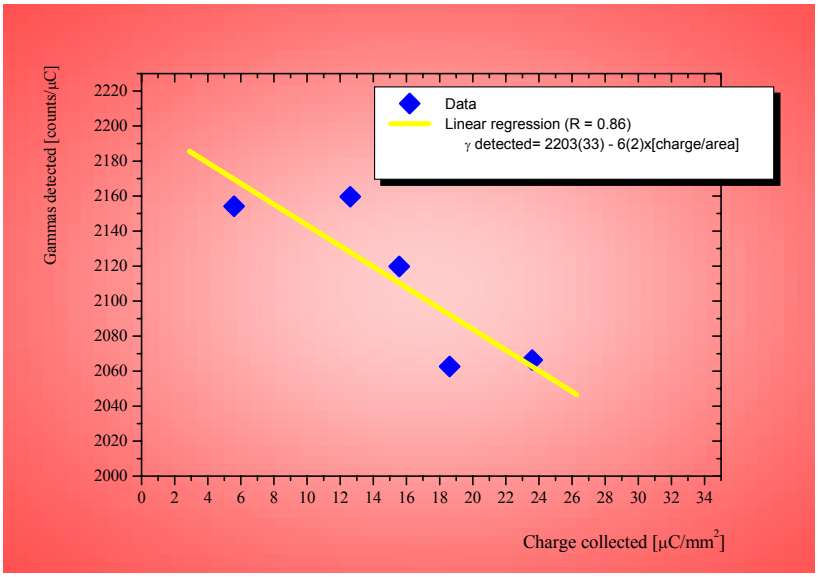

Figure 6-5 *Depletion of fluorine as a function of beam irradiation.*

6.4 RBS iterative method

We describe in this section the iterative data handling method used to extract precise relative charge values, and the fluorine content ultimately. We present the RBS treatment using only the chemistry with the O kept fixed (O-fixed model). However, we have also handled the data assuming a second possible stoichoimetry (O-free model), but we will present only the final results at the end of section 6.5 with all the results altogether for comparison.

6.4.1 Preliminary considerations

We refer the reader back to Figure 6-1 which shows an RBS spectrum obtained for sample #3 (high-fluorine content) together with the relevant features (elemental edges and ROIs). The importance of determining precise relative collected charge values has been highlighted further above in section 6.1.2.3. This can be achieved by using an internally consistent iterative method of data handling (internal normalisation). This iterative process can lead to obtaining the fluorine content ultimately.

Briefly, this iterative method compares the data with simulated spectra through specific regions of interest. Hence the ROIs *I*, *J* and *K* as illustrated in Figure 6-1. We might expect that the integral yield ROI *I* at low energy (LE) to be independent of both F content and film thickness as it is defined below the back edge of all of the elements present in the thin layer (it is a substrate signal). On the other hand, at high energy (HE), we expect the integral yields in ROIs *J* and *K* to be sensitive to the F content as these areas are defined well within the thickness of the film (near the surface). However, as we will see just below, it turns out that the LE yield (ROI *I*) is weakly dependent on both F content and film thickness, and for accurate relative charge normalisation this must be taken into account.

Table 6-2 *Variations of integrated yields* I, J *and* K *with film thickness and fluorine content obtained from simulations. Normalised to 10 μC. 1TFU = 10^{15} atoms/cm^2.*

LE (low energy) *(channels 24-36)*					**HE** (high energy) *(channels 170-190 or 220-250)*		
Constant F content			*Constant layer thickness*		*Constant layer thickness*		
	F = 0 % at.	*F = 5 % at.*	*t = 5100 TFU*		*t = 5100 TFU*		
Layer thickness [TFU]	*Integrated yield I (ch 24-36) [counts]*	*Integrated yield I (ch 24-36) [counts]*	*F content [%]*	*Integrated yield I (ch 24-36) [counts]*	*F content [%]*	*Integrated yield J (ch.220-250) [counts]*	*Integrated yield K (ch 170-190) [counts]*
5000	153130	153550	0	153559	0	61921	47691
5100	153572	153929	1	153681	1	61378	47819
5200	153876	154426	2	153702	2	60834	47950
5300	154080	154487	3	153813	3	60288	48080
5400	154380	154762	4	153969	4	59741	48211
5500	154579	155197	5	153929	5	59193	48341
5600	154686	155416	6	153981	6	58643	48472
5700	155169	155634	7	154116	7	58092	48605
5800	155330	155865	8	154147	8	57539	48736
5900	155905	156370	9	154356	9	56985	48869
–	–	–	10	154374	10	56429	49001
–	–	–	11	154485	11	55872	49133
–	–	–	12	154563	12	55314	49267
–	–	–	13	154543	13	54755	49403
–	–	–	14	154619	14	54194	49539
–	–	–	15	154730	15	53631	49673
Figure 6-6			Figure 6-7		Figure 6-8		

6.4.2 Information from simulated spectra

We have simulated different spectra corresponding to samples with different thicknesses and fluorine contents in order to obtain yield relationships at low energy (LE — ROI *I*) and high energy (HE — ROI *J* and *K*). The charge used was arbitrarily 10 μC. All the values are gathered together in Table 6-2 above. The range of film thicknesses and fluorine contents used are roughly those expected for the set of samples to be analysed. The thickness of the films has been determined as explained below in section 6.4.3.

6.4.2.1 Relation at low energy (LE)

The variation of integrated yield *I* as a function of film thickness (in the range of interest) for both 0% and 5% fluorine content as obtained above have been plotted in Figure 6-6. The integrated yield *I* is found to be relatively sensitive to the variation of film thickness as it varies linearly by nearly 2.5% from a film thickness of 5000 TFU to 5900 TFU (1TFU = 10^{15} atoms/cm^2).

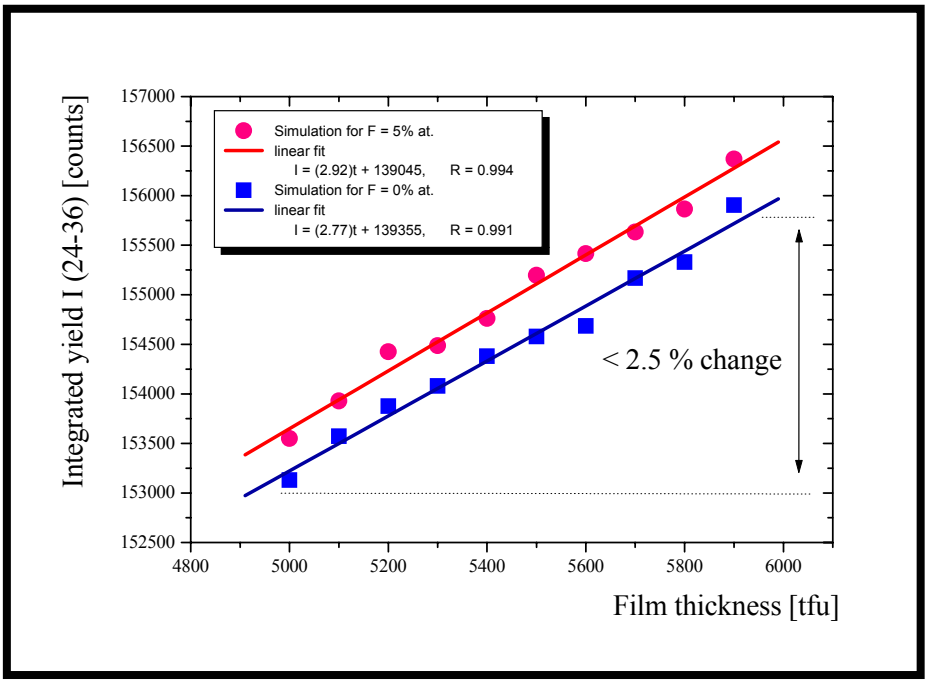

Figure 6-6 *Simulated integrated yield in ROI* I *vs thin film thickness with F content of 0% at. and 5% at. Normalised to 10 μC. 1 TFU = 10^{15} atoms/cm^2. O-fixed model ($(SiO2)_{1-x}:F_x$).*

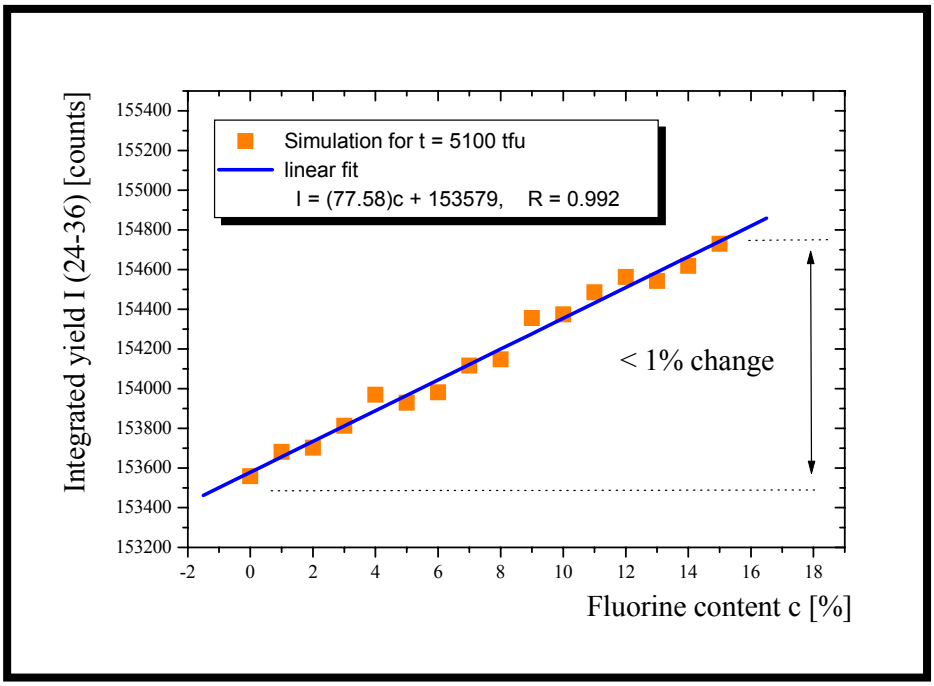

Figure 6-7 *Simulated integrated yield in ROI* I *vs fluorine content with thin film thickness of 5100 TFU. Normalised to 10 μC. 1 TFU = 10^{15} atoms/cm^2. O-fixed model ($(SiO2)_{1-x}$:F_x).*

The integrated yield I versus fluorine content for a constant film thickness of 5100 TFU has also been obtained, and it is illustrated in Figure 6-7. As can be seen, it is less sensitive to any variation of the fluorine content as it increases linearly by less than 1 % from 0 to 12 F% (the range of interest).

Small oscillations can be seen on the plots shown in Figure 6-6 and Figure 6-7. These are thought to be due to systematic small fluctuations (discreteness) in the simulation code used (DataFurnace) to simulate the spectra for the different fluorine content and film thickness conditions.

These LE relationships obtained from these linear regressions can be grouped in a three-parameter equation as following[1]:

$$\{I_i\} = 2.77t_i + 77.58c_i + 139355\,, \qquad (6\text{-}2)$$

where t_i is the thin film thickness in TFU (thin film unit) and c_i the fluorine content in percentage for sample i. This equation will be useful to normalising the yield I_i by

[1] Variables I_i and J_i will refer to yields from the raw data. The same variables in brackets {} will refer to calculated yields from simulated spectra.

reference to features (film thickness and 0% F content) of the control sample (#10) (internal charge normalisation).

6.4.2.2 Relation at high energy (HE)

A linear variation of the integrated yields J_i and K_i as a function of fluorine content has also been found, and it is presented in Figure 6-8. The integrated yield *K* is much less sensitive than ROI *J* for any change in fluorine content however. The explanation is that the yield *K* is the sum of signals coming from backscattering from both Si and F target nuclei. On the one hand, a higher percentage of F leads to an increased yield *K* which implies however a lower percentage of Si that leads to a decreased yield, so that this should result to a decreased yield on account for the cross-sections; on the other hand, the decrease in the Si atoms is not in the same proportions as the increase of F atoms (the matrix is silicon dioxide — approximately 3 F atoms may replace 1 molecule of silicon oxide, therefore 1 Si atom): consequently, the final result is a *slightly* increasing yield *K* with an increasing content of fluorine. Therefore we will retain only the information from ROI *J* for it is much more sensitive.

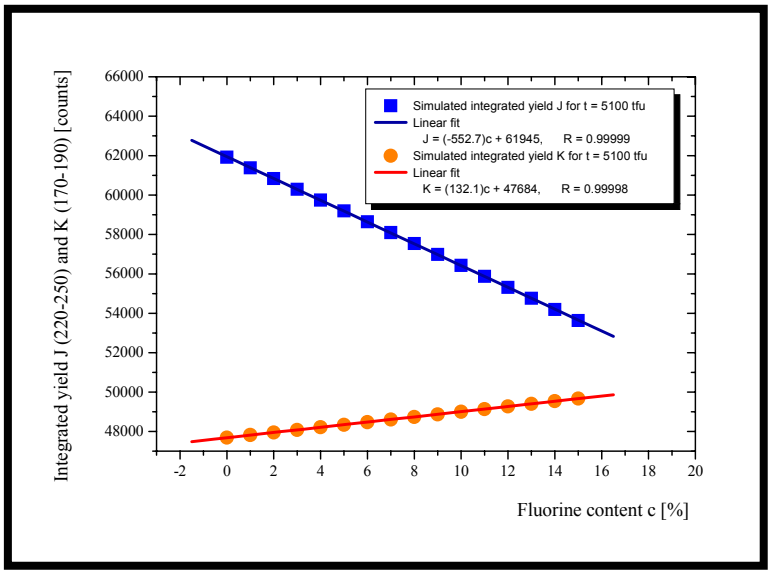

Figure 6-8 *Simulated integrated yield in ROIs* J *and* K *(170-190) vs F content with film thickness of 5100 TFU. Normalised to 10 μC. 1 TFU = 10^{15} atoms/cm^2. O-fixed model ($(SiO2)_{1-x}:F_x$).*

Then the HE relationship that we will have to deal with is:

$$\{J_i\} = -552.7c_i + 61945. \quad (6\text{-}3)$$

This equation will be useful to normalising the yield J_i by reference to features (0% F content) of the control sample (#10) in order to determine the fluorine content subsequently. But the starting point of the iterative process is to get the thickness of the films, which is the subject of the following section.

6.4.3 Start of the iterative process: getting the thickness of the films

First, to start the iterative process, we need to determine the thickness of the fluorinated silicon-oxide film of each sample (regarded as iterative step n = 0). This can be obtained by using the code DataFurnace as explained in section 6.1.2.3, except that the charge is set as a free parameter. If the spectra are fitted well than a *valid* depth profile has been found. Small signals are only interpreted validly by DataFurnace if the total fit is excellent.

Table 6-3 *Thickness* t_i *together with some values from the different spectra of each sample such as charge collected* Q_i*, raw integrated yields* I_i *at low energy (LE) and* J_i *at high energy (HE).*

sample	t_i *[TFU]*	Q_i *[μC]*	*LE raw* I_i *(24-36) [counts]*	*HE raw* J_i *(220-250) [counts]*
1	5102	6.616	125295	44446
2	5153	18.875	358944	125710
3	5169	18.993	363203	121131
4	5000	19.146	356279	123763
6	5138	18.919	363469	126637
7	7291	18.962	465409	126644
9	5726	11.372	224046	76537
10	5099	11.406	209496	78072
11	5351	6.610	126438	43538
12	5310	18.926	362219	122172

In Table 6-3 are displayed the thickness values obtained for each sample from the code DataFurnace in thin film units (TFU). Are also shown in this table the collected charge together with the raw data values for the integrated yields I_i and J_i as described further above. These values of thickness determined at step $n = 0$ ($t_{i,n=0}$) will then be used at each of the following steps n of the iterative process. The collected charge will be used at step $n = 1$; the fitted charge is not determined more precisely.

6.4.4 Iterative process

6.4.4.1 Part I: Internal charge normalisation (using equation (6-2))

We know that the collected charge cannot be known at better than 1% (see sections 3.1.2.1 and 4.5.3). The aim of the first part of the iterative process is to improve the uncertainty of the charge by performing an internal charge normalisation.

We can obtain a normalised integrated yield per μC $A_{i,n}$ at LE by doing:

$$A_{i,n} = I_i \frac{\{I_{c10,n-1}\}}{\{I_{i,n-1}\}} \frac{1}{Q_i}$$

$$= I_i \frac{2.77t_{c10,0} + 139355}{2.77t_{i,0} + 77.58c_{i,n-1} + 139355} \frac{1}{Q_i}. \qquad (6\text{-}4)$$

The subscript *c10* refers to control sample #10. The term $\{I_{c10,n-1}\}/\{I_{i,n-1}\}$ normalises to 0% F content, as the control sample is known to have no fluorine, and also to its thickness. Since we do not know the F content of any of the samples, we will start the process at $n = 0$ with 0% concentration ($c_{i,0} = 0$) for each sample.

Excluding the statistical fluctuations, the uncertainties on the background correction and the linear regression, all $A_{i,n}$ values (for the same step n) should be the same assuming a *perfect* charge integrator (zero-uncertainty charge collection). But since the charge collection is not better than 1% with the system at Surrey, these values fluctuate from spectrum to spectrum. However the average value $\langle A_i \rangle_n$ calculated from a set of 10 samples can be considered as the *right* value with a

confidence of ~0.3% (standard deviation of arithmetic mean). We can therefore make an internal normalisation and correct the charge by doing:

$$Q'_{i,n} = \frac{A_{i,n}}{< A_i >_n} Q_i . \qquad (6\text{-}5)$$

6.4.4.2 Part II: Fluorine content determination (using equation (6-3))

The integrated yield $\{J_i\}$ for a sample with no fluorine is equal to 61945 and a collected charge of 10 μC (see equation (6-3)). We can calculate a normalised yield $B_{i,n}$ to the yield and charge of the control sample, and to this value of 61945 as following:

$$B_{i,n} = 61945 \frac{J_i}{J_{c10}} \frac{Q'_{c10,n}}{Q'_{i,n}}, \qquad (6\text{-}6)$$

which corresponds in fact to the (normalised) yield of sample i with fluorine concentration $c_{i,n}$. Then we can use this normalised yield together with equation (6-3) directly to calculate the fluorine content:

$$c_{i,n} = \frac{61945 - B_{i,n}}{552.7} . \qquad (6\text{-}7)$$

The new values of F concentration $c_{i,n}$ obtained at step n in part II can then be used in part I for a new step $n+1$, and so on until convergence of the F concentration values.

6.5 RBS results and discussion

In Table 6-4 are displayed the values for iteration $n = 6$: $A_{i,6}$, $<A_i>_6$, $Q'_{i,6}$, $B_{i,6}$, $c_{i,6}$, and the discrepancy $D_{i,6}$ of $c_{i,6}$ from $c_{i,5}$. Some interesting conclusions can be drawn from these values.

Table 6-4 *Outcomes from the iteration* n = 6.

Sample	$A_{i,6}$ *[cts/μC]*	$Q'_{i,6}$ *[μC]*	$B_{i,6}$ *[cts]*	$c_{i,6}$ *[%]*	$D_{i,6}$ *[%]*
1	18994	6.589	58791	5.71	0.00004
2	19105	18.908	57946	7.24	0.00004
3	19269	19.189	55018	12.53	0.00003
4	18649	18.722	57616	7.83	0.00004
6	19301	19.147	57646	7.78	0.00004
7	NA	18.962*	58210	6.76	0.00000
9	20035	11.946	55840	11.05	0.00003
10	18367	10.985	61945	0.00	NA
11	19307	6.692	56708	9.48	0.00003
12	19324	19.177	55527	11.61	0.00003
$<A>_6$	19150				
std.dev. [%}	2.45				

** Raw data. The oxygen signal in the spectrum encroaches upon the ROI* I*, so the charge normalisation cannot be worked out using the method for this thick silicon-oxide film.*

As can be seen, the standard deviation on $<A>_6$ is found to be 2.4%. This precision includes the uncertainty on the charge collection, the statistical fluctuations on the integrated yield *I*, the pile-up background (which is very low); the linear regression obtained from the simulations (equation (6-2)) and used to derive this normalisation has a negligible contribution. This uncertainty of 2.4% is somewhat high if we compare with the estimated uncertainties of these effects, which are respectively ~1.1% (as estimated in section 4.5.3), ~0.4% and ~0.2%, and which give a combined uncertainty u_c of ~1.2% (summed in quadrature). However, if we calculate the ratio between the collected charge Q_i (see Table 6-3) and the calculated charge $Q'_{i,6}$, which is displayed in Table 6-5, it can be noticed that there is a 5% discrepancy for sample #9; this difference is relatively high, and we can suspect something wrong with this sample (we will discuss about this further below). The fluctuations of this ratio are governed by the same effects as the ones for $<A>_6$. If we exclude the value from sample #9 in the calculation of the average value, we obtain a standard deviation of 1.9% for this ratio as shown in Table 6-5. This is more consistent with the estimated u_c of ~1.2% on the effects of these variations, although still a little high; this may be due to a charge integration worse than 1.1% for this experiment. Therefore this internal normalisation involving measurements from 8

samples leads to an uncertainty of approximately 0.7% (standard deviation of the arithmetic mean) on the calculated charge *Q'*.

As can be seen also in Table 6-5, the outcomes of the ratio $Q_i/Q'_{i,6}$ obtained for the other model, that is, the O-free model, are similar to the O-fixed model: this measurement is then model-independent, which is an expected result as it is simply a charge normalisation and the fluctuations ought to be dependent to the effects mentioned above exclusively.

Table 6-5 *Ratio between collected charge* Q_i *and calculated chage* $Q'_{i,6}$ *for both models (chemistries).*

Sample	*Ratio* $Q_i/Q'_{i,6}$	
	O-fixed model	*O-free model*
1	1.004	1.002
2	0.998	0.996
3	0.990	0.986
4	1.023	1.020
6	0.988	0.986
7	NA	NA
9	→ 0.952	→ 0.949
10	1.038	1.038
11	0.988	0.985
12	0.987	0.984

	All the values	*Excluding #9*	*All the values*	*Excluding #9*
mean	0.996	1.002	0.994	1.000
std.dev. [%]	2.4	1.9	2.5	2.0

As can be observed from Table 6-4, 6 iterations are ample for convergence. As a matter of fact, after the 6^{th} iteration, the fluorine content that comes out is as close to the one at the previous iteration as $1/10^7$.

From the study on F stability under irradiation, we can estimate the amount of F depleted as a function of charge collected. Note that an integration of fluorine loss over the acquisition time of each spectrum describes better the depletion process in

conjunction with the acquisition of the RBS data leading to the determination of the absolute amount of fluorine; this means half of the collected charge has to be considered for fluorine loss calculation (assuming linear release of fluorine with irradiation as concluded further above, on average half of the depleted fluorine atoms were present all over the acquisition time and were involved in the RBS scattering events). In Table 6-6 are presented the final RBS results of fluorine concentration both with and without correction for depletion due to irradiation for the O-fixed model ($(SiO_2)_{1-x}:F_x$).

Table 6-6 *Results for the F content, including measurements for XRF and RBS. The latter include final values assuming two different chemistries, that it, $(SiO_2)_{1-x}:F_x$ (O fixed) and $SiO_{2-x}:F_x$ (O free). Both with and without F loss correction values are given for the O-fixed model. The ratio between the two chemistries is also shown.*

sample	*F content [%]*				*Ratio O fixed/O free*
	XRF	*RBS*			
		O fixed no F loss correction	*O fixed F loss corrected*	*O free*	
1	5.6	5.71	5.86	8.61	0.681
2	7.2	7.24	7.86	11.55	0.681
3	15.6	12.53	13.62	19.97	0.682
4	15.6	7.83	8.51	12.48	0.682
6	6.2	7.78	8.45	12.42	0.681
7	7	7.19	7.81	11.52	0.678
9	7	11.05	11.62	17.09	0.680
10	0	0.00	0	0	–
11	9.6	9.48	9.75	14.32	0.680
12	13	11.61	12.61	18.51	0.681
				mean	0.681
				std.dev. [%]	0.1

The RBS final results of the O-free model ($SiO_{2-x}:F_x$) are also shown in Table 6-6, along with the ratio between the two different chemistry results. The two measurements are quite different: the O-fixed results are systematically 68% lower than the O-free ones. The standard deviation of the ratio is about 0.1%; this

represents very small fluctuations, and this is consistent with the small uncertainties that can be introduced by the different linear regressions obtained from the simulations. In effect, this ratio depends upon the uncertainties in the linear regressions exclusively, all the other uncertainties are cancelled out. The ratio for sample #7 is slightly lower (0.678) than for the others: this is due to the fact that no charge normalisation was performed for this sample, the raw collected charge was simply used instead (see note at the bottom of Table 6-4 for explanation). If we increase, for instance, the charge by 1% for this sample, we obtain 0.681 as an O-fixed/O-free ratio. If we exclude this sample, the standard deviation of the ratio turns out to be as low as 0.08%. In short, this result shows the negligible effect of the theoretical calculations (negligible uncertainties introduced by the simulations) as expected, and more importantly it proves the consistency of the data handling methods used.

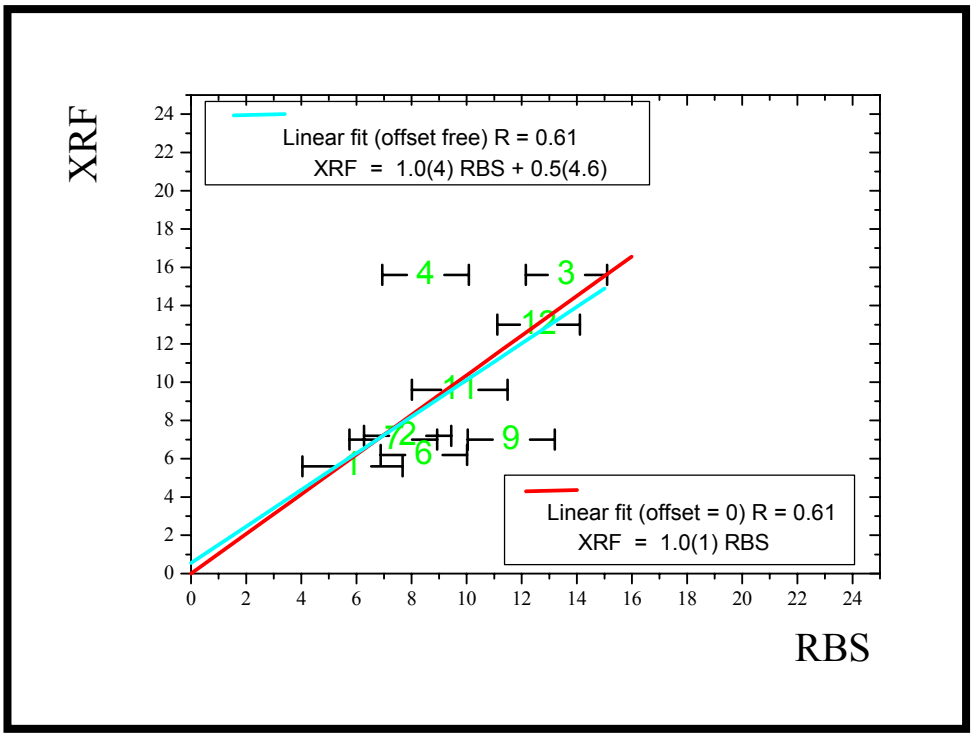

Figure 6-9 *Comparison of the XRF and corrected RBS fluorine content using the O-fixed model $(SiO_2)_{1-x}:F_x$. The error bars are expanded uncertainties with a coverage factor* k = *2. Two linear fits are shown: one where the offset is a free parameter, and another one with the offset set to 0.*

The uncertainty on the F content is governed by equation (6-7), which is a function of $B_{i,n}$, that is, equation (6-6). The latter involves the statistical fluctuations on the integrated yield J_i and the pile-up background, and the uncertainty on the calculated charge $Q'_{i,n}$; these estimated uncertainties are typically ~0.3%, ~0.2% and ~0.7%, respectively. Summed in quadrature, this gives a combined uncertainty u_c of ~0.8%. But a 1% change in u_c leads to an approximately 10% change in the F content. The equation (6-6) is derived from the linear regression as given by equation (6-3), which has a negligible contribution to the total uncertainty.

Since we used fitting processes to obtain the thickness of the films, uncertainties on the stopping powers must be added in the uncertainty analysis. The new Si energy-loss parametrisation for He projectiles has been recently established at the 1% level as discussed in section 6.1.2.1. However, as also mentioned further above, O stopping powers are unfortunately not known at better than 5-10%. This is unequivocally the governing uncertainty of the whole analysis. This expresses the importance for the IBA community of obtaining reliable (at the 1% level) O stopping powers, as silicon-oxide based films are widely used in semiconductors.

Finally, one of the goals of this study was to compare the XRF and RBS results. We have plotted the XRF and O-fixed RBS measurements in Figure 6-9. The error bars are expanded uncertainties with a coverage factor $k = 2$ (level of confidence of approximately 95%). Tow linear regressions have been drawn, one where the offset is a free parameter, and a second one with forcing a zero-offset. They both have a correlation coefficient of $R = 0.61$. The former gives an offset of 0.5 ± 4.6; this is a rather large uncertainty, and this offset is in the vicinity of zero. We expect, in fact, a zero-offset as both XRF and RBS method are likely to find no fluorine for any sample that contains no fluorine. This suggests the use of Occam's razor principle[1] (*assumptions should not be multiplied beyond necessity*), hence the second linear regression with forcing a zero-offset. The slope of this linear fit is 1.0(1), that is, unity within the uncertainties, and this is an expectable result indicating that the two methods compare very well.

[1] William of Ockham (or Occam), 1285-1347, was known for his extensive use of the principle: *non sunt multiplicanda entia praeter necessitatem* (entities are not to be multiplied except of necessity). This principle is often called the *principle of parsimony*. It underlies all scientific modelling and theory building. It admonishes us to choose from a set of otherwise equivalent models of a given phenomenon the simplest one. See [Gar91] for an interesting application of this principle to Bayesian

A relatively good agreement is then found when comparing the XRF and RBS results when using the O-fixed model. Two points in Figure 6-9 are somewhat out, that is, samples #4 #9. The significant discrepancy observed for these two samples may be due to an either more or less sensitivity to beam damage, and/or to uniformity of the films (only sample #3 was submitted to NRA and found to be uniform: the other samples were then assumed to be so). Also, the RBS spectral shape of these samples did not seem consistent with the other spectra in terms of spectral height of the different signals, and this indicates that something might have gone wrong with these samples.

An important result from this study, as can be seen from Table 6-6 and Figure 6-9, is that the F atoms do not appear to substitute for the O atoms. There is a good agreement between XRF and O-fixed model RBS results, and O-fixed results are systematically 68% lower than O-free results: the correlation between XRF and O-free model RBS results is linear but with a slope of 0.69(7), i.e. far from unity.

6.6 Summary

RBS together with an iterative data handling method were used to measure low-fluorine content silicon-oxide samples. This accurate method, which has as a parameter the F content that is extracted iteratively, was described in detail. The IBA DataFurnace code for fitting RBS data was used to start the iterative process by giving as information the thickness of the films.

Evolution of F atoms due to ion beam irradiation was studied using NRA and accounted for. The uniformity of the films was also confirmed using NRA depth profiling.

The F concentration was determined with an estimated uncertainty of ~10% (one percentage point as the fluorine concentration is given in percentage). The uncertainty on O stopping powers is the governing uncertainty; all the other uncertainties added up to only ~0.8%. Obviously this accurate analysis would greatly benefit from reliable O energy-loss values, so would semiconductor technology as

---

probability. Ockham is now a small village about 5 miles from Guildford where the Surrey Ion Beam Centre is located.

silicon-oxide based materials are very important in this field and Si stopping powers have been recently determined at the 1% level [Bar02, Bou02] (see also chapter 4).

As a check, it would be interesting to use the DataFurnace code to fit the data by using the corrected charge values from the iterative process. Moreover, the approach of the manual data reduction method is model-dependent (chemistry has to be assumed) and a little tedious, which is a limitation (other chemistries may give satisfactory results): therefore, a further investigation using DataFurnace would be of greater reliance as such an analysis has the advantages that it is internally consistent on the one hand, and does not have to make any assumption about the stoichoimetry on the other.

CHAPTER 7

ANALYSIS OF RESIDUAL DEPOSITION IN AN ION IMPLANTER BY USING IBA TECHNIQUES

This last study bears upon the elemental characterization of residual deposition in an ion implanter. The composition of these so-called flakes along with the mechanism by which they are produced are not known, hence the importance of determining accurately their nature under a controlled set of beam conditions. The fact that the flakes were inhomogeneous, non-uniform and moreover non-flat added a level of difficulty in the analysis. For a thorough treatment, EBS and NRA are used as complementary techniques in conjunction with RBS.

7.1 Introduction

Fluorinated species are now widely used as source gases in advanced ion implantation systems because of their controllability and relative ease of operation. The extreme reactivity of fluorine can however have a deleterious effect on the source and the liners of the arc chamber, leading to the formation of deposits, which in turn can either directly or indirectly compromise the performance of the source. Formation of flakes of conducting material in and around the arc chamber is in fact a common phenomenon in discharge sources operating in reactive gases such as boron trifluoride; their production inevitably leads to a deterioration in source stability and ultimately to failure due to short circuiting of the arc. These problems

are often observed within the first ten hours of source life. It is worth noting that similar effects are not observed for hydrogenated species such as arsine (AsH_3) and phosphine (PH_3).

Figure 7-1 shows an example of the deterioration of the source during operation. The tick rate is a measure of the stability of the beam, and hence the increase in ticks indicates a progressively unstable plasma. A tick is a fast high-voltage discharge that affects the extraction of the beam. The build up of flakes may contribute also to contamination in the source chamber.

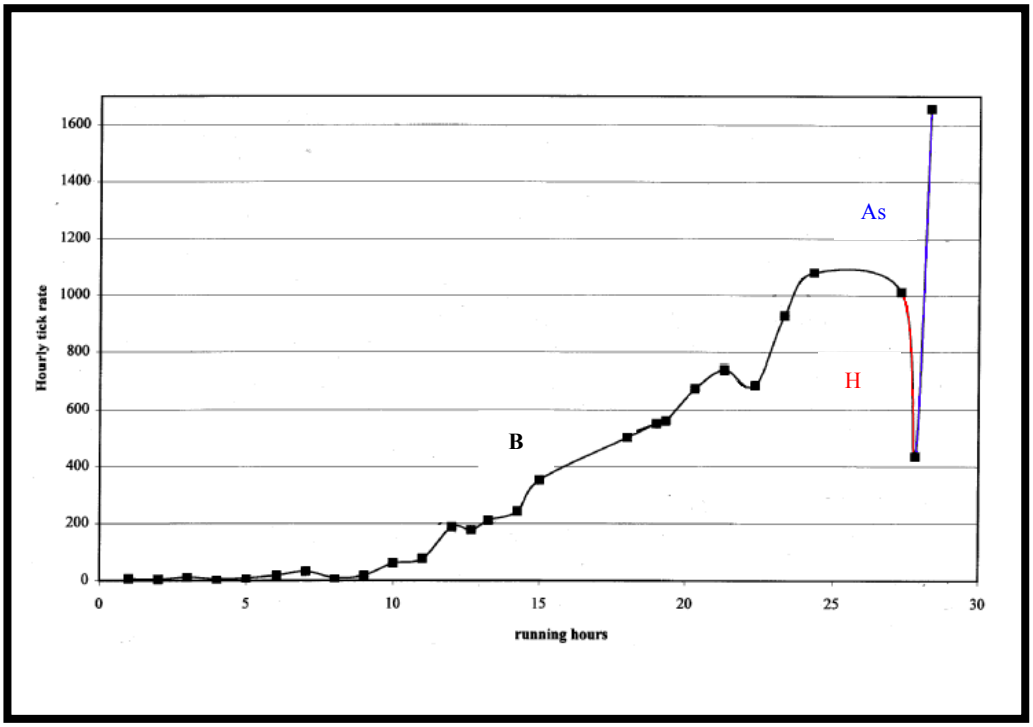

Figure 7-1 *Source deterioration on the M376 ion implanter from Applied Materials UK Ltd. [App] whilst running a 7-keV B beam (25 hours, 9.4 mA), then successively H (1 hour) and AsH_3 (1 hour).*

Although they represent a significant problem, little is known, however, about the mechanisms by which these residual depositions are produced and even their composition has never been fully identified. The purpose of the present analysis is then to determine the composition of the flakes in the source chamber and inside the arc chamber in order to find a solution for reducing the build up of flakes. The knowledge of the composition of these deposits will lead us to the determination of the processes taking place in the arc chamber and what reactions take place between

the plasma/ion beam and the surfaces (which include the extraction electrodes and arc chamber liners).

For the characterisation of such flakes, the main technique used will be RBS, which can allow us to obtain an elemental composition. Preliminary results from SEM/EDAX (Scanning Electron Microscopy/Energy Dispersive Analysis of X-rays) will be used as a guide for the RBS treatment. The analysis could not be complete without the use of two other IBA techniques: EBS will be useful for confirming the presence of carbon as a major constituent, and NRA will help identify the presence of a tiny amount of fluorine.

7.2 Experimental details

We present here an ion beam analysis of deposits from the source chamber and the cooled tube (below the cathode) of a M376 ion implanter from Applied Materials UK Ltd. [App]. A picture of the cooled tube, in which the source sits, is given in Figure 7-2. The cooled tube, source and extraction assembly all fit in the source chamber. The extraction electrodes are shown in the picture; this is where most of the flakes are thought to originate. The source was run with BF_3 as feed material for 25 hours (7 keV, 9.4 mA), and then followed with H for 1 hour and with AsH_3 for 1 hour as well (same experimental conditions as for the example on source deterioration as given in Figure 7-1). Both sides of two deposits were analysed, that is, 4 samples submitted in total, and these include:

- Sample #1: source chamber (deposit #1, side 1);
- Sample #2: source chamber (deposit #1, side 2);
- Sample #3: cooled tube — below cathode (deposit #2, side 1);
- Sample #4: cooled tube — below cathode (deposit #2, side 2).

Deposit #1 came from beneath the extraction electrode, i.e. the base of the source chamber (this cannot be seen in the picture of Figure 7-2), and deposit #2 came from inside the cooled tube below the cathode (as indicated in the picture).

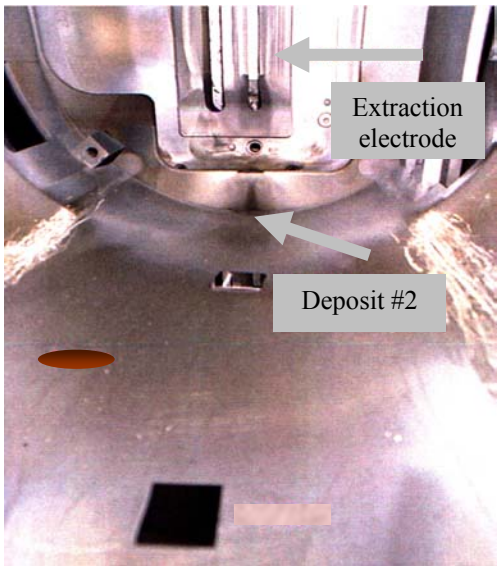

Figure 7-2 *Cooled tube of the M376 ion implanter from Applied Materials UK Ltd. in which the source sits. The cooled tube, source and extraction assembly all fit in the source chamber.*

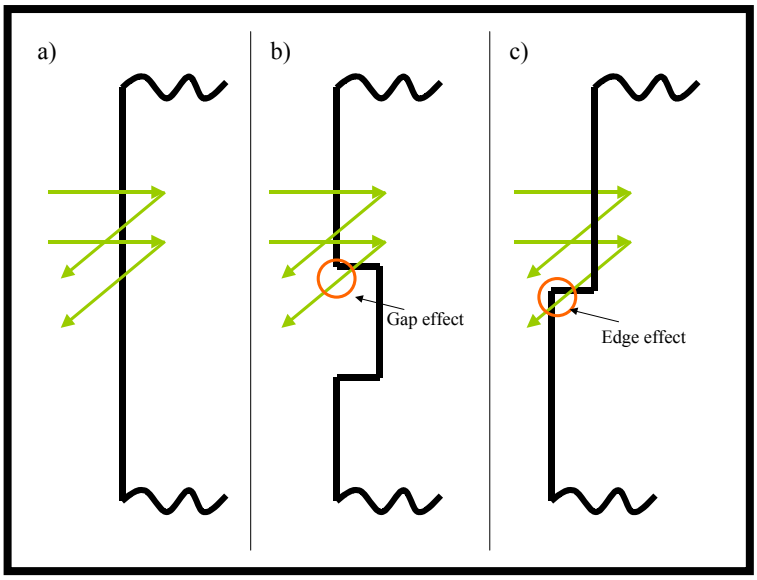

Figure 7-3 *Surface conditions and RBS events. a) Sample with flat surface: no alteration in energy loss. b) gap and c) edge effects due to roughness of the surface: energy-loss pattern is altered.*

The samples were not flat, scattered with cracks, and thought to be non-homogenous; consequently we have to bear in mind here that, even if the analysis is thoroughly done, the accuracy of the analysis is limited by the *bad* condition of the

samples. In an RBS treatment, the samples are assumed to be flat as depicted in Figure 7-3a; the incoming and outgoing paths are not altered by any gap or edge in terms of energy loss. But if a crack is in the way of some of the backscattered particles for example, as shown in Figure 7-3b and Figure 7-3c, the presence of a *gap* or an *edge* in the outgoing path will alter the amount of energy lost corresponding to the depth of the scattering event, and the interpretation of the spectrum will be erroneous. In the edge effect case, if the crack is deep enough, backscattered particles can even be stopped and will not reach the detector, leading to an erroneous decreased yield.

7.3 SEM/EDAX analysis: guide for the RBS treatment

Prior to the RBS treatment, the samples were submitted to an SEM/EDAX (Scanning Electron Microscopy/Energy Dispersive Analysis of X-rays) analysis. The mass spectra obtained are shown in Figure 7-4 and Figure 7-5. A Hitachi S3200N scanning electron microscope along with a 15-keV electron beam were used.

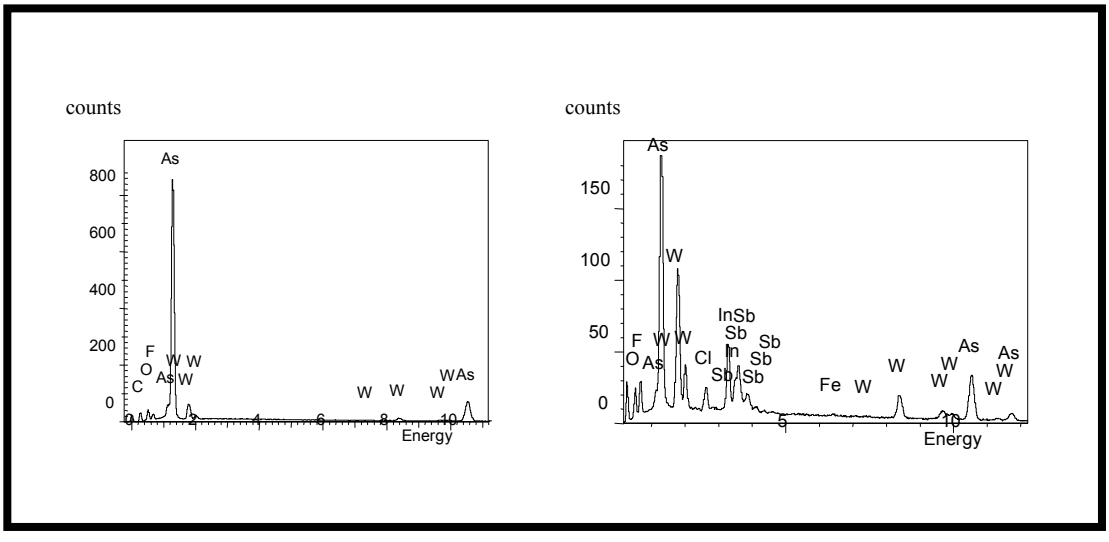

Figure 7-4 *EDAX X-ray spectra for deposit #1. Left: side 1 (sample #1). Right: side 2 (sample #2).*

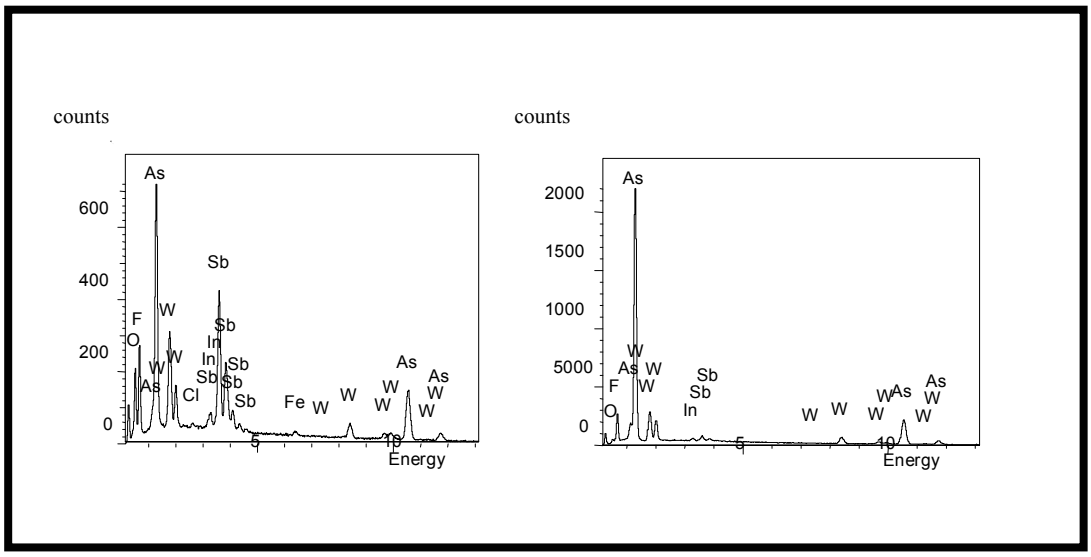

Figure 7-5 *EDAX X-ray spectra for deposit #2. Left: side 1 (sample #3). Right: side 2 (sample #4).*

The SEM/EDAX results suggest a strong presence of arsenic on both sides of the deposits. Sample #1 had 22.5% more counts of arsenic (As) than sample #2 (two sides of the same deposit), whilst sample #4 had 30% more than sample #3 (again two sides of the same deposit). On the sides with less arsenic, more tungsten (W) was detected, along with antimony (Sb) and indium (In). Some C, Fe, F and Cl were also detected. These preliminary results will be used as a guide for the RBS analysis.

7.4 RBS analysis

The RBS experiment was carried out using a 1.0-MeV $^4He^+$ beam. The energy calibration of the accelerator corresponding to this experiment was the one detailed in section B.4. The pumping system failed to make an optimal vacuum; around 10^{-5} torr could be reached, but this was enough to carry out the experiment. Since the samples were non-homogeneous and not well defined, the space of solutions of their RBS spectra is vast. For this reason, we have to proceed by trial and error to start up. Moreover, it must be pointed out that we have also to be careful in handling the data throughout the analysis as interpreting the results at the end.

We used the fitting code DataFurnace and its slow-cooling feature to analyse the collected spectra (see appendix D for more information on the DataFurnace

code). C was most likely to be the substrate (see discussion in section 7.8), and it was assumed as such. Based on preliminary SEM results, W, Sb and As were in a first attempt assumed to be the other constituents (we chose one suggested heavy element from each row of the periodic table). These assumptions led to relatively well fitted spectra. But there was room for improvement in the fitting, particularly for samples #3 and #4 (chi-squared values of 141 and 36, respectively — see end of this section for details on chi-squared values). Spectra from samples #1 and #3 showed another peak-shaped signal at lower energy (around channel 120) preceded by a dip, which indicates the presence of another heavy element (lighter than the others). We assumed it was Fe, as suggested again by SEM results. Then the fits obtained were extremely good. Without assuming the presence of Fe, it was in fact impossible to obtain any real *good* fit for samples #3 and #4. Let us have a look at the results:

➳ Sample #1: source chamber (deposit #1, side 1) — Figures 7-6 to 7-8

Fitting ROI: channels 80-300

Cooling schedule: slow cooling

Chi squared value: 1.89

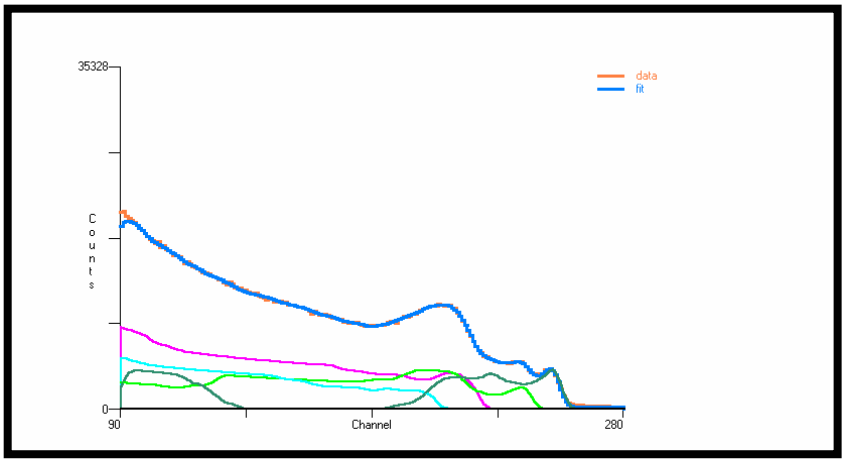

Figure 7-6 *Data (orange) and fitted (blue) spectrum for sample #1 (source chamber, side 1). Partial fitted spectra: As (pink), C (red), Sb (green), Fe (cyan), W (navy).*

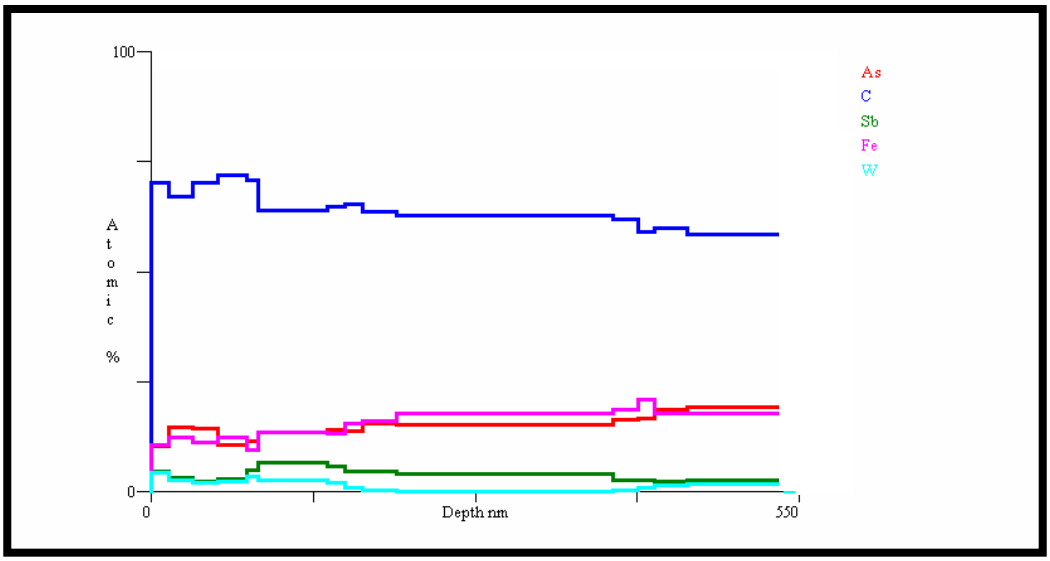

Figure 7-7 *Full scale (0-100 at.%) depth profile of sample #1 (source chamber, side 1).*

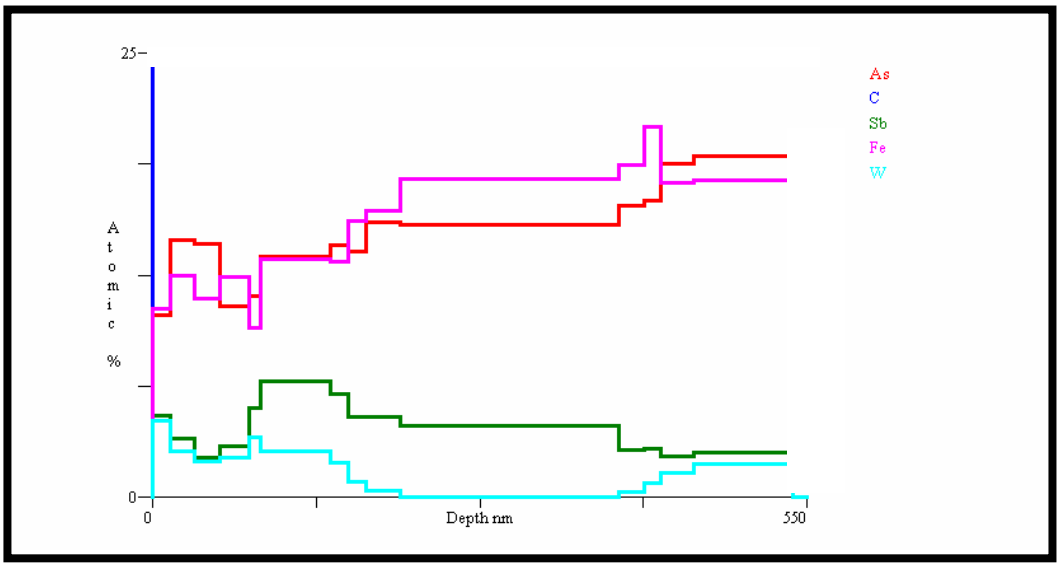

Figure 7-8 *Magnification (0-25 at.%) of Figure 7-7.*

➳ Sample #2: source chamber (deposit #1, side 2) — Figures 7-9 to 7-11

Fitting ROI: channels 80-300

Cooling schedule: slow cooling

Chi squared value: 1.81

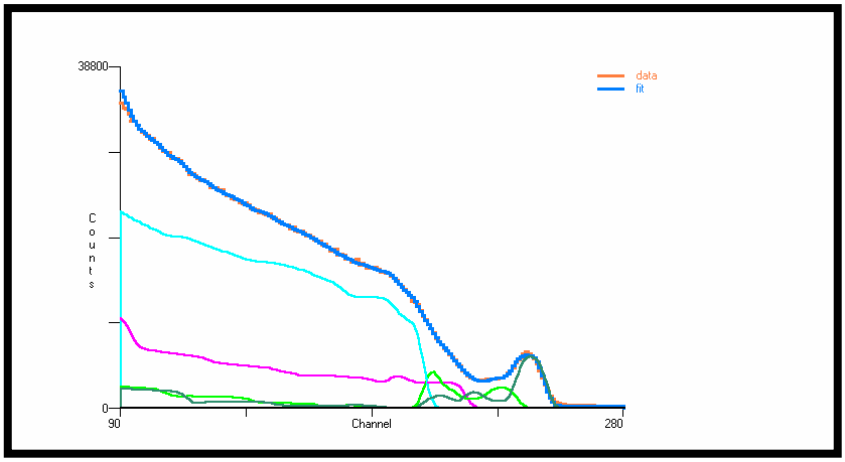

Figure 7-9 *Data (orange) and fitted (blue) spectrum for sample #2 (source chamber, side 2). Partial fitted spectra: As (pink), C (red), Sb (green), Fe (cyan), W (navy).*

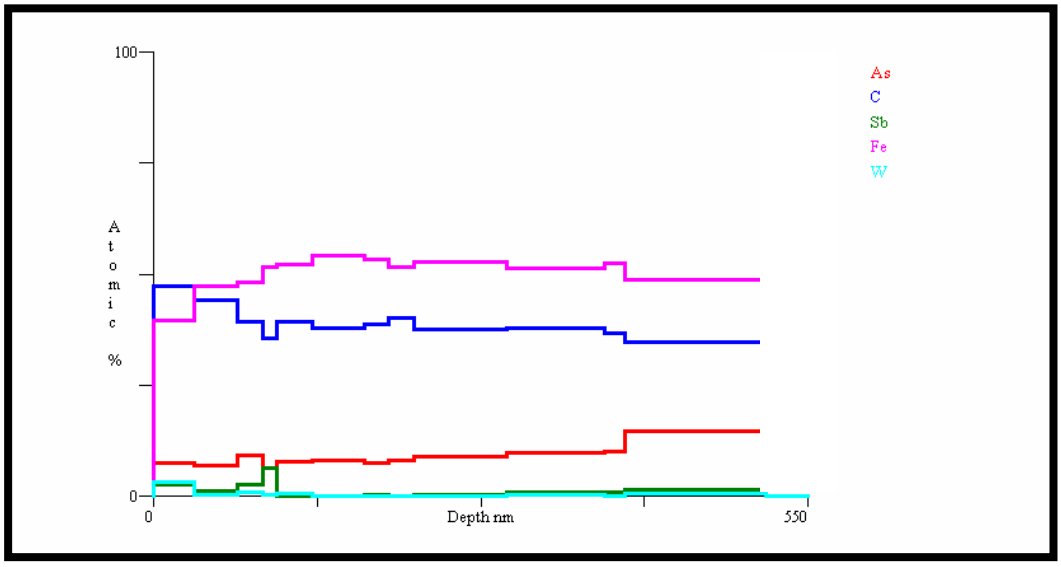

Figure 7-10 *Full scale (0-100 at.%) depth profile of sample #2 (source chamber, side 2).*

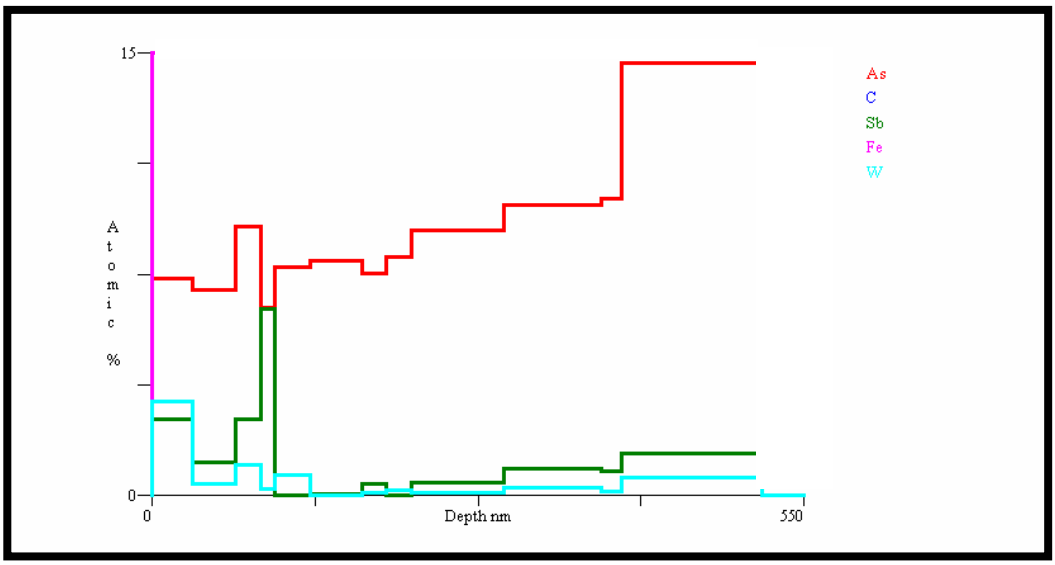

Figure 7-11 *Magnification (0-15 at.%) of Figure 7-10.*

➳ Sample #3: cooled tube — below cathode (deposit #2, side 1) — Figures 7-12 to 7-14

Fitting ROI: channels 80-300

Cooling schedule: slow cooling

Chi squared value: 5.75

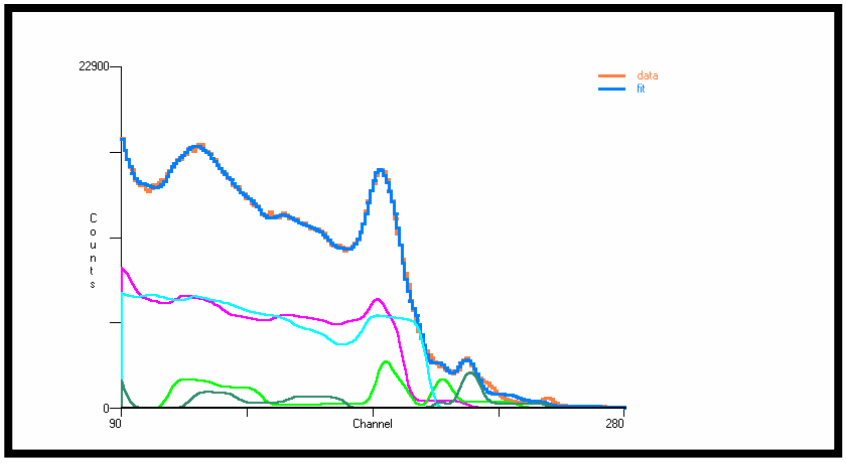

Figure 7-12 *Data (orange) and fitted (blue) spectrum for sample #3 (cooled tube — below cathode, side 1). Partial fitted spectra: As (pink), C (red), Sb (green), Fe (cyan), W (navy).*

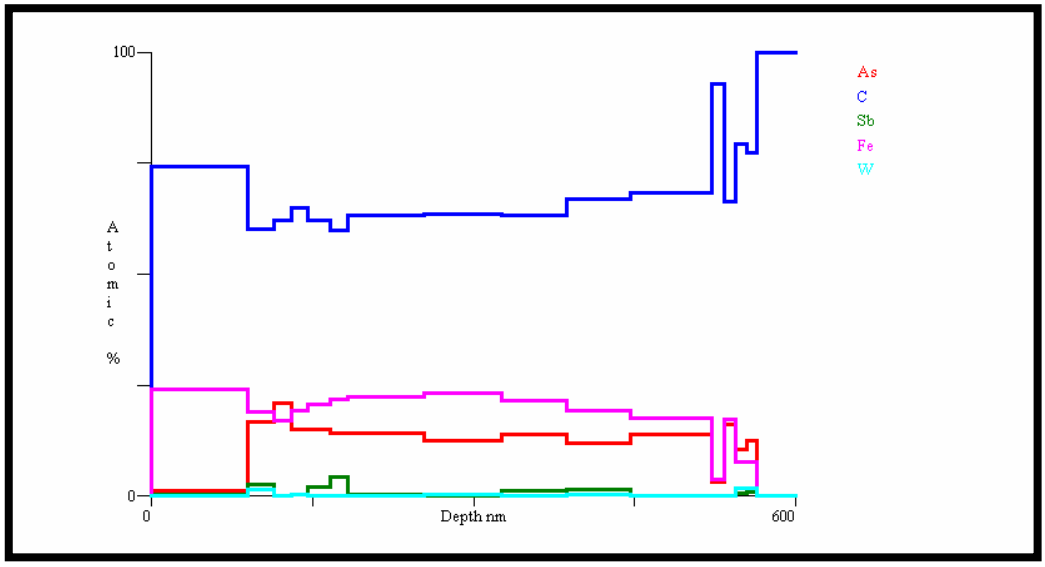

Figure 7-13 *Full scale (0-100 at.%) depth profile of sample #3 (cooled tube — below cathode, side 1).*

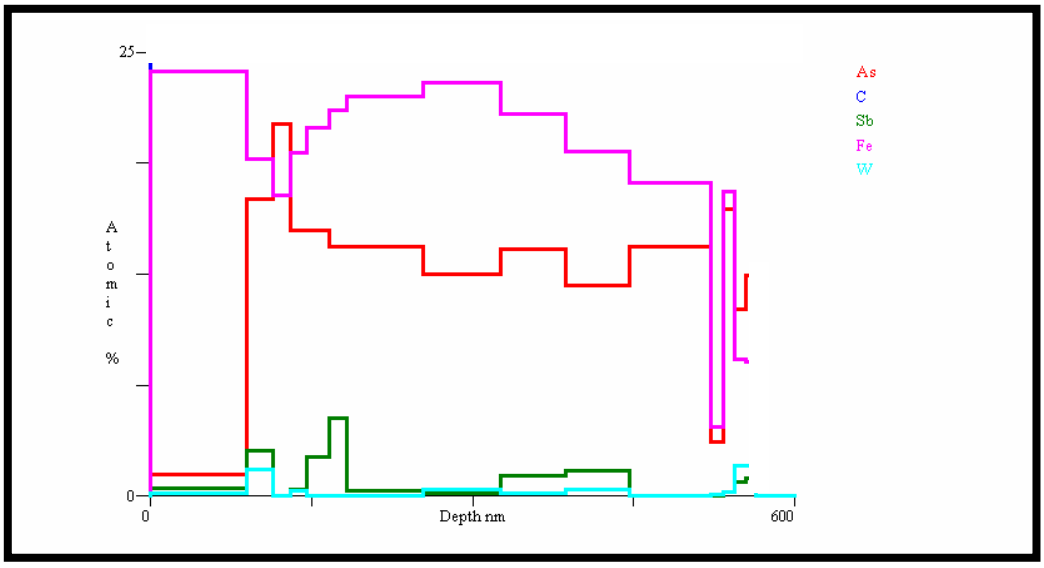

Figure 7-14 *Magnification (0-25 at.%) of Figure 7-13.*

➳ Sample #4: cooled tube — below cathode (deposit #2, side 2) — Figures 7-15 to 7-17

Fitting ROI: channels 120-300

Cooling schedule: slow cooling

Chi squared value: 1.80

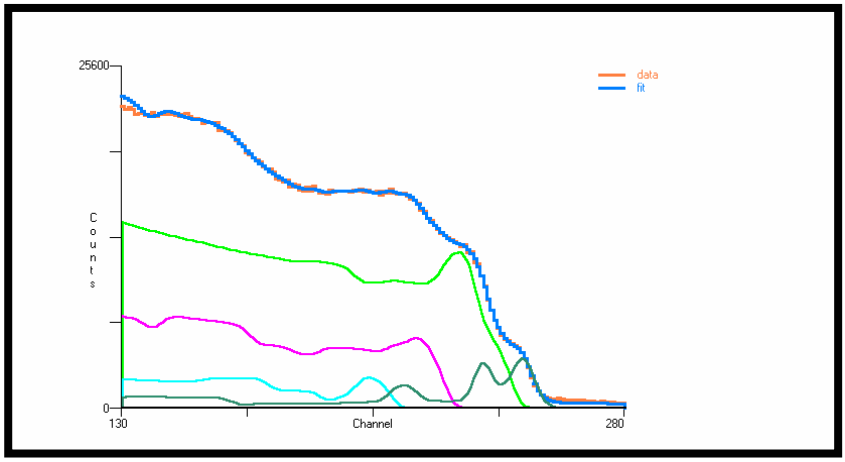

Figure 7-15 *Data (orange) and fitted (blue) spectrum for sample #4 (cooled tube — below cathode, side 2). Partial fitted spectra: As (pink), C (red), Sb (green), Fe (cyan), W (navy).*

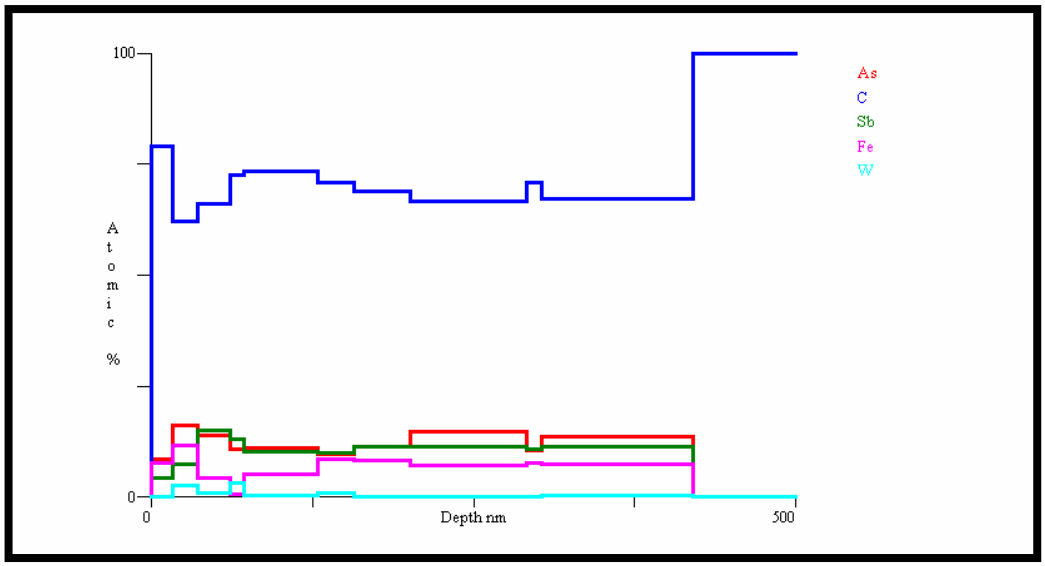

Figure 7-16 *Full scale (0-100 at.%) depth profile of sample #4 (cooled tube — below cathode, side 2).*

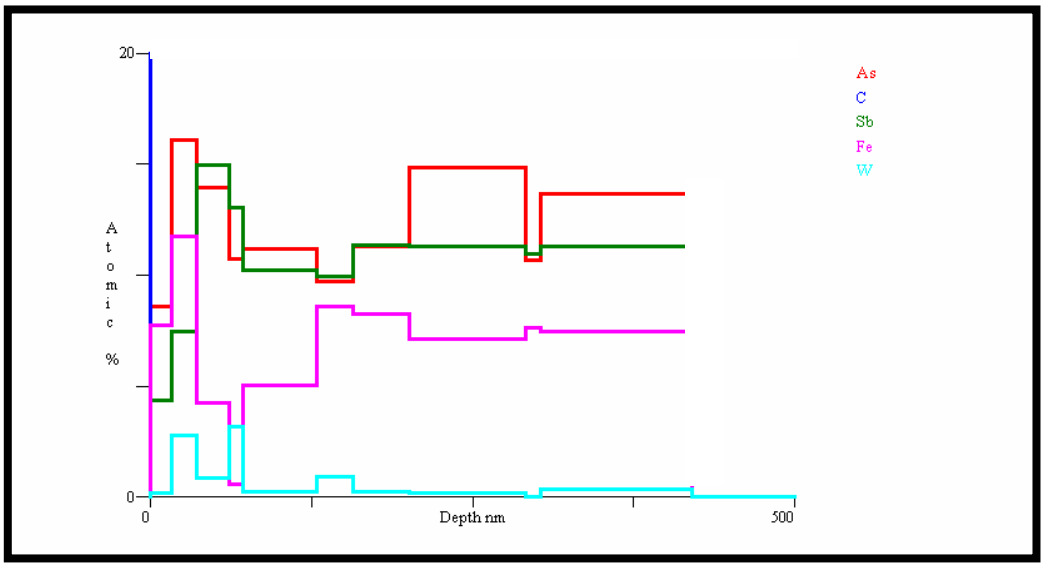

Figure 7-17 *Magnification (0-20 at.%) of Figure 7-16.*

As can be seen, the data for each sample have been fitted rather well within the regions of interest. The chi-squared values are close to unity. Let us recall that the chi-squared value compares the yield of the collected spectrum with the calculated one (see appendix D, or [Jey02] for more details). The chi-squared value is normalised in such a manner as to be approximately equal to unity for a perfect fit; generally, values less than ten are regarded as being excellent [Jey00].

The SEM/EDAX analysis suggested also the presence of In, F and Cl. Using RBS, it is impossible to discriminate between In and Sb, as they are very close elements in the periodic table and the kinematic factor does not change by much for heavy elements (see section 2.1.3); then we assumed only the presence of Sb. F and Cl are relatively light elements and thought to be of tiny concentration; adding F and/or Cl would have not given anything better or worse as fitted spectra: the code would have adjusted the parameters and come out with a good fit anyway, but with an overestimate of the amount of F and Cl at the expense of the other constituents (this has been tested). For these reasons, we have omitted both of them as constituents. However in a subsidiary experiment, using NRA, we shall be able to detect the presence of F and determine its profile; the results will be presented in section 7.6. Beforehand, let us verify whether C is really the substrate material, using backscattering together with non-Rutherford cross-sections, that is, EBS (Elastic Backscattering Spectrometry — which was described in section 2.1.4.2).

7.5 EBS analysis for C detection (samples #3 and #4)

7.5.1 C detection using EBS

The cross-section of H on C is no longer Rutherford at 1.75 MeV. It is in fact sixtyfold the Rutherford cross-section; this means the C signal is greatly enhanced when using a proton beam at 1.75 MeV as compared to a lower incident energy. Thus we can use this non-Rutherford behaviour to validate the presence of carbon in the samples.

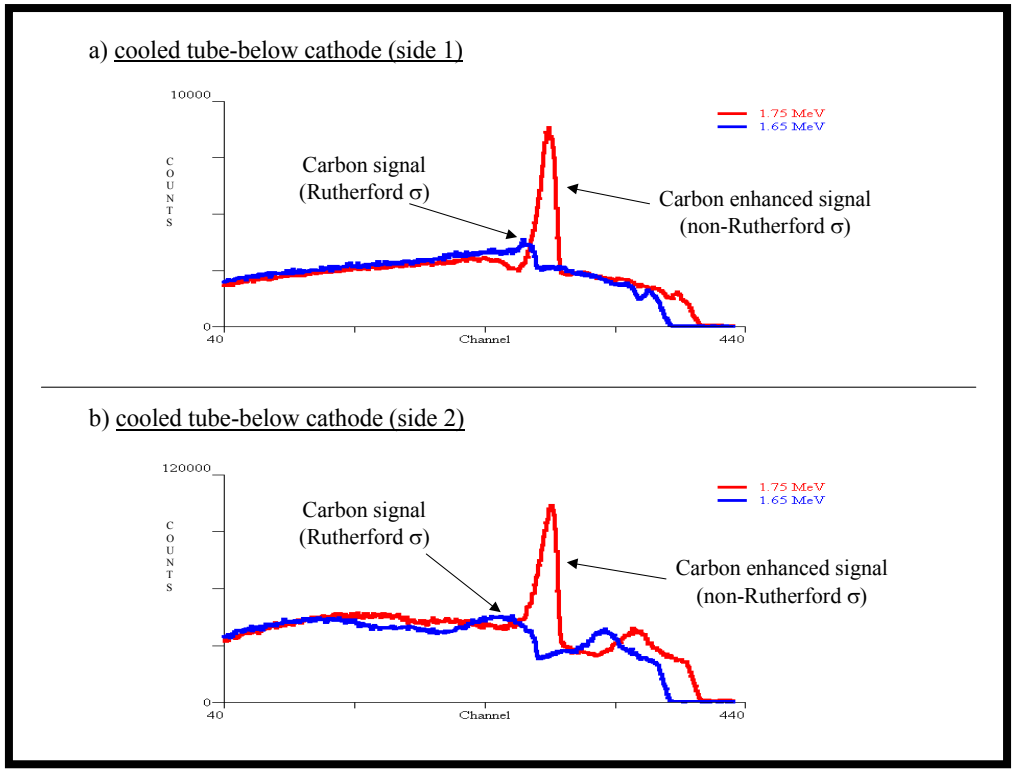

Figure 7-18 *1.65 and 1.75 MeV proton beam backscattering spectra of samples a) #3 and b) #4. The enhanced signal around channel 280 at 1.75 MeV is due to non-Rutherford cross-sections of C; therefore this confirms the assumption of C as a constituent.*

We have bombarded samples #3 and #4 with protons at 1.65 MeV, and then at 1.75 MeV. Figure 7-18 shows the different normalised spectra obtained. First it can be observed that the spectra at 1.65 MeV are shifted towards lower energies as expected. And the 1.65 and 1.75 spectra present the same shape except from a huge

signal around channel 280 for the latter, which can correspond only to a non-Rutherford enhanced C signal. The presence of C inside the samples is then confirmed.

7.5.2 EBS analysis of samples #3 and #4

The EBS spectra are thought to contain more information than the RBS spectra collected and presented in section 7.4, due to the fact that the enhanced non-Rutherford signal for C is likely to play a favourable role in interpreting the spectra and resolving the ambiguity (C is measured more *directly*). For this reason, we have analysed (fitted) again samples #3 and #4 using the EBS spectra. Here are the results:

➳ Sample #3: cooled tube — below cathode (deposit #2, side 1) — Figures 7-19 and 7-20

Fitting ROI: channels 160-430

Cooling schedule: normal cooling

Chi squared value: 4.35

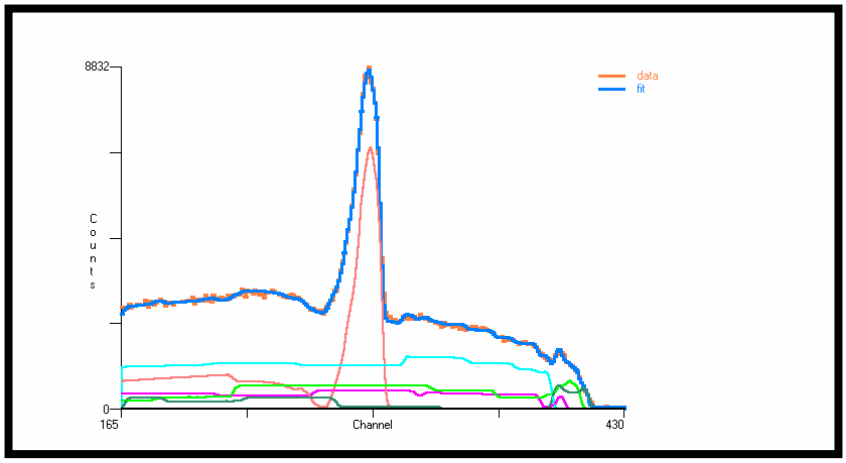

Figure 7-19 *Data (orange) and fitted (blue) EBS spectrum for sample #3 (cooled tube — below cathode, side 1) Partial fitted spectra: As (pink), C (red), Sb (green), Fe (cyan), W (navy).*

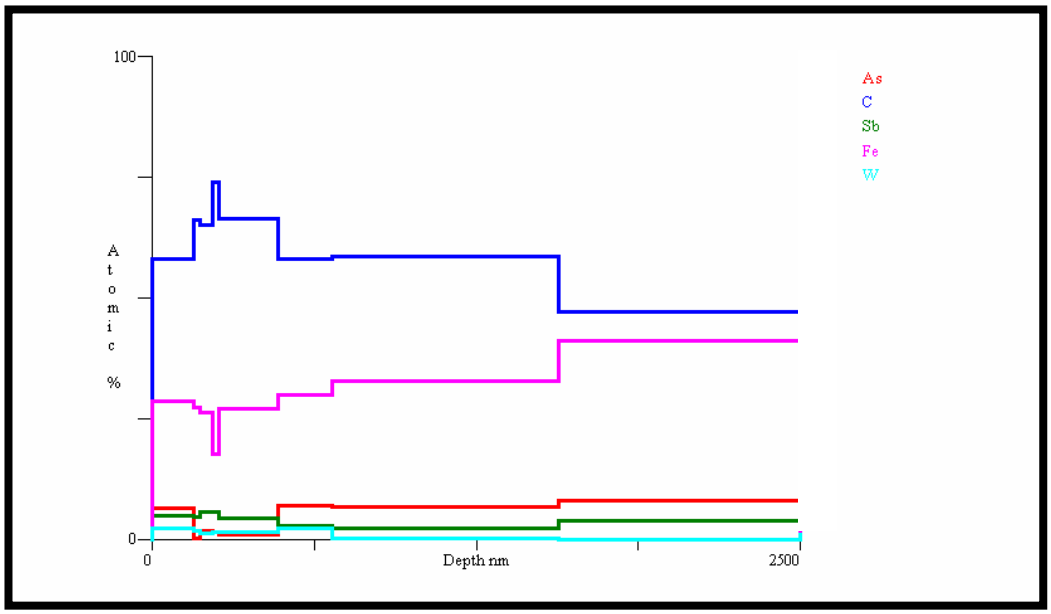

Figure 7-20 *Full scale (0-100 at.%) depth profile of sample #3 (cooled tube — below cathode, side 1).*

➳ Sample #4: cooled tube — below cathode (deposit #2, side 2) — Figures 7-21 and 7-22

Fitting ROI: channels 160-430

Cooling schedule: normal cooling

Chi squared value: 5.51

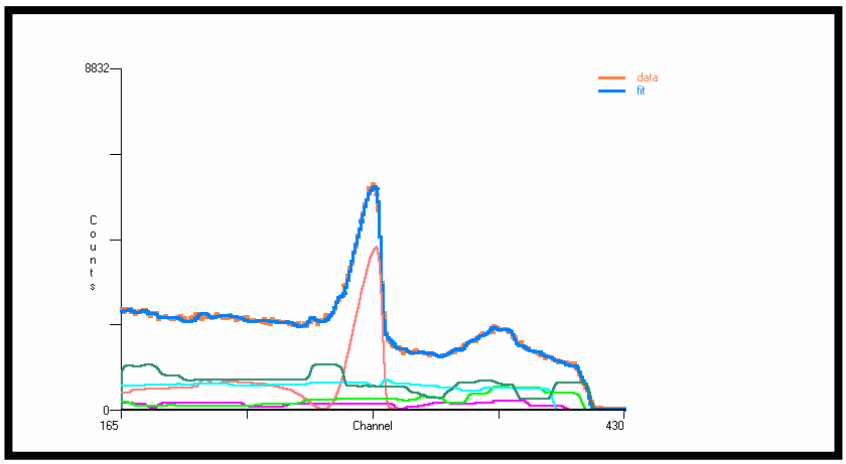

Figure 7-21 *Data (orange) and fitted (blue) EBS spectrum for sample #4 (cooled tube — below cathode, side 2) Partial fitted spectra: As (pink), C (red), Sb (green), Fe (cyan), W (navy).*

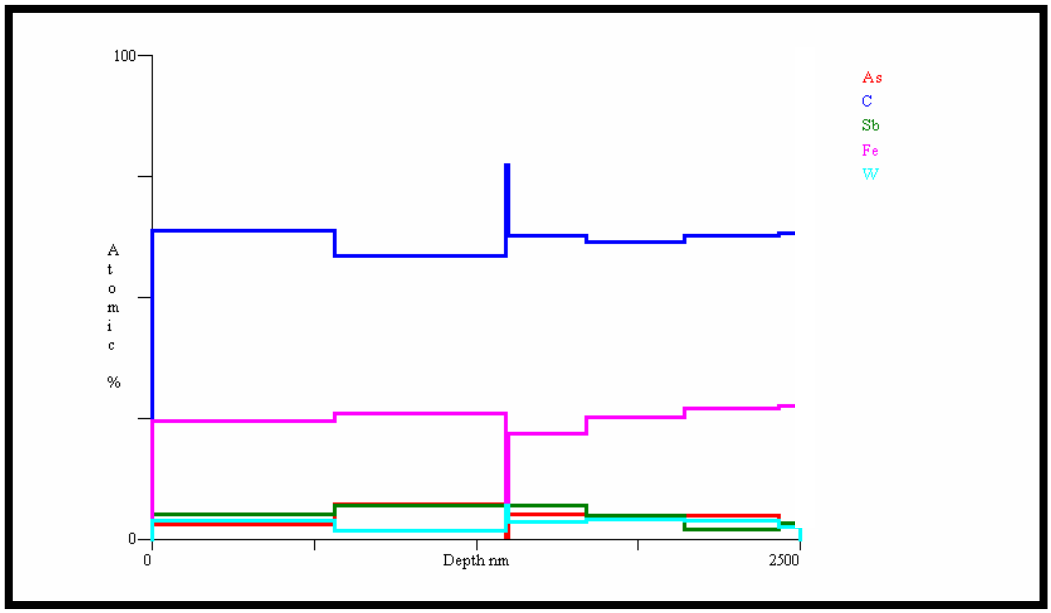

Figure 7-22 *Full scale (0-100 at.%) depth profile of sample #4 (cooled tube — below cathode, side 2).*

As can be observed, the different elements are distributed relatively uniformly throughout the samples, and the results are surprisingly quite similar to those obtained from the RBS analysis in section 7.4. Since the EBS spectra were thought to contain more information, we were expecting major differences between RBS and EBS results.

Nevertheless, there are some little differences. For the heavier elements (Sb, W), the EBS results show a more uniform distribution. Also less C and As are found from the EBS analysis. The RBS treatment gave a significantly different amount of Fe for samples #3 compared to the amount found for sample #4, that is, ~20% and less than 10%, respectively. From the EBS analysis, roughly the same quantity (25-30%) of Fe is found for both samples. The latter result is more *believable*, as samples #3 and #4 come actually from each side (front and back) of the same deposit (cooled tube — below cathode). Besides, the general features of the two EBS depth profiles (from the two samples) are quite similar, which is consistent.

Only a *normal cooling*, as opposed to a *slow cooling* for the RBS treatment, was needed to obtain an excellent fit of the collected EBS spectra. A depth up to 2500 nm was probed with the EBS 1.75-MeV proton beam, as opposed to 550 nm for the RBS 1.5-MeV He beam. These two observations, added to the fact that the two

depth profiles obtained are quite consistent, make us think that the EBS spectra really contain more information.

7.6 Detection of F using NRA (sample #2)

It is possible to detect the presence of and quantify the amount of fluorine in the samples by calling upon NRA (Nuclear Reaction Analysis — which was studied in section 2.1.4.3). We have used the $^{19}F(p,\alpha\gamma)^{16}O$ resonance at 872.1 keV together with a reference sample for this purpose. But since the samples were very brittle and had already been used for previous analysis (RBS and EBS), we could only submit sample #2 to NRA. Again a proton beam is used, but we are now interested in counting the gammas (γ_1= 6.13, γ_2= 6.72 and γ_3= 7.12 MeV) produced by the nuclear reaction mentioned above.

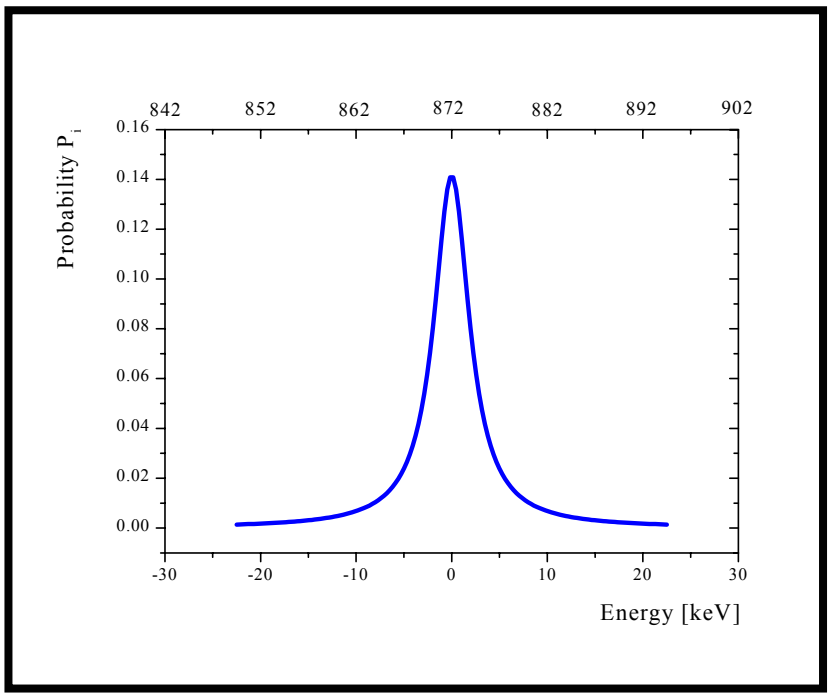

Figure 7-23 *Excitation curve for the reaction $^{19}F(p,\alpha\gamma)^{16}O$ at 872.1 keV. Γ = 4.5 keV.*

7.6.1 Resonance curve

Nuclear resonance curves are not gaussian-shaped, but lorentzian. The 872.1-keV F resonance curve has a width Γ (FWHM) of 4.5 keV. We have simulated this curve from -22.5 to 22.5 keV (which corresponds to 10 Γ) and centred at 0; it is shown in Figure 7-23. The total integral (from -∞ to ∞) is normalised to 1. The curve was generated with 150 points, that is, one point each 0.3 keV.

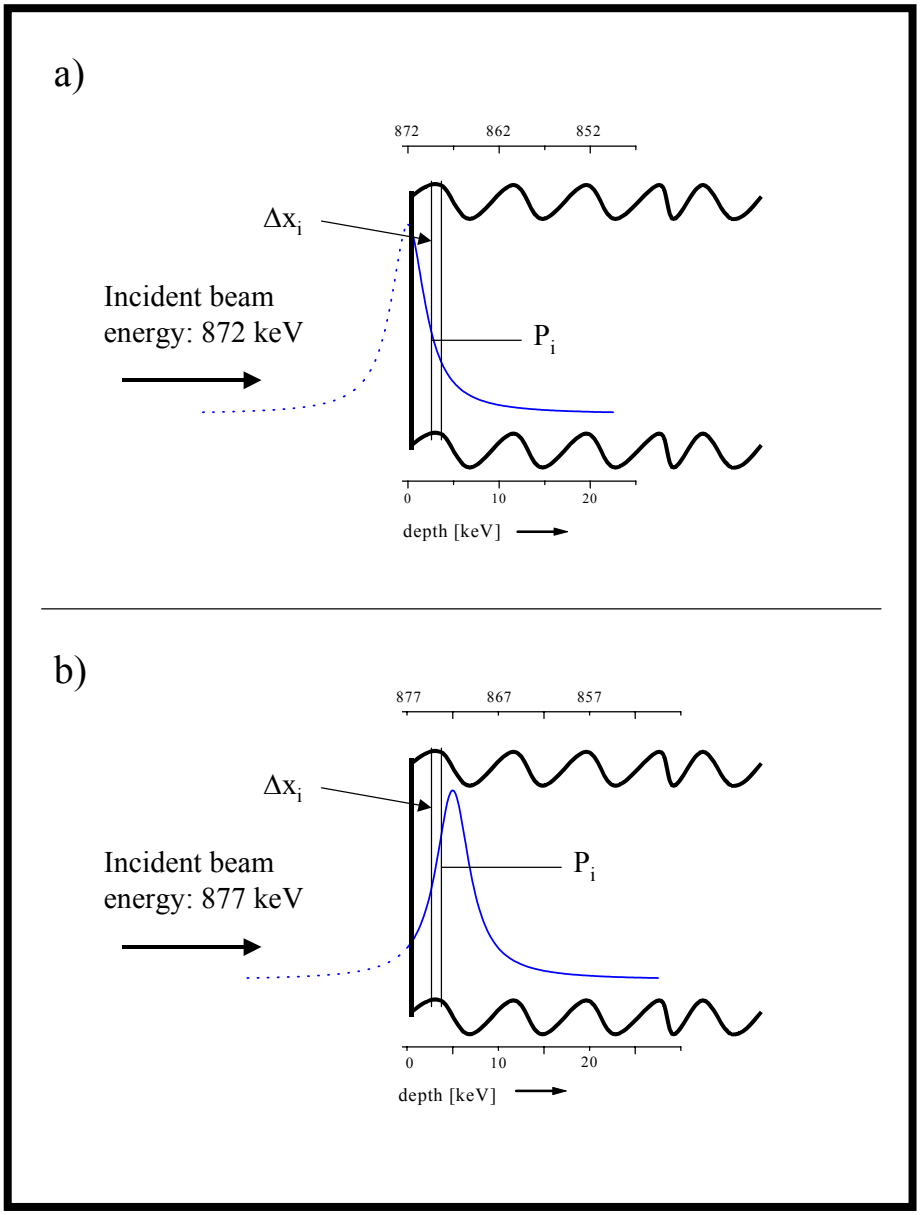

Figure 7-24 *Interaction densities of the pγ nuclear reaction on fluorine throughout the sample for an incident beam energy of a) 872 and b) 877 keV.*

In order to perform quantitative analysis as accurately as possible, we need to take into account the fact that the 872.1-keV F resonance curve is not sharp, and moreover is not gaussian but lorentzian. As a matter of fact, one feature of the latter is its long tails; 99.7% of a gaussian curve integral is covered by 3 Γ whereas 10 Γ scarcely embrace 93.7% of a lorentzian. Since the incident protons lose energy as they traverse matter, for a given incident beam energy around the resonance the number of gammas detected will be a convolution (sum) of all the gammas emitted at each slab Δx_i inside the sample proportionally to the probability of interaction P_i at the depth of the given slab (this probability being given by the height of the excitation curve at the corresponding depth). This situation is depicted in Figure 7-24 with two different incident beam energies.

In Table 7-1 we have listed the integral, labelled I_i, from different regions of interest of the 872.1-keV F resonance curve as presented in Figure 7-23. In Table 7-2 we have calculated the mean probability, labelled $<P_j>$, from different regions of interest; the probability at the maximum height of the curve was normalised to 1. We will need these relative values in the next sections in order to make a proper treatment of the data.

Table 7-1 *Integral from different regions of interest of the 872.1-keV F resonance curve as presented in Figure 7-23.*

Label	*Region of interest [keV]*		*Integral*
	from	*To*	
I_1	-7.0 (or 865.0)	0 (or 872.0)	0.415
I_2	-2.0 (or 870.0)	5.0 (or 877.0)	0.609
I_3	-5.0 (or -867.0)	0 (or 872.0)	0.353
I_4	0 (or 872.0)	5.0 (or 877.0)	0.353
I_5	-4.0 (or 868.0)	0 (872.0)	0.326
I_6	1.0 (or 873.0)	5.0 (or 877.0)	0.228
I_7	5.5 (or 877.5)	9.5 (or 881.5)	0.048

Table 7-2 *Mean probability from different regions of interest of the 872.1-keV F resonance curve as presented in Figure 7-23.*

Label	*Region of interest [keV]*		*Mean Probability*
	From	*To*	
$<P>_1$	0 (or 872.0)	1.5 (or 873.5)	0.88
$<P>_2$	1.5 (or 873.5)	3.0 (or 875.0)	0.51
$<P>_3$	3.0 (or 875.0)	4.5 (or 876.5)	0.27
$<P>_4$	4.5 (or 876.5)	6.0 (or 878.0)	0.15
$<P>_5$	0 (or 872.0)	5.0 (or 877.0)	0.51

7.6.2 Reference F sample: determination of the detection of the sensitivity at the surface

We first need to evaluate the detection sensitivity (in counts·at.$^{-1}$·cm^2·μC^{-1}) at the surface from a reference sample using a 872-keV proton beam in order to determine as accurately as possible the fluorine content of the submitted sample #2. The reference sample used was our accelerator energy calibration sample, which is an aluminium foil exposed to HF vapour for few seconds; a very thin layer of F is then deposited on top of the foil.

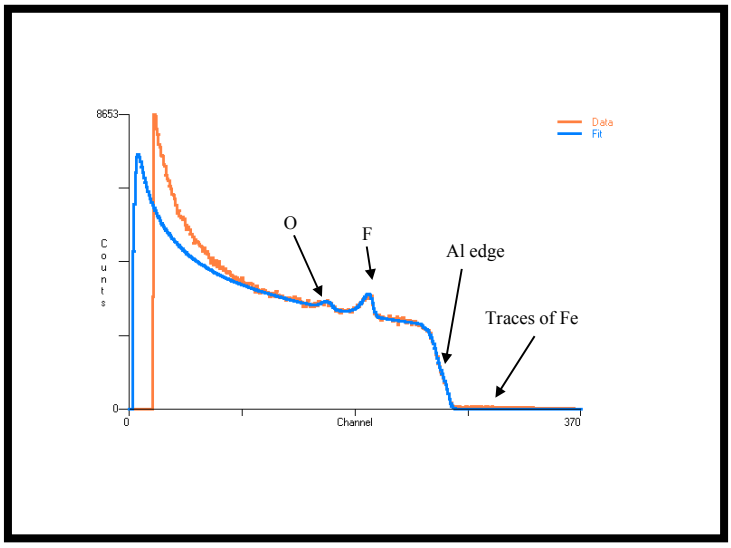

Figure 7-25 *RBS collected and fitted spectra of the reference F sample.*

An RBS spectrum of the reference sample was first collected using a 1.5-MeV He beam in order to determine its depth profile. It is presented together with the fit obtained in Figure 7-25. This sample was a simple kitchen Al foil, which we cleaned before fluorination. Naturally, it is not made of pure Al; there are traces of Fe in the foil as indicated by the residual flat signal at higher energy than the Al substrate edge. But since the Fe content is low we neglected it in the fitting process. We just assumed an O contaminated Al substrate topped with a F loaded surface layer.

a)

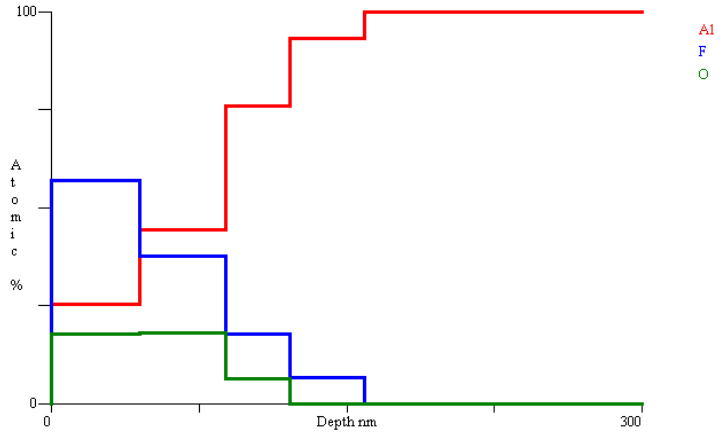

b)

Layer	t (at/cm2)	t (nm)	d (at/cm3)	at. % Al	F	O
1	192	44.7	4.30	25.5	56.9	17.7
2	209	43.9	4.77	44.3	37.6	18.0
3	179	32.8	5.47	75.9	17.7	6.4
4	219	37.3	5.85	93.2	6.8	0.0
5	35428	5882.2	6.02	100.0	0.0	0.0
		Total amount (at/cm2)		3.59E+04	234	83.2

Figure 7-26 *a) Depth profile of the reference F sample for the first 300 nm. b) Details of the whole depth profile obtained.*

The depth profile for the first 300 nm obtained from the fitted spectrum is shown in Figure 7-26a. The details of the depth profile is given in Figure 7-26b. As can be seen, the outcomes of the fit suggest that the fluorine content is distributed in 4 layers of 44.7, 43.9, 32.8 and 37.3 nm with concentration of 56.9, 37.6, 17.7 and 6.8 at.% (or 109.1, 78.8, 31.7 and 14.9×10^{15} at/cm^2), respectively. Of course, this discreteness is not real; this thin F layer is believed to be more realistically continuously decreasing with depth. We have calculated the depth of the 4 layers in keV for a 872-keV proton beam, and we have obtained 1.4, 1.5, 1.4 and 1.6 keV; they can be more *conveniently* approximated as being 1.5 keV each.

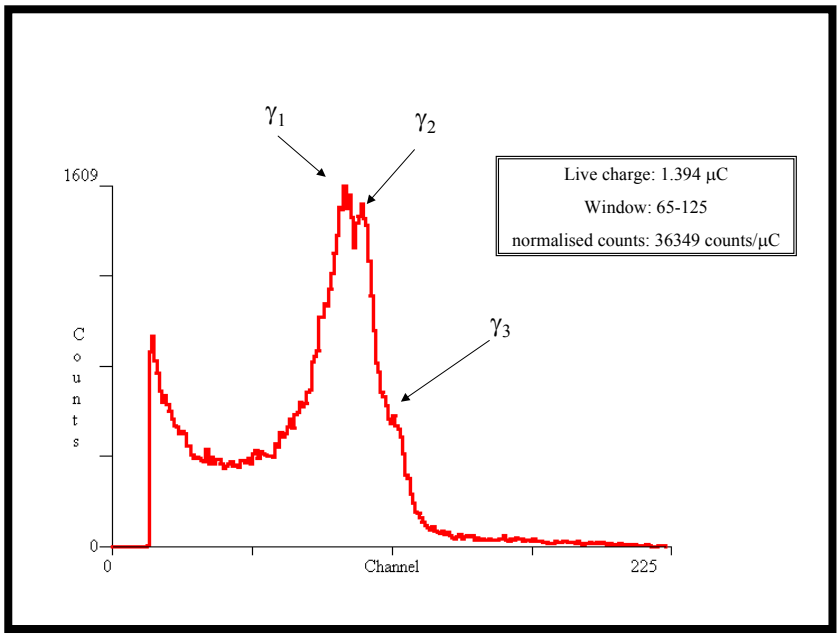

Figure 7-27 *872.1-keV $^{19}F(p,\alpha\gamma)^{16}O$ NRA spectrum (counted gammas) from the reference F sample.*

Using a 872 keV proton beam on the reference sample, we collected an NRA spectrum of the counted gammas. It is given in Figure 7-27. The horizontal axis is an energy scale. The 3 gammas emitted in the cascade can be identified. The background signal at low energy comes mainly from Compton effect (reduction in energy of high-energy photons when they are scattered by [free] electrons, which thereby gain energy) inside the scintillation detector. We have selected a window between channels 65 and 125; the normalised integrated counts for this window is T = 36349 counts/μC.

The detection sensitivity at the surface S_0 in counts·at.$^{-1}$·cm^2·μC^{-1} can be obtained from:

$$S_0 \sum_k x_k < P >_k = T \,, \tag{7-1}$$

where: the subscript k refers to the layer; x_k and $<P>_k$ are the concentration (in at/cm^2) and the mean interaction probability (as described in the previous section) for the corresponding layer k, respectively; and T is the normalised integrated counts (in counts/μC). In our case, we have 4 layers (k varies from 1 to 4), each of them approximately 1.5 keV thick. The values $<P>_1$, $<P>_2$, $<P>_3$ and $<P>_4$ listed in Table 7-2 can then be used. As a result, the detection sensitivity at the surface for an incident proton beam of 872 keV is found to be $S_0 \approx 250$ counts·10^{-15} at.$^{-1}$·cm^2·μC^{-1}.

7.6.3 F content of sample #2

From sample #2, 4 NRA spectra were acquired at 4 different energies, that is, at 850.0, 872.0, 877.0 and 881.5 keV. The normalised spectra are shown in Figure 7-28a. The spectrum at 850.0 keV can be regarded as a background spectrum since the resonance occurs at 872.1 keV. The normalised integrated counts T from the same window as for the reference sample have been calculated for each of the spectra and are listed in Figure 7-28b. The ratios T_{872} to T_{877} and $T_{881.5}$ are also given.

Since we have no idea of the varying composition of fluorine throughout the sample, for simplicity we assume a uniform composition (with depth). Having said that, we expect the ratio T_{872}/T_{877} to be smaller than unity if the F extends over a depth of 5 keV, since the ratio I_3/I_4 (see Table 7-1) is unity and, for instance, the ratio I_1/I_2 is equal to 0.68 and suggests a depth range of 7 keV. But the ratio T_{872}/T_{877} is 1.47, which means that the F must be present at a depth surely not more than 5 keV. The ratio I_5/I_6, which is for a depth range of 4 keV, is equal to 1.43; this suggests that the F content covers a depth scarcely less than 4 keV. But if it was so, the ratio $T_{872}/T_{881.5}$ should be around 6.79 as suggested by the ratio I_5/I_7, and it is embarrassingly equal to 1.69. This can be explained as following: we do not expect the sample to be homogenous, so some parts of the sample are likely to contain F up to a depth of 7 or even 8 keV in such a manner as to make the ratio $T_{872}/T_{881.5}$ lower than expected from the previous assumptions. At the light of this analysis, estimating

a F depth range which oscillates between 2 and 8 keV would be realistic. This means an average depth of around 5 keV.

a)

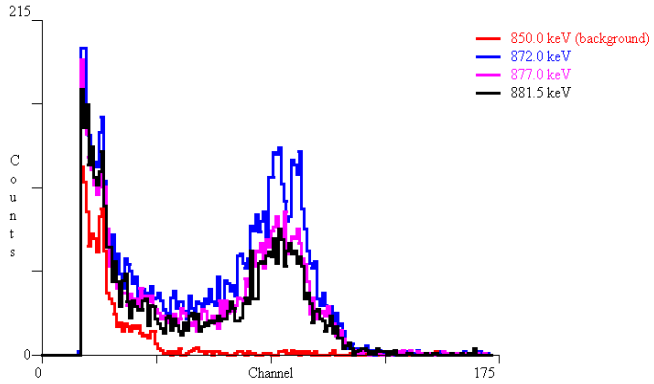

b)

Label	Normalised integrated counts (window: 65-125) [counts/μC]	Ratio T_{872}/T_i
T_{850}	34	—
T_{872}	2365	—
T_{877}	1612	1.47
$T_{881.5}$	1397	1.69

Figure 7-28 *a)* $^{19}F(p,\alpha\gamma)^{16}O$ *NRA normalised spectra (counted gammas) from sample #2 (source chamber, side 2) at different incident energies. b) Table of normalised integrated counts* T *for each energy and their ratio* T_{872} *to* T_i.

Now we can use equation (7-1) to determine the fluorine content. This time, since we assumed a linear composition with depth, the number of layers k is simply 1, and it has been estimated to be 5 keV thick. The mean interaction probability $<P>$ for a 5 keV layer is given by $<P>_5$ in Table 7-2, and it is 0.51. The normalised integrated counts T_{872} is 2365 counts/μC as given in Figure 7-28b, and the detection sensitivity at the surface S_0 is 250 counts·10^{-15} at.$^{-1}$·cm^2·μC^{-1} as calculated further above. Then from equation (7-1) we obtain a concentration x of about 18.7×10^{15} at/cm^2.

The depth of 5 keV corresponds to approximately 500×10^{15} at/cm^2 (or 55 nm) assuming the depth profile obtained from DataFurnace and the RBS analysis in section 7.4. This means that the fluorine content is around 3.5 at.% within the first 55 nm.

7.7 Analytical summary

This analytical study on residual deposits from an ion implanter is an interesting case of complementary use of many analytical methods. Four techniques, namely SEM/EDAX, RBS, EBS and NRA, were used to determine the elemental composition of the so-called flakes (depositions) from the Applied Materials UK Ltd.'s M376 ion implanter. The challenge of this study lay in making an accurate treatment of such non-homogeneous, non-flat and brittle samples.

A preliminary SEM/EDAX analysis showed the presence of As, C, In, Sb, W, Fe, F and Cl. RBS depth profiles were obtained assuming the presence of these constituents, but omitting In (no possible discrimination between In and Sb) together with F and Cl (light elements of tiny concentration.— assuming their presence would have led to an overestimate of their amount at the expense of the other constituents in the fitting process). However using NRA, we were able to detect the presence of a low concentration of F restricted to the surface layer.

The EBS spectra contain more information than the RBS spectra due to the fact that the enhanced non-Rutherford cross-section for carbon played a favourable role in interpreting the spectra and resolving the ambiguity of the substrate composition (carbon is measured more directly). As a result, the EBS analysis confirmed the presence of C as a major constituent. For the heavier elements (Sb, W), the EBS results showed a more uniform distribution, and a less C and As were found. The RBS treatment gave a different amount of Fe for sample #3 compared to the amount found for sample #4, that is, 20% and less than 10%, respectively. From the EBS analysis, roughly the same quantity (25-30%) of Fe is found for both samples. The latter result is of greater reliance, as samples #3 and #4 come actually from the same flake (cooled tube — below cathode: front and back sides of deposit #1). The general features of the two EBS elemental depth profiles (from the two samples) are similar, which shows consistency.

The RBS and EBS depth profiles obtained in sections 7.4 and 7.5 are not real evidently; they can only be used as an indication of the concentration of each element present. In Table 7-3 are summarised the approximate elemental concentrations found for each sample from the whole set of RBS, EBS and NRA results. It is worth recalling that: using DataFurnace along with the Simulated

Annealing fitting algorithm, only a *normal cooling*, as opposed to a *slow cooling* for the RBS treatment, was sufficient to fit satisfactorily the EBS spectra; and a depth up to 2500 nm was probed with the EBS 1.75-MeV proton beam, as opposed to 550 nm for the RBS 1.5-MeV He beam.

Table 7-3 *Elemental concentrations for each sample as found by RBS, EBS and NRA.*

elements	*concentration [%]*						
	RBS (0-550 nm)				*EBS (0-2500 nm)*		*NRA (0-55 nm)*
	sample #1	*sample #2*	*sample #3*	*sample #4*	*sample #3*	*sample #4*	*sample #2*
As	60-70	6-14	10-20	10-15	2-10	3-6	—
C	10-20	35-45	60-75	65-75	55-65	60-65	—
In	—	—	—	—	—	—	—
Sb	2-7	0-6	0-5	5-15	2-5	2-6	—
W	0-5	0-3	0-2	0-3	0-2	2-4	—
Fe	10-20	40-55	15-24	3-10	25-35	20-28	—
F	—	—	—	—	—	—	3.5
Cl	—	—	—	—	—	—	—

This IBA study led to the determination of the elemental composition of the flakes, which reflects both the history of the implanter and the way in which these deposits were formed. Thus an attempt is made in the next section to infer the plausible origin and formation of the flakes.

7.8 Formation of the flakes: discussion

The starting point of describing the formation of the flakes based on the analysis just carried out throughout this chapter is to list the material which parts of the implanter are made of. The arc chamber liners are made from tungsten (2 side and 1 bottom liners) and graphite (2 end liners), whilst the extraction electrodes are also made from graphite. The cooled tube is made from aluminium. Stainless steel is the major material found in the rest of the implanter. We recall that a picture

of the cooled tube is shown in Figure 7-2; unfortunately, this is the only picture of the implanter that Applied Materials UK Ltd. allowed us to display.

It is thought that the most likely mechanism for the creation of the deposits is the thermal cycling that the components undergo in the source region. This is facilitated by diffusion of reactive and inert gases beneath the surface of the liners (carbon and tungsten), and electrodes (carbon). When these gases exceed their relative solid solubility in the liner, they start to form bubble-like structures, and subsequently cause exfoliation of the liners to produce flakes.

The fact that the extraction electrodes are made of graphite explains the strong presence of carbon detected with EBS, hence the assumption that carbon was the main constituent.

A relatively small amount of fluorine was detected, even though BF_3 was implanted, and this could be due to the fact that hydrogen was run for one hour before the arsenic, which clean the system. Basically any fluorine present would react with the hydrogen and be pumped away.

The use of stainless steel in various parts of the source region may explain the presence of iron. These parts can get extremely hot due to heat from the plasma or back streaming electrons (which have energies between 20-30 keV). Other materials have been tried (aluminium and nickel), which eliminate the iron but create other problems.

The presence of arsenic can originate from the arsine which was run for one hour immediately prior to venting the source.

The fact that antimony is detected even though it was not used in the experiment means that by employing techniques used, it is possible to determine some of the history of implantation. As a matter of fact, the ion implanter had previously been used to implant Sb (and In).

In a word, we can conclude that the carbon originates from the graphite extraction electrodes, the iron from the gas feed line and the arsenic from arsine run for one hour immediately prior to venting the source. It is assumed that the deposits were created from thermal cycling of the source components and may have facilitated by the formation of gas bubbles below the surface of the electrodes causing them to exfoliate when the bubbles reached a critical pressure.

CHAPTER 8

CONCLUSION

8.1 Summing-up of this thesis

This thesis focuses on accuracy obtainable in absolute quantitative characterisation of materials, primarily semiconductors, by using IBA (Ion Beam Analysis) methods such as RBS (Rutherford Backscattering Spectrometry), ERDA (Elastic Recoil Detection Analysis), EBS (Elastic Backscattering Spectrometry) and NRA (Nuclear Reaction Analysis). The importance of high-accuracy analysis for the development and constant miniaturisation of the semiconductor field is highlighted. Thus the ultimate goal of this work is to push the boundaries of accuracy obtainable in IBA material characterisation.

RBS is the main technique used throughout this thesis. Typically1.5 MeV He projectiles are used as a probe beam. Head-on collisions with target nuclei (Coulomb interaction) gives scattering in backward direction. This method is shown to be suitable for absolute quantitative measurements (chapter 2): From the collision kinematics, the mass of target nuclei can be identified; depth information can be obtained from the electronic energy loss of the beam in the target; and since Rutherford cross-sections are analytical, quantification of the elemental composition can be achieved. RBS is not matrix dependent, and shows 100% detector efficiency and a very small spectral distortion due to multiple scattering. A simple analytical approach is very accurate. Although RBS is not deliberately destructive, some beam damage may sometimes occur, and has to be evaluated and accounted for when it is suspected.

Incident charge and solid angle measurements are of critical importance for any accurate treatment, and these are in fact the main issues of this thesis. The analytical philosophy followed in this work is to consider the energy-loss parameterisation as the cornerstone of the calibration of the charge·solid angle product. Since RBS is generally performed using an He beam and Si-based material is the most widespread used in the semiconductor field, the starting point is to validate the parameterisation of He stopping power in Si in such a manner so as to use this latter material as a calibration standard (chapter 4). Performing an internal normalisation by calibrating the spectrum height against the silicon yield then leads to an accurate determination of the charge·solid angle product.

Apart from RBS, other analytical techniques are used in this work, namely EBS, ERDA and NRA. The theoretical framework of these IBA methods together with an exhaustive literature review on these analytical approaches in connection with accuracy issues, such as stopping powers and multiple scattering, are presented in chapter 2. The experimental set-ups and procedures are described in chapter 3, which emphasises particularly the critical aspects of work where the highest accuracy is required. This thesis introduces four distinct accurate analyses, which are developed in four separate chapters.

The first study, in chapter 4, aims at establishing the instrumentation for dosimetry on ion implanters at the 1% level for high-dose heavy implants in silicon. The motivation of such an investigation is that ion implantation is ubiquitous in ULSI (Ultra Large Scale Integration) technology, and detailed quality assurance is very expensive for a large number of applications for research implanters, therefore these rely on dosimetry instrumentation. A new parameterisation of He stopping power in Si is used. The certified Sb sample designated IRMM-302/BAM-L001, which has a dose certification of 0.6% traceable to the international standard of weight in Paris, is measured by using RBS, and this measurement demonstrates the reliability of the new stopping power parameterisation at about 1.4%; as a result, incident charge and solid angle can be determined accurately by using the silicon yield as a calibration for any analysis. Following this analytical treatment, the implantation dose determination by using RBS is demonstrated with a precision (standard uncertainty) of 1.5%. Moreover, by comparison with a manual data reduction method, the IBA DataFurnace code is validated for such accurate

measurements; this means high-accuracy measurements can now be made routinely and rapidly.

Chapter 5 bears upon the absolute determination of the H dose of an amorphised Si wafer, implanted with 6-keV H^+ ions, by using ERDA. The final result obtained by using a conventional set-up is an H dose of 57.8(1.0) $\times 10^{15}$ at./cm^2, which is a 1.8% standard uncertainty. The estimated combined uncertainty of this measurement is estimated at around 6%, and it is governed by the determination of the ERDA solid angle by using standard Kapton. The Kapton composition is carefully determined using RBS. As in the dosimetry analysis performed in chapter 4, the RBS solid angle is obtained using the silicon material as a calibration standard. A Round Robin exercise including participants from the four corners of the world was conducted, and this allows comparison of the results. Both He-ERDA and HI-ERDA methods were used, and this includes various detector arrangements. The overall absolute dose obtained of the implant is 57.0(1.2)$\times 10^{15}$ H/cm^2, and this represents an inter-lab reproducibility of 2.2% (standard uncertainty). An unstable surface hydrogen peak was observed and resolved by some of the methods. This implant can now be used as a standard for quantitative analysis of hydrogen. It can be pointed out that conventional ERDA, although the least sophisticated and least costly technique, performed exceedingly well in this application.

The next study presented in chapter 6 concerns the determination of absolute fluorine concentration of SiO_2:F films by using RBS. A preliminary NRA experiment is carried out in order to assess the uniformity of the films and the beam damage effects. It is estimated that typically 7.5% of F is depleted under a 1.5-MeV He beam irradiation for a typical RBS collected spectrum. It is established that the RBS technique is not very sensitive to F and, besides, the F signal has a large matrix background: in order to achieve an accurate treatment, an internally consistent method of data handling, which enables the relative collected charge to be determined very precisely for the spectra from different samples, is proposed. It is an iterative method which has the F content itself as a parameter. The minimum detectable F concentration is about 5 at.%, and a 10 at.% F content is determined with an estimated uncertainty of 10% (one percentage point, i.e. 10 ± 1%). It is shown that the accuracy of this absolute quantification is limited by the O stopping powers. All the other uncertainties account for only about 1%. Different possible

chemistries are investigated, and it turns out that the F atoms do not appear to tend to substitute for the O atoms. The RBS results are compared to XRF results, and a good agreement is found.

The last analytical study presented in chapter 7 is a successful attempt in determining the elemental composition of residual deposits from an Applied Materials UK Ltd.'s ion implanter. This study is an interesting case of complementary use of several analytical methods, and it involves RBS, EBS and NRA. The main challenge lies in making an accurate treatment of such non-homogeneous, non-flat and brittle so-called flakes. Using preliminary SEM/EDAX results as a guide, RBS and EBS depth profiles are obtained, which give an indication of the concentration of the elements present. The latter are found to be As, C, In, Sb, W, Fe, F and Cl. The presence of C is confirmed by EBS via the enhanced proton-on-carbon cross-section, and a tiny amount of F, restricted to the surface layer, is identified by the nuclear reaction experiment. Subsequently, from this complete IBA elemental study, an attempt is made to explain the origin and formation of the flakes, which brings some valuable information on the history of the implanter whose operation is degraded by the presence of these undesirable deposits.

Finally, as a general conclusion of this thorough work, it can be inferred that the boundaries of accuracy obtainable for IBA methods have been substantially pushed further. As a matter of fact, from this work: the energy-loss parameterisation of He into Si has been determined with an unprecedented uncertainty of 1.4%; internal normalisation methods have been proved to be efficient in calibrating the charge·solid angle product at the ½% level for the analysis of virtually many kinds of samples; and the dose of an H-implanted Si sample has been determined with an uncertainty of 2.2%, consequently this implant can now be used as a standard for quantitative analysis of hydrogen. Moreover the IBA fitting code DataFurnace has been validated for work where such high-accuracy treatments are of great importance; this implies that accurate analysis can now be done routinely and rapidly. This study is beneficial to the IBA community along with the semiconductor technology as the constantly growing need of development/miniaturisation in the semiconductor field requires more accurate analysis. In order to improve the analytical accuracy any further, it would be interesting to explore some other aspects of IBA material characterisation. These are outlined in the following section.

8.2 Short-term future work proposed

Firstly, the study conducted on implant dose determination can be extended to very accurate (1.5% level) energy-loss value determination. New reliable values of stopping powers for other elements can be determined using appropriate certified samples similar to the IRMM/BAM Sb, that is, another substrate (instead of silicon) with any ion implanted with a dose certification. This can be achieved by adjusting the substrate stopping power until the dose obtained matches the certified nominal ion implant dose. Besides, this can be done readily using DataFurnace as demonstrated in chapter 4. Silicon-oxide compounds are widely used in the semiconductor field, therefore the first element to be explored should be O. As a matter of fact, it is shown in this thesis (chapter 6) that the lack of good knowledge of O stopping powers limits markedly the accuracy available for the characterisation of silicon-oxide-based materials. Some other important oxide samples like SiO_2, Al_2O_3 or Ta_2O_5 can be well characterised in order to determine energy-loss values, and in addition, with such compounds, Bragg's rule could be tested.

At low energies, RBS spectra are distorted due to plural and multiple scattering. It would be worthwhile to investigate the contribution of double scattering, for instance, to RBS spectra by using the backscattering simulation code for ion beam analysis SIMNRA [May97, www®], which can simulate double scattering. The new parameterisation of the energy loss of He in Si proposed by Barradas *et al*. [Bar02], which has been validated in chapter 4 and used throughout this thesis, has been determined by RBS using Bayesian Inference (BI) with the Markov Chain Monte Carlo (MCMC) algorithm: in fact, a code has been developed to determine both the stopping powers and the confidence limits on the values obtained by comparison of theoretical (simulated) and experimental (measured) RBS spectra from known targets, which are experimentally trivial. All the experimental parameters are well defined since the physics is well known, apart only from the stopping powers. This is why the stopping powers can be extracted from the comparison between the theoretical and experimental spectra. However, due to plural and multiple scattering effects, in order to apply Barradas *et al*.'s data manipulation for the determination of stopping powers at low energies we need to take into

account properly this plural and multiple scattering contribution in the simulations for more reliable energy loss database.

Elastic (non-Rutherford) cross-sections of elements, that is, when the Coulomb barrier is exceeded, are also important in ion beam analysis. They have been studied over many years, but even nowadays they still keep the attention of scientists (see for example [Gur97, Gur98-a-b, Gur99, Gur00, Hea00]). The point is that their function of energy is not a smooth curve but instead it shows a series of peaks which are a signature of the so-called elastic (non-Rutherford) scattering. In fact the non-Rutherford cross-sections are not extremely well known. Some of A.F. Gurbich's data on aluminium (important element as it is widely used in materials) together with the MCMC Barradas *et al*.'s calculations mentioned above could be used to extract accurate values of cross-sections. One may use a similar data handling method as in the case of stopping powers determination: but this time the stopping powers are replaced by the cross-sections as parameters to be defined as a function of energy.

APPENDIX A

GEOMETRIC CONSIDERTIONS

In the light of the concepts of backscattering and recoil kinematics as established and studied in the beginning of sections 2.1 and 2.2, some practical geometric configurations can be inferred. The treatment presented in this appendix can be found in [Chu78] and/or in [Tir96].

A.1 General considerations

The recoil angle φ can be expressed as a function of the scattering angle θ by the following expression:

$$\cos^2\varphi = \frac{(M_1+M_2)^2 - \left(M_1\cos\theta \pm \sqrt{M_2^2 - M_1^2\sin^2\theta}\right)^2}{4M_1M_2}, \qquad \text{(A-1)}$$

where M_1 and M_2 are the mass of the projectile and recoil particles, respectively. Two main considerations can be made in terms of the mass ratio.

If $M_1 < M_2$, the velocity of M_1 after collision may have any direction from 0–π; then only the plus sign holds in equation (A-1). It follows that $\theta + \varphi > \pi/2$.

If $M_1 > M_2$ (as for ^{4}He beam and ^{1}H target), as pointed out in section 2.1.3, there is a maximum value of θ beyond which the particle M_1 cannot be deflected from the incident beam direction. This value of θ_{max} has the simple expression:

$$\sin\theta_{\max} = \frac{M_2}{M_1}. \qquad \text{(A-2)}$$

Scattering ^{4}He from ^{1}H, ^{2}H and ^{3}H, for example, gives θ_{max} = 14.47°, 30° and 48.59°, respectively. Furthermore $\theta + \varphi < \pi/2$, and for the special case $M_1 = M_2$ we find $\theta + \varphi = \pi/2$. It is worth noting that for each scattering angle $\theta < \theta_{max}$, two different recoil angles φ exist as a consequence of the double sign in equation (A-1).

From these relationships, an interesting case emerges: where both the scattered and recoil particles follow in the same forward direction, i.e. when the scattering angle θ goes to 0. Then both possible expressions for the angle φ must be taken into account. First, the easy case, if $M_1 < M_2$, then the recoil angle φ can go to zero only, the relation between θ and φ is a monotone function. But if $M_1 > M_2$, the recoil angle either tends to 0 (corresponding to no collision in fact, i.e. an infinite impact parameter) or tends to $\pi/2$ (corresponding to a head-on collision with a null impact parameter). Therefore the energy of the target particle after the collision has two possible values accordingly. When $\varphi = \pi/2$, the recoil energy is zero, and when $\varphi = 0$, the energy transferred to the recoil has its greatest value, E_{rmax}. The latter can be easily obtained:

$$E_{r\max} = \frac{4M_1M_2E_0}{(M_1 + M_2)^2}. \qquad \text{(A-3)}$$

No further information about the collision can be obtained from the laws of conservation of momentum and energy. It is worth pointing out, however, that the simple kinematic considerations discussed above, that can be interpreted geometrically, are sufficient to carry out significant experiments in elastic spectrometry.

A.2 Backscattering spectrometry

Angles near 180° are of special interest in backscattering spectrometry. The kinematic factor K (see section 2.1.3) has its lowest value at 180°. The factor K can be approximated very well by the first term of an expansion in $(\pi - \theta)$:

$$K \cong \left(\frac{1-M_1/M_2}{1+M_1/M_2}\right)^2 \left(1+\frac{M_1}{M_2}(\pi-\theta)^2\right). \qquad \text{(A-4)}$$

As can be seen, as θ departs from 180°, K increases only quadradically with (π - θ); this increase is proportional to the mass ratio M_1/M_2. When this ratio is small, the kinematic factor can be approximately described by:

$$K \cong 1-4\frac{M_1}{M_2}+(\pi-\theta)^2\frac{M_1}{M_2}. \qquad \text{(A-5)}$$

Consequently backscattering projectile energy varies slowly for $\theta \cong \pi$. Furthermore when a target contains two types of atoms that differ in mass by a small amount ΔM_2, the difference of energy $\Delta E'$ after collision is largest when $\theta = \pi$ (see section 2.1.3). As a result, for a small ratio M_1/M_2 (He projectile typically), the vicinity of this scattering angle is a favourable location for a detector in RBS experiments.

A.3 Recoil spectrometry

The energy E_r of recoil particles is maximum for $\varphi = 0°$, as can be evaluated from the expression of K_r as described in section 2.2.3. Small fluctuations of φ around 0° have only a slight influence on recoil energy; this can be more easily visualised when rewriting K_r in the approximation of small angles:

$$K_r \cong \frac{4M_1M_2\left(1-\varphi^2\right)}{\left(M_1+M_2\right)^2}. \qquad \text{(A-6)}$$

Furthermore the largest energy separation ΔE_r between two signals arising from two different recoil particles is always desirable; this occurs when $\varphi = 0°$. Consequently a recoil angle chosen in this vicinity in transmission mode (outside the incident beam passage evidently) gives *a priori* best results.

However, one has to be careful, and bear in mind straggling effects with using thick targets in transmission geometry for instance. This pitfall can be overcome by using glancing angles, although glancing angle geometries are difficult

experimentally since they are extremely sensitive to small errors in geometry, and they also require flat large samples.

APPENDIX B

ENERGY CALIBRATION OF THE ACCELERATOR AT SURREY IBC

This appendix deals with the energy calibration of the accelerator at the Surrey Ion Beam Centre. A ~12 cm^2 circular NaI scintillation detector was used. See section 3.1.4 for more details on the experimental set-up. The energy calibration was done at five different dates; each multipoint calibration is presented in the following sections. For the first calibration in section B.1, the details on the calibration procedure are given throughout.

B.1 November 3rd, 2000

The first point of energy calibration of the accelerator was obtained using the $^{27}Al(p,\gamma)^{28}Si$ resonance at 991.9 keV. The sample used was simply an aluminium foil. The thick target excitation curve is plotted in Figure B-1. In fact, two sets of measurements were collected. The first set (green points) has been used to determine the nominal energy E_n at which the real energy resonance E_r (991.9 keV) occurred. Since we do not have tools to fit the curve properly with the error-function integral, the points have just been b-spline connected, which gives a satisfactorily smoothed curve. As an attempt to get more points around the rising region of the curve, we ended up with a second set of measurements (blue points) that turned out to be rather odd. We still can recognize the rising curve, but with a slight energy shift and a sort of enhanced yield (ratio counts/charge). The energy shift is probably due to carbon deposition during the experiment. A very poor charge collection, that is, a very crude secondary electrons suppression, may have caused fluctuations in the

yield (ratio counts/charge): for this calibration point, the sample was stuck to the back wall of the L5 chamber, so that we could not achieve a proper secondary electrons suppression. Having said that, using only the first set of measurements, we found: a nominal energy E_n = 998.8 keV corresponding to a real energy of E_r = 991.9 keV. Since for this reaction the resonance width is very small, only 0.1 keV, the broadening of the thick target excitation curve is mainly due to the Gaussian beam width; the latter can then be extracted from the curve as being approximately the width between the 12% and 88% height, and it is found to be not more than 1.5 keV. This broadening was found previously to be due to the effect of the oscillation wire monitor on the slit energy control feedback.

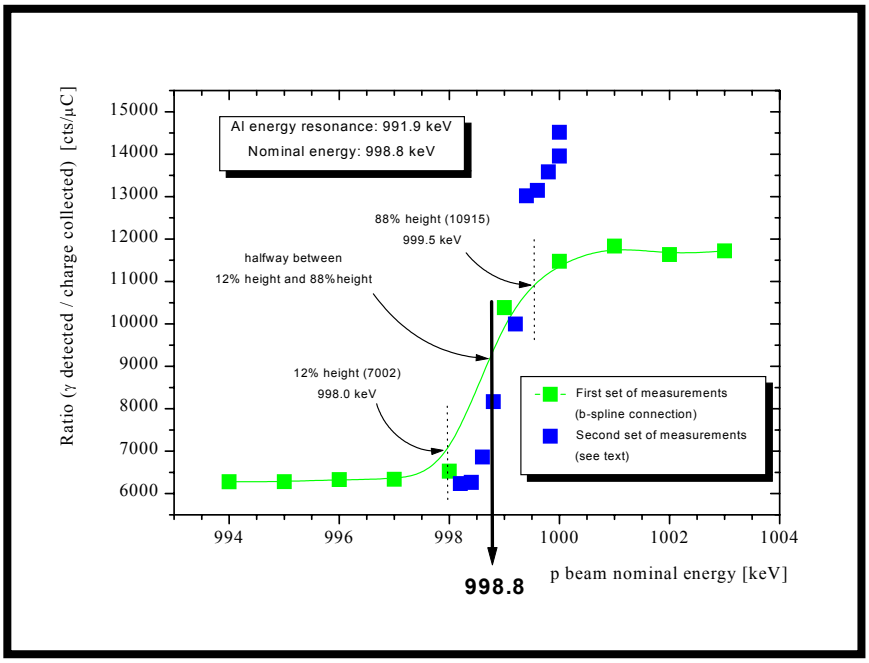

Figure B-1 *Excitation curve of the $^{27}Al(p,\gamma)^{28}Si$ resonance at 991.9 keV (energy calibration, November 3rd, 2000).*

Another calibration point was taken using again an aluminium foil, this time put on the holder to get a good charge collection, and the same reaction but at a lower energy: another resonance can effectively be found at 632.0 keV. Three sets of measurements, shown in Figure B-2, were taken in order to depict the carbon deposition during the measurements. But the cross-section for this reaction is six times as small as the previous one at 991.9 keV, consequently the signal-to-noise ratio is rather low (the resonance signals are *lost* in the background signals); since we

collected the data rather quickly because we were running out of time, it turns out that we cannot really see the evolution of carbon deposition with time from this data. And it is only approximately that we can determine the 12% and 88% height of the step function. As a result, we obtained: a nominal energy E_n = 637.0 keV for a real energy E_r = 632.0 keV. The resonance width for this reaction is nearly seven times as narrow as the previous one at 991.9 keV, i.e. about two orders of magnitude smaller than the beam spread, so the broadening of the curve is practically only due to the latter. It is found to be ~1.2 keV, which agrees satisfactorily with the value of 1.5 keV obtained from Figure B-1.

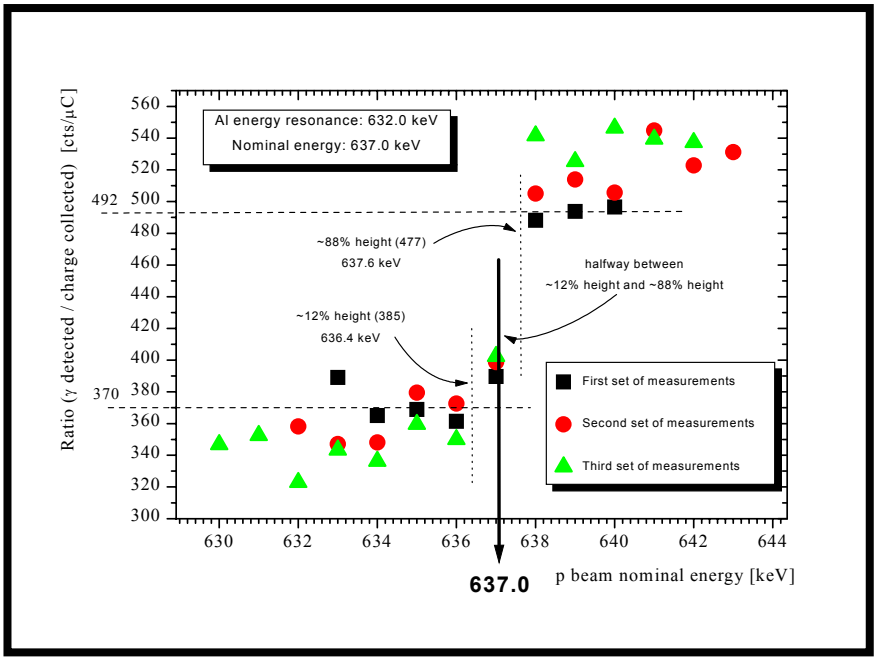

Figure B-2 *Excitation curve of the $^{27}Al(p,\gamma)^{28}Si$ resonance at 632.0 keV (energy calibration, November 3rd, 2000).*

A third calibration point was obtained using the $^{19}F(p,\alpha\gamma)^{16}O$ resonance at 872.1 keV. The sample was prepared by vaporizing HF acid on an aluminium foil for roughly 50 seconds. The resonance curve obtained is presented in Figure B-3. From the results it can be seen that the fluorine layer was very thin; as a matter of fact, the points describe a peak instead of an integrated step function as in Figure B-1 and Figure B-2. However, here the resonance width is 4.5 keV, which is in the same order of magnitude as the ~1.35 keV beam width (average between the 1.2 and 1.5 keV values as obtained further above); this means the peak is a convolution of a

Lorentzian (resonance curve) with a Gaussian (beam spread). As well described by Amsel and Maurel [Ams83], there is no analytical expression relating Lorentzian and Gaussian features (we refer here to their width Γ_l and Γ_g); their composition law is something intermediate between linear (Lorentzian behaviour) and quadratic (Gaussian behaviour). Moreover, the peak in Figure B-3 is probably not a *single* peak; it is more likely to be an integrated peak (which causes both a broadening and a high energy shift of the maximum height of the peak), as the fluorine layer, although it is very thin, it has a certain thickness. In fact, as an indication of this, the peak has a width > 6 keV, which is much more than the expected ~4.8 keV width for an infinitesimal fluorine layer as determined by using Amsel and Maurel's numerical calculations for the convolution of a 4.5-keV Lorentzian (resonance) with a 1.35-keV Gaussian (beam spread) [Ams83]. Although bearing in mind all these considerations, we shall not treat properly this fluorine data, considering that they do not affect significantly the final results. Therefore we just b-spline connected the points in order to get a smooth curve and considered the maximum height as the resonance point. Thus we obtained as a third calibration point: a nominal energy E_n = 878.5 keV for a real energy E_r = 872.1 keV.

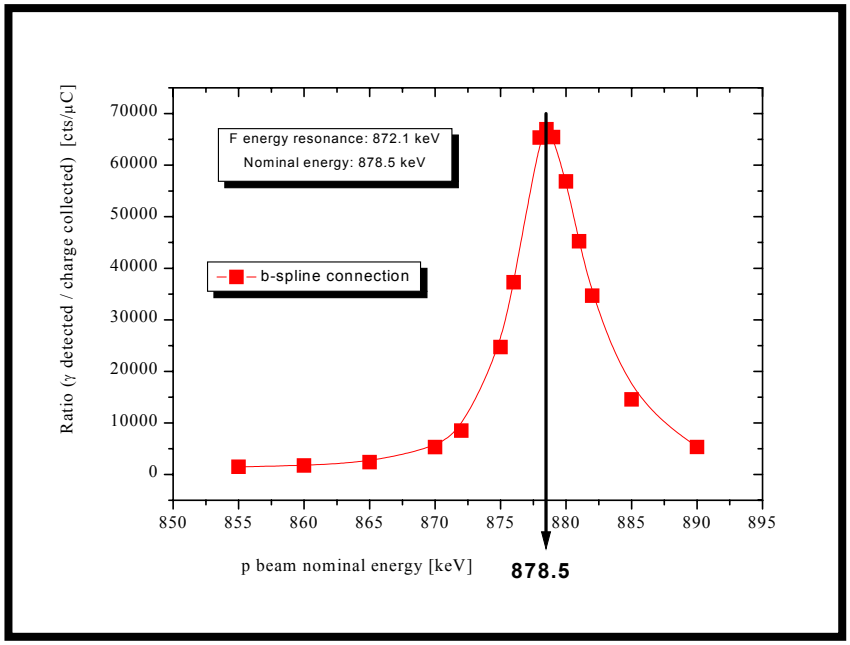

Figure B-3 *Excitation curve of the $^{19}F(p,\alpha\gamma)^{16}O$ resonance at 872.1 keV (energy calibration, November 3rd, 2000).*

Finally, the linear regression of these three calibration points is presented in Figure B-4. Then as an energy calibration curve we obtain:

$$E_n = -1.6(3) + 0.947(4)E_r . \qquad \text{(B-1)}$$

The numbers in brackets are the uncertainties in the last figures. The linear regression is astonishingly good, showing a correlation coefficient R = 0.9999998; therefore the energy calibration is considered to be reliable for any accurate work. A typical RBS helium beam energy E_r = 1500.0 keV gives a nominal energy E_n = 1490.4(9) keV; the uncertainty is then as small as 0.06%.

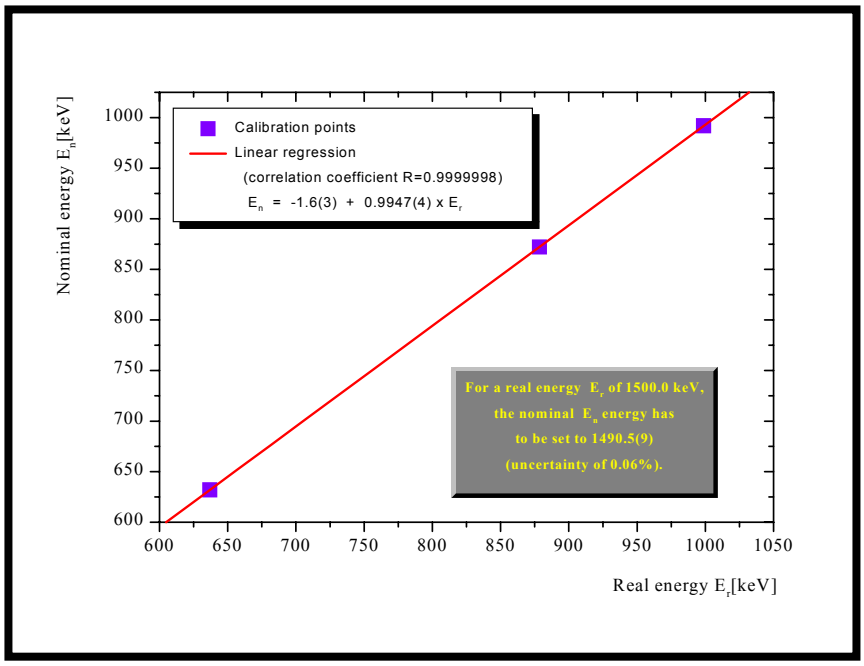

Figure B-4 *Energy calibration curve of Surrey accelerator, November 3rd, 2000.*

B.2 February 15th, 2001

The calibration was done using the same excitation curves as presented in the previous section. No attempt to measure carbon deposition was made. The excitation curves together with the final energy calibration curve follow below.

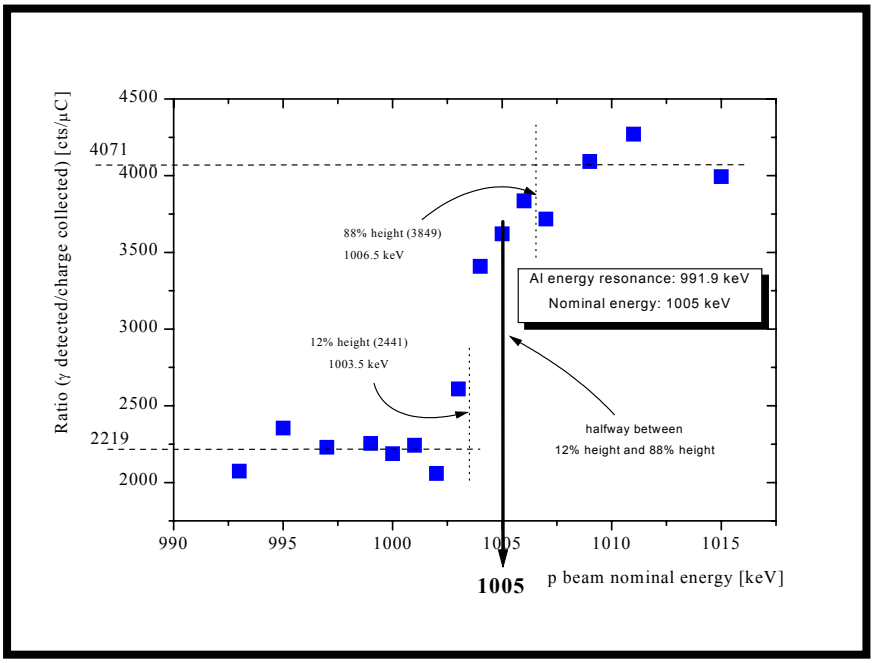

Figure B-5 *Excitation curve of the $^{27}Al(p,\gamma)^{28}Si$ resonance at 991.9 keV (energy calibration, February 15th, 2001).*

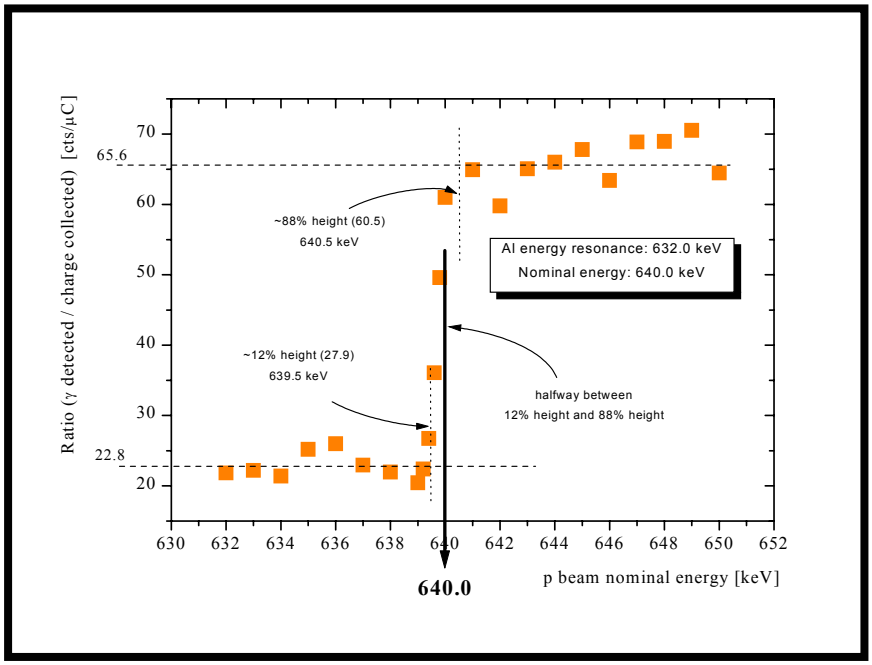

Figure B-6 *Excitation curve of the $^{27}Al(p,\gamma)^{28}Si$ resonance at 632.0 keV (energy calibration, February 15th, 2001).*

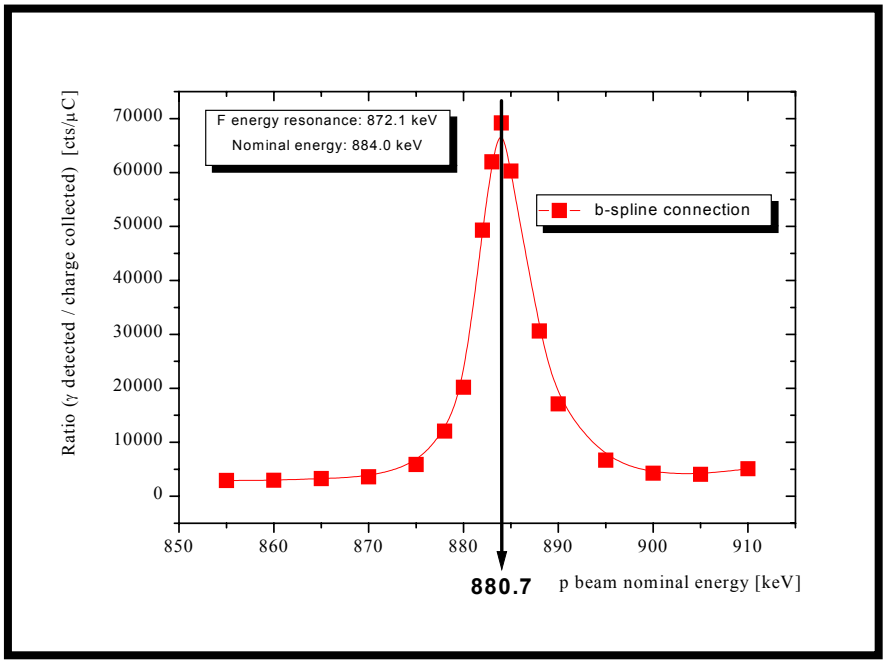

Figure B-7 *Excitation curve of the $^{19}F(p,\alpha\gamma)^{16}O$ resonance at 872.1 keV (energy calibration, February 15th, 2001).*

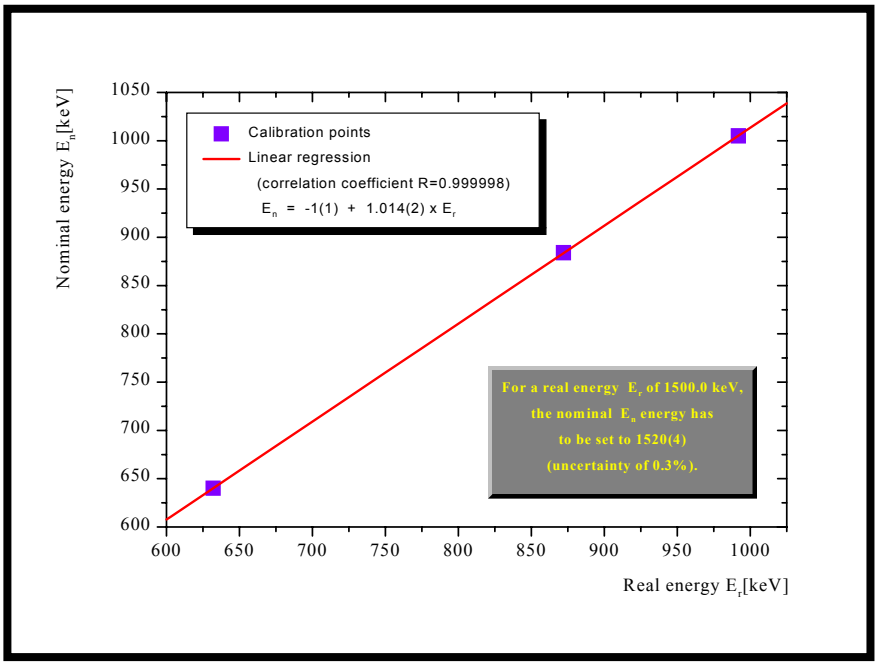

Figure B-8 *Energy calibration curve of Surrey accelerator, February 15th, 2001.*

As can be seen from Figure B-8, the linear regression for this three-point energy calibration yields:

$$E_n = -1(1) + 1.014(2)E_r \,. \qquad \text{(B-2)}$$

The correlation coefficient is R = 0.999998, which is slightly smaller than for the previous calibration (0.9999998). For an energy E_r = 1500 keV, one finds a nominal energy E_n = 1520(4). This leads to an uncertainty of 0.3%; this is not a precision as good as previously obtained (0.06%), nonetheless this is still good enough for any work where the highest accuracy is required.

B.3 April 4th, 2001

This time, we used a fourth nuclear resonance from the reaction $^{19}F(p,\alpha\gamma)^{16}O$ at 1371.0 keV. This gives an additional calibration point at high energy near the typical energy used in RBS (1500 keV); in principle, this four-point energy calibration should be more accurate, as the determination of the nominal value at 1500 keV is effectively no longer an extrapolation as it was the case for the previous three-point calibrations (the calibration is believed to be not totally linear at high energy — therefore this should lead to a more accurate but less precise calibration). However, this fourth resonance has a relatively large width of 11 keV; then the accuracy may not be improved this much. The four excitation curves together with the final energy calibration curve are shown further below.

The linear regression for this four-point energy calibration as given in Figure B-13 yields:

$$E_n = 1.2(9) + 1.0049(9)E_r \,. \qquad \text{(B-3)}$$

The correlation coefficient is R = 0.999998. For an energy E_r = 1500 keV, the nominal energy value is found to be E_n = 1508.6(2.2). This is an uncertainty of 0.15%.

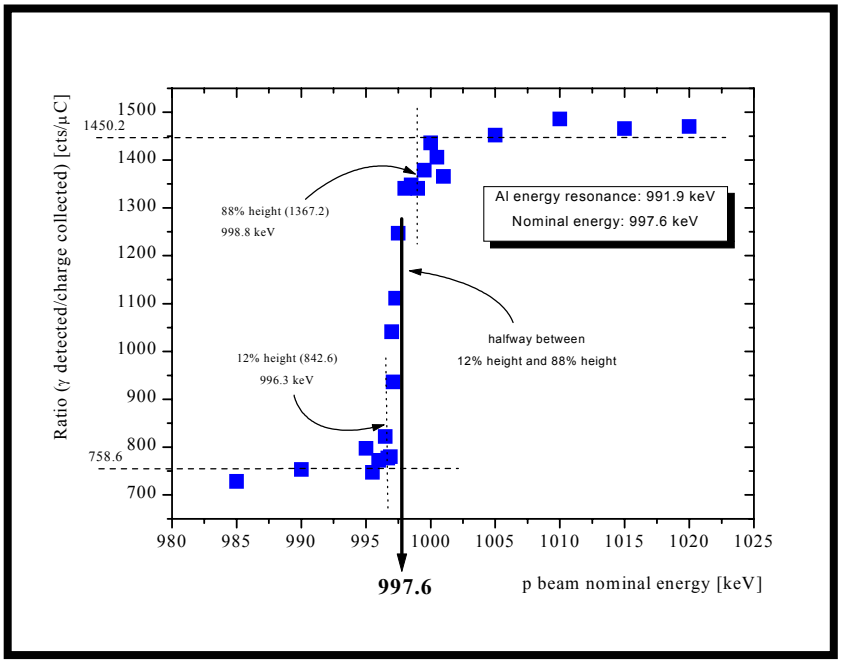

Figure B-9 *Excitation curve of the $^{27}Al(p,\gamma)^{28}Si$ resonance at 991.9 keV (energy calibration, April 4th, 2001).*

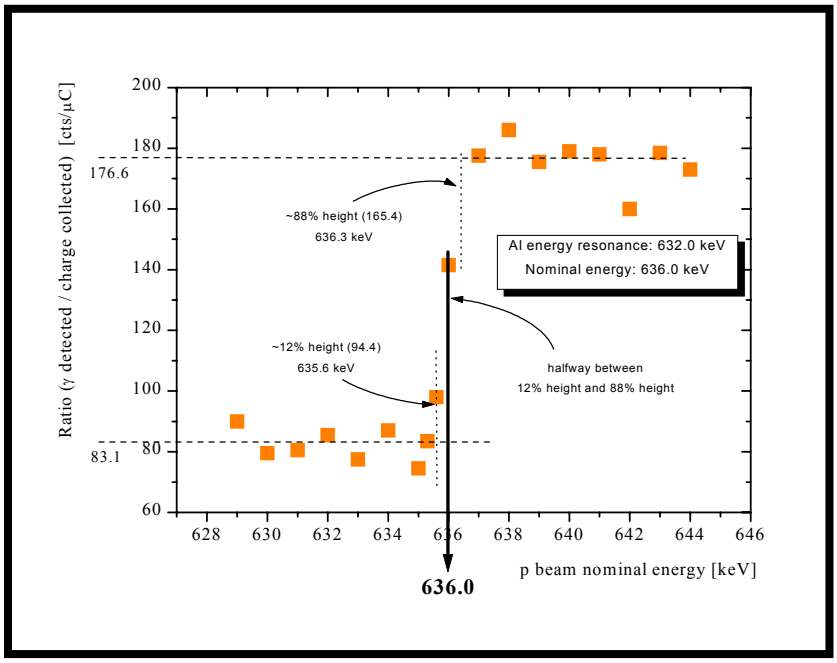

Figure B-10 *Excitation curve of the $^{27}Al(p,\gamma)^{28}Si$ resonance at 632.0 keV (energy calibration, April 4th, 2001).*

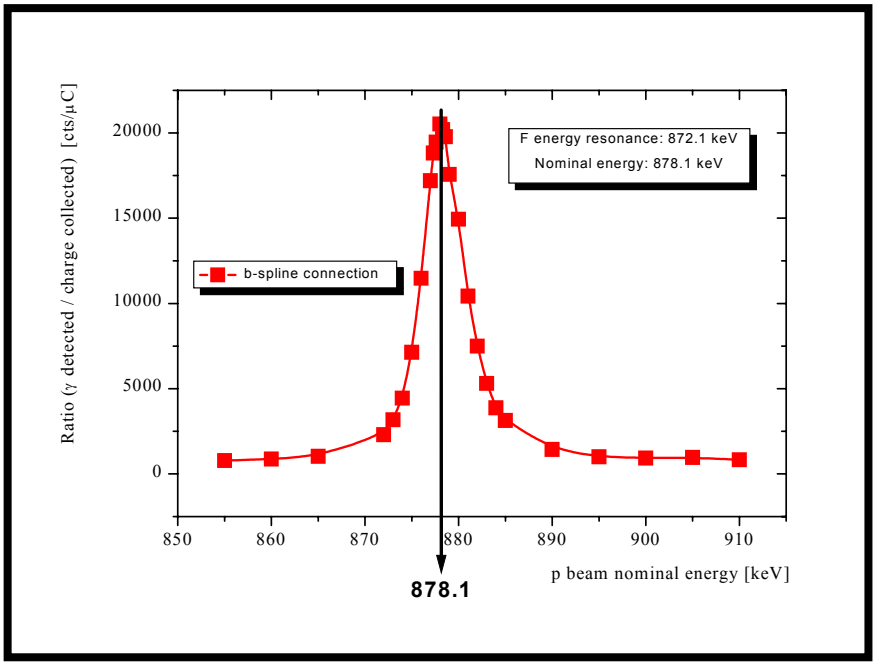

Figure B-11 *Excitation curve of the $^{19}F(p,\alpha\gamma)^{16}O$ resonance at 872.1 keV (energy calibration, April 4th, 2001).*

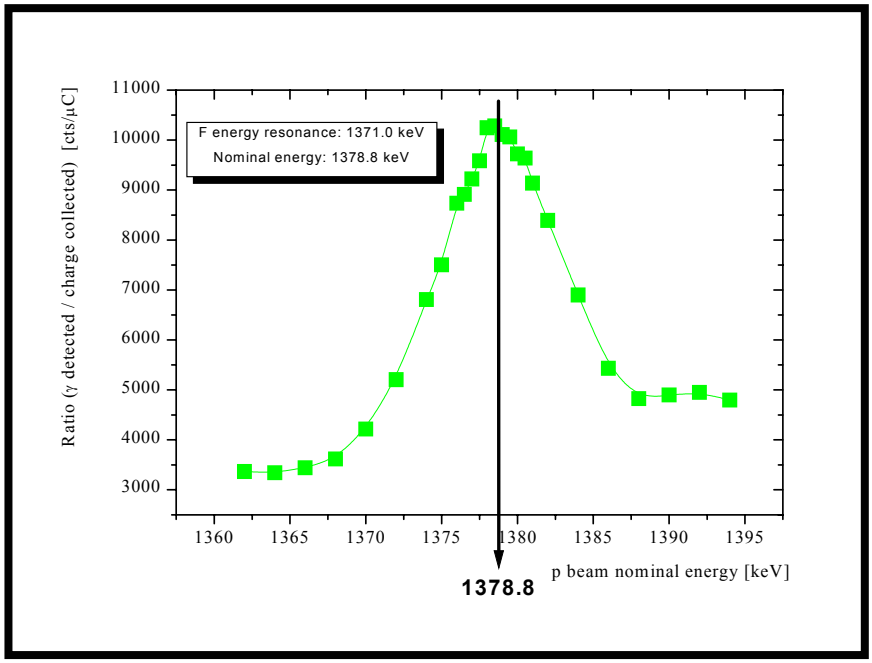

Figure B-12 *Excitation curve of the $^{19}F(p,\alpha\gamma)^{16}O$ resonance at 1371.0 keV (energy calibration, April 4th, 2001).*

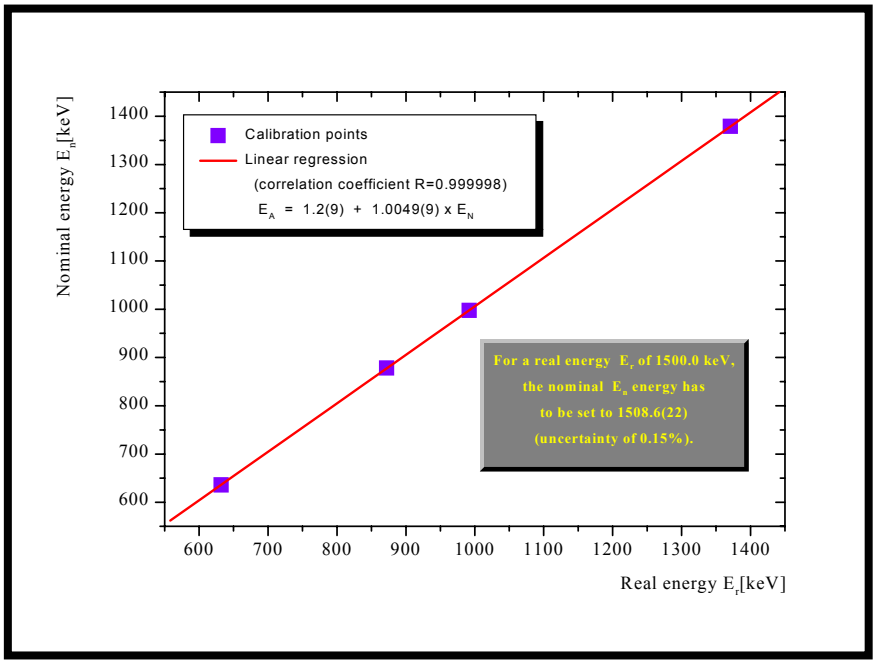

Figure B-13 *Energy calibration curve of Surrey accelerator, April 4th, 2001. Erratum: in the top inset box,* E_n *and* E_r *must be substituted to* E_A *and* E_n*, respectively.*

B.4 June 13th, 2001

This energy calibration was performed by using three points as in section B.1 and section B.2. The figures further below show the three excitation curves and the energy calibration curve obtained.

From the results in Figure B-17, it comes out that the relationship between the real and nominal energies is:

$$E_n = 16.5(1.9) + 0.9918(23)E_r\,. \qquad \text{(B-4)}$$

The correlation coefficient is again very close to unity, as it is R = 0.999995. An energy value of E_r = 1500.0 keV corresponds to a nominal energy E_n = 1504.2(5.4). The uncertainty in the energy is then 0.36%.

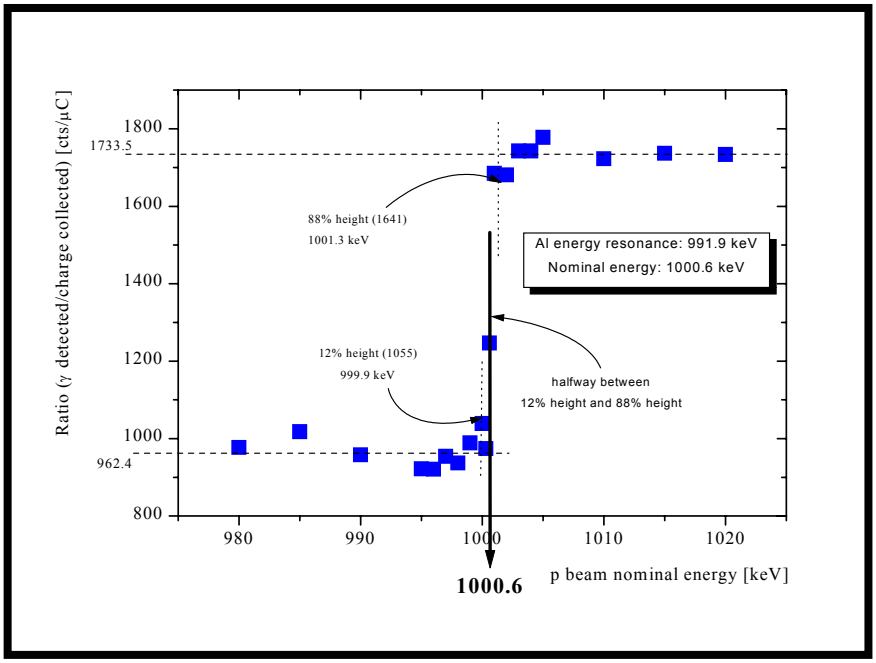

Figure B-14 *Excitation curve of the $^{27}Al(p,\gamma)^{28}Si$ resonance at 991.9 keV (energy calibration, June 13th, 2001).*

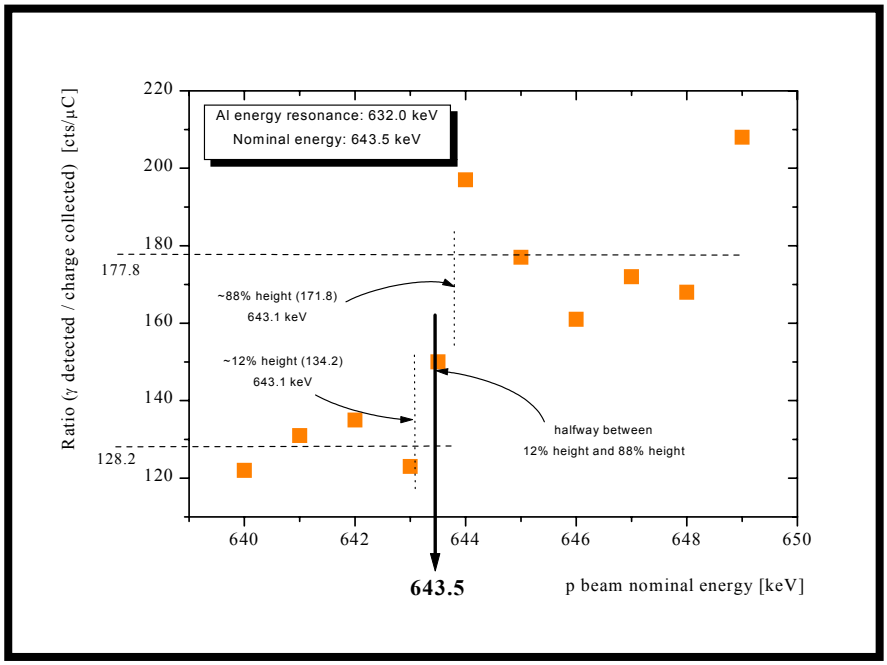

Figure B-15 *Excitation curve of the $^{27}Al(p,\gamma)^{28}Si$ resonance at 632.0 keV (energy calibration, June 13th, 2001).*

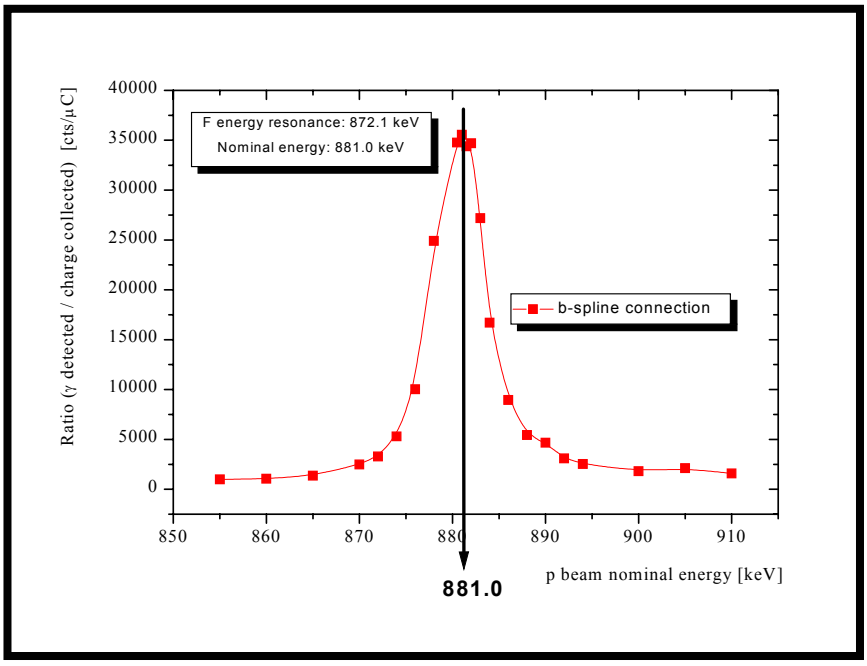

Figure B-16 *Excitation curve of the $^{19}F(p,\alpha\gamma)^{16}O$ resonance at 872.1 keV (energy calibration, June 13th, 2001).*

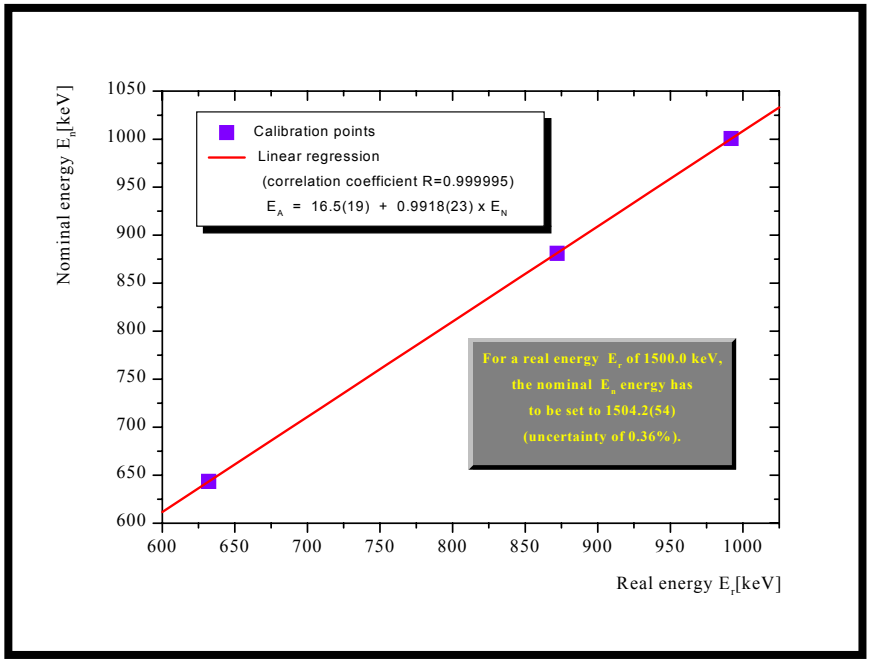

Figure B-17 *Energy calibration curve of Surrey accelerator, June 13th, 2001. Erratum: in the top inset box,* E_n *and* E_r *must be substituted to* E_A *and* E_n*, respectively.*

B.5 September 14th, 2001

As in section B.3, this energy calibration was done using four points. The excitation curves together with the energy calibration curve follow further below.

From the four-point linear regression given in Figure B-22, the conversion from real to nominal energy is:

$$E_n = 4(5) + 1.002(5)E_r \,. \qquad \text{(B-5)}$$

This time the correlation coefficient is R = 0.99997, and this is the lowest value of the five energy calibrations performed. For a real energy E_r = 1500.0 keV, the nominal energy is E_n = 1507(12). The uncertainty of the latter value is 0.8%; this is by far the worst result obtained (more than twice as much as the second highest uncertainty), though it is still a reasonably small uncertainty.

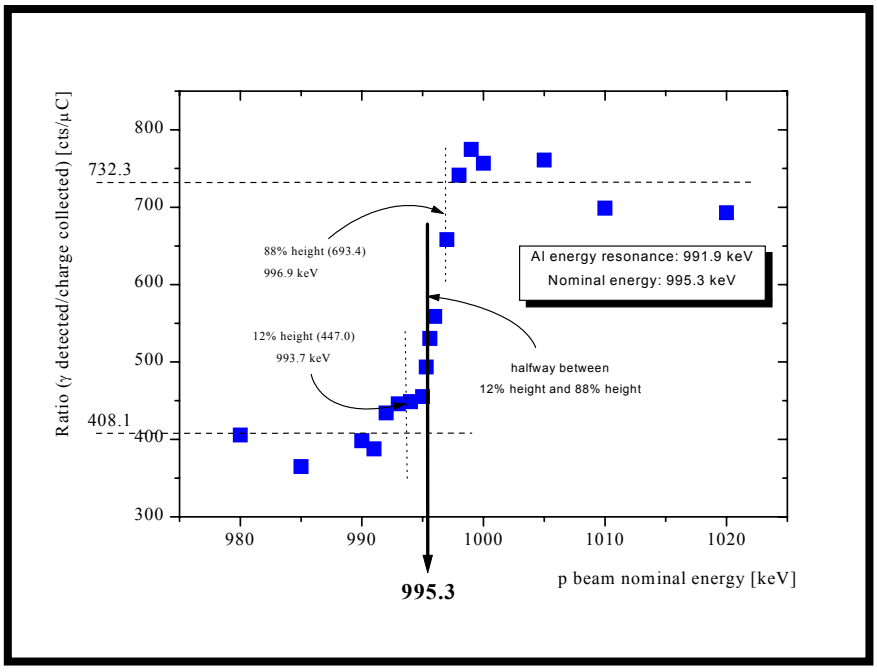

Figure B-18 *Excitation curve of the $^{27}Al(p,\gamma)^{28}Si$ resonance at 991.9 keV (energy calibration, September 14th, 2001).*

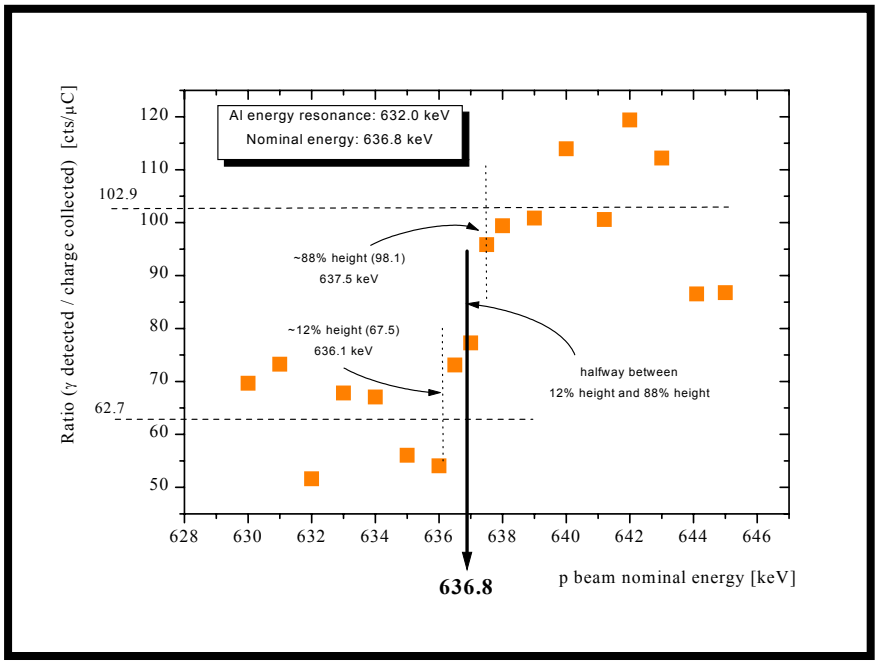

Figure B-19 *Excitation curve of the $^{27}Al(p,\gamma)^{28}Si$ resonance at 632.0 keV (energy calibration, September 14th, 2001).*

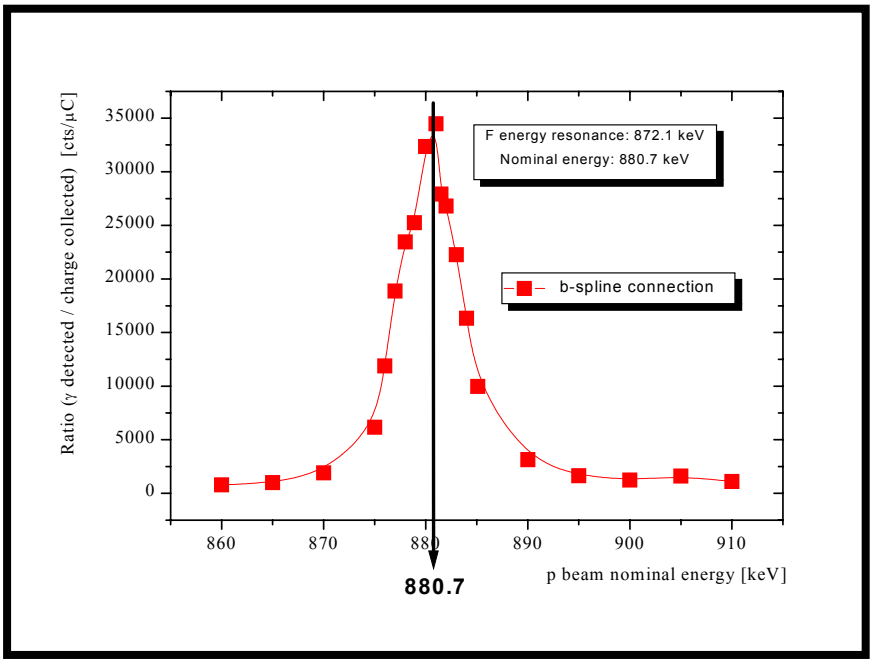

Figure B-20 *Excitation curve of the $^{19}F(p,\alpha\gamma)^{16}O$ resonance at 872.1 keV (energy calibration, September 14th, 2001).*

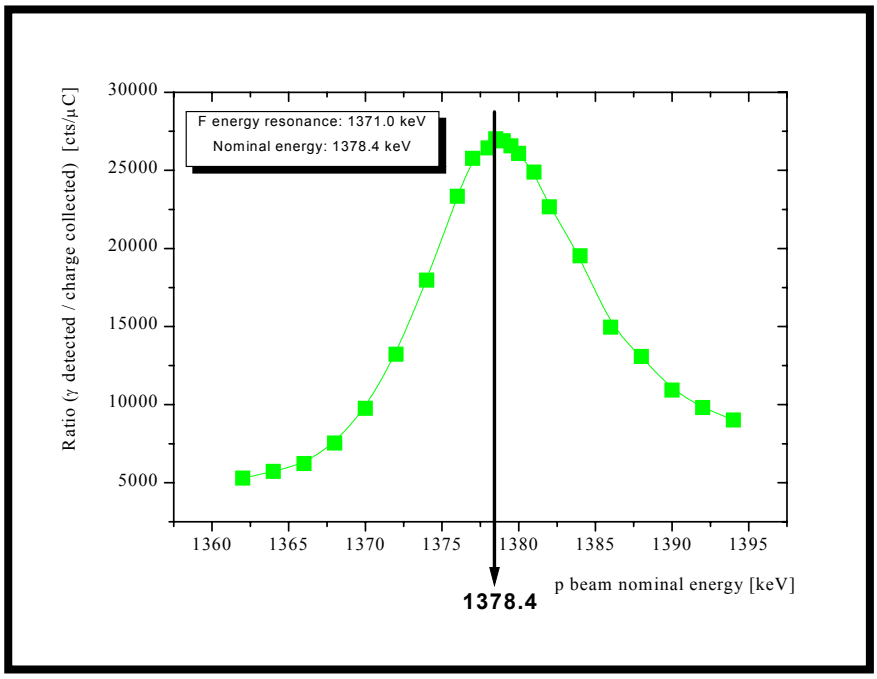

Figure B-21 *Excitation curve of the $^{19}F(p,\alpha\gamma)^{16}O$ resonance at 1371.0 keV (energy calibration, September 14th, 2001).*

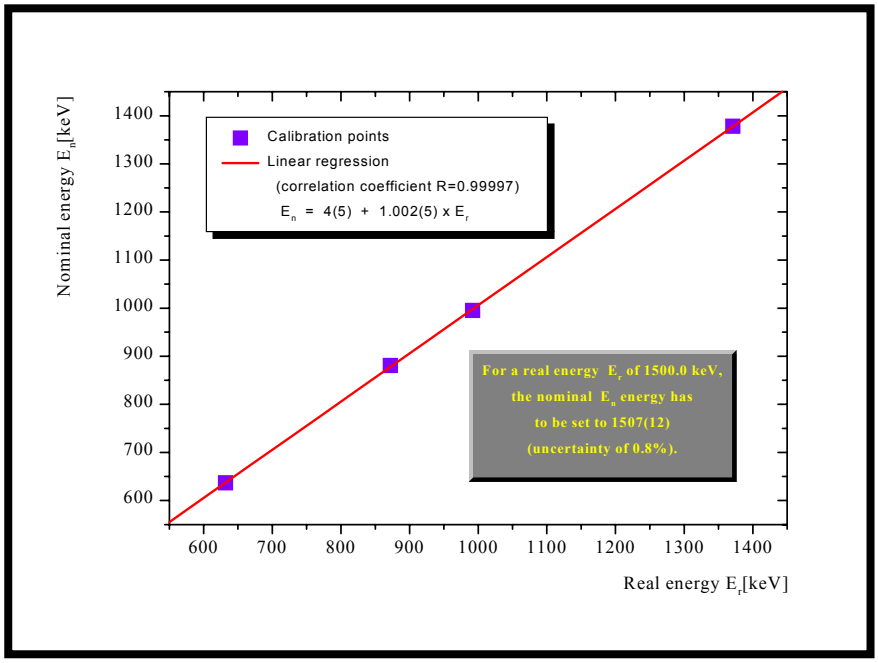

Figure B-22 *Energy calibration curve of Surrey accelerator, September 14th, 2001.*

B.6 Summary

The history of the accelerator energy calibration is summarised in Table B-1. The final results are given, that is, the nominal energy E_n corresponding to a real energy E_r = 1500.0 keV for each calibration date.

Table B-1 *History of accelerator energy calibration: the nominal energy corresponding to a real energy of 1500.0 keV for each calibration date.*

Calibration date	*Nominal energy E_n [keV]*
November 3, 2000	1490.4 (9)
February 15, 2001	1520 (4)
April 4, 2001	1508.6 (2.2)
June 13, 2001	1504.2 (5.4)
September 14, 2001	1507 (12)

Numbers in () are the uncertainties in the last figures.

It can be seen that the nominal energy corresponding to the same real energy fluctuates with calibration dates. This energy shift is believed to be due to the different insulating gas conditions subsequent to removal of the tank each time the service was done on the machine (see section 3.1.1.2).

The uncertainty obtained on the determination of the nominal energy also varies with calibration dates. This is believed to be due to the relative instability of the machine at those particular dates, and not to the accuracy of the calibration procedure. The uncertainty of 0.06% obtained on November 3, 2001 is astonishingly good, and is probably accidental.

APPENDIX C

TERMINOLOGY OF THE GUIDE TO THE EXPRESSION OF UNCERTAINTY IN MEASUREMENT (GUM)

This thesis deals with *accuracy*. It is then imperative that a rigorous terminology be followed throughout. Reporting the result of a measurement of a physical quantity requires that some quantitative indication of the quality of the result be given so that reliability of the latter can be assessed. Besides, it is necessary that no confusion arises when terms such as *uncertainty*, *error*, *precision* or *accuracy* are used for instance. In the years following 1978, a great deal of effort has been made by the Bureau International des Poids et Mesures (BIPM) in order to obtain an international consensus on the expression of the uncertainty in measurement along with establishment of a proper vocabulary of metrological and statistical terminology. The task of developing a detailed guide fell to the International Organisation for Standardization (ISO), and in 1993 they came out with the *Guide to the expression of uncertainty in measurement*, or GUM [ISO93]. Throughout the thesis we have followed narrowly the recommendations and the terminology as given in GUM. This appendix aims at highlighting some of the more important definitions found in the guide; these are presented as (nearly) literally given in GUM, with some extra details added for better clarity.

C.1 Measurand

The measurand is the particular quantity subject to measurement. For example: the vapour pressure of a given sample of water at 20ºC. Note that the

specification of a measurand may require statements about quantities such as time, temperature, pressure, etc.

C.2 Conventional true value

The conventional true value of a quantity (measurand) is the value attributed to that particular quantity and accepted, sometimes by convention, as having an uncertainty (see further below for the definition of uncertainty) appropriate for a given purpose. For example, at a given location, the value assigned to the quantity realized by a reference standard may be taken as a conventional true value. Another example would be the 1986 CODATA (Committee on Data for Science and Technology) recommended value for the Avogadro constant: 6.0221367×10^{23} mol^{-1}.

"Conventional true value" is sometimes called "assigned value", "best estimate" of the value, "conventional value" or "reference value". The term "certified value" may be added to the list. Frequently, a number of results of measurements of a quantity is used to establish a conventional true value.

C.3 Accuracy and precision

Accuracy and precision are two terms often misunderstood and confused. The accuracy of a measurement is the closeness of the agreement between the results of a measurement and a conventional true value of the measurand; in other words, accuracy is how close to the accepted value a measurement lies. In contrast, precision is a measurement of how closely the analytical results can be duplicated; thus precision measures how far from the mean of replicate measurements a particular measurement lies, and it can be reported as a standard deviation. Accuracy is a qualitative concept; the term precision should not be used for accuracy.

If a conventional true value is represented as a bull's eye on a target, a group of guesses or measurements represented by closely grouped points have a high degree of precision. If this group is near the centre, it is highly accurate as well. On the other hand, if the points are widely scattered around the centre, the measurements

can be said accurate but not highly precise. These situations are depicted in Figure C-1.

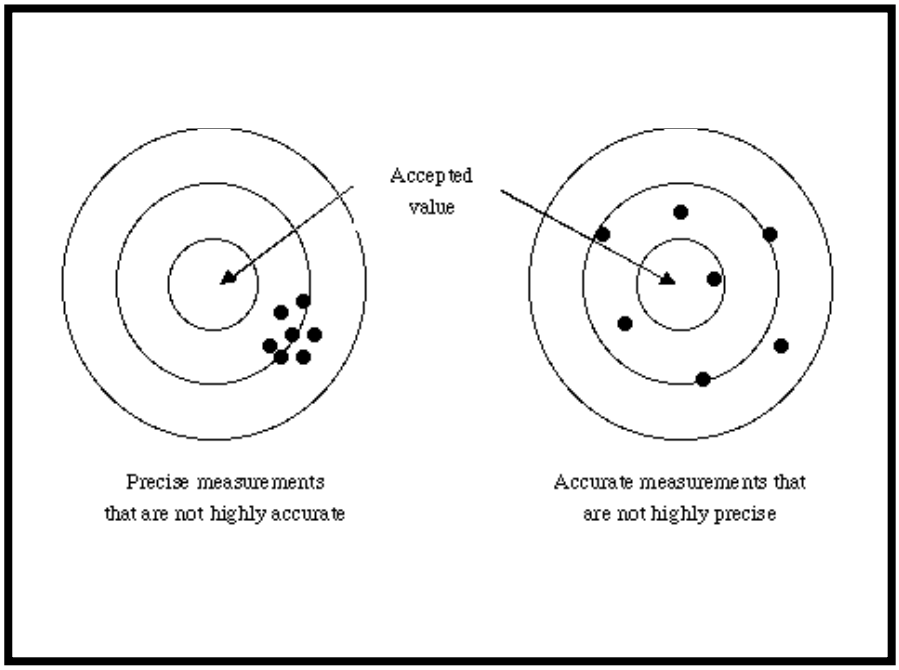

Figure C-1 *Distinction between accuracy and precision.*

C.4 Basic statistical terms and concepts

C.4.1. Expectation — mean value of random variable

The expectation of the random variable z, denoted by μ_z, and which is also termed the expected value or the mean of z, is given by:

$$\mu_z = \int z p(z) dz \,, \tag{C-1}$$

where $p(z)$ is the probability density function of the random variable z. From the definition of $p(z)$

$$\int p(z) dz = 1 \,. \tag{C-2}$$

This expectation is estimated statistically by $\bar{z}$, the arithmetic mean or average of n independent observations z_i of the random variable z (measurand), the probability density function of which is $p(z)$:

$$\bar{z} = \frac{1}{n}\sum_{i=1}^{n} z_i \ . \tag{C-3}$$

C.4.2. Variance of random variable

The variance of a random variable is the expectation of its quadratic deviation about its expectation. Thus the variance of random variable z with probability density function $p(z)$ is given by:

$$\sigma^2(z) = \int (z - \mu_z)^2 \, p(z) dz \ . \tag{C-4}$$

The variance may be estimated by:

$$u^2(z_i) = \frac{1}{n-1}\sum_{i=1}^{n} (z_i - \bar{z})^2 \ , \tag{C-5}$$

where the z_i are n independent observations of z. Note that the factor $n-1$ arises from the correlation between z_i and $\bar{z}$ and reflects the fact that there are only $n-1$ independent items in the set $\{z_i - \bar{z}\}$.

C.4.3. Variance of arithmetic mean

The variance of arithmetic mean or average of the observations, rather than the variance of the individual observations (variance of random variable), is sometimes used to measure the uncertainty of a measurement result. The variance of a variable z should be carefully distinguished from the variance of the mean $\bar{z}$. The variance of the arithmetic mean of a series of n independent observations z_i of z is estimated by the experimental variance of the mean:

$$u_m^2 = \frac{u^2(z_i)}{n} = \frac{1}{n(n-1)}\sum_{i=1}^{n} (z_i - \bar{z})^2 \ . \tag{C-6}$$

C.4.4. Standard deviation of random variable

The standard deviation for a series of n measurements of the same random variable z (measurand) is the positive square root of the variance, i.e. u, and it characterizes the dispersion of the results.

C.4.5. Standard deviation of arithmetic mean

The value u_m (square root of the variance of the mean as expressed further above) is an estimate of the standard deviation of the distribution of the arithmetic mean $\bar{z}$, and it is called the standard deviation of the mean.

C.5 Uncertainty

The word "uncertainty" means doubt, and thus in its broadest sense "uncertainty of measurement" means doubt about the validity of the result of a measurement. Because of the lack of different words for this *general concept* of uncertainty and the specific quantities that provide *quantitative measures* of the concept, e.g. the standard deviation, it is necessary to use the word "uncertainty" in these two different senses.

C.5.1. Uncertainty of measurement

Uncertainty of measurement is the parameter, associated with the result of a measurement, that characterizes the dispersion of the values that could reasonably be attributed to the measurand. The parameter may be, for example, a standard deviation (or a given multiple of it), or the half-width of an interval having a stated level of confidence.

Uncertainty of measurement comprises, in general, many components. Some of these components may be evaluated from the statistical distribution of the results of series of measurements and can be characterized by experimental standard deviations. The other components, which also can be characterized by standard

deviations, are evaluated from assumed probability distributions based on experience or other information.

It is understood that the result of the measurement is the best estimate of the value of the measurand, and that all components of uncertainty, including those arising from systematic effects, such as components associated with corrections and reference standards, contribute to the dispersion.

C.5.2. Standard uncertainty

The standard uncertainty is when the uncertainty of the result of a measurement is expressed as a standard deviation.

C.5.3. Categories of uncertainty

The uncertainty in the result of a measurement generally consists of several components which may be grouped into two categories, denoted Type A and Type B, according to the way in which their numerical value is estimated. The purpose of the Type A and Type B classification is to indicate two different ways of evaluating uncertainty components and is for convenience of discussion only; the classification is not meant to indicate that there is any difference in the nature of the component resulting from the two types of evaluation. Both types are based on *probability distributions*, and the uncertainty components resulting from either type are quantified by variances or standard deviations.

C.5.3.1. Uncertainty: Type A

Components that are evaluated by statistical methods (statistical analysis of series of observations). They are characterized by the estimated variances or standard deviations. The estimated variance u^2 characterizing an uncertainty component obtained from a Type A evaluation is calculated from series of repeated observations and is the familiar statistically estimated variance as given by equation (C-5).

C.5.3.2. Uncertainty: Type B

Components whose method of evaluation of uncertainty is by means other that the statistical analysis of series of observations. For an uncertainty component obtained from a Type B evaluation, the estimated variances (or standard deviations) are evaluated using available knowledge, and may be also denoted u^2, which may be considered as approximations to the corresponding variances, the existence of which is assumed. These quantities u^2 may be treated like variances.

C.5.4. Combined standard uncertainty

The standard uncertainty of the result of a measurement, when that result is obtained from the values of a number of other quantities, is termed combined standard uncertainty and denoted u_c. It is the estimated standard deviation associated with the result and is equal to the positive square root of the combined variance obtained from all variance components summed (law of propagation of uncertainty — sum in quadrature).

C.5.5. Expanded uncertainty

The expanded uncertainty can be said the quantity defining an interval about the result of a measurement that may be expected to encompass a large fraction of the distribution of values that could reasonably be attributed to the measurand. The fraction may be viewed as the coverage probability or level of confidence of the interval.

When it is necessary to multiply the combined uncertainty by a factor, called coverage factor, to obtain an overall uncertainty, the multiplying (coverage) factor used must always be stated. A coverage factor, usually denoted k, is typically in the range 2 to 3.

C.6 Error of measurement

The error of measurement corresponds to the result of a measurement minus a (conventional or accepted) true value of the measurand.

C.6.1. Relative error

The relative error is the error of measurement divided by a (conventional or accepted) true value of the measurand (usually expressed in percentage).

C.6.2. Random error

The random error is the result of a measurement minus the mean that would result from an infinite number of measurements of the same measurand carried out under repeatability conditions. Because only a finite number of measurements can be made, it is possible to determine only an estimate of random error. Note that the random error is equal to error minus systematic error.

C.6.3. Systematic error

The systematic error is equal to the mean that would result from an infinite number of measurements of the same measurand carried out under repeatability conditions minus a (conventional or accepted) true value of the measurand. Like true value, the systematic error and its causes cannot be completely known. Note that the systematic error is equal to error minus random error.

C.6.4. Correction factor

The numerical factor by which the uncorrected result of a measurement is multiplied to compensate for systematic error is called correction factor. Since the systematic error cannot be known perfectly, the compensation cannot be complete.

C.7 Repeatability and reproducibility of results of measurements

C.7.1. Repeatability

The repeatability of results of measurements is the closeness of the agreement between the results of successive measurements of the same measurand carried out under the same conditions of measurement. The repeatability conditions include: the same measurement procedure; the same observer; the same measuring instrument, used under the same conditions; the same location; repetition over a short period of time. Repeatability may be expressed quantitatively in terms of the dispersion characteristics of the results.

C.7.2. Reproducibility

The reproducibility of results of measurements is the closeness of the agreement between the results of measurements of the same measurand carried out under changed conditions of measurement. A valid statement of reproducibility requires specification of the conditions changed. The latter may include: principle of measurement; method of measurement; observer; measuring instrument; reference standard; location; conditions of use; time. Reproducibility may be expressed quantitatively in terms of the dispersion characteristics of the results.

APPENDIX D

IBA FITTING CODE DATAFURNACE

The IBA data treatment of the work presented in this thesis has been performed using the fitting code DataFurnace, developed here at the Surrey Ion Beam Centre. This appendix gives a brief overview on the utilization of this code for interpreting IBA spectra. The information contained in this general survey can be found in [Jey00, NDF02].

D.1 General description

The ion beam analysis DataFurnace is a computer code to extract depth profiles from Rutherford backscattering and related ion beam analysis spectra. It is able to solve the inverse problem ("given the spectrum, what is the profile") automatically, without user intervention. It was first published in Applied Physics Letters [Bar97-b], and the implementation of the code and examples of applications can be found in several publications [Bar98-a-b-c-d, Bar99-a-b-c, Mar98, Jey02] and on the web [www②, www③]. DataFurnace has generated considerable interest, having 74 citations listed to date in the ISI (Institute for Scientific Information) Web of Science index [www⑨].

This new thin film depth profiling tool has a core code to do the physics called NDF written in Fortran, and a user interface code called WiNDF written in Visual Basic. It is designed to facilitate *accurate* analysis of large batches of complex samples. NDF, which stands for "Nuno's DataFurnace" (Dr Nuno Barradas wrote the code) makes fully automatic fits to experimental data, the user is only

required to input the analytical conditions and the elements present. NDF uses the simulated annealing algorithm (hence the idea of a "Furnace") [Aar89, Kir83], which is a very powerful global minimisation calculation process. The data is put, mathematically speaking, in an annealing furnace.

The name "WiNDF" is a contraction of "Windows Nuno's DataFurnace"; the two names WiNDF and DataFurnace are used interchangeably. WiNDF is still DOS compatible for historical reasons, and still insists on DOS compatible file names. WiNDF runs on PCs with Windows or NT operating systems; it is a Windows user interface to the NDF code. It is designed to enable the user to create batch files for NDF: batches of spectra can be analysed from up to 99 samples each with up to 10 spectra that can be fitted simultaneously. Each spectrum is associated with a geometry file which gives the experimental details for that spectrum. Each sample has a structure file which allows the user to constrain the expected target structure; this is necessary because of the ambiguity typically present in IBA data. The geometry and structure files can be created and maintained using WiNDF. WiNDF enables one to keep track of the many output files that are generated by the DataFurnace. It also includes comprehensive graphical spectral manipulation tools, a spectrum simulator and other utilities.

NDF is actually a hybrid code involving spectral pre-processing (simulation), the (global minimisation) simulated annealing algorithm, and a final local minimisation algorithm. The purpose is to find an elemental depth profile that is consistent with the IBA data collected. NDF can be used very simply, where all the internal structure is transparent to the user, or it can be used in much more sophisticated ways for more experienced analysts.

D.2 DataFurnace: getting started

D.2.1. DataFurnace algorithm: introduction

We should emphasise that WiNDF is a *fitting* program: the user does not have to specify any sort of layer structure to extract the elemental depth profile. This is why it is a radically new type of code: all the standard IBA codes are

simulation codes which enable one to calculate the spectrum from a given layer structure.

In the fitting process many test elemental depth profiles are generated, and a calculation is made of the chi-squared difference between the spectrum simulated from the current test profile and the real spectrum to be fitted. Thus, for one fit many thousands of spectra may be *simulated*. The algorithm is able to increase or reduce the number, stoichiometry and thickness of individual layers in the test profiles at will, completely independently of the analyst.

In principle, the whole of state space is searched for the optimal solution with an arbitrary starting point selected automatically by the program. DataFurnace implements a *global optimisation algorithm* where the chi-squared function is *minimised*. In the last part of the fit the solution is assumed to be close to optimum and a *local optimisation* routine is used to find the optimum.

Thus, DataFurnace can be viewed as a machine which repeatedly simulates the data, from a test structure (depth profile) that it intelligently modifies so as to improve the fit between the simulations and the data. Of course it contains a simulator residing in the repeatedly executed core, but this is only a small part of the code.

D.2.2. The sample

The analyst has a sample whose elemental depth profile he wishes to determine. He could take a single RBS spectrum from it. He could collect spectra from the same sample with different beam energies, or different beam incident angles. He could collect RBS and ERDA spectra from the same sample. At Surrey for instance, we usually collect at least two spectra for each sample from detectors mounted at two different scattering angles; this has the advantage that no extra beam time is required. There are many possibilities. The point is that multiple spectra reduce the ambiguity of the data and are highly desirable in principle.

WiNDF allows the analyst to specify a series of spectra collected for the same sample: it will find an elemental depth profile consistent with all of this data simultaneously with no further effort on his part.

D.2.3. The geometry

Each spectrum has certain parameters associated with it, and that can be fed in a ".geo file". These parameters are collected in the *geometry* file, so called since the beam incident or scattering geometries are often the easiest parameters to change when collecting multiple spectra for a sample. So-called IBM (Ion Beam Modification) geometry (when the beam incident direction, the sample normal and the detector scattering direction are in the same plane) and Cornell geometry (when the plane defined by the beam incident direction and the sample normal is perpendicular to the plane defined by the detector scattering direction and the sample normal) can be chosen. The general geometry with a separate azimuth and elevation for both beam incident and scattering directions has not been implemented yet.

The detector resolution is folded into the spectrum calculated for each simulation in the algorithm. Usually the fit is not very sensitive to the precise value of this parameter.

The solid angle is one of the critical parameters. The charge·solid angle product determines the total height of the spectrum. Because in all IBA spectra the scattering probability is strongly dependent on the atomic number Z (for RBS it is proportional to Z^2), the average Z of the sample dominates the total number of counts in the spectrum. DataFurnace *will not* find correct depth profiles if the charge·solid angle product is not *nearly* correct. In the local minimisation part of the fit the charge is tweaked a little for best fit.

It is also critical to get the electronics calibration correct. The energy E of the scattered particle at the detector is assumed to be a linear function of the channel number C: $E = \kappa C + offset$ where the gain, κ, is in keV/channel and the *offset* in keV. The energy to channel conversion function determines where the edges and peaks of the *calculated* spectra lie. But it is these high contrast features of the spectrum that dominate the chi-squared function. Therefore, again, DataFurnace *will not* find correct depth profiles if the gain and offset are not *nearly* correct. In the local minimisation part of the fit both κ and *offset* are tweaked a little for best fit.

Lastly, there is an opportunity to specify regions of interest of the spectrum. The chi-squared function will only be calculated on data inside this region.

D.2.4. Association

It is anticipated that batches of samples will be analysed under similar conditions. Then the same geometry file will be valid for the spectra from each of these samples. WiNDF implements this assumption by separating the spectral data from the associated instrumental information contained in the geometry file and using the "association" function. Different geometry files can be associated to different spectra acquired under different conditions (beam energy, scattering angle, etc). The association can be broken if any change is required.

Some file formats include information on the collected charge with the spectra. In these cases "association" also enters the charge. Otherwise a default value (settable) is inserted. In any case the charge for any association can be changed manually. We recall here that the collected charge is a critical parameter (see section above for comments on charge·solid angle product).

D.2.5. The structure

In principle, because the average Z of the sample dominates the total number of counts in the spectrum and surface stoichiometry of the sample typically determines the position of high contrast features of the spectrum, a single spectrum can often determine the sample structure remarkably unambiguously. Therefore one can conceive fitting software that need be told nothing about the sample. However, state space in this unconstrained case is absolutely gigantic! For realistic computation times it is necessary to constrain state space. This is what the structure file ".str" does.

We emphasise that each *spectrum* has one associated geometry file, but each *sample* (which may have several spectra) has one associated structure file.

Because the DataFurnace is searching in all the state space not excluded by the structure file, a correct solution is often dependent on finding a suitable structure file. Note that there are two possibilities: DataFurnace can find a good fit with an unacceptable structure, in this case the spectrum is ambiguous; alternatively DataFurnace can fail to find a fit, in this case the state space is too large and has to be restricted.

The simplest structure file merely specifies the elements that are present. For each element the user can control the minimum and maximum depth (in thin film units, see below) and the minimum and maximum concentrations.

In specifying the structure file the analyst should be mindful of Occam's Razor: the principle that *assumptions should not be multiplied beyond necessity* (see footnote on page 6-24). It is easy to make the structure file very restrictive: this is a mistake, the user should impose as few restrictions as he can get away with.

The great virtue of the DataFurnace is that it is an excellent systematic tool to explore the validity of different sets of assumptions, as expressed in different structure files.

D.2.6. The batch

Extra samples can be added to the batch with the "Batch/Add extra sample" command. This leaves the previous geometry and structure files, allowing the user to simply add spectra and associate them with the appropriate geometry. The modified batch can be saved in a ".spc" file.

There are normally at least two samples in every batch: the sample the analyst is interested in and a calibration sample. It is also often useful to make a batch where each *sample* has the same spectra but with different conditions.

D.2.7. Thin film units of depth

The units of depth used are the so-called *Thin Film Units* (TFU, or tfu), and they are defined as: one *Thin Film Unit* equals 10^{15} atoms/cm^2. Reference is often made to measures of depth in TFU rather than nm or Å. The natural unit of depth in IBA is the unit in which the energy loss of the ion beam in the sample is measured. This is because IBA spectra are measured as counts per channel where each channel is calibrated as a certain energy width: that is, depth is expressed in IBA spectra as an energy loss.

Energy loss tables have units of 10^{-15} eV·cm^2. This can be cited more explicitly as an energy loss per unit depth by writing eV/(10^{15} atoms/cm^2) which is equivalent to eV/(mg/cm^2). The thickness unit of g/cm^2 can be converted into a linear

thickness by dividing by the density (mg/cm^3). Thin film thicknesses are always given as a mass per unit area because of various definitional difficulties as materials get thinner and thinner. One important such difficulty is that the density of a thin film of a material is often quite different from the density of the bulk material.

Therefore DataFurnace uses thin film units of depth in all the calculations. A conversion to linear depth is provided for the convenience of users, but this is done only by assuming the density of the elements (or molecules) in the sample (which can be specified by the user). But this is, in general, a poor assumption.

D.3 Running DataFurnace

D.3.1. Simulation and the ndf.prf file

It has already been pointed out that it is critical to give DataFurnace correct (or very nearly correct) parameters. Before trying to fit the data one should validate the parameters he has chosen. To do this one simply simulates his calibration spectrum and checks whether the simulated spectrum and the data match.

This can be done by executing the command “Run NDF/Simulate sample”. The user is then asked to edit the “ndf.prf” file, in which he can specify the representations of the layer structures of the sample. The simulation will create one spectrum for this structure for each geometry file. The results of the simulation can be seen by executing the command “View NDF/Data fit”.

If the yield is wrong, the user can either change the solid angle (in the geometry file) or the charge (in the batch file). Clearly the solid angle is not going to change in principle, so when the value is found it should stay fixed (it is a constant). However, the collected charge can fluctuate depending on how well the electron suppression is working. This can be poor in some systems. This is the reason that the charge has been allowed to be specified for each spectrum.

If the energy calibration is wrong (this can be seen by comparison of the spectral edges as given by the data and the simulation) then the user should use his

calibration procedure more carefully to get better values. It is not easy to get good enough values by trial and error.

D.3.2. Fitting the data

Now that the geometry file and the charge have been validated we can run NDF in earnest. The next step is pressing the "Run NDF/Run sample" command. The analyst has now no influence on the result: the machine finds the best fit it can given the set parameters, which include the charge, the geometry file and the structure file.

NDF makes comments during its execution. This is because it can potentially take a very long time and it is important for the analyst to see what it is up to. Most important is the simulated annealing part where the temperature of each Markov chain is given together with the best chi-squared value found for that chain. The chi-squared values are roughly normalised so that a perfect fit would give a chi-squared value of about unity. Of course, with counting noise this best value should never be reached, and in practice values less than ten are generally excellent. If the chi-squared value does not fall sharply during the fit and the final value fails to fall below 100 or so then DataFurnace is not finding a solution. In these circumstances the analyst should check the parameters carefully. If these are OK then he has to ask what it is that is confusing DataFurnace (several sorts of approaches can be taken). The comments made by NDF are stored in the log file, which can be viewed by using the command "View NDF/View log".

To see the result of the fit, one has to execute the command "View NDF/Data fit". Note that this can be executed while the fit is proceeding, so one can get an idea of how NDF *thinks* throughout the fitting process. When the fit is completed, the user can see the partial spectra for one spectrum by executing "File/Open separated spectra". The depth profile is displayed using "View NDF/Best structure".

It is also important to look at the results file with "View NDF/View results". Particular attention must be paid to the way NDF tweaks the charge and the energy calibration. It is sometimes desirable to take a hint, adjust these parameters and rerun the fit for a better fit. The resulting depth profile is at the end of the file. This profile is also stored in the appropriate ".prf" file (thus, if the results file is called

"nam01.res" the profile is called "nam01.prf"). It is possible to take this file, change its name to "ndf.prf" and put it directly back into the simulation if need be.

An important warning appears in the results file just before the depth profile if NDF was unable to obey your restrictions in the structure file (it is quite easy to inadvertently specify inconsistent restrictions). In these cases the analyst must modify the structure file and run NDF again: the results are unreliable.

D.4 The DataFurnace algotithm

D.4.1. The forward model

DataFurnace solves the *inverse IBA problem*: given the spectrum, what is the profile? The *forward model* is the physical model used to answer the inverse question: given the profile, what is the spectrum? All the existing standard IBA codes are simulation codes, that is, they are implementations of the forward model. A forward model is always in the core of any Simulated Annealing algorithm (see the discussion of this further below).

DataFurnace uses a standard forward model for RBS and EBS. For NRA however it implements a more general (although more cumbersome) algorithm than usual. Users have direct access to DataFurnace's forward model, i.e. they can easily use DataFurnace to do simulations.

D.4.2. Simulated annealing

Simulated Annealing is a mathematical algorithm that has been used for many different difficult problems including automatic language parsers and the Travelling Salesman problem, for instance. An excellent introduction to it is in [Kir83], and a more complete discussion is found in [Aar89].

Simulated Annealing is an algorithm for finding the *global* minimum of an *objective function*. The entire *state space* of this function is explored. A sequence of states (a *Markov chain* — see below for more detail on Markov Chain Monte Carlo calculation) is constructed in which succeeding states have an objective function that

is either reducing or has a Boltzmann-like probability of increasing according to a parameter analogous to *temperature*. Hence the idea of *annealing*. A sequence of Markov chains is then constructed with reducing temperature, the end point being an *optimal solution*. The way in which this sequence is constructed is called the *cooling schedule.*

For IBA the objective function for a proposed depth profile is constructed from the difference between the spectrum being fitted and that calculated with a forward model (a standard simulation code) from the proposed depth profile. Then the state space explored is the space of all possible depth profiles.

In the implementation of the Simulated Annealing algorithm in the DataFurnace the given spectrum (or spectra) to be fitted, together with the geometry file, defines the state space. In the structure file are provided facilities to exclude regions (which may be very large) of this state space.

D.4.3. The cooling schedule

The details of the Simulated Annealing algorithm include a (fairly large) number of parameters controlling the construction of the Markov chains and the cooling schedule. Consideration of hundreds of spectra of different types have given rise to the development of algorithms that make these largely transparent to the user

In particular, in many cases the user will only need to tell the DataFurnace how *fast* to run the cooling schedule. There are five options from “ultra-fast” to “ultra-slow”. “Normal” is normally good enough for a satisfactory fit. Experienced users of DataFurnace will occasionally need to use the greater control of the cooling schedule available with “custom cooling”.

It has been observed that the best way to use DataFurnace is always to start with “ultra-fast”. This rapidly reveals if there are severe problems with the calibration (which has to be correct before anything else will work) or with the structure file. Only when it is starting to get the right *type* of solution is it worth going slower, and only when “normal” cooling gives a good fit is it usually worth using “ultra-slow” cooling to give an excellent fit.

D.4.4. Uncertainty estimation using Markov Chain Monte Carlo

The Simulated Annealing algorithm is built on the mathematics of Markov chains. A Markov chain S is a sequence $\{s_1, s_2, \ldots, s_i, \ldots, s_n\}$ where each element s_i depends *only* on the previous element s_{i-1}. The Monte Carlo aspect comes in when generating each state s_i from the previous one s_{i-1}.

It turns out that various theorems can be proved about the statistics of Markov chains. In particular it is possible to calculate the density of states function from the Markov chain. In other words the Markov chain can explore the states in the vicinity of the optimal solution found, and therefore an estimation of the uncertainty of the solution can be determined.

Since the Simulated Annealing algorithm is based on constructing Markov chains it is clearly a natural extension to collect the statistical information needed to estimate the uncertainties. A very simple algorithm is implemented in the present version of DataFurnace. Intense mathematical work is currently underway to improve the efficiency of the algorithm and dramatically enhance its performance.

D.4.5. Grid search local minimisation

Simulated Annealing is a very efficient algorithm for finding the vicinity of the global minimum of a function. But it is very inefficient in searching for local minima. Therefore an effective local minimisation algorithm is supplied. DataFurnace decides when to switch to this algorithm automatically, but the user can control this if he wishes using the facilities in the “ndf.tcn” file.

DataFurnace users can use the local minimisation routine by itself: this is very useful when one already knows the structure of the sample and only wants to refine the details.

APPENDIX E

REFERENCES

E.1 Books and papers

[Aar89] Aarts E., Korst J., *Simulated Annealing and Boltzmann Machines: A Stochastic Approach to Combinatorial Optimization and Neural Computing* (John Wiley & Sons, Chicester, 1989)

[Ams83] Amsel G., Maurel B., *High resolution techniques for nuclear reaction narrow resonance width measurements and for shallow depth profiling*, Nucl. Instr. and Meth. **218** (1983) 183-196

[Ams92] Amsel G., Girard E., Viskelethy G., Battistig G., Girard Y., Szilágyi E., *High pulse rate and pileup handling in precision RBS*, Nucl. Instr. and Meth. **B64** (1992) 811-816

[And80-a] Andersen H.H., Besenbacher F., Loftager P., Möller W., *Large-angle scattering of light ions in the weakly screened Rutherford region*, Phys. Rev. **A21** (1980) 1891-1901

[And80-b] Andersen J.U., Nucl. Instr. and Meth. **170** (1980) 1

[Aon89] Aono M., Katayama M., Nomura E., Chasse T., Choi D., Kato M., *Recent developments in low-energy ion scattering spectroscopy (ISS) for surface structural analysis*, Nucl. Instr. and Meth. **37-38** (1989) 264-269

[Arn92] Arnoldbik W.M., de Laat C.T., Habraken F.H., *On the use of a d*E-E *telescope in elastic recoil detection*, Nucl. Instr. and Meth. **B64** (1992) 832-835

[Arn93] Arnoldbik W.M., Habraken F.H., *Elastic recoil detection*, Rep. on Prog. in Phys. **56** (1993) 859-902

[Ass94] Assman W., Huber H., Steinhausen Ch., Dobler M., Glückler H., Weidinger A., *Elastic recoil detection analysis with heavy ions*, Nucl. Instr. and Meth. **B89** (1994) 131-139

[Ban98] Banks J.C., Doyle B.L., Knapp J.A., Werho D., Gregory R.B., Anthony M., Hurd T.Q., Diebold A.C., *Using heavy ion backscattering spectrometry (HIBS) to solve integrated circuit manufacturing problems*, Nucl. Instr. and Meth. **B138** (1998) 1223-1228

[Bar97-a] Barradas N.P., *QA/QC – Automatic RBS calibration – Update 1*, Internal Report 14/02/97, Dept. Elec. Elec. Eng., University of Surrey, unpublished

[Bar97-b] Barradas N.P., Jeynes C., Webb R.P., *Simulated annealing analysis of Rutherford backscattering data*, Appl. Phys. Lett. **71** (1997) 291-293

[Bar98-a] Barradas N.P., Marriott P.K., Jeynes C., Webb R.P., *The RBS DataFurnace: Simulated annealing*, Nucl. Instr. and Meth. **B136-138** (1998) 1157-1162

[Bar98-b] Barradas N.P., Jeynes C., Harry M.A., *RBS/Simulated annealing analysis of iron-cobalt silicides*, Nucl. Instr. and Meth. **B136-138** (1998) 1163-1167

[Bar98-c] Barradas N.P., Jeynes C., Jackson S.M., *RBS/Simulated annealing analysis of buried SiCOx layers formed by implantation of O into cubic silicon carbide*, Nucl. Instr. and Meth. **B136-138** (1998) 1168-1171

[Bar98-d] Barradas N.P., Jeynes C., Homewood K.P., Sealy B.J., Milosavljevic M., *RBS/simulated annealing analysis of silicide formation in Fe/Si systems*, Nucl. Instr. and Meth. **B139** (1998) 235-238

[Bar99-a] Barradas N.P., Jeynes C., Jenkin M., Marriott P.K., *Bayesian error analysis of Rutherford backscattering spectra*, Thin Solid Films **343-344** (1999) 31-34

[Bar99-b] Barradas N.P., Knights A.P., Jeynes C., Mironov O.A., Grasby T., Parker E.H.C., *High depth resolution Rutherford backscattering data and error analysis using the Simulated Annealing and Markov Chain Monte Carlo algorithms*, Phys. Rev. **B59** (1999) 5097-5105

[Bar99-c] Barradas N. P., Jeynes C., Webb R.P., Kreissig U., Grvtzschel R., *Unambiguous automatic evaluation of multiple ion beam analysis data with simulated annealing*, Nucl. Instr. and Meth. **B149** (1999) 233-237

[Bar02] Barradas N.P., Jeynes C., Webb R.P., Wendler E., *Accurate determination of the stopping power of ^{4}He in Si using Bayesian inference,* Nucl. Instr. and Meth. **B194** (2002) 15-25

[Bau90] Bauer P., *Stopping power of light ions near the maximum*, Nucl. Instr. and Meth. **B45** (1990) 673-683

[Beh87] Behrooz A., Headrick R., Seiberling L., Zurmühle W., *A UHV-compatible ΔE-E gas telescope for depth profiling and surface analysis of light elements*, Nucl. Instr. and Meth. **B28** (1987) 108-112

[Ben86] Benenson R.E., Wielunski L.S., Lanford W.A., *Computer simulation of helium-induced forward recoil proton spectra for hydrogen concentration determinations*, Nucl. Instr. and Meth. **B15** (1986) 453-458

[Bes80] Besenbacher F., Andersen J.U., Bonderup E., *Straggling in energy loss of energetic hydrogen and helium ions*, Nucl. Instr. and Meth. **168** (1980) 1-15

[Bes86] Besenbacher F., Stensgaard L., Vase P., *Absolute cross section for recoil detection of deuterium*, Nucl. Instr. and Meth. **B15** (1986) 459-463

[Bia00] Bianconi M., Abel F., Banks J.C., Climent Font A., Cohen C., Doyle B.L., Lotti R., Lulli G., Nipoti R., Vickridge I., Walsh D., Wendler E., *The Si surface yield as a calibration standard for RBS*, Nucl. Instr. and Meth. **B161-163** (2000) 293-296

[Bir89] Bird J.R., Brown R.A., Cohen D.D., Williams S. in: Bird J.R., Williams S. (eds), *Ion beams for Materials Analysis* (Academic Press, New York, 1989) p. 620

[Bis75] Bishel H., Saxon R.P., *Comparison of calculational methods for straggling in thin absorbers*, Phys. Rev. **A11** (1975) 1286-1296

[Boh15] Bohr N., Phil. Mag. **30** (1915) 318

[Boh48] Bohr N., Mat.-Fys. Medd. Kgl. Dan. Vid. Selsk. **18** (1948) 8

[Boi97] Boie R.A., Wildnauer K.R., *A hybrid pulse pile-up rejection system as applied to Rutherford backscattering*, IEEE Trans. on Nucl. Sci. **NS-24** (1997) 339-347

[Bon71] Bonderup E., Hvelplund P., *Stopping power and energy straggling for swift protons*, Phys. Rev. **A4** (1971) 562-569

[Bør82] Børgesen P., Behrisch R., Scherzer B.M.U., Appl. Phys. **A27** (1982) 183-195

[Bou02] Boudreault, G., Jeynes, C., Wendler, E., Nejim, A., Webb, R.P. and Wätjen, U., *Accurate RBS measurement of ion implant doses in silicon*, Surf. and Interf. Anal. **33** (2002) 478-486

[Boz90] Bozoian M., Hubbard K.M., Nastasi M., *Deviations from Rutherford-scattering cross sections*, Nucl. Instr. and Meth. **B51** (1990) 311-319

[Boz91-a] Bozoian M., *Threshold of non-Rutherford nuclear cross sections for ion beam analysis*, Nucl. Instr. and Meth. **B56-57** (1991) 740-743

[Boz91-b] Bozoian M., *Deviations from Rutherford backscattering for Z = 1, 2 projectiles*, Nucl. Instr. and Meth. **B58** (1991) 127-131

[Bra05] Bragg W.H., Kleemann R., *On the α Particles of Radium, and their Loss of Range in passing through various Atoms and Molecules*, Phil. Mag. **10** (1905) 318-340

[Bre98] Breese M.B.H., Amaku A., Wilshaw P.R., *A comparison between the use of EBIC and IBIC microscopy for semiconductor defect analysis*, Nucl. Instr. and Meth. **B136-138** (1998) 1355-1360

[Bri73] Brice D.K., *Theoretical analysis of the energy spectra of backscattered ions*, Thin Solid Films **19** (1973) 121-135

[Bri90] Brice D.K., Doyle B.L., *A curved detection slit to improve ERD energy and depth resolution*, Nucl. Instr. and Meth. **B45** (1990) 265-269

[Bru96] Bruel M., *Application of hydrogen ion beams to Silicon On Insulator material technology*, Nucl. Instr. and Meth. **B108** (1996) 313-319

[Buc83] Buck T.M., Wheatley G.H., Jackson D.P., *Quantitative analysis of first and second surface layers by LEIS (TOF)*, Nucl. Instr. and Meth. **218** (1983) 257-265

[Buj82] Bujdoso E., Lyon E.S., Nozlospi I., *Prompt nuclear analysis — growth and trends — a scientometric study*, J. of Radioanal. Chem. **74** (1982) 197-238

[Bul87] Bullot J., Schmidt M.P., *Physics of amorphous-silicon carbon alloys*, Phys. Stat. Sol. **143** (1987) 345-418

[Cam96] Campbell S.A., *The Science and Engineering of Microelectronic Fabrication* (Oxford University Press, New-York, 1996)

[Car77] Carlson D.E., *Amorphous silicon solar cells*, IEEE Trans. Electron. Dev. **ED-24** (1977) 449-453

[Cha78] Chan E.K.L., Powers D., Lodhi A.S., Brown R.B., Appl. Phys. **49** (1978) 2346

[Che94] Cheng Huan-sheng, Shen Hao, Yang Fujia, Tang Jiayong, *Cross sections for non-Rutherford backscattering of ^{4}He from five light elements*, Nucl. Instr. and Meth. **B85** (1994) 47-50

[Che99] Chekirine M., Ammi H., *Stopping power of 1.0-3.0 MeV helium in Mylar, Mikrofol and Kapton foils*, Rad. Meas. **30** (1999) 131-135

[Chu76] Chu W.K., Phys. Rev. **A13** (1976) 2057

[Chu78] Chu W.K., Mayer J.W., Nicolet M.-A., *Backscattering Spectrometry* (Academic Press, New York, 1978)
i) Chapter 3.3.1: Energy Loss Ratio Method
ii) Chapter 3.5.1: Spectrum Height for Scattering from the Top Surface Layer
Chapter 3.5.2: Spectrum Height for Scattering at a Depth
iii) Appendix A: Transformation of the Rutherford Formula from Center of Mass to Labarotary Frame of Reference

[Chu89] Chu W.K., *Large-angle coincidence spectrometry from neutron depth profiling*, Radioanal. Eff. And Defects in Solids **108** (1) (1989) 125-126

[Chu98] Chu W.K., Wu D.T., *Scattering recoil coincidence spectrometry*, Nucl. Instr. and Meth. **B35** (1998) 518-521

[Coc32] Cockcroft D., Walton E.T.S., Proc. of the Roy. Soc. **A136** (1932) 619

[Coh72] Cohen B.L., Fink C.L., Degnan J.H., *Nondestructive analysis for trace amounts of hydrogen*, J. of Appl. Phys. **43** (1972) 19-25

[Dar14] Darwin C.G., Phil. Mag. **28** (1914) 499

[Dea73] Dearnaley S., Freeman J.H., Nelson R.S., Stephen J., *Ion Implantation* (North Holland Publishing Company, Amsterdam, 1973)

[Din01-a] Ding S.J., Chen L., Wan X.G., Wang P.F., Zhang J.Y., Zhang D.W., Wang J.T., *Structure characterization of carbon and fluorine-doped silicon oxide films with low dielectric constant*, Mat. Chem. and Phys. **71** (2001) 125-130

[Din01-b] Ding S.J., Zhan Q.Q., Zhan W., Wang J.T., *Characterization of fluorine and carbon-doped silicon oxide film deposited by PECVD*, J. of Inorgan. Mat. **16** (6) (2001) 1169-1173

[Doo85] Doolittle L.R., *Algorithms for the rapid simulation of Rutherford backscattering spectra*, Nucl. Instr. and Meth. **B9** (1985) 344-351

[Doy79] Doyle B.L., Peercy P.S., *Technique for profiling ^{1}H with 2.5-MeV Van de Graaff accelerators*, Appl. Phys. Lett. **34** (1979) 811-813

[Doy88] Doyle B.B., Brice D.K., *The analysis of elastic recoil detection data*, Nucl. Instr. and Meth. **B35** (1988) 301-308

[Eck01] Ecker K.H., Berger A., Grötzschel R., Persson L., Wätjen U., *Antimony implanted in silicon – a thin layer reference material for surface analysis*, Nucl. Instr. and Meth. **B175-177** (2001) 797-801

[Eck02] Ecker K.H., Wätjen U., Berger A., Persson L., Pritzkow W., Radtke M., Riesemeier H., *RBS, SY-XRF, INAA and ICP-IDMS of antimony implanted in silicon – a multi-method approach to characterize and certify a reference material*, Nucl. Instr. and Meth. **B188** (2002) 120-125

[Eck99] Eckstein W., Mayer M., *Rutherford backscattering from layered structures beyond the single scattering model*, Nucl. Instr. and Meth. **B153** (1999) 337-344

[Ell00] Elliman R.G., Timmers H., Ophel T.R., Weijers T.D.M., Wielunski L.S., Harding G.L., *Simultaneous hydrogen detection with an ERD gas ionization detector*, Nucl. Instr. and Meth. **B161/163** (2000) 231-234

[Fel82] Feldman L.C., Mayer J.W., Picraux S.T., *Materials Analysis by Ion Channeling* (Academic Press, New-York, 1982)

[Fel86] Feldman L.C., Mayer J.W., *Fundamentals of Surface and Thin Film Analysis* (North-Holland, New York, 1986)
i) Chapter 12

[Fen74] Feng J.S.Y., Chu W.K., Nicolet M.A., *Stopping cross-section additivity for 1-2 MeV $^{4}He^{+}$ in solid oxides*, Phys. Rev. **B10** (1974) 3781-3788

[Fin01] Finnis R., Boudreault, G., Webb, R.P., Jeynes, C., Fellows, D.F. and van den Broek, R., *A six movement goniometer for accurate automatic ion beam analysis*. Proceedings of the 15th IBA (Ion Beam Analysis) conference (2001)

[Fut00] Futako W., Sugawara T., Kamiya T., Shimizu I., *High electric field photocurrent of Vidicon and diode devices using wide band gap a-Si : H prepared with intentional control of silicon network by chemical annealing*, J. of Organomet. Chem. **611** (1-2) (2000) 525-530

[Gar91] Garrett A., *Ockham's Razor*, Physics World **4** (May 1991) 39-42

[Gei13] Geiger H., Marsden E., *On the Laws of Deflexion of α Particles through Large Angles*, Phil. Mag. **25** (1913) 604-623

[Gem74] Gemmell D.S., *Channeling and related effects in the motion of charged particles through crystal*, Rev. of Mod. Phys. **46** (1974) 129-227

[Gol59] Golsdtein H., *Classical Mechanics* (Addison-Wesley, Reading, Massachusetts, 1959)
i) Chapter 3.7: Scattering in a central force field

[Gra31] Van de Graaff R.J., Phys. Rev. **38** (1931) 1919A

[Gro83] Groleau R., Gujrathi S.C., Martin J.P., *Time-of-flight system for profiling recoiled light elements*, Nucl. Instr. and Meth. **218** (1983) 11-15

[Guj90] Gujrathi S.C., *Depth profiles of thin-films and interfaces by ERD*, Am. Chem. Soc. Symp. Ser. **440** (1990) 88-109

[Gün88] Günzler R., Schüler V., Seeliger G., Weiser M., Böhringer K., Kalbitzer S., Kenner J., *A multisegment annular Si-detector system for RBS analysis*, Nucl. Instr. and Meth. **B35** (1988) 522-529

[Gur97] Gurbich A.F., *Evaluation of non-Rutherford proton elastic cross section for oxygen*, Nucl. Instr. and Meth. **B129** (1997) 311-316

[Gur98-a] Gurbich A.F., *Evaluation of non-Rutherford proton elastic cross section for carbon*, Nucl. Instr. and Meth. **B138** (1998) 60-65

[Gur98-b] Gurbich A.F., *Evaluation of non-Rutherford proton elastic cross section for silicon*, Nucl. Instr. and Meth. **B145** (1998) 578-583

[Gur99] Gurbich A.F., *Proton elastic cross section for carbon: confrontation of theory and experiment*, Nucl. Instr. and Meth. **B152** (1999) 403-405

[Gur00] Gurbich A.F., *Evaluation of the cross-section for elastic scattering of He-4 from carbon*, Nucl. Instr. and Meth. **B161** (2000) 125-129

[Har73] Hart R.R., Dunlap H.L., Mohr A.J., Marsh O.J., *The detection sensitivity of heavy impurities in Si using 280 keV He^{2+} and C^{2+} back-scattering*, Thin Solid Films **19** (1973) 137-144

[Hau80] Hautala M., Luomajärvi M., *Correction of the Rutherford Scattering cross section in the backscattering analysis*, Rad. Effects **45** (1980) 159-162

[Hea00] Healy M.J.F, Gurbich A.F., *New data on the proton elastic scattering cross-section for silicon*, Nucl. Instr. and Meth. **B161** (2000) 136-140

[Hem83] Hemment P.L.F., Mynard J.E., Maydell-Ondrusz E.A., Stephens K.G., *Ion Implantation: Equipment and Techniques*, eds., Ryssel H. and Glawischnig (Springer, Berlin, 1983)

[Her91] Herault J, Bimbot R., Gauvin H., Kubica B., Anne R., Bastin G., Hubert F., *Stopping powers of gases for heavy-ions (O, Ar, Kr, Xe) at intermediate energy (20-100 MeV/u)-Vanishing of the gas solid effect*, Nucl. Instr. and Meth **B61** (1991) 156-166

[Hir91] Hirvonen J.K., *Ion-beam assisted thin-film deposition*, Mat. Sci. Rep., **6** (6) (1991) 215-274

[Hjö89] Hjörvarsson B., Rydén J., Ericsson T., Karlsson E., *Hydrogenated tantalum: a convenient calibration substance for hydrogen profile analysis using nuclear resonance reactions*, Nucl Instr. and Meth. **B42** (1989) 257-263

[Hof90] Hofsäss H.C., Parikh N.R., Swanson M.L., Chu W.K., *Depth profiling of light elements using elastic recoil coincidence spectrometry (ERCS)*, Nucl. Instr. and Meth. **B45** (1990) 151-156

[Hof91] Hofsäss H.C., Parikh N.R., Swanson M.L., Chu W.K., *Elastic recoil coincidence spectrometry (ERCS)*, Nucl. Instr. and Meth. **B58** (1991) 49-70

[Hol00] Hollander B., Heer H., Wagener M., Halling H., Manti S., *New high-precision 5-axes RBS/channeling goniometer for ion beam analysis of 150 mm diameter wafers*, Nucl. Instr. and Meth. **B161** (2000) 227-230

[Hom93] Homma T., Yamaguchi R., Murao Y., *A room temperature chemical vapour deposition SiOF film formation technology for the interlayer in submicron multilevel interconnections*, J. of Electrochem. Soc. **140** (1993) 687-692

[Hom96] Homma T., *Properties of fluorinated silicon oxide films formed using fluorotriethoxysilane for interlayer dielectrics in multilevel interconnections*, J. of Electrochem. Soc. **143** (1996) 1084-1087

[How83] Howe L.M., Swanson M.L., Davies J.A., *Methods of Experimental Physics*, Vol. 21 (Academic Press, New-York, 1983)

[Hub91] Hubbard K.M., Tesmer J.R., Nastasi M., Bozoian M., *Measured deviations from Rutherford backscattering cross sections using Li-ion beams*, Nucl. Instr. and Meth. **B58** (1991) 121-126

[Hüt96] Hüttner D., Meyer O., Reiner J., Linker G., *High resolution RES study of the growth and the crystalline quality of ultrathin YBaCuO films*, Nucl. Instr. and Meth. **B118** (1996) 578-583

[ISO93] *Guide to the Expression of Uncertainty in Measurement*, ISO, Geneva (1993)

[Jey85] Jeynes C., Kimber A.C., *High accuracy data from Rutherford back-scattering spectra: measurements of the range and straggling of 60-400 keV As implants into Si*, J. Phys. **D18** (1985) L93-L97

[Jey97] Jeynes C., Jafri Z.H., Webb R.P., Kimber A.C., Ashwin M.J., *Accurate RBS measurements of the indium content in InGaAs thin films*, Surf. and Interf. Anal. **25** (1997) 254-260

[Jey98-a] Jeynes C., RBS training course, University of Surrey, England, 1998

[Jey98-b] Jeynes C., Barradas N.P., Blewett M.J., Webb R.P., *Improved ion beam analysis facilities at the University of Surrey*, Nucl. Instr. and Meth. **B136-138** (1998) 1229-1234

[Jey00] Jeynes C., Barradas N.P. Webb R.P., *IBA DataFurnace Users Guide for the automatic extraction of elemental depth profiles from ion beam analysis data – the WiNDF v.6.5/7.0* (Manual, University of Surrey Ion Beam Centre, Guildford, England, 2000) p.8

[Jey02] Jeynes C., Barradas N.P., Marriott P.K., Boudreault G., Jenkin M., Wendler E., *Elemental thin film depth profiles by ion beam analysis using simulated annealing — a new tool*, submitted to J. of Phys. D topical review (2002)

[Joh88] Johansson S.A.E., Campbell J.L., *PIXE: A Novel Technique for Elemental Analysis* (Wiley, Chichester, UK, 1988)

[Jok96] Jokinen J., Keinonen J., Tikkanen P., Kuronen A., Ahlgren T., Nordlund K., *Comparison of TOF-ERDA and nuclear resonance reaction techniques for range profile measurements of keV energy implants*, Nucl. Instr. and Meth. **B119** (1996) 533-542

[Kim96] Kim D.S., Lee Y.H., Park N.H., *Deposition of thermally stable, low dielectric constant fluorocarbon/SiO_2 composite thin film*, Appl. Phys. Lett. **69** (1996) 2776-2778

[Kir83] Kirkpatrick S., Gelatt C.D.Jr, Vecchi M.P., *Optimization by Simulated Annealing*, Science **220** (1983) 671-680

[Kla98] Klatt C., Kalbitzer S., Konac G., *Low energy ion backscattering spectrometry of multi-layer targets*, Nucl. Instr. and Meth. **B136-138** (1998) 153-158

[Kon98] Konac G., Kalbitzer S., Klatt C., Niemann D., Stoll R., *Energy loss and straggling of H and He ions of keV energies in Si and C*, Nucl. Instr. and Meth. **B136-138** (1998) 159-165

[Kót94] Kótai E., *Computer methods for analysis and simulation of RBS and ERDA spectra*, Nucl. Instr. and Meth. **B85** (1994) 588-596

[Kre80] Kreutz R., Neuwirth W., Pietsch W., *Electronic stopping cross sections of liquid organic compounds for 200-840-keV Li ions*, Phys. Rev. **A22** (1980) 2598-2605

[Lan44] Landau L., J. Phys. USSR **8** (1944) 201

[Lan76] Lanford W.A., Trautvetter H.P., Ziegler Z.F., Keller J., *New precision technique for measuring the concentration versus depth of hydrogen in solids*, Appl. Phys. Lett. **28** (1976) 566-568

[Lax95] Laxman R.K., Semiconductor Int. **5** (1995) 71

[Lec76] L'Ecuyer J., Brassard C., Cardinal C., Chabball J., *An accurate and sensitive method for the determination of the depth distribution of light elements in heavy material*, J. of Appl. Phys. **47** (1976) 381-382

[Lec78] L'Ecuyer J., Brassard C., Cardinal C., *The use of ^{6}Li and ^{35}Cl ion beams in surface analysis*, Nucl. Instr. and Meth. **149** (1978) 271-277

[Lec79] L'Ecuyer J., Davies J.A., Matsunami N., *How accurate are absolute Rutherford backscattering yields*, Nucl. Instr. and Meth. **160** (1979) 337-346

[LeC79] Le Comber P.G., Spears W.E., Allan D., *Transport studies in doped amorphous silicon*, J. of Non-Cryst. Solids **32** (1979) 1-15

[Lee96] Lee S.M., Park M., Park K.C., Bark J.T., Jang J., *Low dielectric constant fluorinated oxide films prepared by remote plasma chemical vapor deposition*, Jpn. J. of Appl. Phys. **35 (2b)** (1996) 1579-1582

[Lee98] Lee S., Park J.W., *Effect of fluorine on moisture absorption and dielectric properties of SiOF films*, Mater. and Chem. Phys. **53** (1998) 150-154

[Len90] Lennard W.N., Tong S.Y., Massoumi G.R., Wong L., *On the calibration of low-energy ion accelerators*, Nucl. Instr. and Meth. **B45** (1990) 281-284

[Len99-a] Lennard W.N., Massoumi G.R., Simpson T.W., Mitchell I.V., *Improved stoichiometry measurements using ^{4}He backscattering: experiment and simulation*, Nucl. Instr. and Meth. **B152** (1999) 370-376

[Len99-b] Lennard W.N., private communication, November 1999

[Leo94] Leo W.R., *Techniques for Nuclear and Particles Physics Experiments* (Springer-Verlag, Berlin, 1994)

i) Chapter 2: Passage of Radiation Through Matter
ii) Chapter 3: Radiation Protection. Biological Effects of Radiation

[Lin53] Lindhard J., Scharff M., Mat. Fys. Medd. Dan. Vid. Selsk. **27** (1953) 15

[Liv37] Livingston M.S., Bethe H.A., Rev. Mod. Phys. **9** (1937) 245

[Liv80] Livingston M.S., *Early history of particle accelerators*, Adv. in Elect. and Electron Phys. **50** (1980) 1-88

[Lub99] Lubguban J. Jr, Saitoh A., Kurata Y., Inokuma T., Hasegawa S., *Stability of the dielectric properties of PECVD deposited carbon-doped SiOF films*, Thin Solid Films **337** (1999) 67-70

[Lul00] Lulli G., Albertazzi E., Bianconi M., Bentini G.G., Nipoti R., Lotti R., *Determination of He electronic energy loss in crystalline Si by Monte-Carlo simulation of Rutherford backscattering channeling spectra*, Nucl. Instr. and Meth. **B170** (2000) 1-9

[Mar14] Marsden E., *The passage of particles through hydrogen*, Philos. Mag. **27** (1914) 824

[Mar98] Marriott P.K., Jenkin M., Jeynes C., Barradas N.P., Webb R.P., Sealy B.J., *Rapid accurate automated analysis of complex ion beam analysis data*; Proceedings of the 15th CAARI (Conference on Application of Accelerators in Research and Industry) conference (Denton 1998)

[May77] Mayer J.W., Rimini E., *Ion Beam Handbook for Material Analysis* (Academic Press, New-York, 1977) ("Catania Handbook")

[May97] Mayer M., *SIMNRA Users Guide*, Technical Report IPP 9/113, (Max-Planck-Institüt für Plasmaphysik, Garching, Germany, 1997)

[Mcd83] Mcdonald J.R., Davies J.A., Jackman T.E., Feldman L.C., *How well does ^{4}He backscattering from low-Z nuclei obey the Rutherford formula?*, Appl. Phys. **54** (1983) 1800-1803

[Mer93] Mercier F., Toulhoat N., Trocellier P., Durand C., Bisiaux M., *Characterization of organic matter in oil-related rocks: Experimental approach and illustration*, Nucl. Instr. and Meth. **B77** (1993) 492-498

[Moo75] Moore J.A., Mitchell I.V., Hollis M.J., Davies J.A., Howe L.M., *Detection of low-mass impurities in thin film using MeV heavy-ion elastic scattering and coincidence detection techniques*, J. of Appl. Phys. **46** (1975) 52-61

[Moo80] Moore J., *An analysis of Rutherford backscattering spectra to determine dechanneling in single crystals*, Nucl. Instr. and Meth. **174** (1980) 577-584

[Mor73] Morgan D.V., *Channeling: Theory, Observations and Applications* (Wiley {interscience}, New-York, 1973)

[Myn85] Mynard J.E., Jeynes C., Thornton J., Way A., Webb R.P., Albury D., Hemment P.L.F., Stephens K.G., *Improved facilities for ion beam surface analysis at the University of Surrey*, Nucl. Instr. and Meth. **B6** (1985) 264-269

[NDF02] *The IBA DataFurnace NDF manual v7.7a*, Surrey Ion Beam Centre, 2002 (available at: http://www.ee.surrey.ac.uk/SCRIBA/ndf/page1.html#examples)
i) Section 21: ^{4}He on H non-Rutherford cross-sections

[Nee00] Neelmeijer C., Brissaud I., Calligaro T., Demortier G., Hautojaervi A., Maeder M., Martinot L., Schreiner M., Tuurnala T., Weber G., *Paintings : a challenge for XRF and PIXE analysis*, X-ray spectrometry **Vol.29 No.1** (2000) 101-110

[Oco89] O'Connor D.J., Chunyu T., *Application of heavy ions to high depth resolution RBS*, Nucl. Instr. and Meth. **B36** (1989) 178-188

[Odd89] Oddershede J., Sabin J.R., *Bragg rule additivity of bond stopping cross-sections*, Nucl. Instr. and Meth. **B42** (1989) 7-10

[Orl97] Orlic I., Wenlan B., Watt F., Tang S.M., *Air pollution in Singapore : Its multielemental aspect as measured by nuclear analytical techniques*, Environmental monitoring and assessment **Vol.44 No.1-3** (1997) 455-470

[Oxo90] Oxorn K., Gujrathi S.C., Bultena S., Cliché L., Miskin J., *An iterative computer-analysis package for elastic recoil detection (ERD) experiments*, Nucl. Instr. and Meth. **B45** (1990) 166-170

[Pás86] Pászti F., Kótai E., Mezey G., Manuaba A., Pócs L., Hildebrandt D., Strusny H., *Hydrogen and deuterium measurements by elastic recoil detection using alpha particles*, Nucl. Instr. and Meth. **B15** (1986) 486-491

[Pás91] Pászti F., Szilágyi E., Kótai E., *Optimization of the depth resolution in elastic recoil detection*, Nucl. Instr. and Meth. **B54** (4) (1991) 507-512

[Pee81] Peercy P.S., *Hydrogen in amorphous silicon*, Nucl. Instr. and Meth. **182/183** (1981) 337-349

[Pet84] Petrascu M., Berceanu I., Brancus I., Buta A., Duma M., Grama C., Lazar I., Mihai I., Petrovici M., Simon V., Mihaila M., Ghita I., *A*

method for analysis and profiling of boron, carbon, and oxygen impurities in semiconductor wafers by recoil atoms in heavy ion beams, Nucl. Instr. and Meth. **B4** (1984) 396-398

[Pie99] Pierson H.O., *Handbook of Chemical Vapor Deposition*, (William Andrew Publishing, New York, 1999)

[Pre88] Pretorius R., Peisach M., Mayer J.W., *Hydrogen and deuterium depth profiling by elastic recoil detection analysis*, Nucl. Instr. and Meth. **B35** (1988) 478-483

[Pri02] Pritzkow W., Vogl J., Berger A., Ecker K.H., Grötzschel R., Klingbeil P., Persson L., Riebe G., Wätjen U., *Contribution of ICP-IDMS to the certification of antimony implanted in a silicon wafer – comparison with RBS and INAA results*, Fresenius J. Anal. Chem. **371** (2001) 867-873

[Pro94] Prozesky V., Churms C., Pilcher J., Springhorn K., Behrish R., *ERDA measurements of hydrogen isotopes with a ΔE-E telescope*, Nucl. Instr. and Meth. **B84** (1994) 373-379

[Ren86] Rennie J., Elliot S.R., Jeynes C., *Rutherford backscattering study of the photodissolution of Ag in amorphous $GeSe_2$*, Appl. Phys. Lett. **48(21)** (1986) 1430-1432

[Riv00] Rivière J.P., *Structure and properties of hard coatings produced by dynamic ion mixing*, Journal de physique IV **10 (P6)** (2000) 53-58

[Ros84] Ross G.G., Terreault B., Gobeil G., Abel G., Boucher C., Veilleux G., *Inexpensive quantitative hydrogen depth profiling for surface probes*, J. of Nucl. Mater. **128-129** (1984) 730-733

[Ros92-a] Ross G.G., Leblanc L., *Depth profiling of hydrogen and helium isotopes by means of the ERD-E×B technique*, Nucl. Instr. and Meth. **B62** (1992) 484-492

[Ros92-b] Ross G.G., Leblanc L., Terreault B., Pageau J.F., Gollier P.A., *Nuclear microanalysis by means of 350-keV Van de Graaff accelerator*, Nucl. Instr. and Meth. **B66** (1992) 17-22

[Rou95] Roux B., Chevarier A., Chevarier N., Wybourn B., Antoine C., Bonin B., Bosland P., Cantacuzene S., *High-resolution hydrogen profiling in superconducting materials by ion beam analysis (ERD-E×B)*, Vacuum **46** (1995) 629-632

[Rud86] Rudolph W., Bauer C., Brankoff K., Grambole D., Grotzschel R., Heiser C., Hermann F., *Plastic foils as primary hydrogen standards for nuclear reaction analysis*, Nucl. Instr. and Meth. **B15** (1986) 508-511

[Rut11] Rutherford E., *The Scattering of α and β Particles by Matter and the Structure of the Atom*, Phil. Mag. **21** (1911) 669-688

[Saa92] Saarilahti J., Rauhala E., *Interactive personal-computer data-analysis of ion backscattering spectra*, Nucl. Instr. and Meth. **B64** (1992) 734-738

[Sab85] Sabin J.R., Oddershede J., Sigmund P., *On the proton stopping power maximum in gases and vapours*, Nucl. Instr. and Meth. **B12** (1985) 80-83

[Sea88] Seah M.P., David D., Davies J.A., Jackman T.E., Jeynes C., Ortega C., Read P.M., Sofield C.J., Weber G., *An intercomparison of absolute measurements of the oxygen and tantalum thickness of tantalum pentoxide reference materials, BCR 261, by six laboratories*, Nucl. Instr. and Meth. **B30** (1988) 140-151

[Ses01] Seshan K., *Handbook of Thin Film Deposition Processes and Techniques*, (William Andrew Publishing, New York, 2001)

[Sig69] Sigmund P., *Theory of sputtering I: Sputtering yield of amorphous and polycrystalline targets*, Phys. Rev. **184** (1969) 383-416

[Sig74] Sigmund P., Winterbon L.B., *Small-angle multiple scattering of ions in the screened Coulomb region*, Nucl. Instr. and Meth. **119** (1974) 541-557

[Smi74] Smidt F.A. Jr., Pieper A.G., *Studies of the mobility of helium in vanadium*, J. of Nucl. Mater. **51** (1974) 361-365

[Sof90] Sofield C.J., *Heavy-ion energy loss*, Nucl. Instr. and Meth. **B45** (1990) 684-688

[Sop01] Sopori B., Zhang Y., Ravindra N.M., *Silicon device processing in H-ambients: H-diffusion mechanisms and influence on electronic properties*, J. of Electr. Mat. **30** (12) (2001)1616-1627

[Spe75] Spear W.E., Le Comber P.G., *Substitutional doping of amorphous silicon*, Solid State Commun. **17** (1975) 1193-1196

[Suz91] Suzuki K. in: Kanicki J., Editor, *Amorphous and Microcrystalline Semiconductors Devices*, (Artech House, Norwood, MA, 1991)

[Swa82] Swanson M.L., *The study of lattice defects by channelling*, Rep. on Prog. in Phys. **45** (1982) 47-93

[Sym48] Symon K.R., Thesis (Harvard University, Cambridge, Mass, 1948)

[Szi94] Szilágyi E., Pászti F., *Theoretical calculation of the depth resolution of IBA methods*, Nucl. Instr. and Meth. **B85** (1994) 616-620

[Szi95] Szilágyi E., Pászti F., Amsel G., *Theoretical approach of depth resolution in IBA geometry*, Nucl. Instr. and Meth. **B100** (1995) 103-121

[Taw81] Tawada Y., Okamoto H., Hamakawa Y., *a-SiC:H/a-Si:H heterojunction solar cell having more than 7.1% conversion efficiency*, Appl. Phys. Letters **39** (1981) 237-239

[Tes95] Tesmer J.R., Nastasi M. (Eds), *Handbook of Modern Ion Beam Materials Analysis* (Materials Research Society, Pittsburg, 1995)

i) Chapter 2: Energy Loss (Rauhala E.)
ii) Chapter 4: Backscattering Spectrometry (Leavitt J.A. McIntyre L.C. Jr. and Weller M.R.)
iii) Chapter 4.2.2.3: Non-Rutherford cross sections (Leavitt J.A., McIntyre L.C. Jr. and Weller M.R.)
iv) Chapter 6: Nuclear Reaction Analysis: Particle-Particle Reactions (Vizkelethy G.)
v) Chapter 7: Nuclear Reaction Analysis: Particle-Gamma Reactions (Hirnoven J.P.)
vi) Chapter 10: Channeling (Swanson M.L.)
vii) Chapter 12.4.3: Bi calibration standard (Davies J.A., Lennard W.N. and Mitchell I.V.)
viii) Chapter 13: Radiological Safety (Deluca P.M. Jr. and Tesmer J.R.)
ix) Appendix 3: Stopping and Range (Rauhala E.)
x) Appendix 6: Rutherford Cross Sections (Dick A. and Tesmer J.R.)
xi) Appendix 7: Non-Rutherford Elastic Backscattering Cross Sections (Cox R.P., Leavitt J.A. and McIntyre L.C. Jr.)
xii) Appendix 10: Deuterium-Induced Nuclear Reaction Parameters (Vizkelethy G.)
xiii) Appendix 11: Particle-Particle Nuclear Reaction Cross Sections (Foster L., Vizkelethy G., Lee M., Tesmer J.R. and Nastasi M.)
xiv) Appendix 12: Particle-Gamma Data (Hirvonen J.P. and Lappalainen R.)
xv) Appendix 13: Hydrogen Nuclear Reaction Data (Lanford W.A.)
xvi) Appendix 18: Radiation Hazards of (α,n) Reactions (Basu S.N., Nastasi M. and Tesmer J.R.)

[Tho83] Thomas J.P., Fallavier M., Ramdane D., Chevarier M., Chevarier A., *High-resolution depth profiling of light elements in high atomic mass materials*, Nucl. Instr. and Meth. **218** (1983)125-128

[Tho96] Thong P.S.P., Makjanic J., Watt F*., A review of nuclear microscopy and applications in medicine*, Singapore medical journal **Vol.37 No.5** (1996) 527-531

[Thw85] Thwaites D.I., *Current status of physical state effects on stopping power*, Nucl. Instr. and Meth. **B12** (1985) 84-89

[Thw87] Thwaites D.I., *Review of stopping powers in organic materials*, Nucl. Instr. and Meth. **B27** (1987) 293-300

[Tim98] Timmers H., Palmer G.R., Ophel T.R., O'Connor D.J., Elliman R.G., *The development of a facility for heavy-ion elastic recoil detection analysis at the Australian National University*, Nucl. Instr. and Meth. **B136/138** (1998) 611-615

[Tim00-a] Timmers H., Ophel T.R., Elliman R.G., *Simplifying position-sensitive gas-ionization detectors for heavy ion elastic recoil detection*, Nucl. Instr. and Meth. **B161/163** (2000) 19-28

[Tim00-b] Timmers H., Ophel T.R., Elliman R.G., *New design features of gas-ionization detectors used for elastic recoil detection*, Nucl. Instr. and Meth. in Phys. Res. **A447** (2000) 536-543

[Tir89-a] Tirira J., Frontier J.P., Trocellier P., *Hydrogen analysis by elastic recoil spectrometry: a new approach for absolute quantitative measurement*, J. of Radioanal. and Nucl. Chem. **130** (2) (1989) 279-286

[Tir89-b] Tirira J., Trocellier P., *Elastic recoil detection analysis: theoretical analysis of scattering cross section and basic parameters*, J. Radioanal. and Nucl. Chem. **130** (1989) 311-319

[Tir90-a] Tirira J., Trocellier P., Frontier J.P., Trouslard P., *Theoretical and experimental study of low energy 4He-induced 1H elastic recoil with application to hydrogen behaviour in solids*, Nucl. Instr. and Meth. **B45** (1990) 203-207

[Tir90-b] Tirira J., Trocellier P., Frontier J.P., Massiot P., Constantini J.M., Mori V., *3D hydrogen profiling by elastic recoil detection analysisin transmission geometry*, Nucl. Instr. and Meth. **B50** (1990) 135-139

[Tir91-a] Tirira J., Frontier J.P., Trocellier P., Trouslard P., *Development of a simulation algorithm for energy spectra of elastic recoil spectrometry*, Nucl. Instr. and Meth. **B54** (1991) 328-333

[Tir91-b] Tirira J., Trocellier P., Mosbah M., Metrich N., *Study of hydrogen content in solids by ERDA and radiation-induced damage*, Nucl. Instr. and Meth. **B56-57** (1991) 839-842

[Tir96] Tirira J., Serruys Y., Trocellier P., *Forward Recoil Spectrometry — Applications to Hydrogen Determination in Solids* (Plenum Press, New York and London, 1996)

i) Chapitre 2: Basic Physical Processes of Elastic

Spectrometry
ii) Chapitre 3: Elastic Scattering: Cross-Section and Multiple Scattering
iii) Chapitre 5: Conventional Recoil Spectrometry (Hofsäss H.)
iv) Chapitre 6: Time of Flight ERDA (Dytlewski N.)
v) Chapitre 7: Depth Profiling by Means of the ERDA E×B Technique (Ross G.)
vi) Chapitre 8: Recoil Spectrometry with a ΔE-E Telescope
vii) Chapitre 9: Coincidence Techniques (Hofsäss H.)
viii) Chapitre 9.7: Position-Sensitive Detectors for Coincidence ERDA Techniques (Hofsäss H.)
ix) Chapitre 13: Elastic Recoil Spectrometry Using High-Energy Ions for Hydrogen and Light Element Profiling

[Tou89] Toulemonde M., Balanzat E., Bouffard S., Jousset J.C., *Structural modifications induced by electronic energy deposition during the slowing down of heavy ions in matter*, Nucl. Instr. and Meth. **B39** (1989) 1-6

[Tow76] Townsend P.D., Kelly J.C., Hartley N.E.W., *Ion Implantation, Sputtering and their Applications* (Academic Press, London, 1976)

[Tro91] Trocellier P., Tirira J., Massiot Ph., Gosset J., Costantini J.M., *Nuclear microprobe study of the composition degradation induced in polyimides by irradiation with high-energy heavy ions*, Nucl. Instr. and Meth. **B54-55** (1991) 118-122

[Tro94] Trocellier P., *Sputtering yields of thin films for MeV microbeam irradiation: Preliminary results*, Rad. Effects **132** (1994) 305

[Tsc68] Tschalär C., *Straggling distributions of extremely large energy losses*, Nucl. Instr. and Meth. **64** (1968) 237-243

[Tur68] Turkevich A.L. *et al*., in *Surveyor Project Final Report*, Part II. Scientific Results, Nat. Aeronaut. and Space Administration Tech. Rep. 32-1265, pp. 303-387. Jet Propulsion Lab., California Inst. Of technol., Pasadena, California, 1968)

[Tur84] Turos A., Meyer O., *Depth profiling of hydrogen by detection of recoil protons*, Nucl. Instr. and Meth. **B4** (1984) 92-97

[Ugg80] Uggerhoj E., Nucl. Instr. and Meth. **170** (1980) 105

[Vav57] Vavilov P.V., Sov. Phys. JETP **5** (1957) 749

[Ver01] Verda R.D., Maggiore C.J., Tesmer J.R., Misra A., Hoechbauer T., Nastasi M., Bower R.W., *Depth profiling of hydrogen in crystalline*

silicon using elastic recoil detection analysis, Nucl. Instr. and Meth. **B183** (2001) 401-412

[Vic97] Vickerman J.C., *Surface Analysis: the Principal Techniques* (John Wiley & Sons Ltd, Chichester, 1997)
i) Chapter 6: Low-energy Ion Scattering and Rutherford Backscattering (Taglauer E.)

[Viz90] Vizkelethy G., *Simulation and evaluation of nuclear-reaction spectra*, Nucl. Instr. and Meth. **B45** (1990) 1-5

[Wan00-a] Wang P.F., Ding S.J., Zhang W., Zhang J.Y., Wang J.T., Wei W.L., *FTIR characterization of fluorine doped silicon dioxide thin films deposited by plasma enhanced chemical vapour deposition*, Chin. Phys. Lett. **17** (2000) 912-914

[Wan00-b] Wang Lianwei, Huang Jipo, Duo Xinzhong, Song Zhitang, Lin Chenglu, Zetterling C.M., Oestling M., *Investigation of damage behaviour and isolation effect of n-type 6H-SiC by implantation of oxygen*, Journal of physics D, Applied physics, **Vol.33 No.12** (2000) 1551-1555

[Wät92] Wätjen U., Bax H., Rietveld P., *Evaporated and implanted reference layers for calibration in surface-analysis*, Surf. and Interf. Anal. **19** (1992) 253-258

[Wät94] Wätjen U., Bax H., *Bi-implanted silicon reference material revisited — uniformity of the remaining batch*, Nucl. Instr. and Meth. **B85** (1994) 627-632

[Wei01] Weijers T.D.M., Orphel T.R., Timmers H., Elliman R.G., *Systematic study of the pulse height deficit in propane-filled gas ionisation detectors*, Nucl. Instr. and Meth. **A483** (2002) 676-688

[Wen52] Wenzel W.A., Whaling W., *The stopping cross section of D_2O Ice*, Phys. Rev. **87** (1952) 499-503

[Whi87] Whitlow H.J., Possnert G., Petersson C.S., *Quantitative mass and energy-dospersive elastic recoil spectrometry: Resolution and efficiency considerations*, Nucl Instr. and Meth. **B27** (1987) 448-457

[Wie96] Wielunski L.S., *Multiple and double scattering contributions to depth resolution and low energy background in hydrogen elastic recoil detection*, Nucl. Instr. and Meth. **B118** (1996) 256-261

[Wie98] Wielunski L.S., Szilágyi E., Harding G.L., *Multiple scattering effects in depth resolution of elastic recoil detection*, Nucl. Instr. and Meth. **B136/138** (1998) 713-718

[Yan91] Yang Q., O'Connor D.J., Wang Z., *Empirical formulae for energy loss straggling of ions in matter*, Nucl. Instr. and Meth. **B61** (1991) 149-155

[Zie74] Ziegler J.F., Chu W.K., Atom. Data and Nucl. Data Tables **13** (1974) 463

[Zie77] Ziegler J.F., *Helium: Stopping Powers and Ranges in All Elements* (Pergamon Press, New-York, 1977)

[Zie78] Ziegler J.F. *et al*., *Profiling hydrogen in materials using ion beams*, Nucl. Instr. and Meth. **149** (1978) 19-39

[Zie80] Ziegler J.F., *Handbookof Stopping Cross Sections for Energetic Ions in All Elements* (Pergamon Press, New-York, 1980)

[Zie82] Ziegler J.F., Biersack J.P., Littmark U., *Empirical Stopping Powers for Ions in Solids*, IBM Research Report **RC9250**, 1982

[Zie85] Ziegler J.F., Biersack J.P., Littmark U., *The Stopping and Range of Ions in Solids* (Pergamon Press, New-York, 1985)

[Zie88] Ziegler J.F., Manoyan J.M., *The stopping of ions in compounds*, Nucl. Instr. and Meth. **B35** (1988) 215-228

[Zie92] Ziegler J.F., *Ion Implantation Technology* (Elsevier Science Publishers B.V., Amsterdam, 1992)

E.2 Companies

[App] Applied Materials UK Ltd., Foundry Lane, Horsham, W.-Sussex, RH13 5PX, England, UK (http://www.appliedmaterials.com/)

[Axc] Axcelis Technologies Inc., 55 Cherry Hill Drive, Beverly, MA 01915-1053, USA (http://www.axcelis.com/)

[Goo] Goodfellow Cambridge Ltd., Ermine Business Park, Huntingdon, Cambridgeshire, PE29 6WR, England, UK (http://www.goodfellow.com/)

E.3 World Wide Web sites

[www①] http://calspace.ucsd.edu/marsnow/library/mars_exploration/robotic_missions/landers/rovers/pathfinder_sojouner/mission2-rover/v4-3d-rover/b-f3-v4-08-01b.htm

[www②] http://www.ee.surrey.ac.uk/SCRIBA/ndf/

[www③] http://www.ee.surrey.ac.uk/SCRIBA/ndf/IBA14.htm, Barradas N.P., Webb R.P., Jeynes C., *WiNDF: a Windows interface to the DataFurnace code for analysing IBA data*, presented in IBA-14 conference in Dresden, July 1999

[www④] http://www.phys.tue.nl/FOG/techniques/LEIS.html

[www⑤] http://www.warwick.ac.uk/asp/

[www⑥] http://www.dl.ac.uk/MEIS/

[www⑦] http://www.srim.org/, Ziegler J.F., SRIM2000

[www⑧] http://www.physics.isu.edu/sigmabase/programs/simnra40.html

[www⑨] http://wos.mimas.ac.uk/